
A Dress Code for Galaxies: How the Interplay of Gas, Stars, Dark Matter and Environment Shapes Their Appearance in Simulations

Adelheid Franziska Teklu



München 2018

A Dress Code for Galaxies: How the Interplay of Gas, Stars, Dark Matter and Environment Shapes Their Appearance in Simulations

Adelheid Franziska Teklu

Dissertation
an der Fakultät für Physik
der Ludwig-Maximilians-Universität
München

vorgelegt von
Adelheid Franziska Teklu
aus München

München, den 31.10.2018

Erstgutachter: PD Dr. Klaus Dolag
Zweitgutachter: PD Dr. Martin Kerscher
Tag der mündlichen Prüfung: 20.12.2018

Für Lishan, Nahum, Yaron und yene bunama buna

Contents

Zusammenfassung	xi
1 Introduction	1
1.1 Galaxies Come in Different Shapes	1
1.2 Structure Formation in the Λ CDM Cosmology	5
1.2.1 Some Equations	5
1.2.2 How the Universe Evolved	6
1.3 The <i>Magneticum Pathfinder</i> Simulations	10
2 State-of-the-Art Galaxy Formation	17
2.1 Galaxy Formation and the Role of Angular Momentum	20
2.2 Satellites as an Estimate of the Morphology-Density Relation	24
2.3 Stellar Populations as Tracers of the Formation History?	26
2.4 Tracing Dark Matter Over Cosmic Time	27
3 The Interplay between Spin, Mass, & Morphology	29
3.1 Properties of Halos	30
3.1.1 The Angular Momentum	30
3.1.2 The Spin Parameter λ	32
3.1.3 Alignments	35
3.2 Kinematical Split-Up	35
3.2.1 The Circularity Parameter ε	36
3.2.2 The λ -Parameter	41
3.2.3 Alignments of the Central Components	42
3.3 Classification of Simulated Galaxies	43
3.3.1 Selection Criteria	43
3.3.2 Comparison of the Simulated Stellar Specific Angular Momentum with Observations	45
3.3.3 The Simulated Stellar Specific Angular Momentum at $z = 2$	46
3.3.4 The Gas and Stellar Specific Angular Momentum in Simulations and Observations	47
3.3.5 Comparison of the Gas and DM Specific Angular Momenta	49

3.3.6	Misalignment Angles	51
3.4	The Host Halos of Different Galaxy Types	54
3.4.1	The Alignment of the Host Halos with Their Centers	54
3.4.2	The Spin Parameter λ of the Host Halos	56
3.5	Further Details and Tests	61
3.5.1	Details on the Classification	61
3.5.2	The Alignment of the Galaxy with Its DM Halo	63
3.5.3	The Spin Parameter λ	64
3.5.4	The Radial Specific Angular Momentum Profiles	66
3.6	Discussion and Conclusions	68
4	Morphology, Environment, and Satellites	71
4.1	Classification of Simulated Galaxies	72
4.2	The Relation between the Stellar and Halo Mass of Central Galaxies	73
4.3	The Abundance of Satellites	78
4.3.1	Comparison of the Satellite Number with Recent Observations	79
4.3.2	Abundance of Satellites for $z > 0$	80
4.3.3	Radial Distribution of Satellites	82
4.3.4	Comparison of Companions and Centrals	85
4.3.5	Average Number of Satellites in Dependence of the Virial Mass	86
4.3.6	Massive Galaxies at High Redshift	87
4.4	Relation between Host and Satellite Properties	88
4.4.1	SFR and Formation Redshift of Satellites and Central Galaxies	89
4.4.2	Evolution of the SFR- z_{form} relation	92
4.4.3	The Relation between the Environment and the SFR	93
4.5	The World in Physical Units	96
4.5.1	Satellite Fraction in Physical Units	96
4.5.2	Morphology-Density Relation in Physical Units	96
4.6	Discussion and Conclusions	97
5	Stellar Populations, Kinematics & Morphology	101
5.1	Classification of Simulated Galaxies	102
5.1.1	Subclasses of Early-Type Galaxies	102
5.2	Stellar Populations in Galaxies of Different Types	103
5.2.1	Stellar Populations in Poster Child Disks and Spheroids	104
5.2.2	Stellar Populations in Disks, Intermediates and Spheroids	107
5.3	Stellar Populations in Late-Type Galaxies	114
5.4	Stellar Populations in Early-Type Galaxies	115
5.4.1	ETGs Divided into Slow and Fast Rotators	115
5.4.2	ETGs Divided into Kinematical Groups	118
5.5	Dependence of the Mass of the Old Component on Galaxy Type	122
5.6	Discussion and Conclusions	125

6 Declining Rotation Curves in ΛCDM	127
6.1 Sample of Galaxies	129
6.2 Rotation Curves at $z = 2$	130
6.3 DM Fractions	131
6.4 Surface Density, Dispersion and Theoretical Rotation Curve	133
6.5 Discussion and Conclusions	133
7 Summary and Conclusion	137
List of Figures	168
List of Tables	171
Danksagung	174

Zusammenfassung

Die Entstehung und Entwicklung von Galaxien ist noch immer nicht vollständig verstanden. Insbesondere die Details der Bildung unterschiedlicher Galaxientypen stehen seit vielen Jahrzehnten zur Diskussion. In Beobachtungen werden nur Momentaufnahmen der Galaxien gesehen und viele Teile eines komplexen Puzzles müssen zusammengesetzt werden.

In dieser Arbeit nutzen wir modernste hydrodynamische kosmologische Simulationen aus dem *Magneticum Pathfinder* Simulations-Set. In diesen bilden sich Galaxien, die viele beobachtete Skalierungsrelationen reproduzieren. Dank der Einbeziehung relevanter physikalischer Prozesse, verbesserter numerischer Methoden und hoher räumlicher Auflösung bilden sich sphäroidale Galaxien und Scheibengalaxien. Dies ermöglicht uns der Entwicklung von Galaxien zu folgen und deren sichtbare und dunkle Komponente zu erforschen. Jedes Kapitel dieser Arbeit befasst sich mit einem anderen Aspekt des Zusammenspiels zwischen Dunkle-Materie-Halo und der sich in ihm befindenden Galaxie. Hierfür werden verschiedene Indikatoren für die verschiedenen Wege der Galaxienentstehung diskutiert, z.B. die Kinematik der einzelnen Galaxienkomponenten, das Verhalten der die Galaxien umgebenden Satellitengalaxien, die Umgebung sowie die Sternpopulationen.

Zuerst fokussieren wir uns auf den Drehimpuls der sichtbaren Komponente, d.h. des Gases und der Sterne, und den sie umgebenden Dunkle-Materie-Halo. In Einklang mit Beobachtungen finden wir, dass, wenn man stellare Masse und den spezifischen (massegewichteten) Drehimpuls gegeneinander aufträgt, Scheiben- und sphäroidale Galaxien verschiedene Bereiche dieses Diagramms ausfüllen. Simulationen mit der baryonischen Komponente weisen eine Dichotomie in der Verteilung des Spinparameters auf, wobei Scheibengalaxien Halos mit leicht höherem Spin bewohnen als sphäroidale Galaxien. Betrachten wir die gleichen Galaxien in einer Simulation, die nur Dunkle Materie enthält, aber sonst dieselben Anfangsbedingungen hat, ist diese Dichotomie in der Verteilung des Spinparameters dennoch vorhanden. Dies legt nahe, dass der Halo "weiß", welche Art von Galaxie sich in seinem Zentrum befindet, und dass die Morphologie sowohl durch Prozesse während der Entstehung als auch durch die Umgebung geformt wird.

Weiterhin beschäftigen wir uns mit der Frage, ob die Eigenschaften der Satellitengalaxien den darunter liegenden Dunkle-Materie-Halo sowie dessen Zentralgalaxie gut repräsentieren. Unsere Simulation reproduziert die beobachtete Beziehung, wonach sphäroidale Galaxien von mehr Satelliten umgeben sind als Scheibengalaxien. Jedoch verschwindet

dieses Signal, wenn nur die Zentralgalaxien betrachtet werden. Dies zeigt, dass die größere Satellitenzahl für sphäroidale Galaxien von jenen sphäroidalen Satellitengalaxien verursacht wird, die große Satelliten im Dunkle-Materie-Halo einer Zentralgalaxie sind, allerdings ist die Unterscheidung in Satelliten und Zentralgalaxien in Beobachtungen schwer zu treffen. Daraus schließen wir, dass das Zählen von Satelliten die Morphologie-Dichte-Beziehung widerspiegelt und dass die Anzahl der Satelliten kein guter Indikator für die Masse des Dunkle-Materie-Halos ist, sofern das Sample von Hostgalaxien nicht auf Zentralgalaxien beschränkt ist. Zudem finden wir, dass sich die Morphologie-Dichte-Beziehung erst ab $z \approx 2$ aufzubauen beginnt und für sternbildende und inaktive Galaxien ähnlich ist.

Als nächstes untersuchen wir den Zusammenhang zwischen der Morphologie einer Galaxie und der Rotation der Sternpopulationen unterschiedlichen Alters. Die kinematische Analyse stützt ein Szenario, in dem sich die Scheibengalaxien relativ ruhig entwickelt haben, so dass die Scheiben intakt bleiben konnten, während der Drehimpuls der sphäroidalen Galaxien durch mehrere Merger gesenkt wurde. Wenn wir die sphäroidalen Galaxien nach ihrer Kinematik unterteilen, finden wir, dass jene Galaxien mit separat rotierenden Kernen verglichen zu den anderen sphäroidalen Galaxienklassen weniger alte Sterne enthalten. Dies deutet darauf hin, dass diese sphäroidalen Galaxien über verschiedene Entwicklungswege entstanden sind, die unterschiedliche Signaturen im Alter der stellaren Populationen und der stellaren Kinematik hinterlassen.

Im letzten Kapitel untersuchen wir, ob die beobachteten radial abnehmenden Rotationskurven und niedrige zentrale Anteile Dunkler Materie bei hohen Rotverschiebungen dem Λ CDM Modell widersprechen. Im Einklang mit Beobachtungen finden wir, dass etwa die Hälfte unserer Scheibengalaxien radial abnehmende Rotationskurven und niedrige zentrale Dunkle Materie-Anteile aufweist. Im Gegensatz zu den Vermutungen der Beobachter, dass diese Galaxien zu den heutigen massiven elliptischen Galaxien mit niedrigen Dunkle-Materie-Anteilen anwachsen, entwickeln sich unsere Scheibengalaxien zu verschiedenen Galaxientypen bei $z = 0$, einschließlich Scheibengalaxien mit allen Merkmalen typischer Scheibengalaxien der nahen Milchstraßenumgebung. Daher tritt die Existenz der beobachteten niedrigen Dunkle-Materie-Anteile und der abnehmenden Rotationskurven bei hoher Rotverschiebung natürlich aus dem Λ CDM Modell hervor. Zudem finden wir sphäroidale Galaxien bei $z = 2$, die Gasscheiben mit abnehmenden Rotationskurven besitzen. Mit derzeit verfügbaren Beobachtungstechniken ist es jedoch schwierig, diese zwei Populationen zu unterscheiden, was auf eine weitere Komplikation in der Klassifizierung von Galaxien bei hoher Rotverschiebung hindeutet.

Zusammenfassend konnten wir in dieser Arbeit zeigen, dass die Morphologie einer Galaxie eng mit den Details ihrer Entwicklungsgeschichte verknüpft ist, insbesondere auf die Verteilung des Drehimpulses und der stellaren Population. Des Weiteren haben wir den Einfluss der Umgebung, in der eine Galaxie entsteht, auf ihren Drehimpuls, ihre Kinematik und ihre Morphologie dargestellt. Daraus können wir klar schlussfolgern, dass das Zusammenspiel von Masse und Drehimpuls ein wichtiger Indikator für die Morphologie und andere kinematische und intrinsische Eigenschaften der Galaxie ist.

Abstract

The formation and evolution of galaxies is still not fully understood. Especially the details of how the different types of galaxies have formed has been a matter of debate for many decades. Observations only show snap-shots of galaxies and one has to put together many pieces of this complex puzzle.

In this work we profit from the advantage of state-of-the-art hydrodynamical cosmological simulations taken from the *Magneticum Pathfinder* simulation set, in which galaxies form that reproduce many observational scaling relations. Due to the inclusion of the relevant physical processes, the improved underlying numerical methods, and a high spatial resolution, populations of spheroidal and disk galaxies are produced self-consistently. This allows us to follow the evolution of galaxies and to study the visible as well as dark component. Each chapter of this thesis addresses a different aspect of the interplay of the halo and the galaxy residing within it. For this, various estimators and indicators of galaxy formation channels, such as the kinematics of the galaxy components, the satellites and the environment, as well as the stellar populations, are discussed.

We first focus on the angular momentum of the visible components, i.e. the gas and the stars, and the surrounding dark matter halo. In agreement with observations, we find that disk and spheroidal galaxies occupy different regions on the so-called stellar-mass-specific angular-momentum-of-stars plane ($M_* - j_*$ -plane). Simulations including the baryonic component show a dichotomy in the distribution of the spin parameter, with disk galaxies populating halos with slightly larger spin compared to spheroidal galaxies. We cross-match these galaxies to halos of the dark matter only run, with exactly the same initial conditions, but the initial gas particles are treated as collisionless dark matter particles. Even in this run, the distribution of the spin parameter reveals the dichotomy. This suggests that the halo “knows” what kind of galaxy lies in its center and that the morphology is shaped by the processes during its formation and environment simultaneously.

Then we explore if the properties of satellite galaxies represent well the underlying dark matter halo as well as the central galaxy. Our simulation reproduces the observed relation that spheroidal galaxies are surrounded by more satellites than disk galaxies. However, this signal disappears when only considering central galaxies. This shows that the split-up of the abundance of satellites is caused by the companion galaxies, which are large satellites in the dark matter halo of a central galaxy and which are difficult to distinguish

in observations. From this we conclude that counting the satellite galaxies around host galaxies is simply reflecting the morphology-density relation and that the number of satellites is not a good tracer for the dark matter halo mass, unless the sample of host galaxies is restricted to central galaxies. Furthermore, we find that the morphology-density relation starts to build up at $z \approx 2$ and is similar for star-forming and quiescent galaxies (centrals and companions).

Next, we investigate the connection between the morphology of a galaxy and the rotation of the stellar populations of different ages. The kinematical analysis supports a scenario in which the disk galaxies have evolved relatively quietly, so the disks could stay intact over time, while the angular momentum of the spheroidal galaxies has been lowered by several merger events. When we subdivide the early-type galaxies (ETGs) according to their kinematics, we find the galaxies with distinct cores to have a lower amount of old stars compared to the other classes of ETGs. This indicates that ETGs have formed via different evolutionary paths.

In the final chapter we study whether the observed decreasing rotation curves and low dark matter fractions at high redshifts contradict the Λ CDM paradigm. About half of our poster child disk galaxies exhibit declining rotation curves and low dark matter fractions. Contrary to the suggestion that these galaxies grow into present day's massive ellipticals with low dark matter fractions, our galaxies evolve to different kinds of galaxies at $z = 0$, including disks with observed dark matter fractions. Thus, the existence of the observed low dark matter fractions and declining rotation curves at high redshift emerge naturally from the Λ CDM paradigm. In addition, we find spheroidal galaxies at $z = 2$ that have gas disks, showing declining rotation curves. With currently available observation techniques it is difficult to separate these two populations.

In summary, we have shown in this work that the morphology of a galaxy is closely related to the details of its evolutionary history, in particular to the distribution of the angular momentum and the stellar population. Furthermore, we have shown the influence of the environment, in which a galaxy forms, on its angular momentum, its kinematics and its morphology. From this we can conclude that the interaction of mass and angular momentum is an important tracer of the morphology and other kinematic and intrinsic properties of the galaxy.

Chapter 1

Introduction

“The Arabs mentioned two lines of stars surrounding an image resembling a large fish below the throat of the Camel. Some of these stars belong to this constellation (Andromeda) and others belong to the constellation Pisces which Ptolemy mentioned as the twelfth constellation of the Zodiac. These two lines of stars begin from the *al-Laṭkhā al-Saḥābiya* (nebulous smear) located close to the fourteenth star which is found at the right side of the three (stars) which are above the girdle.”

ʿAbd al-Raḥmān al-Ṣūfi in his Book of the Fixed Stars, translation from Arabic to English by [Hafez \(2010\)](#)

These are the first known recordings of our neighbor galaxy Andromeda. At that time, around 964, the author, the Persian astronomer ʿAbd al-Raḥmān al-Ṣūfi, also known as Azophi, did not know that this nebula he was describing was far outside of our own galaxy. It took some time - to be more precise a millennium - until astronomers realized that some of the observed nebulae were not part of our own galaxy but large systems of stars and gas of their own. However, there were early speculations in the 18th century about the possibility that there might be other systems outside of our own ([Kant, 1755](#); [Swedenborg, 1734](#); [Wright, 1750](#)). In the 1920s there was the “great debate” about these nebulae; Harlow Shapley insisted they were part of our own galaxy, while Heber Curtis claimed they were outside of it. The debate was finally ended by [Hubble \(1925, 1926a\)](#), who proved that these nebulae were too far away to be inside the Milky Way (e.g., [Schneider, 2008](#)).

1.1 Galaxies Come in Different Shapes

There are different kinds of galaxies, which are most commonly classified into the main types ellipticals, lenticulars, spirals and irregular galaxies. As this classification was proposed by [Hubble \(1926b, 1936\)](#), it is referred to as the “**Hubble sequence**”. It is based on

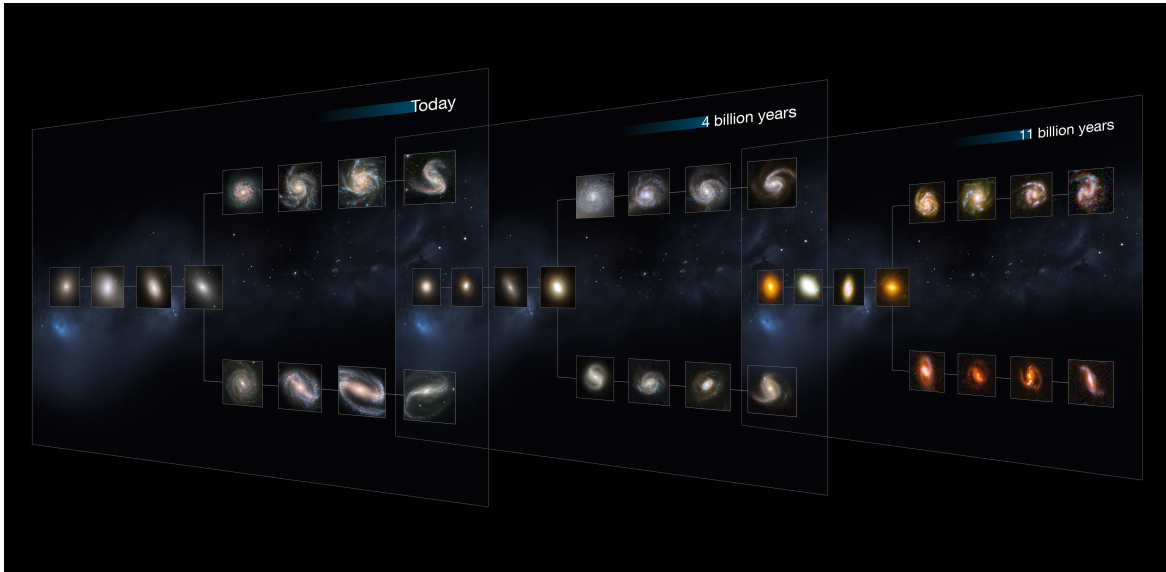


Figure 1.1.1: Hubble classes at present day (left slice), 4 billion (middle slice) and 11 billion years ago (right slice). On each slice the ellipticals are to the left, the S0 lie on the parting of the ways and the spirals are on the different branches, where those with bars are found at the bottom. When going further back in time, the galaxies become smaller and less evolved. Copyright: NASA, ESA, M. Kornmesser

the appearance of the galaxies on the optical photometric image, and was later extended by [de Vaucouleurs \(1959\)](#) and [Sandage \(1961\)](#). Fig. 1.1.1 illustrates the different galaxy types, where each slice shows galaxies at different times. When going from the left to the right slice we see further back in time.

On the left side of each slice we find the **elliptical galaxies**, also historically called “early-type” galaxies (ETGs). Usually they are additionally labeled E_n , with n being their ellipticity $\epsilon = (1 - b/a)$ without the decimal point, where a is the major and b the minor axis of the isophotes. The left most ellipticals due to their round appearance are classified as E0. From left to right the ellipticals become more elliptical, so the right most ellipticals are labeled as E7. In general, elliptical galaxies are dominated by the stellar bulge, do not have any obvious structure, and are red in the optical, indicating that they consist mainly of old stars.

On the right side of the scheme are the **spiral galaxies**, also called “late-type” galaxies (LTGs). In general, they consist of a disk with a spiral structure and a central bulge, which is often a pseudobulge ([Kormendy and Kennicutt, 2004](#)). On the Hubble sequence they divide into two branches, where the spirals on the lower branch have bars, therefore SB, while those on the upper branch do not show this feature, and are denoted by S. Additionally, from left to right they are ordered from a, ab, b, bc, c, cd to d, by the opening angle of their spiral arms, the resolution of the spiral arms into stars, and decreasing bulge-to-disk ratio (see e.g. [Longair, 2008](#)). Along this sequence, the spirals become bluer and

the amount of gas compared to the total mass increases (see e.g. [Schneider, 2008](#)).

In between the ellipticals and the spiral galaxies we find the **lenticular galaxies**, also called S0s. They appear as an intermediate morphological type, as they have a central bulge as well as a disk-like component but without a spiral structure. They can further be subdivided into normal and barred lenticulars, as many of them host a bulge with a bar-like appearance (e.g. [Longair, 2008](#)). Our Galaxy resembles an Sbc spiral (e.g. [Gerhard, 2002](#)) with a central bar (e.g. [Churchwell et al., 2009](#)).

Irregular galaxies have only very little (Irr I) or no (Irr II) obvious structure. Commonly, the Hubble sequence of the spirals is extended to Sdm, Sm, and Im, where m denotes “Magellanic” as they have a similar appearance to the Magellanic clouds.

In the local Universe, the galaxy population is made up of 8% elliptical, 70% spiral and 22% lenticular galaxies (e.g. [Cappellari et al., 2011a](#)). When going back in time the fractions of the various types, their shapes and their properties change; [van den Bergh et al. \(2000\)](#) (but also see [van den Bergh et al. \(1996\)](#)) report for 241 galaxies in the Hubble Deep Field up to a redshift of $z = 1.2$ that, in general, peculiar and merging galaxies become more frequent with increasing redshift (see also e.g., [Abraham et al., 1996](#)). Beyond $z = 0.3$ grand design spiral galaxies become rare, and for $z > 0.5$ also spirals with bars become very uncommon. Beyond $z = 0.6$, the spiral arms of Sa and Sb galaxies are less well-defined and those of Sc spirals are more chaotic. About 20% of the galaxies at $z > 0.8$ resemble local ellipticals, S0 or Sa galaxies. In general, galaxies become smaller with increasing redshift (see e.g., [Elmegreen et al., 2007](#)). When going further back in time it becomes increasingly difficult to detect the galaxies, as they become fainter. In addition, there are selection effects depending on the detection method which was used. However, [Förster Schreiber et al. \(2011\)](#) found the star-forming galaxies in their sample at $z \approx 2$ to be significantly clumpy. In a sample of so-called Lyman break galaxies, which are essentially actively star-forming galaxies (e.g. [Schneider, 2008](#)), at $z \approx 4$, [Lotz et al. \(2006\)](#) find a fraction of major mergers of 10-25%, 50% galaxies with smooth bulges and disks (which are likely star-forming disks, minor mergers or post merging systems) and about 30% spheroidal systems. At $z \approx 7$, [Oesch et al. \(2010\)](#) find the galaxies in their sample to be extremely compact.

Alternatively to the Hubble classification, which is based solely on the morphological appearance of the galaxies, other methods are in use to classify galaxies. Amongst others, it is common to separate disk-dominated and bulge-dominated systems by looking at their light distributions. This is done by evaluating the **Sérsic index** n ([Sersic, 1968](#)) by fitting the Sérsic profile, which can be seen as a generalization of the de Vaucouleurs’ law for bulges and elliptical galaxies ([de Vaucouleurs, 1948](#), often referred to as the $r^{1/4}$ law). Disk galaxies usually have $n \approx 1$, which corresponds to an exponential distribution of the light. Elliptical galaxies and bulges of disk galaxies have a value of $n \approx 4$ (e.g. [Longair, 2008](#)). The transition between these two types is found at $n \approx 2$ (e.g. [Driver et al., 2006](#)).

Another method is to decompose the disk and bulge component, i.e. to use the **bulge-to-total ratio** (B/T) (e.g., [Lilly et al., 1998](#); [Scott et al., 2017](#)). Galaxies with $B/T > 0.5$

can be seen as ETGs, and galaxies with $B/T < 0.5$ as LTGs (e.g. [Romanowsky and Fall, 2012](#)).

Galaxies can also be divided according to their color (see e.g. [Strateva et al., 2001](#)). As most disk galaxies are actively star-forming, they host massive and bright young stars, which are at the blue end of the main sequence for stars. Galaxies without star-forming activity mainly consist of old stellar populations, so they appear red (see e.g., [Rowan-Robinson, 2004](#)). On the color-magnitude diagram ETGs and LTGs populate different regions (e.g. [Baldry et al., 2004](#); [Tully et al., 1982](#)). Galaxies lying on the “red sequence” are mostly ETGs, while galaxies on the “blue cloud” are, in general, LTGs.

However, all of these classifications have their respective weaknesses; the Hubble classification, for example, is somewhat subjective, i.e. depending on the observer’s eye, and fault-prone due to the inclination of galaxies. Especially for ETGs the global morphology alone is not a good tracer ([Emsellem et al., 2011](#)). For the calculation of the Sérsic profile, one has to know the effective radius. However, it is not always straight forward to determine the effective radius, for example due to the sky background (e.g., [Trujillo et al., 2001](#)). The distinction of a galaxy according to its color does not always correspond to the morphological type, as the two populations overlap, where the spirals show a relatively large scatter (e.g. [Strateva et al., 2001](#)); in the local Universe there are red spirals (e.g. [Masters et al., 2010](#); [Wolf et al., 2009](#)) as well as blue ETGs (e.g. [Kannappan et al., 2009](#); [Schawinski et al., 2009](#)).

As the observational instruments became more and more advanced, especially the classical picture of the ETGs changed over the past decades. [Kormendy and Bender \(1996\)](#) proposed a revised classification scheme for the ETGs, which takes their physical properties into account. Therefore, the ETGs should be ordered by the shapes of their isophotes, i.e. from slowly rotating boxy ETGs to rapidly rotating disky ETGs.

Another physically motivated approach is to evaluate their ratio of rotational velocity to velocity dispersion, V/σ (e.g. [Lang et al., 2017](#)). Galaxies with $V/\sigma > 1$ are usually considered as disk-like galaxies; they are dynamically cold, as their rotational velocity dominates the overall kinematics. Those galaxies with $V/\sigma < 1$ are dominated by random motion and thus considered as dynamically hot systems.

However, [Emsellem et al. \(2007\)](#) introduced the λ_R parameter, which is a proxy for the specific angular momentum. Galaxies with $\lambda_R < 0.1$ were considered as slow rotators, while ETGs with $\lambda_R > 0.1$ were labeled as fast rotators. [Emsellem et al. \(2007, 2011\)](#) (see [Fig. 1.1.2](#)) demonstrated that slow and fast rotators could be separated better when λ_R was used instead of V/σ . Subsequently, this classification was refined by including the ellipticity ϵ .

Moreover, modern instruments reveal that the idea of all ETGs being “red and dead” is obsolete: ETGs are found to also have populations of young stars (e.g. [Kaviraj et al., 2007](#); [Trager et al., 2000](#)). In addition, they can also have gas disks (e.g. [Young, 2002](#)).

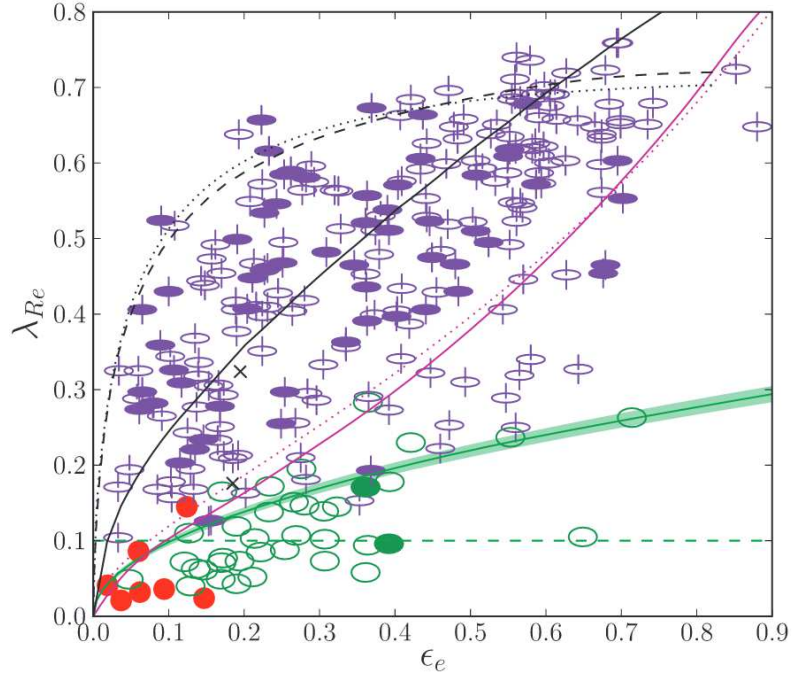


Figure 1.1.2: The λ_R parameter, which is a proxy for the specific stellar angular momentum versus the ellipticity ϵ . Elliptical galaxies split up into galaxies with no apparent rotation (red circles), nonregular rotators (green ellipses) and regular rotators (purple symbols). Galaxies with bars are represented by filled symbols. This figure is taken from [Emsellem et al. \(2011\)](#).

Before we discuss the possible formation scenarios of the galaxies, we briefly sketch the cosmology in which the picture is embedded.

1.2 Structure Formation in the Λ CDM Cosmology

In this section we describe how the Universe evolved from the beginning to today's state with all the structures we see. To start, we show the basic equations that describe the expanding universe.

1.2.1 Some Equations

The evolution of our Universe can be described by Einstein's field equations of general relativity. Commonly used are the solutions proposed by [Friedmann \(1922\)](#), also known as the Friedmann equations:

$$H^2 = \frac{8\pi G}{3}\rho - \frac{kc^2}{a^2} + \frac{\Lambda}{3}, \quad (1.1)$$

and

$$\frac{\ddot{a}}{a} = -\frac{4\pi G}{3}\left(\rho + \frac{3P}{c^2}\right) + \frac{\Lambda}{3}, \quad (1.2)$$

where $H := \dot{a}/a$ is the Hubble expansion rate, k is the curvature, a the scale factor, ρ is the density, Λ the cosmological constant, and P the pressure (see e.g., [Schneider, 2008](#), for a brief derivation). This solution assumes a completely homogeneous and isotropic Universe. In fact, on large scales, the distribution of matter and radiation is homogeneous and isotropic, as can be seen in the cosmic microwave background (CMB), in which this information is imprinted before structures could form (see e.g., [Perkins, 2003](#), and references therein).

The densities of matter and radiation are time-dependent; for pressureless matter we find $\rho_m \propto 1/a^3$ and for radiation $\rho_r \propto 1/a^4$. For the vacuum energy it is constant, $\rho_\Lambda = \Lambda/8\pi G = \text{const}$. It is useful to define the dimensionless density parameters for matter, radiation and vacuum: $\Omega_m = \rho_{m,0}/\rho_{\text{crit}}$, $\Omega_r = \rho_{r,0}/\rho_{\text{crit}}$, and $\Omega_\Lambda = \rho_\Lambda/\rho_{\text{crit}} = \Lambda/3H_0^2$, where $\rho_{\text{crit}} = 3H_0^2/8\pi G$ and the subscript 0 indicates the present-time values (see e.g., [Schneider, 2008](#), for a brief summary).

Another important parameter is the redshift. It is a measure of distance and time. As the Universe expands, the wavelength of a photon is redshifted. The redshift of a photon from a distant source emitted at t_{em} and which is observed today is defined as (see e.g., [Mukhanov, 2005](#))

$$z = \frac{\lambda_{\text{obs}} - \lambda_{\text{em}}}{\lambda_{\text{em}}}. \quad (1.3)$$

With $\lambda_{\text{obs}}/\lambda_{\text{em}} = a(t_{\text{obs}})/a(t_{\text{em}})$ this becomes

$$1 + z = \frac{a(t_{\text{obs}})}{a(t_{\text{em}})}. \quad (1.4)$$

1.2.2 How the Universe Evolved

The visible matter like the stars and gas of galaxies contributes just a small part ($\sim 5\%$) of the Universe's present-day content (see right pie chart of [Fig. 1.2.1](#)). The rest is made up of (cold) dark matter ($\sim 24\%$) and the major part is dark energy ($\sim 71\%$). However, the composition was different in the past, as one can see from the scalings of the densities ρ , described above.

About the very beginning of the Universe only speculations can be made. (If not noted otherwise, in this paragraph we follow [Mukhanov \(2005\)](#).) During the Planck epoch, which lasts until the Universe was 10^{-43}s old (which is comparable to a temperature $T \approx 10^{19}\text{GeV}$), quantum gravity effects dominated. It is assumed that the fundamental forces were unified to one single force during this time. The gravitational force first separated from the unified force of the Standard Model ([Rowan-Robinson, 2004](#)). Then, when the Universe was 10^{-35}s old ([Rowan-Robinson, 2004](#)), at a temperature of 10^{16}GeV , the electroweak and

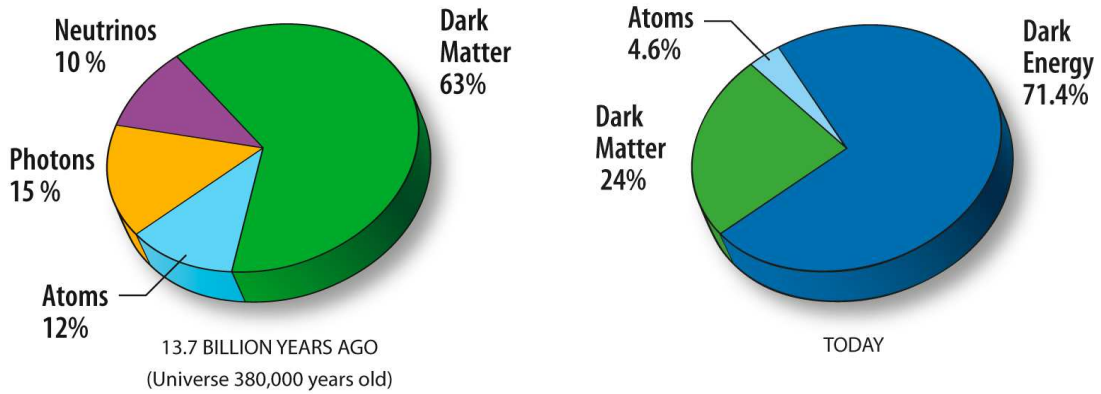


Figure 1.2.1: Content of the Universe at CMB (*left*) and today (*right*). At the time of the CMB, the Universe was matter dominated, while today it is dominated by the dark energy. Credit: NASA / WMAP Science Team

strong forces separated. At approximately the same time, inflation began and ended at 10^{-32} s (Schneider, 2008). When the temperature dropped below 100GeV, the gauge bosons of the weak interaction, Z^0 and W^\pm , became massive. Then, at temperatures of $T \approx 200$ MeV, free quarks and gluons formed hadrons, i.e. baryons (i.a., protons and neutrons) and mesons. After that, when the Universe was about 0.2s old (or $T \approx 1 - 2$ MeV), the primordial neutrinos decoupled, as the cross sections for the weak interaction had further decreased. In addition, the ratio of protons and neutrons “froze out”. This is important, as the number of neutrons determines the amount of primordial elements. When the temperature dropped below the rest mass of electrons and positrons, the pair production ($\gamma + \gamma \rightarrow e^+ + e^-$) became inefficient. Thus, only the reverse reaction, i.e. the annihilation of the pairs, continued (Schneider, 2008), where only the electrons are left over. From around 200s to 300s on, the so-called primordial nucleosynthesis took place, where protons and neutrons started to form atomic nuclei, especially helium (${}^4_2\text{He}$), but also other light elements as deuterium (${}^2_1\text{H}$), helium-3 (${}^3_2\text{He}$) and lithium-7 (${}^7_3\text{Li}$). At around 10^{12} s to 10^{13} s, which corresponds to $z \approx 1000$, the free electrons and protons recombined to neutral hydrogen. Thus, the Universe became transparent for radiation and thus, the photons and matter decoupled. The distribution of the matter at that time is therefore encoded in the CMB, in form of the measurable fluctuations. The left pie chart of Fig. 1.2.1 shows the composition of the Universe at that time. Since recombination, matter in the Universe is neutral (Schneider, 2008). As the following era is difficult to study observationally, it is called the “dark ages” (Longair, 2008).

(In the following part we follow Schneider (2008), where not noted otherwise.) The density fluctuations grow due to self gravitation, as overdense regions increase the density contrast δ , while in underdense regions the density contrast decreases. For the description of the growth of the density fluctuations (on large scales) one can use linear perturbation theory. For this we consider a fluid, which can be described by these equations of motion. The

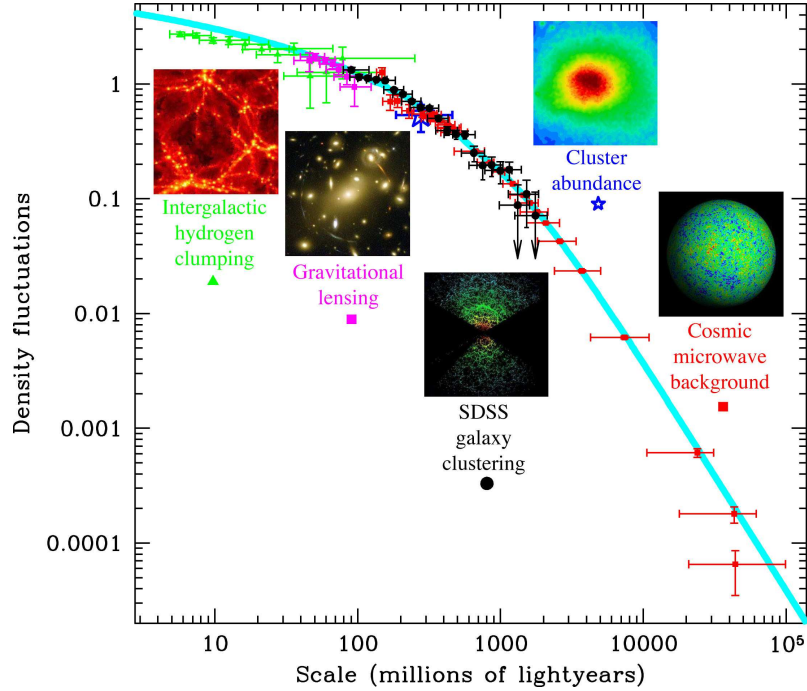


Figure 1.2.2: The density fluctuations as a function of time. The symbols/pictures indicate how they can be measured. The Λ CDM model is well in agreement with the measured values. Image credit: Max Tegmark, <http://space.mit.edu/home/tegmark/sdss.html>

continuity equation

$$\frac{\partial \rho}{\partial t} + \nabla \cdot (\rho \mathbf{v}) = 0 \quad (1.5)$$

describes that matter is conserved; if particles in the fluid move apart, the density decreases and if the field is convergent, the density increases. The Euler equation

$$\frac{\partial \mathbf{v}}{\partial t} + (\mathbf{v} \cdot \nabla) \mathbf{v} = -\frac{\nabla P}{\rho} - \nabla \Phi \quad (1.6)$$

characterizes the behavior under the influence of external forces and the conservation of momentum. As we only consider dust, we can set $P=0$. The current, on which the observer sits, is influenced by the gravitational field Φ . This field obeys the Poisson equation

$$\partial^2 \Phi = 4\pi G \rho. \quad (1.7)$$

However, this approximation breaks down for a density contrast $\delta \sim 1$ (which corresponds to the scale of superclusters, ~ 10 Mpc) and higher.

The formation and evolution of the structures that we see today is nonlinear, which is, in general, only numerically solvable. Qualitatively it can be described by the “spherical” or “gravitational collapse”. Regions with higher density than the average will expand slower due to gravity and thus, the density contrast increases further. When the density of the

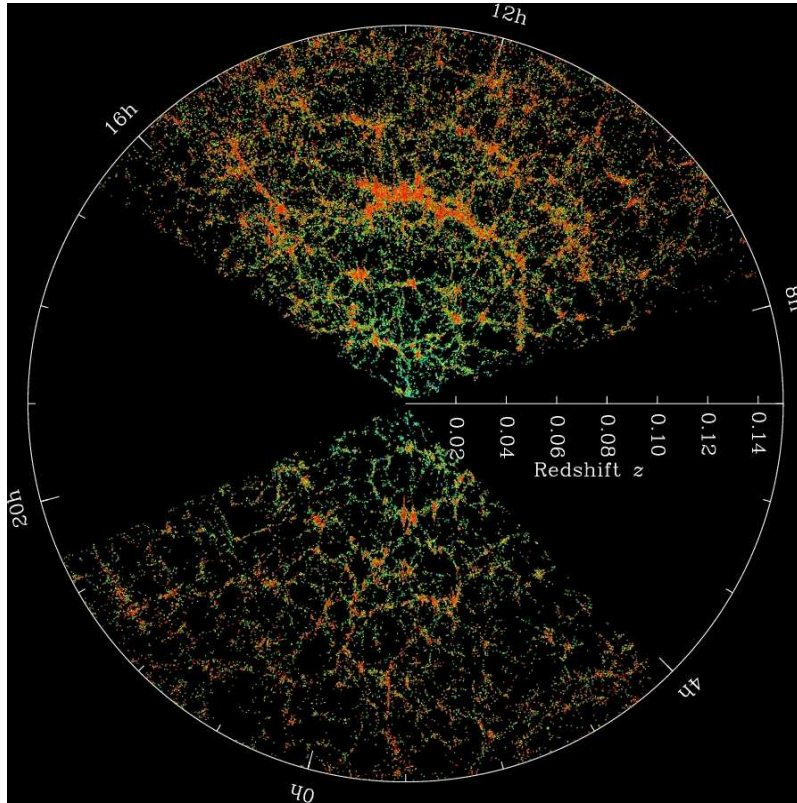


Figure 1.2.3: The map of the Universe as seen by the Sloan Digital Sky Survey (SDSS). The galaxies form the cosmic web. Credit: M. Blanton and SDSS

structures has become twice as high as the average density, they stop expanding (Primack, 2015). As a result, the structures that collapse earlier, are denser than those collapsing later. Therefore, dark matter halos of galaxies are denser than those of clusters (Primack, 2015).

At time of recombination, the dark matter has a higher density contrast, as it has decoupled earlier, and has formed potential wells. The baryons, i.e. the gas, can fall in these potential wells, so after some time the distribution of baryons becomes similar to that of the dark matter. When the baryons are dense enough, they start to form stars (Primack, 2015). These first stars are called Population III stars, and are assumed to have had high temperatures. The first generation of these Population III stars has formed at $z \sim 30$ in small dark matter halos. Later, at $z \sim 15$, in more massive halos the star formation becomes more efficient and the first protogalaxies form. These reionize the surrounding intergalactic medium, and finally, at a redshift of $z > 6$, the Universe becomes fully ionized.

The small structures then subsequently undergo merging events (White, 1978). Because of this hierarchical growth the small halos form larger halos and this finally leads to the large bound structures that we see today: groups, clusters, and superclusters.

Groups of galaxies consist of up to 50 gravitationally bound members within a sphere of diameter $1.5\text{Mpc}/h$ and have a typical mass of $3 \cdot 10^{13}M_{\odot}$ (e.g. [Schneider, 2008](#)). Special types of groups are compact and fossil groups. A *compact group* is a “small, relatively isolated system of typically four or five galaxies in close proximity to one another” ([Hickson, 1997](#)). The most famous example is Stephan’s Quintet. *Fossil groups* are brighter in the X-Ray compared to nonfossil groups (e.g. [D’Onghia et al., 2005](#)). Most of the member galaxies have merged to form a giant elliptical galaxy, which contributes about 70% to the optical light of the group. The second brightest galaxy is about 10 times fainter than the dominant elliptical (e.g. [Jones et al., 2000](#)).

The next larger structures are **clusters of galaxies**. They contain more than 50 members within a sphere of more than $1.5\text{Mpc}/h$ in diameter and have masses higher than $3 \cdot 10^{14}M_{\odot}$ (e.g. [Schneider, 2008](#)). Clusters are an important probe for the distribution and nature of dark matter and the formation of structure on large scales (e.g. [Longair, 2008](#)). In addition, they are good laboratories for studying the effects of the environment on the evolution of galaxies.

Superclusters are “clusters of clusters of galaxies” ([Abell, 1958](#)), which can contain a mass of up to $10^{17}M_{\odot}$. The diameter is in the order of 50Mpc (e.g. [Abell, 1961](#)).

In order to study how these structures grow, one needs to push the observations to higher redshifts. Another possibility is to use cosmological simulations, in which we can follow the nonlinear evolution and growth of the structures in the Universe like e.g. galaxies. In the following section we describe the simulations that were used for this work.

1.3 The *Magneticum Pathfinder* Simulations

The major part of this chapter has been published in [Teklu et al. \(2015, 2017, 2018\)](#)

In order to study the properties of galaxies in a statistically relevant manner, we need both a large sample size and high enough resolution to resolve the morphology and underlying physics of galaxies. Since the newest generation of cosmological simulations can achieve both, they are a valuable tool for this study. We take the galaxies for our studies from the *Magneticum Pathfinder* simulations, which are a set of state-of-the-art, cosmological hydrodynamical simulations with different volumes and resolutions (K. Dolag et al., in preparation). The simulations were performed with an extended version of the N -body/SPH code GADGET-3, which is an updated version of GADGET-2 ([Springel, 2005](#); [Springel et al., 2001b](#)). It includes various updates in the formulation of SPH regarding the treatment of artificial viscosity and the used kernels (see [Beck et al., 2016](#); [Dolag et al., 2005](#); [Donnert et al., 2013](#)).

It also includes a treatment of radiative cooling, heating from a uniform time-dependent ultraviolet (UV) background, and star formation with the associated feedback processes.

The latter is based on a subresolution model for the multiphase structure of the interstellar medium (Springel and Hernquist, 2003). Radiative cooling rates are computed following the same procedure presented by Wiersma et al. (2009). We account for the presence of the cosmic microwave background (CMB) and of UV/X-ray background radiation from quasars and galaxies, as computed by Haardt and Madau (2001). The contributions to cooling from each one of 11 elements (H, He, C, N, O, Ne, Mg, Si, S, Ca, Fe) have been precomputed using the publicly available photoionization code CLOUDY (Ferland et al., 1998) for an optically thin gas in (photo)ionization equilibrium.

In the multiphase model for star formation (Springel and Hernquist, 2003), the ISM is treated as a two-phase medium where clouds of cold gas form from cooling of hot gas and are embedded in the hot gas phase assuming pressure equilibrium whenever gas particles are above a given threshold density. The hot gas within the multiphase model is heated by supernovae (SNe) and can evaporate the cold clouds. A certain fraction of massive stars (10%) is assumed to explode as SNe II. The released energy by SNe II (10^{51} erg) is modeled to trigger galactic winds with a mass loading rate being proportional to the star formation rate (SFR) to obtain a resulting wind velocity of $v_{\text{wind}} = 350\text{km/s}$. Our simulations also include a detailed model of chemical evolution according to Tornatore et al. (2007). Metals are produced by SNe II, by SNe Ia, and by intermediate- and low-mass stars in the asymptotic giant branch (AGB). Metals and energy are released by stars of different mass by properly accounting for mass-dependent lifetimes (with a lifetime function according to Padovani and Matteucci (1993)), the metallicity-dependent stellar yields by Woosley and Weaver (1995) for SNe II, the yields by van den Hoek and Groenewegen (1997) for AGB stars, and the yields by Thielemann et al. (2003) for SNe Ia. Stars of different mass are initially distributed according to a Chabrier initial mass function (Chabrier, 2003).

Most importantly, our simulations also include a prescription for black hole (BH) growth and for feedback from active galactic nuclei (AGNs). based on the model presented in Springel et al. (2005) and Di Matteo et al. (2005), including the same modifications as in the study of Fabjan et al. (2010) and some new, minor changes.

As for star formation, the accretion onto BHs and the associated feedback adopt a subresolution model. BHs are represented by collisionless “sink particles” that can grow in mass by accreting gas from their environments, or by merging with other BHs. The gas accretion rate \dot{M}_{\bullet} is estimated using the Bondi-Hoyle-Lyttleton approximation (Bondi, 1952; Bondi and Hoyle, 1944; Hoyle and Lyttleton, 1939):

$$\dot{M}_{\bullet} = \frac{4\pi G^2 M_{\bullet}^2 f_{\text{boost}} \rho}{(c_s^2 + v^2)^{3/2}}, \quad (1.8)$$

where ρ and c_s are the density and the sound speed of the surrounding (ISM) gas, respectively, f_{boost} is a boost factor for the density, which typically is set to 100 and v is the velocity of the BH relative to the surrounding gas. The BH accretion is always limited to the Eddington rate (maximum possible accretion for balance between inward-directed gravitational force and outward-directed radiation pressure): $\dot{M}_{\bullet} = \min(\dot{M}_{\bullet}, \dot{M}_{\text{edd}})$. Note

that the detailed accretion flows onto the BHs are unresolved, and thus we can only capture BH growth due to the larger-scale gas distribution, which is resolved. Once the accretion rate is computed for each BH particle, the mass continuously grows. To model the loss of this gas from the gas particles, a stochastic criterion is used to select the surrounding gas particles to be removed. Unlike in [Springel et al. \(2005\)](#), in which a selected gas particle contributes with all its mass, we included the possibility for a gas particle to lose only a slice of its mass, which corresponds to 1/4 of its original mass. In this way, each gas particle can contribute with up to four ‘generations’ of BH accretion events, thus providing a more continuous description of the accretion process.

The radiated luminosity L_r is related to the BH accretion rate by $L_r = \epsilon_r \dot{M}_\bullet c^2$, where ϵ_r is the radiative efficiency, for which we adopt a fixed value of 0.1 (standardly assumed for a radiatively efficient accretion disk onto a nonrapidly spinning BH according to [Shakura and Sunyaev, 1973](#), see also [Di Matteo et al., 2005](#); [Springel, 2005](#)). We assume that a fraction ϵ_f of the radiated energy is thermally coupled to the surrounding gas so that $\dot{E}_f = \epsilon_r \epsilon_f \dot{M}_\bullet c^2$ is the rate of the energy feedback; ϵ_f is a free parameter and typically set to 0.1 (see discussion in [Steinborn et al. \(2015\)](#)). The energy is distributed kernel weighted to the surrounding gas particles in an SPH-like manner. Additionally, we incorporated the feedback prescription according to [Fabjan et al. \(2010\)](#): we account for a transition from a quasar- to a radio-mode feedback (see also [Sijacki et al., 2007](#)) whenever the accretion rate falls below an Eddington ratio of $f_{\text{edd}} := \dot{M}_r / \dot{M}_{\text{edd}} < 10^{-2}$. During the radio-mode feedback we assume a 4 times larger feedback efficiency than in the quasar mode. This way, we want to account for massive BHs, which are radiatively inefficient (having low accretion rates), but which are efficient in heating the ICM by inflating hot bubbles in correspondence to the termination of AGN jets. Note that we also, in contrast to [Springel et al. \(2005\)](#), modify the mass growth of the BH by taking into account the feedback, e.g., $\Delta M_\bullet = (1 - \eta_r) \dot{M}_\bullet \Delta t$. Additionally, we introduced some technical modifications of the original implementation, for which readers can find details in [Hirschmann et al. \(2014\)](#), where we also demonstrate that the bulk properties of the AGN population within the simulation are similar to observed AGN properties.

The simulation additionally follows thermal conduction, similar to [Dolag et al. \(2004\)](#), but with a choice of 1/20 of the classical Spitzer value ([Spitzer, 1962](#)). The choice of a suppression value significantly below 1/3 can be justified by comparison with full MHD simulations including an anisotropic treatment of thermal conduction (see discussion in [Arth et al. \(2014\)](#)).

The initial conditions are using a standard Λ CDM cosmology with parameters according to the seven-year results of the *Wilkinson Microwave Anisotropy Probe* (*WMAP7*; [Komatsu et al., 2011](#)). The Hubble parameter is $h = 0.704$, and the density parameters for matter, dark energy, and baryons are $\Omega_M = 0.272$, $\Omega_\Lambda = 0.728$, and $\Omega_b = 0.0451$, respectively. We use a normalization of the fluctuation amplitude at 8 Mpc of $\sigma_8 = 0.809$ and also include the effects of baryonic acoustic oscillations.

The *Magneticum Pathfinder* simulations have already been successfully used in a wide range

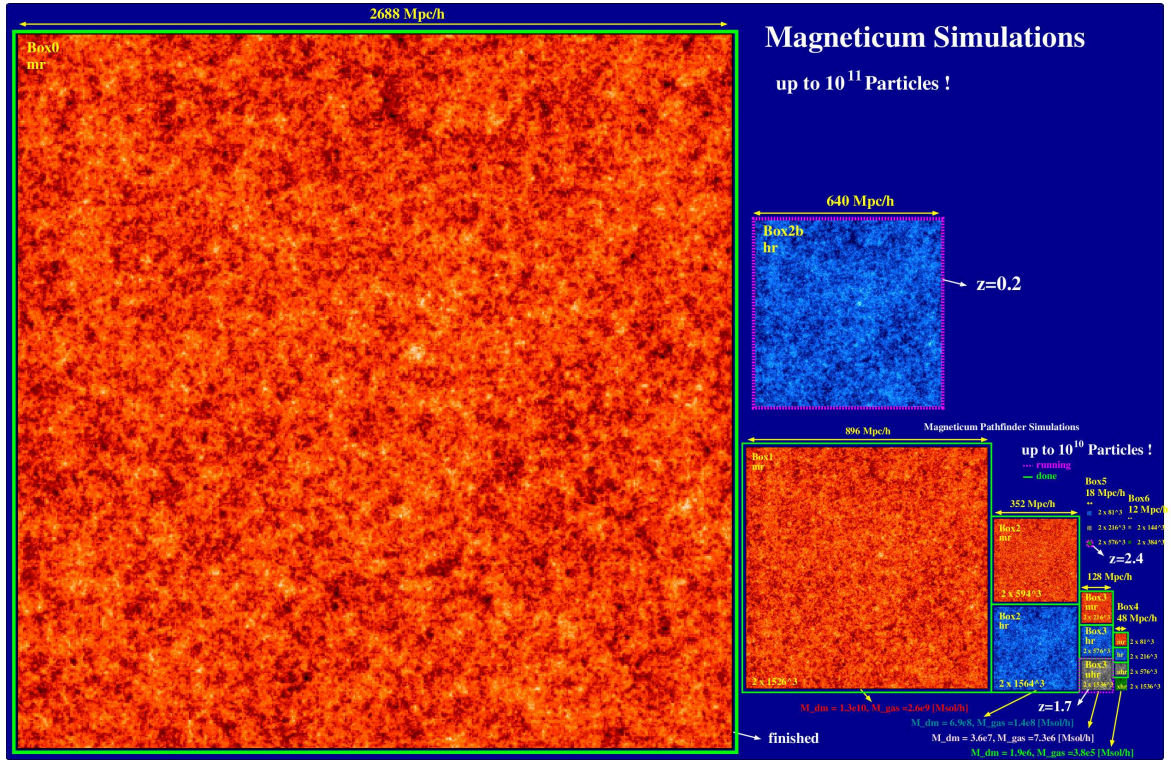


Figure 1.3.1: An overview of the *Magneticum Pathfinder* boxes of different sizes and resolutions. Courtesy of Klaus Dolag, www.magneticum.org

of numerical studies, showing good agreement with observational results for the pressure profiles of the intracluster medium (McDonald et al., 2014; Planck Collaboration et al., 2013), the predicted Sunyaev Zeldovich signal (Dolag et al., 2016), for the properties of the AGN population (Hirschmann et al., 2014; Steinborn et al., 2015, 2016), and for the dynamical properties of massive spheroidal galaxies (Remus et al., 2013, 2015). Furthermore, Steinborn et al. (2015) showed that the stellar mass functions are in good agreement with the observed ones at different redshifts and that the quiescent and star-forming populations have become more realistic. Also, Remus et al. (2015) presented mass-size relations of disc and elliptical galaxies that match the observed ones. In addition, internal properties were found to be in broad agreement with observational studies; Remus et al. (2017b) studied the radial density slopes and the DM fractions of ETGs. Especially, detailed properties of galaxies of different morphologies can be recovered and studied, for example the mass-size relations and their evolution (see e.g. Remus and Dolag, 2016; Remus et al., 2017b), global properties like the fundamental plane (Remus and Dolag, 2016), the baryon conversion efficiency (see e.g. Steinborn et al., 2015; Teklu et al., 2017), as well as the dynamical properties of early type galaxies (Schulze et al., 2018). Finally, Dolag et al. (2017) demonstrated that the simulations very well reproduce the observed relations for the metal abundances within the different parts of galaxies.

Table 1.1: Sizes, resolutions, particle numbers N_{part} , particles masses m_{DM} and m_{gas} , for DM and gas, and the softening length $\epsilon_{\text{DM/gas}}$ and ϵ_{star} for DM/gas and stars, respectively, of the *Magneticum Pathfinder* boxes

Box	Size [Mpc/h]	Resolution	N_{part}	m_{DM} [M_{\odot}/h]	m_{gas} [M_{\odot}/h]	$\epsilon_{\text{DM/gas}}$ [kpc/h]	ϵ_{star} [kpc/h]
Box0	2688	mr	2×4536^3	1.3×10^{10}	2.6×10^9	10	5
Box1	896	mr	2×1526^3	1.3×10^{10}	2.6×10^9	10	5
Box2b	640	hr	2×2880^3	6.9×10^8	1.4×10^8	3.75	2
Box2	352	mr	2×594^3	1.3×10^{10}	2.6×10^9	10	5
		hr	2×1584^3	6.9×10^8	1.4×10^8	3.75	2
Box3	128	mr	2×216^3	1.3×10^{10}	2.6×10^9	10	5
		hr	2×576^3	6.9×10^8	1.4×10^8	3.75	2
		uhr	2×1536^3	3.6×10^7	7.3×10^6	1.4	0.7
Box4	48	mr	2×81^3	1.3×10^{10}	2.6×10^9	10	5
		hr	2×216^3	6.9×10^8	1.4×10^8	3.75	2
		uhr	2×576^3	3.6×10^7	7.3×10^6	1.4	0.7
Box5	18	hr	2×81^3	6.9×10^8	1.4×10^8	3.75	2
		uhr	2×216^3	3.6×10^7	7.3×10^6	1.4	0.7
		xhr	2×576^3	1.9×10^6	3.9×10^5	0.45	0.25

The simulation set covers a huge dynamical range with a detailed treatment of key physical processes that are known to control galaxy evolution, thereby allowing to reproduce the properties of the large-scale, intragalactic, and intracluster medium (see e.g. Dolag et al., 2016; Gupta et al., 2017; Remus et al., 2017a). It contains boxes of different sizes and resolutions (see Table 1.1). The largest and smallest boxes have a volume of $(2688 \text{ Mpc}/h)^3$ and $(18 \text{ Mpc}/h)^3$, respectively. The resolutions in mass cover a range of $1.3 \cdot 10^{10} > m_{\text{DM}} > 1.9 \cdot 10^6 M_{\odot}/h$ for the dark matter and $2.6 \cdot 10^9 > m_{\text{gas}} > 3.9 \cdot 10^5 M_{\odot}/h$ for the gas particles. Each gas particle can form up to four star particles. For that reason the mass of an individual gas particle can decrease over time.

In this work we mainly used a medium-sized $(48 \text{ Mpc}/h)^3$ cosmological box *Box4* at the *uhr* resolution level, initially sampled with $2 \cdot 576^3$ particles (dark matter and gas), leading to a mass resolution of $m_{\text{DM}} = 3.6 \cdot 10^7 M_{\odot}/h$ for the dark matter, $m_{\text{gas}} = 7.3 \cdot 10^6 M_{\odot}$ for the gas and $m_{\text{stars}} = 1.8 \cdot 10^6 M_{\odot}$ for stellar particles, with a plummer equivalent gravitational softening corresponding to $0.23 \text{ kpc}/h$ at $z = 2$ and $0.7 \text{ kpc}/h$ at $z = 0$ for the star particles and twice this value for the dark matter and gas particles. This box is chosen to guarantee a meaningfully statistical number of galaxies as well as a sufficient resolution for studying galaxies and, in particular, their kinematics.

Additionally, we performed a DM-only reference run, where we kept exactly the same initial conditions, e.g., the original gas particles were treated as collisionless DM particles. This box is used in Chapter 3. For the studies in Chapter 4, we use the new cosmological box

Box3 with a larger volume of $(128 \text{ Mpc}/h)^3$ at the same resolution level, evolved with a slightly updated black hole treatment, as described by [Steinborn et al. \(2015\)](#), reaching a redshift of $z = 2$.

To identify subhalos we used a version of SUBFIND ([Springel et al., 2001a](#)), adapted to treat the baryonic component ([Dolag et al., 2009](#)). SUBFIND detects halos based on a standard Friends-of-Friends algorithm ([Davis et al., 1985](#)) and self-bound subhalos around local density peaks within the main halos. The virial radius of halos is evaluated according to the density contrast based on the top-hat model ([Eke et al., 1996](#)). For comparison with some observations, we also use an overdensity with respect to 200 times the critical density for calculating global properties when needed.

In further post-processing steps we then extract the particle data for all halos and compute additional properties for the different components and within different radii, using the full (thermo) dynamical state of the different particle species.

Chapter 2

State-of-the-Art Galaxy Formation

Parts of this section have been published in [Teklu et al. \(2015\)](#)

The question of how the different types of galaxies formed, and, in particular, which properties determine a galaxy to become a disk or spheroidal, has been a matter of debate since the discovery that the Universe is full of stellar islands of different morphology. Are there differences in the very beginning, during the assembling of the underlying dark matter halo, before the galaxy even forms? Or do the differences arise during the epoch of the formation of the galaxy itself?

The basic formation process of a galaxy can be sketched as follows (see e.g., [Schneider, 2008](#)): The gas that assembles in the halo is expected to settle in a disk, as it has a finite angular momentum and can dissipate heat. In this disk the gas then becomes dense, so it can cool and finally form stars. This would naturally lead to a galaxy with a star-forming disk.

Does that mean that all galaxies were born as disk galaxies? If so, then what kind of processes can shape the galaxies and lead to the variety of morphologies of galaxies seen today?

There are several processes that can be involved in the further evolution of a galaxy. Among these processes are, e.g. stellar feedback, SNe feedback, AGN feedback, (internal) secular evolution, gas accretion from the hot halo or cosmic filaments (cold streams), and processes that are associated with the environment. Among these environmental processes are minor and major mergers, and effects particularly related to a cluster or group environment, such as ram-pressure stripping, tidal stripping, harassment, or strangulation.

In the following we briefly describe some of the processes at work and their effects on the galaxies:

- The feedback processes of (massive) stars and SNe work similarly by heating the surrounding gas and preventing it from cooling. In this way there will be only a

moderate star formation (see e.g. [Schneider, 2008](#)).

- The AGN feedback also suppresses star formation. This kind of feedback is particularly important for massive galaxies (see e.g. [Steinborn et al., 2015](#)).
- Secular evolution acts on long time scales. Due to interactions that involve bars, the spiral structure, or triaxial dark matter halos, the energy and mass in the galaxy are slowly redistributed. These processes can lead to the formation of pseudobulges and seem to be most important for intermediate LTGs (i.e. Sbc's) (for a review see [Kormendy and Kennicutt, 2004](#)).
- Cold gas streams feed the galaxies at high redshift ($2 < z < 3$). Smooth streams build up an unstable, dense, gas-rich disk, while very clumpy streams can lead to the formation of a passive spheroid-dominated galaxy ([Dekel et al., 2009](#)).
- In the classical picture, major mergers (mass ratio $> 1:3$, see Fig. 2.0.1 for an example) of two (spiral) galaxies result in an elliptical galaxy; during the merging process the gas is violently shocked, so there is a short event of rapid star formation, i.e. a starburst (see e.g. [Binney and Tremaine, 2008](#)). In addition, the gas is heated to the virial temperature of the halo, so the future star formation is suppressed (see e.g. [Schneider, 2008](#)). The galaxy is left with a dominant spheroidal component. However, if we also take different parameters like for example the orbital configurations or the gas fractions into account, this picture becomes more complex. [Springel and Hernquist \(2005\)](#), for example, showed that it is possible to form a spiral during a gas-rich major merger.
- In a minor merger, the larger galaxy accretes the gas from the smaller galaxy and can form new stars. While the satellite orbits around the large galaxy it is slowly disrupted by tidal forces. The Magellanic Clouds or the Sagittarius Dwarf Galaxy are in the process of merging with our Milky Way (see e.g. [Schneider, 2008](#)).
- Ram-pressure stripping ([Abadi et al., 1999](#); [Gunn and Gott, 1972](#)) acts on shorter time scales: as the galaxy falls towards the center of a cluster, the gas is removed from the galaxy by the hot gaseous medium and the star formation is rapidly shut down (e.g. [Boselli et al., 2008](#)). For an example of an ongoing stripping in observations, see [Jaffé et al. \(2015\)](#).
- Tidal stripping (e.g. [Merritt, 1984](#)) occurs when galaxies have a close inelastic encounter, which then causes them to lose mass, but also occurs on a first passage of a merger.
- One speaks of harassment ([Moore et al., 1996](#)) when the galaxy undergoes (repeatedly) high speed encounters. This only happens in a cluster environment, where galaxies have relatively high speed due to the deep potential of the cluster. As shown by [Moore et al. \(1998\)](#), small disk galaxies get distorted, and after a phase of star bursts they evolve to spheroidal systems.



Figure 2.0.1: Arp87: two (former) spirals NGC 3808A and NGC 3808B which are involved in an ongoing merging. One can clearly see a bridge of gas between these two. Credit: NASA, ESA, Hubble Space Telescope, D. Gardener

- Strangulation ([Balogh et al., 2000](#); [Larson et al., 1980](#); [Peng et al., 2015](#)) is a process that acts on longer time scales: the galaxies are cut off from their cold gas supply, but they can continue to form stars with the remaining gas. Thus, they increase their stellar mass and become enriched in metals, but eventually run out of gas and “die”.

The relative importance of the various mechanisms is still not clear and a matter of debate, especially regarding the question if the environmental effects or the intrinsic properties of the galaxies are more important for their evolution. This issue is also known as “nature versus nurture” ([Cooper et al., 2007](#)).

There might not be an easy and definite answer to this matter. However, simulations can help to shed light on the life of galaxies. One of the advantages of simulations is that the impact of different processes on the evolution of galaxies can be probed in detail.

[Oser et al. \(2010\)](#) analyzed cosmological zoom simulations and proposed a detailed two-phase formation scenario: At redshifts $z > 2$, stars form “in-situ” from infalling cold gas. Then via small satellite galaxies, they accrete “ex-situ” stars, which have formed before $z > 3$ outside the galaxy. Thereby, the galaxies grow in mass and size. This also explains the “downsizing” ([Cowie et al., 1996](#)), where more massive galaxies are older, which is at first sight a contradiction to a hierarchical scenario. With this two-phase scenario one can explain why the stars in massive galaxies are old. But this does not mean that the galaxies themselves are old, as they can have assembled late.

For elliptical galaxies the following formation scenarios are discussed: from observations of ongoing mergers between galaxies of similar masses we know that spheroids can form in a major merger event between (spiral) galaxies. This has been supported by many simulations (e.g. [Barnes and Hernquist, 1996](#); [Naab et al., 2006](#); [Toomre, 1977](#); [White, 1978, 1979](#)). However, this scenario is not sufficient to explain certain observational properties, especially for the most massive galaxies. Thus, an alternative formation scenario through a series of multiple minor merger events was proposed by [Meza et al. \(2003\)](#) and established by, e.g., [Naab et al. \(2009\)](#), [González-García et al. \(2009\)](#), [Oser et al. \(2010\)](#), and [Johansson et al. \(2012\)](#).

For the formation scenarios of (today's) spiral galaxies, the details of their formation processes are less well known, but all the different channels discussed in the literature over the past decades are connected to the detailed buildup of the angular momentum and how the gaseous component transports intrinsic angular momentum into the central part of the halo, where the galaxy assembles. Initially, the dark matter (DM) halo and the infalling gas have identical angular momenta, but during the formation of the galaxy the gas cools and condenses in the center of the halo to form a disk. Assuming that the angular momentum of the gas is conserved during this process, the angular momentum of the halo of a disk galaxy can be estimated directly from the angular momentum of the disk of the galaxy ([Fall, 1983](#); [Fall and Efstathiou, 1980](#); [Mo et al., 1998](#)).

In the following subsections we focus on various influences that play a role in the evolution of galaxies. We will give a short overview of the work that has been done so far by other authors in the according field.

2.1 Galaxy Formation and the Role of Angular Momentum

... or the Influence of Your Parental Home...

The content of this section has been published in [Teklu et al. \(2015\)](#)

In hierarchical scenarios of structure formation, structures form through the gathering of clumps owing to the gravitational force ([Peebles, 1993](#), and references therein). The DM collapses at high redshifts into small objects, which grow into larger objects through merging and finally build halos. Those halos are not completely spherically symmetric owing to tidal torques induced by neighboring halos. The baryons condense in the centers of these DM halos and form the first protogalaxies ([White and Rees, 1978](#)). Since the baryons and the DM originally gained the same amount of angular momentum through these tidal torques ([Doroshkevich, 1970](#); [Peebles, 1969](#)) and the angular momentum of the gas should be conserved during the collapse, the disk is expected to have a similar specific angular momentum to that of its hosting halo ([Fall and Efstathiou, 1980](#)).

In contrast to observations, numerical N -body simulations have the advantage that structures can be followed through time, enabling the detailed understanding of the early stages of galaxy formation. Until recently, simulations using traditional smoothed particle hydrodynamics (SPH) codes suffered from the so-called angular momentum problem, where the objects became too small compared to observations because the gas had lost too much angular momentum (e.g. [Navarro and Benz, 1991](#); [Navarro and Steinmetz, 1997](#); [Navarro and White, 1994](#)). [Sijacki et al. \(2012\)](#) showed that SPH simulations overestimate the number of elliptical galaxies owing to the lower amount of mixing, and therefore causing this spurious “angular momentum crisis” of the baryons. On the opposite side, adaptive mesh refinement (AMR) or moving mesh simulations tend to overpredict the amount of disk-like galaxies in the absence of any feedback ([Scannapieco et al., 2012](#)). As simulations become better in resolution and also include feedback from stars, supernovae (SNe), and active galactic nuclei (AGNs), the gas is prevented from cooling too soon. Hence, early star formation is suppressed and the associated loss of angular momentum can be minimized. There are several studies that investigate the influence of star formation and the associated SN feedback on the formation of galactic disks (e.g. [Brook et al., 2004](#); [Governato et al., 2007](#); [Okamoto et al., 2005](#); [Scannapieco et al., 2008](#); [Zavala et al., 2008](#)). They find that strong feedback at early times leads to the formation of more realistic disk galaxies. A more recent study on the effect of stellar feedback on the angular momentum is presented in [Übler et al. \(2014\)](#), where they found that strong feedback favors disk formation. A recent, detailed summary of disk galaxy simulations can be found in [Murante et al. \(2015\)](#).

One parameter to describe the rotation of a system is the so-called spin parameter λ , which was introduced by [Peebles \(1969, 1971\)](#) and has since been investigated in several studies. With λ it is possible to measure the degree of rotational support of the total halo. It has the advantage that it is only weakly depending on the halo’s mass and its internal substructures ([Barnes and Efstathiou, 1987](#)). The connection of this parameter with galaxy formation has been studied by many authors.

At first, DM-only simulations were employed. [Bullock et al. \(2001\)](#) introduced a modified version of the λ -parameter by defining the energy of the halo via its circular velocity. In addition, they studied the alignment of the angular momentum of the inner and outer halo parts. They found that most halos were well aligned but that about 10% of the halos showed a misalignment. [Aubert et al. \(2004\)](#) investigated the alignment between the inner spin of halos and the angular momentum of the outer halo and also the alignment between the inner spin and the angular momentum of the inflowing material. The misalignment angle of the angular momentum vectors at different radii was studied in more detail by [Bailin and Steinmetz \(2005\)](#), who showed that with increasing separation of the radii the misalignment of the vectors increases. In another study, [Macciò et al. \(2008\)](#) focused on the spin parameter’s dependency on the mass and the cosmology and found no correlations. [Trowland et al. \(2013\)](#) studied the connection of the halo spin with the large-scale structure. They confirmed that the spin parameter is not mass dependent at low redshift but found a tendency to smaller spins at higher redshifts.

Other authors included nonradiative gas in their analysis. The misalignment of the gas and DM angular momentum vectors and their spin parameters at redshift $z = 3$ were investigated by [van den Bosch et al. \(2002\)](#). They found the angular momentum vectors to be misaligned by a median angle of about 30° . However, the overall distributions of the spin parameters of the gas and the DM were found to be very similar. Another detailed study by [Sharma and Steinmetz \(2005\)](#) and [Sharma et al. \(2012\)](#) found that the spin parameter of the gas component is on average higher than that of the DM, and they reported a misalignment of the angular momentum of the gas and the DM of about 20° .

[Chen et al. \(2003\)](#) compared the spin parameter and the misalignment angles between the DM and gas angular momentum vectors obtained in simulations, which include radiative cooling. This enables a splitting of the gas into a cold and a hot component. In their nonradiative model they confirmed that the spin parameter of the gas component has higher spin than the DM, while in their simulations with cooling the two components had approximately the same spin. The misalignments of the global angular momentum vectors were 22.8° and 25° for the two different cooling models and 23.5° for the nonradiative case. [Stewart et al. \(2011, 2013\)](#) focused on the specific angular momentum and the spin parameter in relation to the cold/hot mode accretion by following the evolution of individual halos over cosmic time. They found that the spin of cold gas was the highest compared to all other components and about 3 – 5 times higher than that of the DM component. [Scannapieco et al. \(2009\)](#) investigated the evolution of eight individual halos from zoom simulations and did not find a correlation between the spin parameter and the morphology of the galaxy. However, they found a correlation between the morphology and the specific angular momentum: for disks, the specific angular momentum can be higher than that of the host halo, while spheroids tend to have lower specific angular momentum. In addition, they saw a misalignment between stellar disks and infalling cold gas. Also, [Sales et al. \(2012\)](#) reported no correlation between the spin parameter and the galaxy type and concluded that disks are predominantly formed in halos where the freshly accreted gas has similar angular momentum to that of earlier accretion, whereas spheroids tend to form in halos where gas streams in along misaligned cold flows. The angular momentum properties of the inflowing gas were studied by [Pichon et al. \(2011\)](#). They found that the angular momentum of the cold dense gas is well aligned with the angular momentum of the DM halo, in contrast to the hot diffuse gas. Additionally, an increase of the advected specific angular momentum of the gas component with cosmic time was noticed. They proposed a scenario in which the angular momentum of the galaxies is fed by the collimated cold flows that are amplified with time and make the disks larger. [Kimm et al. \(2011\)](#) studied the different behavior of the gas and DM specific angular momentum by following the evolution of a Milky-Way-type galaxy over cosmic time. They also found that the gas has higher specific angular momentum and spin parameter than the DM. [Hahn et al. \(2010\)](#) investigated a sample of about 100 galactic disks and their alignment with their host halo at three different redshifts. Both the stellar and gas disks had a median misalignment angle of about 49° with respect to the hosting DM halo at $z = 0$.

Some works focused explicitly on the effect that baryons have on the DM halo by run-

ning parallel DM-only simulations. [Bryan et al. \(2013\)](#), who extracted halos from OWLS ([Schaye et al., 2010](#)), did not find a dependency of the spin parameter on mass, redshift, or cosmology in their DM-only runs. In the simulations that included baryons and strong feedback, the overall spin was found to be affected only very little, while the baryons had a noticeable influence on the inner halo, independent of the feedback strength. [Bett et al. \(2010\)](#) investigated the specific angular momentum and the misalignment of the galaxy with its halo. They obtained a median misalignment angle of about 25° for the DM-only runs and about 30° for the run including baryons. The baryons were found to spin up the inner region of the halo.

Recently, [Welker et al. \(2014\)](#) studied the alignment of the galaxy spins with their surrounding filaments, using the Horizon-AGN simulation ([Dubois et al., 2014](#)). They find that halos experiencing major mergers often lower the spin, while in general minor mergers can increase the amount of angular momentum. If a halo does not undergo any mergers but only smooth accretion, the spin of the galaxy increases with time, in contrast to that of its hosting DM halo. Since the gas streams and clumps in general move along the filaments, the galaxies realign with their filaments. [Danovich et al. \(2015\)](#) have investigated the buildup of the angular momentum in galaxies, using a sample of 29 resimulated galaxies at redshifts from $z = 4$ to 1.5. Overall the spin of the cold gas was about three times higher than that of the DM halo, in line with previous studies. [Genel et al. \(2015\)](#) explored the importance of stellar and AGN feedback for the evolution of the angular momentum of the galaxies in the Illustris simulations, finding the angular momentum of their simulated galaxies to be in good agreement with observations for a chosen feedback similar to the one used in this work.

Observations indicate that the morphology of galaxies is strongly influenced by the relation between mass and angular momentum (see [Fall, 1983](#), Fig. 2.1.1). The angular momentum of disk galaxies was found to be about six times higher than that of the ellipticals of equal mass. [Romanowsky and Fall \(2012\)](#) and [Fall and Romanowsky \(2013\)](#) revisited and extended this work, analyzing 67 spiral and 40 early-type galaxies. They found that lenticular (S0) galaxies lie between spiral and elliptical galaxies in the so-called $M_{\text{star}} - j_{\text{star}}$ -plane. The bulges of spiral galaxies follow a similar relation because they behave like “mini-ellipticals.” [Obreschkow and Glazebrook \(2014\)](#) used data from high-precision measurements of 16 nearby spiral galaxies to calculate the specific angular momentum of the gas and the stars. They confirmed observationally that the mass and angular momentum are strongly correlated with the morphology of galaxies. [Hernandez and Cervantes-Sodi \(2006\)](#) calculated the λ -parameter for two galaxy samples with a total of 337 observed spirals and found that with decreasing bulge-to-disk ratio the spirals have increasing λ -values. In a further study [Hernandez et al. \(2007\)](#) investigated a sample of 11,597 spiral and elliptical galaxies from the Sloan Digital Sky Survey (SDSS) and found that ellipticals on average have lower λ -values than spiral galaxies.

In Chapter 3 we investigate the connection between the dark matter halos and the baryonic component, i.e. the galaxies, in their centers, focusing on the angular momentum and the

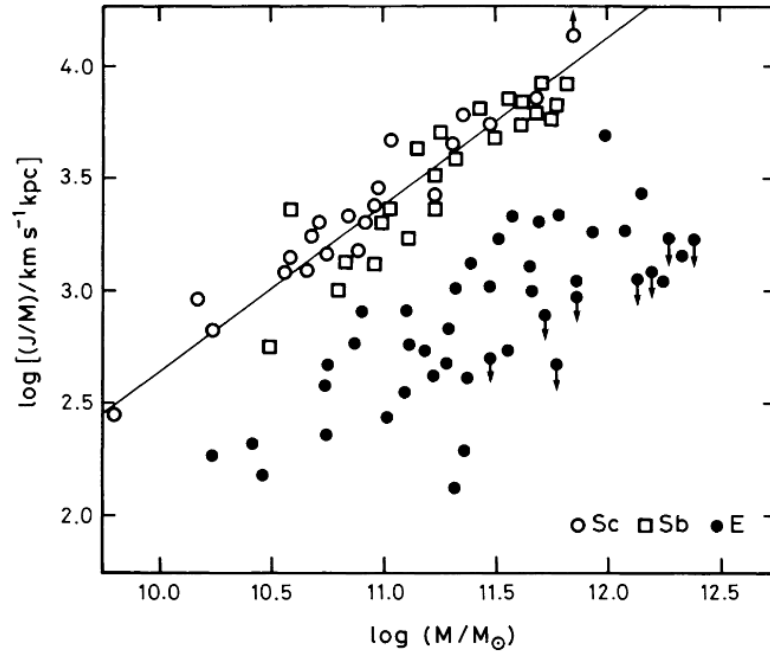


Figure 2.1.1: The stellar-mass–angular-momentum ($M_* - j_*$) plane. Spiral galaxies and elliptical galaxies populate separate regions. This figure is taken from Fall (1983).

influence on the morphology of the galaxy.

2.2 Satellites as an Estimate of the Morphology-Density Relation

... or the Influence of Your Neighborhood...

The content of this section has been published in Teklu et al. (2017)

Observationally, dark halo masses for galaxies are difficult to measure. Indirect measurement methods are needed to infer the halo mass from observable quantities, for example from hot X-ray halo gas (e.g. Gonzalez et al., 2013; Kravtsov et al., 2018), weak galaxy-galaxy lensing (e.g. Leauthaud et al., 2012; Mandelbaum et al., 2006), satellite velocities (e.g. Conroy et al., 2007) or the number of satellites (e.g. Wang and White, 2012), although discrepancies exist between the results of the different methods (Dutton et al., 2010).

Several observational studies find that the number of satellite galaxies depends on the morphology of the host galaxy, namely that ETGs have more satellite galaxies than LTGs of the same stellar mass (e.g. Nierenberg et al., 2012; Ruiz et al., 2015; Wang and White, 2012), leading to the conclusion that ETGs live in more massive dark matter halos than LTGs. Furthermore, López-Sanjuan et al. (2012) find that the ETGs have three times

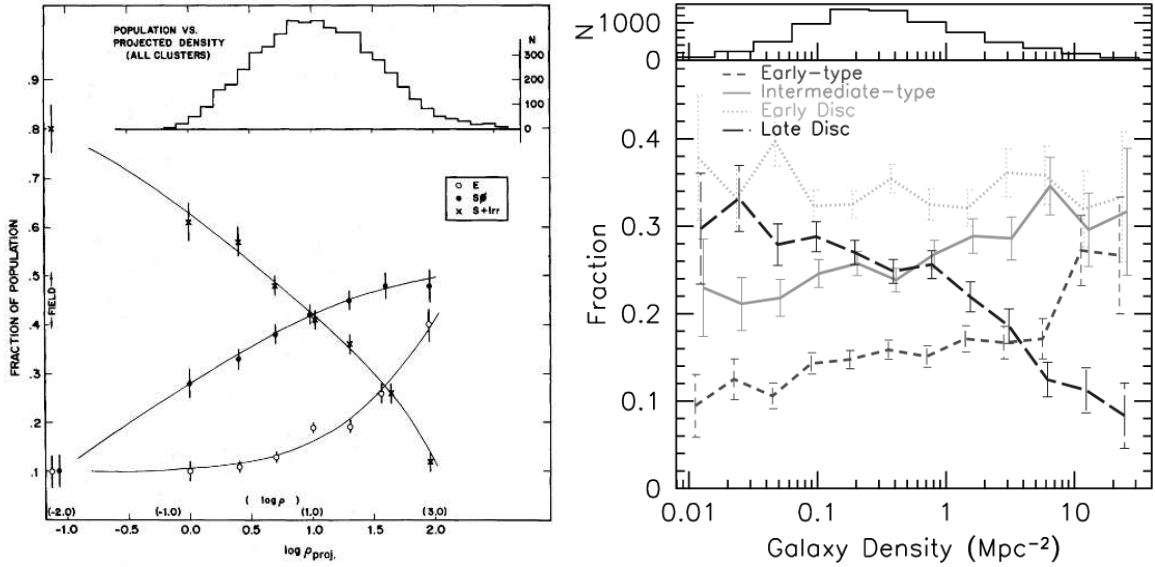


Figure 2.2.1: The morphology-density relation. ETGs galaxies live in dense regions, whereas LTGs mainly populate low density regions. The *left* figure is taken from Dressler (1980) and the *right* from Goto et al. (2003).

more minor mergers than LTGs, with a basically constant rate since $z = 1$, which supports the idea that ETGs have more satellites than LTGs. However, Liu et al. (2011) do not find a different satellite fraction for red and blue Milky Way mass galaxies from the Sloan Digital Sky Survey (SDSS).

The number of satellite galaxies is also correlated with the stellar mass of the central galaxy (e.g. Bundy et al., 2009; Nierenberg et al., 2012, 2016; Wang and White, 2012), in that more massive galaxies have more satellites. This implies that the dark halo mass and the stellar mass of a host galaxy are also correlated, which has been shown by observations (e.g. Conroy et al., 2007; Gonzalez et al., 2013; Kravtsov et al., 2018; Mandelbaum et al., 2006, 2016; More et al., 2011; Velander et al., 2014; Wang et al., 2016), with indications for different relations for the different morphological types (e.g. Mandelbaum et al., 2006, 2016; More et al., 2011; Velander et al., 2014). The former is also supported by theoretical work using semi-analytic modeling (Guo et al., 2013; Mitchell et al., 2016), abundance matching (Behroozi et al., 2013; Moster et al., 2013), and simulations (e.g. Tonnesen and Cen, 2015). From their simulations, Tonnesen and Cen (2015) also find that the stellar-to-halo-mass ratio is higher in overdense environments than in underdense regions. However, observations do not find a dependence of either the stellar-to-halo-mass relation (van Uitert et al., 2016) nor the average halo mass of central galaxies Brouwer et al. (2016) on the environment.

For the environment, Dressler (1980) already found a relation between galaxy number density and morphological type. He showed that the ETGs are the dominant morphological type in galaxy cluster environments, while the field environment is dominated by LTGs (see

Fig. 2.2.1). Thus, there must be a mechanism depending on the environment that leads to a change in morphology. Over the years there have been several attempts at explaining this phenomenon: in dense environments, the likelihood for galaxy-galaxy merger is enhanced, especially in the group environment (Mamon, 1992), and it is well known that (dry) merger events can lead to morphological transformations (e.g. Hernquist, 1989; Springel, 2000; White, 1978, among other). However, in galaxy cluster environments the relative velocities of galaxies are so large that the likelihood for a merger between two arbitrary galaxies is decreasing again for all galaxies but the central galaxy. While the merger likelihood in the densest environments decreases again, there are other effects inside these clusters that could lead to morphological transformations, for example ram-pressure stripping (Abadi et al., 1999; Gunn and Gott, 1972) and strangulation (Larson et al., 1980), by removing the gas from the galaxies and preventing them from accreting new gas. These processes are generally summed up as environmental quenching. While there is increasing observational evidence for ongoing stripping processes in cluster environments (Abramson et al., 2011; Boissier et al., 2012; Vollmer et al., 2012), there is also evidence that these mechanisms are only dominant for low mass galaxies and at low redshifts (Darvish et al., 2016; Erfanianfar et al., 2016; Hirschmann et al., 2016; Huertas-Company et al., 2016; Peng et al., 2010). At higher redshifts ($z \geq 1$) and for more massive galaxies, they find that internal quenching mechanisms like mass quenching or feedback quenching from AGN and stellar winds seem to play a more important role in quenching the star formation inside galaxies and thus transform them into quiescent galaxies in addition to the known channels of morphological transformations through merger events.

In Chapter 4 we study the origin of the observed differences in the satellite abundance around LTGs and ETGs of a given mass and study the connection of this difference with the environment.

2.3 Stellar Populations as Tracers of the Formation History?

... or the Influence of Your Contemporaries...

In the past years, observational instruments and methods have further and further improved. The integral field units (IFU) like e.g. SAURON (Bacon et al., 2001; de Zeeuw et al., 2002), ATLAS^{3D} (Cappellari et al., 2011a), CALIFA (Sánchez et al., 2012), SAMI (Bryant et al., 2015; Croom et al., 2012), and MaNGA (Bundy et al., 2015) provided data, which could better resolve the kinematical structures of galaxies. This led to the awareness that especially ETGs are not all the same but show a large variety of kinematical properties (e.g. Emsellem et al., 2007). By studying these differences one hopes to gain better insight on the different formation scenarios of galaxies, as the stellar kinematics are signatures of the accretion history (e.g., Cox et al., 2006; Schulze et al., 2018).

The formation processes not only leave footprints on the kinematics of a galaxy but also on the distribution of the stellar populations of different age. So the age can also be used as tracer of formation and assembly history (e.g. [Guérou et al., 2015](#)). Several observational studies have studied the age gradients along the radii of their galaxies: [González Delgado et al. \(2015\)](#), using CALIFA, report negative gradients, i.e. the center is populated by older stars and the outer parts by younger stars, in their galaxy sample, especially in their sample of LTGs. They favor the “inside-out” growth scenario, in which the star formation progresses from the center outwards, where they have continued forming in situ stars in disks. They find the profiles to flatten beyond 2 half-light radii and conclude that the stars were formed in a more uniformly distributed manner or that stars migrated from the center outwards. [Boardman et al. \(2017\)](#) confirm these findings for intermediate mass ETGs, and [Goddard et al. \(2017\)](#), studying the MaNGA sample, also see negative age gradients for LTGs. For ETGs, however, [Goddard et al. \(2017\)](#) find positive age gradients, i.e. towards the center the stars become younger, which indicates an “outside-in” formation scenario. These findings are supported by [Guérou et al. \(2015\)](#), who detect positive age gradients in half of their low mass ETGs (see also e.g. [Chilingarian, 2009](#); [Paudel et al., 2011](#)). In massive ETGs of the ALHAMBRA survey [San Roman et al. \(2018\)](#) find, on average, flat age gradients. Their results support a scenario in which ETGs formed through major mergers, where the gradients reflect the ages of accreted systems.

Another important relation, which captures the evolution of galaxies, is the relation between the stellar mass of the galaxy and its age. Mean ages are found to increase with increasing galaxy mass (e.g., [Gallazzi et al., 2005](#); [McDermid et al., 2015](#)). This is referred to as “downsizing” and implies that more massive galaxies have formed earlier than younger ones ([Cowie et al., 1996](#)). [González Delgado et al. \(2015\)](#) show that the age-mass relation scales with Hubble type, where the ETGs are found to be more compact and older than LTGs, at fixed stellar mass. They conclude that quenching is related to the morphology of the galaxies rather than to the stellar mass.

Up to now, only few studies investigating the kinematics have divided the stars into different populations according to their age. Exploring the kinematics of different stellar populations in the early type disk galaxy NGC 3115, [Guérou et al. \(2016\)](#) identify a fast rotating spheroid that consists of old stars and a thin fast rotating stellar disk that consists of younger stars.

In Chapter 5 we investigate the influence of the age of the stellar component on the kinematics of the galaxies, and study the connection with the morphology of the galaxies.

2.4 Tracing Dark Matter Over Cosmic Time

... or the Influence of Your Dark Side...

The content of this section has been published in [Teklu et al. \(2018\)](#)

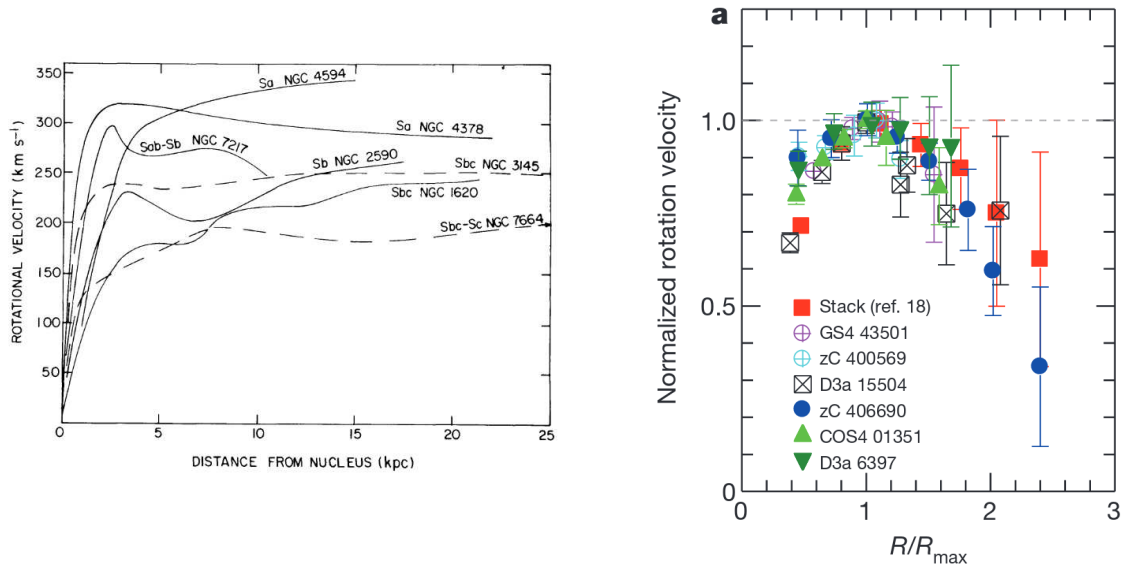


Figure 2.4.1: *Left:* Observed rotation curves at $z = 0$. The curves remain flat due to the dark matter. This figure is taken from Rubin et al. (1978). *Right:* Observed rotation curves at $z = 2$. Here, the rotation curves decline. This figure is taken from Genzel et al. (2017).

Since the postulation of dark matter (DM) by Zwicky (1933), many observational studies analyzing rotation curves of galaxies (e.g. Rubin et al., 1978) have supported this picture: While rotational velocities (V^{rot}) deduced from the visible matter should decrease proportional to $r^{-1/2}$ in the outer parts of galaxies, they were found to remain flat (see left panel of Fig. 2.4.1). The knowledge of this discrepancy in the mass content and thus the need for an explanation for this missing mass lead to the acceptance of dark matter as the dominant mass component of galaxies (see Naab and Ostriker (2017) for a detailed review).

Recently, Genzel et al. (2017, see right panel of Fig. 2.4.1) (see also Lang et al., 2017) presented measurements of rotation curves at redshift $z \approx 2$ that do not stay flat but decrease with increasing radius, opening a debate about the importance and even presence of DM in the outer disks and inner halos of these massive systems (and generally at higher redshift).

In Chapter 6 we study whether the existence of decreasing rotation curves at high redshifts contradicts or actually is a natural outcome of the Λ CDM paradigm.

Chapter 3

Connecting Angular Momentum and Galactic Dynamics: The Complex Interplay between Spin, Mass, and Morphology

This chapter has been published in [Teklu et al. \(2015\)](#)

Abstract

The evolution and distribution of the angular momentum of dark matter (DM) halos have been discussed in several studies over the past decades. In particular, the idea arose that angular momentum conservation should allow to infer the total angular momentum of the entire DM halo from measuring the angular momentum of the baryonic component, which is populating the center of the halo, especially for disk galaxies. To test this idea and to understand the connection between the angular momentum of the DM halo and its galaxy, we use a state-of-the-art, hydrodynamical cosmological simulation taken from the set of Magneticum Pathfinder simulations. Thanks to the inclusion of the relevant physical processes, the improved underlying numerical methods, and high spatial resolution, we successfully produce populations of spheroidal and disk galaxies self-consistently. Thus, we are able to study the dependence of galactic properties on their morphology. We find that (1) the specific angular momentum of stars in disk and spheroidal galaxies as a function of their stellar mass compares well with observational results; (2) the specific angular momentum of the stars in disk galaxies is slightly smaller compared to the specific

angular momentum of the cold gas, in good agreement with observations; (3) simulations including the baryonic component show a dichotomy in the specific stellar angular momentum distribution when splitting the galaxies according to their morphological type (this dichotomy can also be seen in the spin parameter, where disk galaxies populate halos with slightly larger spin compared to spheroidal galaxies); (4) disk galaxies preferentially populate halos in which the angular momentum vector of the DM component in the central part shows a better alignment to the angular momentum vector of the entire halo; and (5) the specific angular momentum of the cold gas in disk galaxies is approximately 40% smaller than the specific angular momentum of the total DM halo and shows a significant scatter.

3.1 Properties of Halos

From our data set we extract all halos with a virial mass above $5 \cdot 10^{11} M_{\odot}$. At a redshift of $z = 2$ there are 396 halos, at $z = 1$ there are 606 halos, at $z = 0.5$ we find 629 halos, and at $z = 0.1$ there are 622 halos. The lower limit is chosen to obtain a sample of halos that contain a significant amount of stellar mass and for which the resolution is sufficient to resolve the inner stellar, and gas structures. We transform the positions and velocities of all gas, stellar and DM particles into the frame of the halo, where the position given by SUBFIND is the position of the minimum of the potential and the velocity of the host halo is the mass-weighted mean velocity of all particles belonging to the halo.

Exemplary, Fig. 3.1.1 shows six galaxies within the chosen mass range demonstrating that the galaxies in the simulations look like observed disk and spheroidal galaxies. The middle panel is a picture of the full cosmological box at redshift $z = 0.5$.

3.1.1 The Angular Momentum

The mass and the angular momentum of galaxies are observed to be closely correlated with their morphology (e.g. Fall, 1983; Obreschkow and Glazebrook, 2014; Romanowsky and Fall, 2012). In a closed system without external forces, the angular momentum is a conserved quantity. However, in the context of galaxy formation and the interaction between collapsing objects and the large-scale structure, the assumption of the conservation is not necessarily fulfilled for a single galaxy. The total angular momentum of a galactic halo is given by

$$\mathbf{J} = \sum_k \left(\sum_{i \in N_k} m_{k,i} \mathbf{r}_{k,i} \times \mathbf{v}_{k,i} \right), \quad (3.1)$$

where k are the different particle types of our simulation (gas, stars, and DM) and N_k is their corresponding particle number with the loop index i .

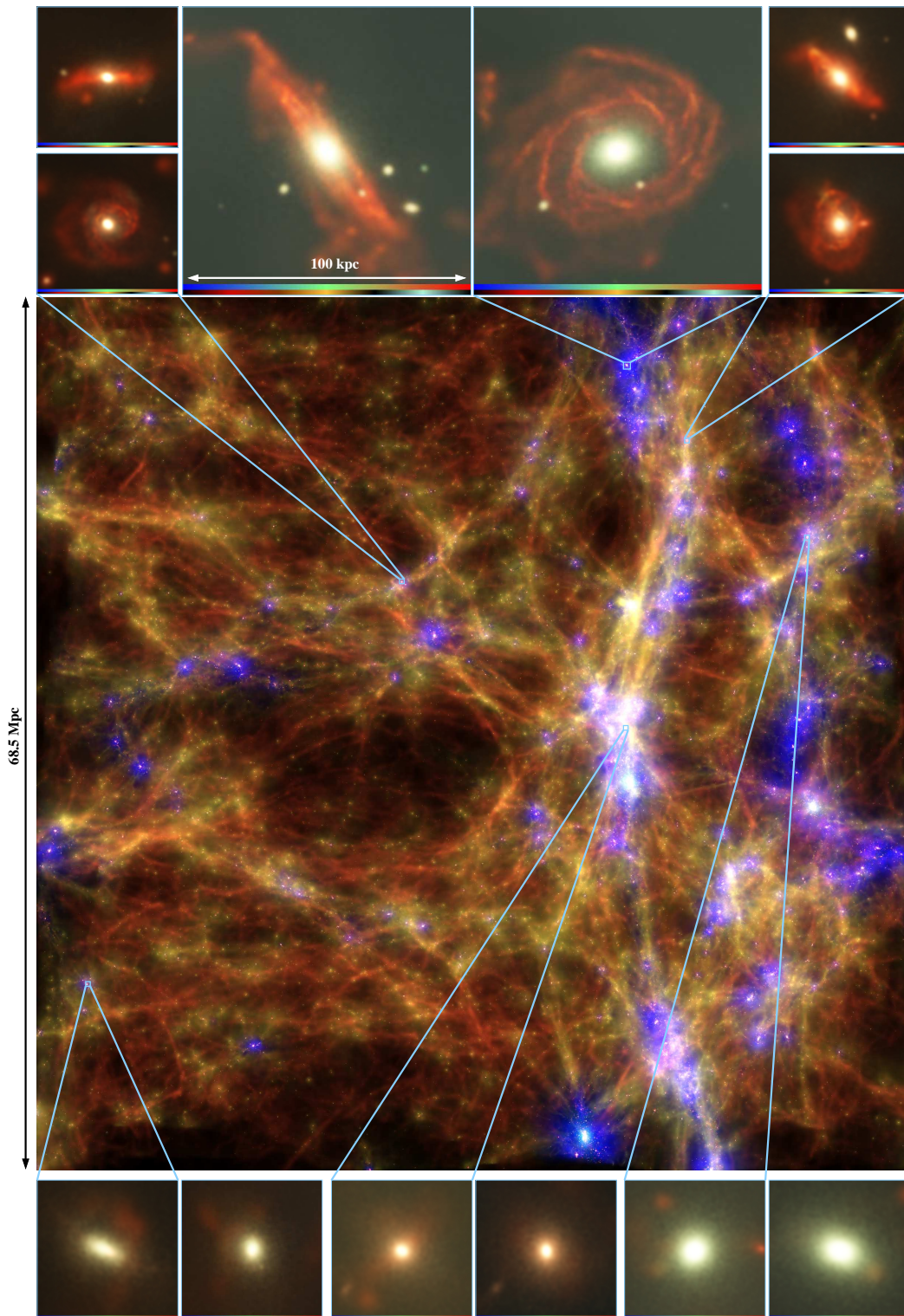


Figure 3.1.1: Main panel: complete cosmological box at redshift $z = 0.5$. The upper panels show exemplary spiral galaxies, and the lower panels show spheroidal galaxies. We show two random projection directions for each of the galaxies. In all panels we color-code the stellar particles by their cosmological formation epoch, where the upper color bars represent the age of the stars from old to young and the lower color bars represent the gas temperature from cold to hot. We also marked the position of the halos within the cosmological box.

In our simulations, each particle carries its own mass. The initial mass is different for gas, star, and DM particles. Later on, the mass of individual gas particles varies owing to mass losses during star formation. Thus, we remove the mass dependence and use the specific angular momentum

$$\mathbf{j}_k = \frac{\sum_i m_{k,i} \mathbf{r}_{k,i} \times \mathbf{v}_{k,i}}{\sum_i m_{k,i}}, \quad (3.2)$$

where k are the species of matter, as above. Therefore, we firstly calculate the angular momentum of each particle of a species. Afterward, we sum over all individual particles and divide by the total mass of the corresponding species to obtain the absolute value.

3.1.2 The Spin Parameter λ

In the following section we want to study the dimensionless λ -parameter. As defined by Peebles (1969, 1971) and adopted by, e.g., Mo et al. (1998), the general λ -parameter, which is used for the total halo, is given by

$$\lambda = \frac{J|E|^{1/2}}{GM^{5/2}}, \quad (3.3)$$

where $E = -GM^2/2 R_{\text{vir}}$ is the total energy of the halo. This total spin parameter can only be used considering all matter inside the halo. To evaluate the different components (gas, stars, and DM), this parameter needs to be modified. We follow Bullock et al. (2001), who defined a component-wise spin parameter as follows:

$$\lambda'(r) := \frac{J(r)}{\sqrt{2}M(r)V_{\text{circ}}(r)r}, \quad (3.4)$$

where $J(r)$ is the angular momentum, $M(r)$ the mass, and $V_{\text{circ}} = \sqrt{GM(r)/r}$ the circular velocity within a radius r . Another advantage of $\lambda'(r)$ is that it can be used for the calculation at different radii. When calculated over the entire virial¹ radius, $\lambda'(r) \approx \lambda$. For simplicity we will drop the prime for the remaining part of our study. For the evaluation of the different components λ can be expressed in terms of the specific angular momentum, as done by van den Bosch et al. (2002):

$$\lambda_k = \frac{j_k}{\sqrt{2}R_{\text{vir}}V_{\text{circ}}}, \quad (3.5)$$

where k stands for the different components.

Independent of the definition, the distribution of the λ -parameter can be fitted by a log-normal distribution of the following form:

$$P(\lambda) = \frac{1}{\lambda\sqrt{2\pi}\sigma} \exp\left(-\frac{\ln^2(\lambda/\lambda_0)}{2\sigma^2}\right), \quad (3.6)$$

¹Formally, if the true energy E is used, this is equal for a truncated, isothermal sphere. However, for an NFW halo the correction term is of order unity, see Bullock et al. (2001) and references therein

with the fit parameter λ_0 , which is about the median value, and the standard deviation σ .

The left panels of Fig. 3.1.2 show the histograms of the λ_k -distribution in linear bins of all halos in the selected mass range for stars (yellow), DM (black), and gas (turquoise) from redshift $z = 2$ (upper panels) to $z = 0.1$ (lower panels). The histograms and fit curves (smooth lines) are each normalized to the number of halos. The distribution of spin parameters of the stellar component has significantly lower values compared to the distribution of the spin parameter for DM, in agreement with the results presented by Danovich et al. (2015). This is due to the fact that within the halo the stars are more concentrated toward the center, whereas the spin of the DM component is dominated by the outer part of the halo, where most of the angular momentum of the DM component resides, as also shown in the right panel of Fig. 3.5.4 in Section 3.5. In addition, major mergers result in a reduction of the specific angular momentum, as shown in Welker et al. (2014). On the contrary, the gas component always has a spin parameter distribution shifted toward larger values, in agreement with more recent studies by Sharma and Steinmetz (2005), Kimm et al. (2011), Sharma et al. (2012), and Danovich et al. (2015), but in contrast to previous studies by van den Bosch et al. (2002) and Chen et al. (2003), who found nearly the same spin distributions for gas and DM. The larger spin values for the gas reflect the continuous transport of the larger angular momentum from the outer parts into the center due to gas cooling. While this leads even to a spinning up of the gas component with time, the distributions for the stars and DM remain relatively constant. This spin-up of the gas component might be caused by the continuously accreted cold gas, which brings in large angular momentum from farther away along the filaments (Pichon et al., 2011). When dividing the gas into hot and cold phases, we note that the hot gas (red) has lower values than the cold gas (blue), which has a long tail to high λ -values. This is in contrast to Chen et al. (2003), who found that the spin parameter for the hot gas is higher than that of the cold gas. On the other hand, our results agree well with more recent studies by Danovich et al. (2015). This trend for the cold gas to high values was also seen by Stewart et al. (2011), who have calculated λ -values for the cold gas and found values around 0.1 – 0.2. For a better overview we have listed the fit value of the λ -distribution for the different components in Table 3.1.

Table 3.1: The λ_0 Fit Value for the Different Components at Different Redshifts

Redshift	λ_{stars}	λ_{DM}	λ_{gas}	λ_{hot}	λ_{cold}
2	0.023	0.043	0.061	0.053	0.074
1	0.026	0.046	0.078	0.069	0.097
0.5	0.021	0.042	0.085	0.078	0.107
0.1	0.020	0.042	0.090	0.083	0.123

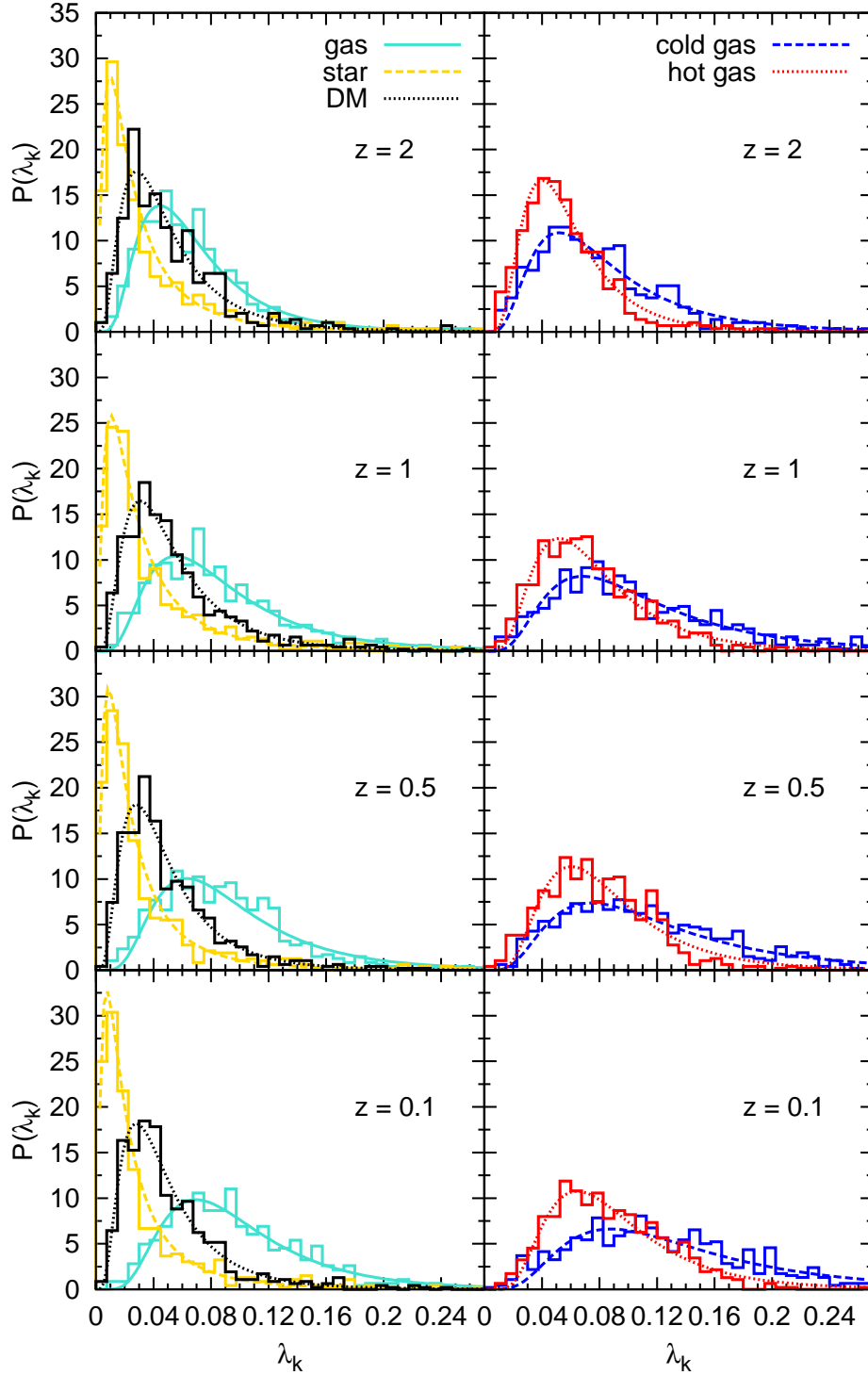


Figure 3.1.2: Left panels: histograms for the λ -parameter for the different components within R_{vir} ; the DM (black) is the dominant component, the stars (yellow) peak at lower values, whereas the gas (turquoise) is distributed around higher values. While λ_0 stays relatively constant for the DM and stellar component, it increases for the gas with decreasing redshift. Right panels: the gas component splits into hot (red) and cold (blue) gas. Both components spin up with cosmic time, whereas for the cold gas this happens faster. Overplotted are the best-fit lognormal distributions (smooth lines), for which the parameters are reported in Table 3.1.

3.1.3 Alignments

In this subsection we want to study the orientation of the angular momentum vectors of the different components in comparison to each other within the innermost region of the halo. For the calculation of the innermost region of the halo we only take particles within the inner 10% of the virial radius (R_{vir}) into account, which corresponds roughly to the size of the galaxies. We chose this radius as an approximate medium value, since smaller disks have a size of about 5% while extended gaseous disks can reach out up to 20% of the virial radius.

The angle between two vectors of the species i and j is calculated by

$$\cos(\theta) = \frac{\mathbf{J}_i \cdot \mathbf{J}_j}{|\mathbf{J}_i| \cdot |\mathbf{J}_j|}. \quad (3.7)$$

We then bin the angles from 0 to 180 degrees in 18 bins of a size of 10° each and count the number of halos within each bin. For the plots the number is normalized to unity.

As shown in Fig. 3.1.3, the distribution of the angles between the angular momentum vectors of gas and stars (green dotted) generally shows a good alignment at higher redshifts and becomes less aligned with decreasing redshift. This is in contrast to the alignment between the DM and stellar components (yellow dashed), which shows a better alignment with decreasing redshift. The angles between the DM and the gas component (turquoise solid) are an intermediate case, and their distribution does not change with redshift. For comparison, a random distribution of alignment angles is shown as a gray dot-dashed line in Fig. 3.1.3, demonstrating that none of the angle distributions found in the simulations are of random nature. The difference between the behavior and especially the evolution of the alignment of the gas and the stellar component can be explained by the fact that the angular momentum of the gas reflects the freshly accreted material (similar to the stars at high redshift), while the stars at low redshift reflect the overall formation history, similar to the DM content. These trends are in qualitative agreement with results obtained from simulations at very high redshift ($z > 9$) by [Biffi and Maio \(2013\)](#), who also found the angular momentum of the gas component in the center to reflect the recent accretion history.

3.2 Kinematical Split-Up

In this section we investigate properties of our galaxies as a function of their stellar mass and angular momentum. We therefore calculate the angular momentum \mathbf{J} of the stars within the innermost 10% of the virial radius. Furthermore, we ignore all particles within the innermost 1% of the virial radius because of their potentially unknown contributions caused by bulge components or numerical resolution effects. We rotate the positions and velocities

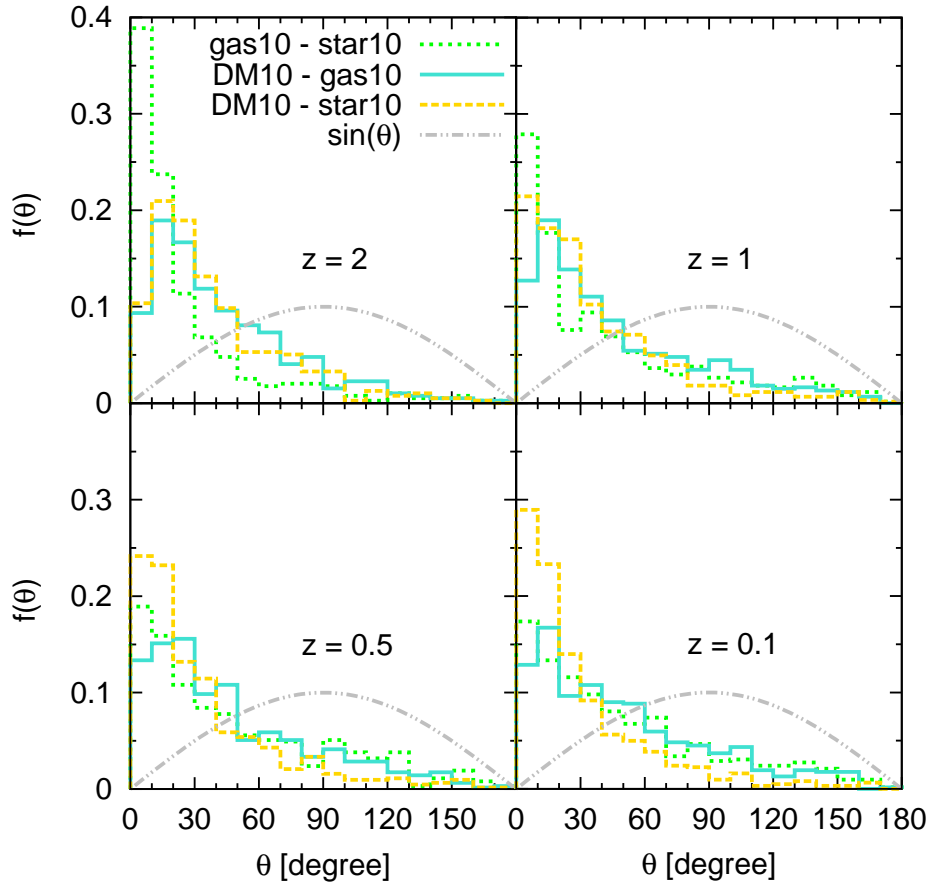


Figure 3.1.3: Angle between the total angular momentum vectors of the different components within the innermost 10% of R_{vir} as indicated in the plots for different redshifts. The gray dot-dashed line is expected for a random distribution of the angles. At higher redshift the gas and stellar components (green dotted) are well aligned, and their alignment gets worse with decreasing redshift. In contrast, the alignment of the DM and the stars (yellow dashed) gets better with decreasing redshift.

of all particles such that their z -components are aligned with the angular momentum vector \mathbf{J} of the stellar component. In the same manner we produce another data set that is rotated such that the z -components are aligned with the angular momentum vector \mathbf{J} of the gas component. These data are used for the ε_{gas} -distribution because the gas circularity calculated with the data rotated according to the angular momentum of the stars can fail to detect a gas disk that is misaligned with the stellar disk and vice versa.

3.2.1 The Circularity Parameter ε

Since in the Magneticum simulations disk and spheroidal galaxies are formed, we need to categorize them for our analysis according to their morphology. In order to distinguish

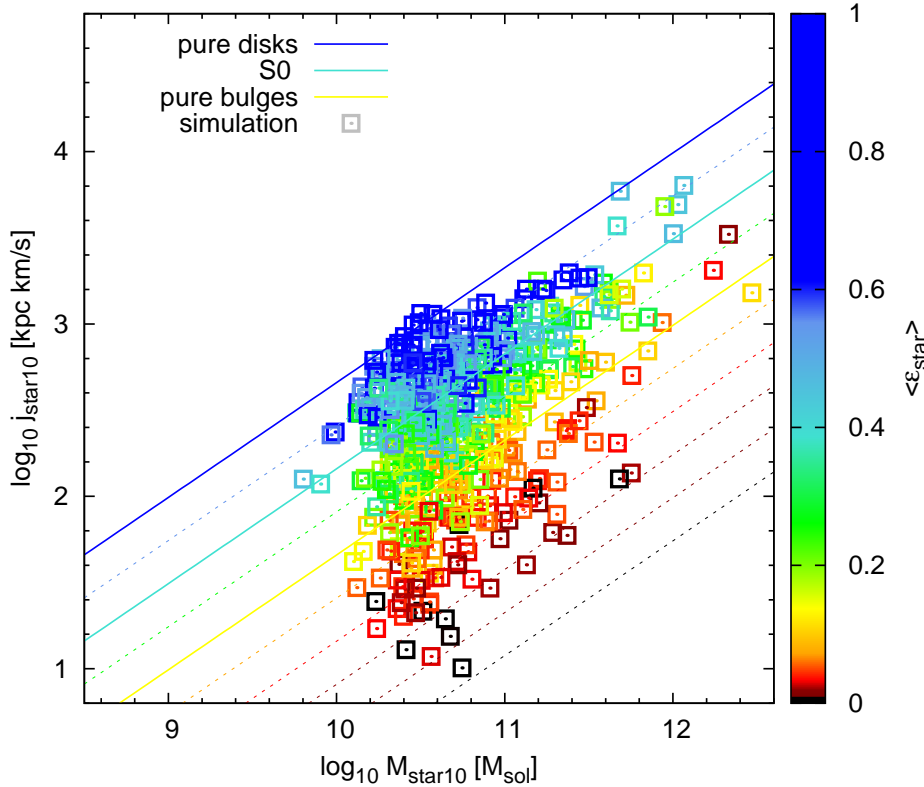


Figure 3.2.1: Stellar mass in the inner 10% of the virial radius vs. the specific angular momentum of the stars for all halos at redshift $z = 0.1$. The mean circularity $\varepsilon_{\text{star}}$ of the halos is color-coded. We adopted the scaling relations of Romanowsky and Fall (2012) (their Figure 2), where the blue line stands for pure disks, the turquoise one for S0, and the yellow one for pure bulges.

between different types of galaxies, we use the circularity parameter ε . The ε -parameter was first introduced by Abadi et al. (2003) as $\varepsilon_J = J_z/J_{\text{circ}}(E)$. For our study we use the definition of Scannapieco et al. (2008), which is given by

$$\varepsilon = \frac{j_z}{j_{\text{circ}}} = \frac{j_z}{rV_{\text{circ}}}, \quad (3.8)$$

where j_z is the z -component of the specific angular momentum of an individual particle and j_{circ} is the expected specific angular momentum of this particle assuming a circular orbit with radius r around the halo center of mass, with an orbital velocity of $V_{\text{circ}}(r) = \sqrt{GM(r)/r}$.

We compute the circularity ε for every individual particle between 1% and 10% of the virial radius. This is done for the stellar and the gas component, where we use the data that were rotated according to the angular momentum of the stars or the gas, respectively. To obtain the circularity distribution for our selected halos, we compute the fractions $f(\varepsilon)$ of particles within equal-distant bins, using a bin size of $\Delta\varepsilon = 0.1$. In a dispersion-dominated system

there is usually a broad peak in the distribution at $\varepsilon \simeq 0$, while in a rotation-supported system there is usually a broad peak at $\varepsilon \simeq 1$.

To test the hypothesis that the mass and the angular momentum of galaxies are the most important ingredients in their formation history and the resulting morphology (e.g. Fall, 1983; Obreschkow and Glazebrook, 2014; Romanowsky and Fall, 2012), we plot our galaxies at $z = 0.1$ in the stellar mass vs. stellar angular momentum plane in Fig. 3.2.1. There to we take *all* star particles within the innermost 10% into account. We color-code the simulated galaxies according to the absolute² value of the mean of their stellar circularity parameter. Adopting the classification diagram of galaxies by Romanowsky and Fall (2012) (their Figure 2), we overplot lines where the specific angular momentum follows the relation $j \propto M^\alpha$ with $\alpha \approx 2/3$. We plot different lines with distance $\Delta b = 0.25$. As can clearly be seen in Fig. 3.2.1, the mean circularity parameter is following this relation. Inspired by this result, we classify our galaxies according to what we will in the following refer to as the “ b -value”:

$$b = \log_{10} \left(\frac{j_{\text{star}}}{\text{kpc km/s}} \right) - \frac{2}{3} \log_{10} \left(\frac{M_{\text{star}}}{M_{\odot}} \right), \quad (3.9)$$

which is the y -intercept of the linear relation $f(x) = ax + b$ in the log-log of the stellar-mass-specific-angular-momentum plane.

According to Romanowsky and Fall (2012), galaxies with b -values close to -4 (blue line) are expected to be disks, while $b \approx -5$ indicates pure spheroidals (yellow). In our simulations we even find galaxies with b -values down to $b = -6.25$ for the galaxies with the smallest specific stellar angular momentum.

Fig. 3.2.2 shows the averaged ε -distribution of the stellar component at four redshifts, colored according to the different b -value bins shown in Fig. 3.2.1. Each ε bin is averaged over the halos that reside in the chosen b -value bin. There is a clear transition between the galaxies with different dynamics, from rotational-supported ($\langle \varepsilon \rangle = 1$) to dispersion-supported ($\langle \varepsilon \rangle = 0$) systems, reflected by their b -value from the M_{star} - j_{star} -plane: While galaxies with $b \approx -4$ clearly have most stars around $\varepsilon = 1$, and thus are dominated by rotation, galaxies with $b \approx -6$ peak around $\varepsilon = 0$, indicating that there is no significant rotation. This is true for all redshifts. However, we see a slight trend with redshift at intermediate b -values: for example, the distribution of the halos in a b -value bin of -4.75 (green squares) at $z = 2$ has the higher of the two peaks around $\varepsilon = 1$, whereas at $z = 0.1$ it only peaks around $\varepsilon = 0$. It is also interesting that the galaxies in the b -value bin of -4.5 (turquoise stars) at redshift $z = 2$ have a dominant rotationally ordered component, which becomes more dispersion dominated with decreasing redshift. We also note that the distributions around $\varepsilon = 0$ become slightly more distinct at lower redshifts. This indicates that there is an evolution of the different galaxy types with cosmic time along the M_{star} - j_{star} -plane.

²We take the absolute value, since there is a tiny fraction of halos with small b -values for which ε can have a slightly negative value owing to the different weightings in the definitions of the specific angular momentum (eq. (3.2)) and the circularity (eq. (3.8)).

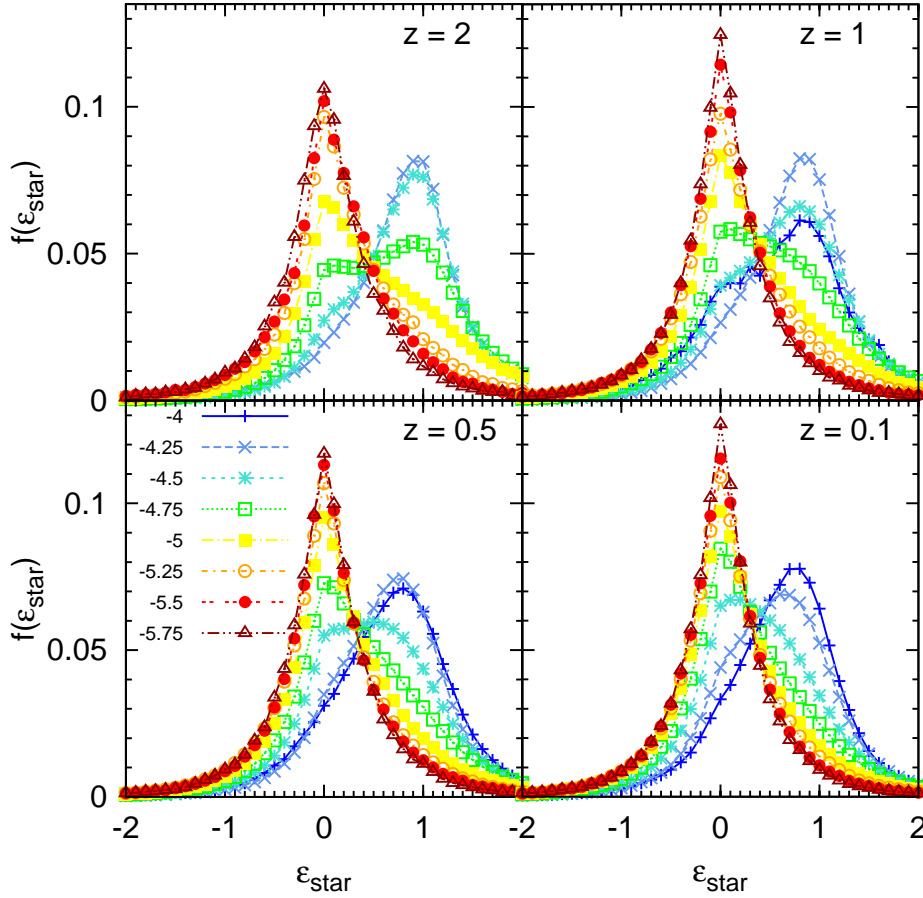


Figure 3.2.2: Averaged ε -distributions of the stellar component for four redshifts. Thereby, each ε bin is averaged over all halos that lie in the corresponding b -value bin. We see a clear transition of the galaxy types from rotational-supported systems to dispersion-dominated systems at all redshifts.

This additional evolutionary trend gets more evident in Fig. 3.2.3, which shows $\varepsilon_{\text{star}}$ (top), ε_{gas} (middle), and the mass fraction of the cold gas with respect to the stellar mass (bottom) versus the b -value, with spheroidal systems at the left and disk-like systems on the right. Thereby, each of these properties is averaged over the halos in the corresponding b -value bin. We can clearly see that the average $\varepsilon_{\text{star}}$ increases with increasing b -value at all four redshifts. Additionally, the average stellar circularity is generally larger at higher redshifts for all types of galaxies, albeit this trend is stronger for galaxies with larger b -values. This clearly shows that disk galaxies at higher redshifts had less prominent central bulges that would shift the value toward $\langle \varepsilon \rangle = 0$. For $\langle \varepsilon_{\text{gas}} \rangle$ we do not find any clear trend. The bottom panel of Fig. 3.2.3 shows a similar trend for the mean cold gas fraction. The spheroidal systems at present day with small b -values have only low amounts of gas, compared to the stellar mass, usually below 10%, whereas disks have gas fractions of 20% or more. For higher redshifts this fraction increases successively, and the strongest evolution is visible between redshifts $z = 2$ (pink solid line) and $z = 1$. Below $z = 1$ there is only a mild but

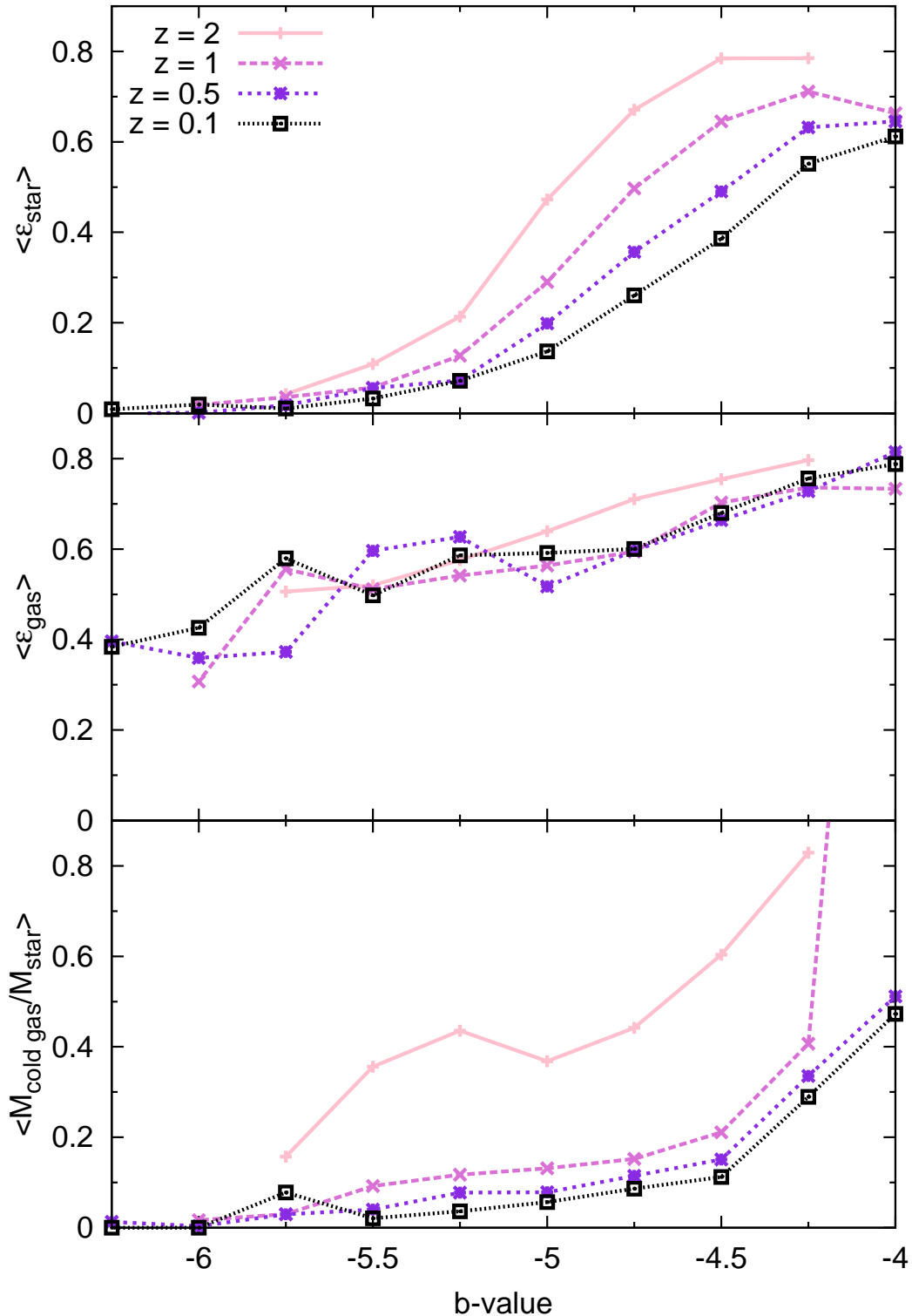


Figure 3.2.3: Top: mean circularity ϵ of the star component averaged over all halos in the corresponding b -value bin. There is a clear trend for decreasing mean ϵ when moving from the pure disks (high b -value) down to the pure bulges (smaller b -value) for all four redshifts. Middle: same as the top panel, but for the ϵ of the gas component. Bottom: The mass fraction of cold gas with respect to the stars, both within the inner 10% of the virial radius, averaged over all halos in the corresponding bin. At high redshift (pink solid line) there is much more cold gas, even in halos with a smaller b -value.

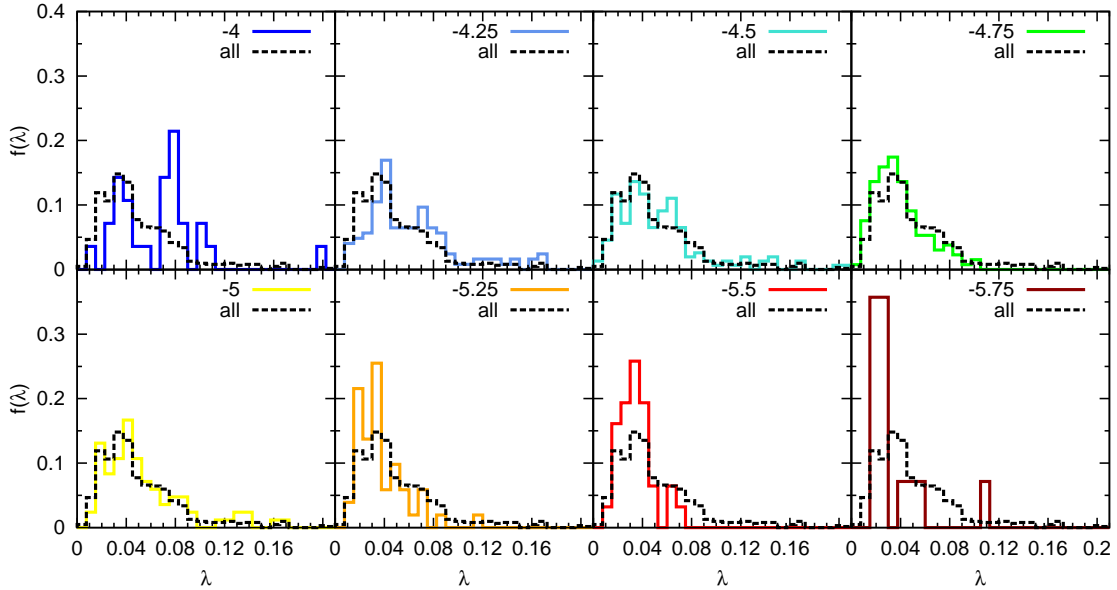


Figure 3.2.4: Distribution of the total λ -parameter for the halos according to their b -values at $z = 0.1$. There is a transition from the disks (upper left) to the bulges (lower right), i.e., from rotation-dominated systems (higher λ -values) to dispersion-dominated systems (lower λ -values). Interestingly, the halos with the highest b -values show a dichotomy in their distribution.

continuous³ evolution, but at $z = 2$ even spheroidals have gas fractions of 20% or more, while disk galaxies can contain more than 40% gas compared to their stellar content. For the largest b -values the galaxies can even be dominated by gas, i.e., the gas fraction is larger than 50%. Thus, we conclude also that galaxies that are spheroidal systems have a nonnegligible cold gas fraction at high redshifts.

3.2.2 The λ -Parameter

We want to understand whether this classification of the galaxies according to their position on the $M_{\text{star}}-j_{\text{star}}$ -plane has an effect on the spin parameter λ . In Fig. 3.2.4 we show the distribution of the total λ -parameter of the whole halo content (see Equation 3.3), exemplary for redshift $z = 0.1$. We divide the halos according to their b -value. The first interesting thing to note is that there is a double peak in the λ -distribution for galaxies with disk-like kinematics (upper left panel). This could indicate that there are different formation channels for disk-like systems, e.g., gas-rich major mergers, as discussed in Springel and Hernquist (2005) and Schlach Berger, D.P. (2014). The peak at higher λ -values becomes smaller as we move to the right and seems to disappear at a b -value of -4.75 . Galaxies with b -values below -5.25 are hosted in halos with significantly smaller

³At $z = 1$ (magenta dashed line) the value for the galaxies with the highest b -value exceeds the scale, since there are six galaxies that on average have a cold gas fraction of 2.53 with respect to the stars.

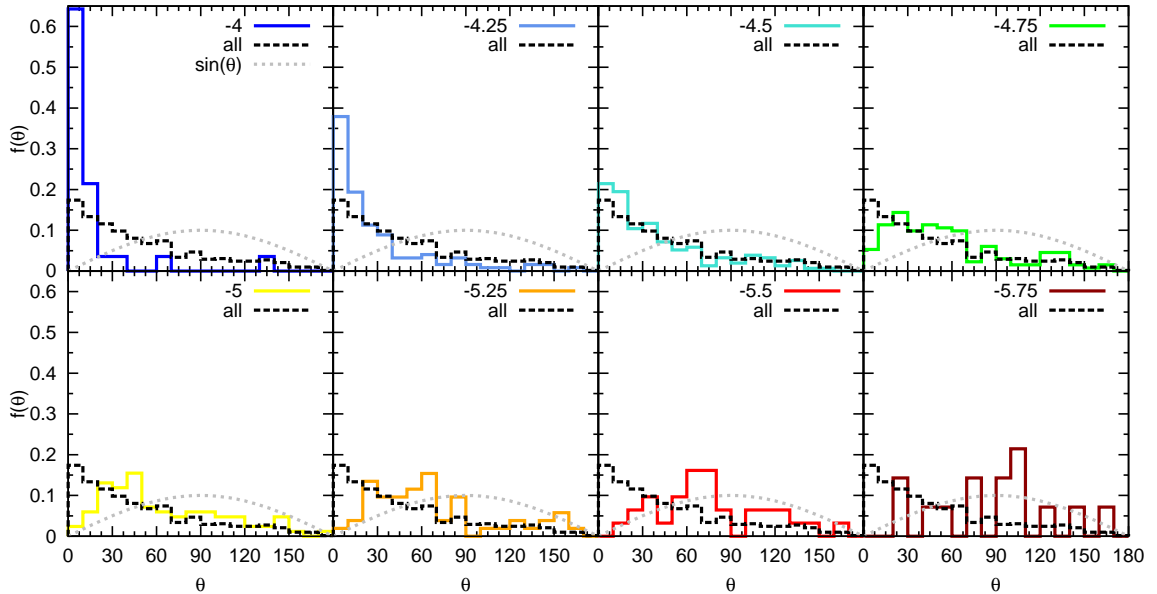


Figure 3.2.5: Angle between the angular momentum vector of the gas and that of the stars within the innermost 10% of the virial radius according to their b -values at redshift $z = 0.1$. There is a clear transition between the galaxy types. The higher the b -value, the better aligned the stellar and gas components are. When going to lower b -values, i.e., moving down on the $M_{\text{star}}-j_{\text{star}}$ -plane to the bulges, the angles of the two components seem to be randomly distributed (compare gray dotted sinusoidal distribution).

λ -values compared to the overall distribution (black dashed line). Therefore, on average there seems to be a connection between the galaxy types and the spin parameter λ of the hosting halos, reflected in a continuous transition of the spin parameter distribution of the host halo with the b -value obtained from the $M_{\text{star}}-j_{\text{star}}$ -plane.

3.2.3 Alignments of the Central Components

To verify the dynamical connection between the different baryonic components within the galaxies, we show in Fig. 3.2.5 the distributions of the alignment between the central angular momentum of the stellar and the gas component. As before, we classify our galaxies according to the b -value. By moving from high (upper left) to low (lower right) b -values we immediately see that the alignment between the angles is good for the disk galaxies (large b -values) and gets increasingly more random for decreasing b -values. This is indicated by the gray dotted line, which again illustrates a random distribution (as in Fig. 3.1.3). We find a continuous transition from the disk-like to the bulge-dominated galaxies. It illustrates that in spheroidal systems the stars are significantly misaligned with an eventually present gaseous disk. This result is supported by the findings of the ATLAS^{3D}-project (Cappellari et al., 2011a) that a kinematical misalignment of the gas component with respect to the stars is not unusual (Davis et al., 2011).

3.3 Classification of Simulated Galaxies

So far we have seen that there is a continuous transition between the different types of galaxies within the $M_{\text{star}}-j_{\text{star}}$ -plane, orthogonal to $j \propto M^\alpha$ with $\alpha \approx 2/3$. We now want to study the kinematical properties of our simulated galaxies depending on their classification as disk and spheroidal galaxies.

3.3.1 Selection Criteria

In our simulations, many spheroidal galaxies show extended, ring-like structures of cold gas, in good agreement with recent observations (Salim and Rich, 2010). Therefore, including the circularity of the gas within 10% of the virial radius as a tracer of morphology can lead to a misinterpretation. Additionally, there can be huge uncertainties for galaxies that have almost no gas left. Using a criterion only based on the b -value of the galaxies also is not straightforward because of the existence of fast rotators among the spheroidal galaxies. Observationally there seems to exist some overlap between the different galaxy types within the $M_{\text{star}}-j_{\text{star}}$ -plane. In principal, the luminosity of the stars could be taken into account, since old stars that make up the bulge and the halo stars are not as luminous as young stars that build up the disk. Hence, in observations a galaxy with an old massive stellar bulge and an extended disk of young stars and gas is very likely to be classified as a spiral galaxy.

However, here we will stick to a classification of galaxies based on the circularity distribution (Equation 3.8) of their stars, which allows us to capture rotationally supported stellar disk structures or dispersion-dominated spheroidal structures. We combine this criterion with the mass fraction of the cold gas with respect to the stars, following our result from Fig. 3.2.3. As before, circularity distributions are evaluated within 10% of the virial radius, excluding the central 1%, while we include the central 1% in our calculation of the cold gas fraction as the resolution is not important in this case. We use the results from the previous section to justify the threshold values used to select dispersion-dominated, gas-poor spheroidal and rotational-supported, gas-rich disk galaxies to reflect counterparts of classical, observed elliptical, and spiral galaxies.

As shown in Fig. 3.2.2, there is a clear, bimodal behavior of the epsilon distribution within different b -value bins. We show in Section 3.5 in detail the cumulative distributions that allow us to define the proper thresholds bracketing the transition regions. These thresholds are then applied to the circularity distributions of the individual galaxies, which of course in general show a more complex shape than the averaged distributions. The left panel of Fig. 3.5.2 in Section 3.5 shows the cold gas mass fraction of the galaxies classified only by their circularity ϵ_{star} , illustrating our choice of including a gas criterion. In short, we are using the following selection criteria:

- We classify a galaxy as a spheroidal galaxy if the majority of particles is in a close

interval around the origin (i.e., $f(-0.4 \leq \varepsilon \leq 0.4) \geq 0.6$). This percentage cut is adapted to the redshift. For the details see the left panels of Fig. 3.5.1 in Section 3.5.

In addition, it has to have a cold gas mass fraction with respect to the stars lower than 0.35 at $z = 2$, 0.2 at $z = 1$, 0.125 at $z = 0.5$, and 0.065 at $z = 0.1$. This criterion is chosen such that the fraction values satisfy the linear function $f(z) = 0.15 \cdot z + 0.05$. The upper limit for the spheroidal galaxies at redshift $z = 0.1$ seems plausible, since Young et al. (2014) found that massive elliptical galaxies (of the red sequence) have mass fractions of HI and H_2 , compared to the stars, up to 6% and 1%, respectively.

- We classify a galaxy as a disk galaxy if the majority of particles are off-centered from the origin (i.e., $f(0.7 \leq \varepsilon \leq 3) \geq 0.4$; for the dependence on the redshift see right panels of Fig. 3.5.1 in Section 3.5).

Additionally, the constraint on the mass fraction of the cold gas is such that it has to be higher than 0.5 at $z = 2$, 0.35 at $z = 1$, 0.275 at $z = 0.5$, and 0.215 at $z = 0.1$. This criterion is chosen such that the values of the mass fraction satisfy the linear function $f(z) = 0.15 \cdot z + 0.2$.

- All remaining galaxies, which fulfill neither of the two criteria, are classified as “others.”

The total number of galaxies above the mass cut of $5 \cdot 10^{11} M_\odot$ selected from our simulation at redshift $z = 0.1$ is 622 (for other redshifts see Table 3.2). According to the above criteria, 64 galaxies are classified as classical disks and 110 as classical spheroids, while 448 are classified as “others.” Such unclassified galaxies include merging objects, bulge-dominated spirals, spheroids with extended gas disks, barred galaxies, or irregular objects.

In order to identify parts of the unclassified objects, the classification could be refined in such a way that we additionally divide into spheroids that have a gaseous star-forming disk or galaxies that have a large stellar disk with only little gas (S0 galaxies). At lower redshifts our classification becomes increasingly difficult since there are a lot of galaxies that have a very dominant stellar bulge but, on the other hand, also possess an extended gaseous disk containing many young stars.

Table 3.2: Number of Halos in the Selected Mass Range

Redshift	N	N_{spheroid}	N_{disk}
2	396	34	89
1	606	87	73
0.5	629	146	59
0.1	622	110	64

Total number of halos N in the selected mass range, the number of spheroids N_{spheroid} and disks N_{disk} (classified by the circularity of the stellar component and the mass fraction of the cold gas with respect to the stars) at different redshifts.

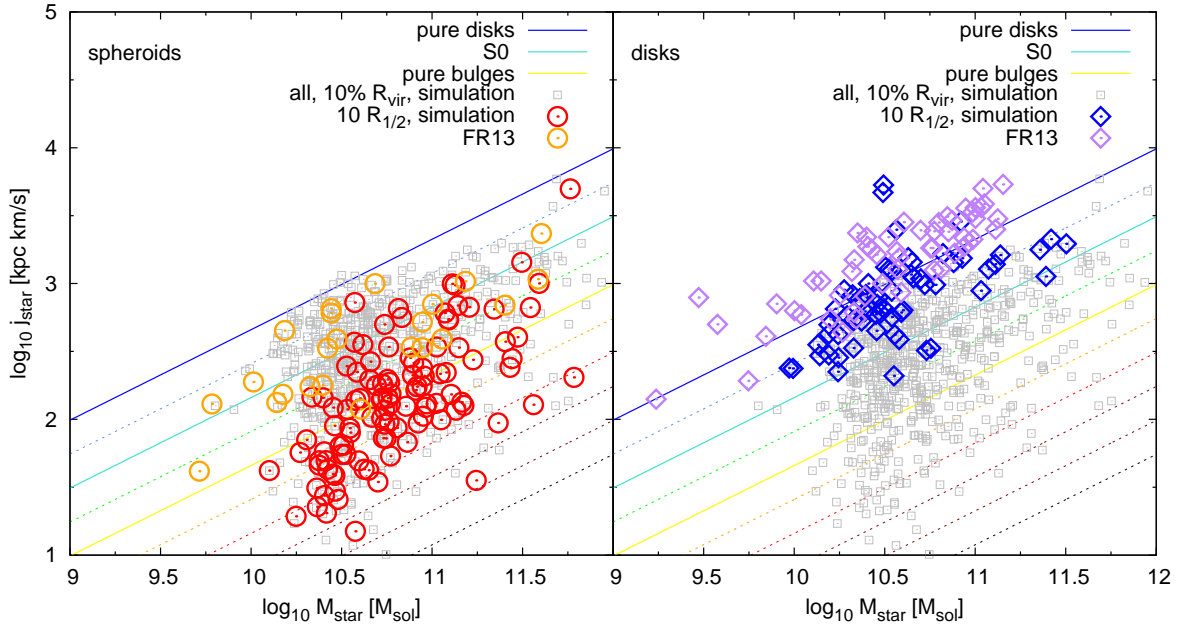


Figure 3.3.1: Galaxies within the stellar-mass–specific-angular-momentum plane at $z = 0.1$. Gray symbols represent all galaxies extracted from the simulations (as in Fig. 3.2.1), where angular momentum and stellar mass are measured within 10% of the virial radius. The left panel shows the simulated galaxies classified as spheroids (red circles) compared to data from observed elliptical galaxies by Fall and Romanowsky (2013) (orange circles, denoted by “FR13”). The right panel shows disks in our simulation (blue diamonds) compared to observational data of spiral galaxies by FR13 (purple diamonds). For the disks and the spheroids, we evaluated the mass and the specific angular momentum within $10 R_{1/2}$, which more closely resembles the radii studied by FR13. The colored lines correspond to the b -values (see Fig. 3.2.1).

Although the criterion for the gas mass fraction is relatively arbitrary and may overestimate the number of spheroids, we checked that changing this selection criterion does not change the results qualitatively, although adding/removing galaxies from the spheroidal sample. At higher redshifts an additional difficulty might be that the transition of galaxy types is less strict, as seen in Fig. 3.2.2. At these redshifts, remaining dynamical signatures of the current formation process will be more pronounced and individual distributions of the circularity parameter might be more complex. Thus, a clear assignment might fail.

3.3.2 Comparison of the Simulated Stellar Specific Angular Momentum with Observations

After having extracted a set of spheroidal and disk galaxies, we can evaluate the relation between the specific angular momentum and the mass of the stellar component and compare them with observations, as shown in Fig. 3.3.1. To compare with observations presented by Fall and Romanowsky (2013) (hereafter FR13) we calculate the mass and specific angular

momentum for all stellar particles within $10 R_{1/2}$ instead of $10\%R_{\text{vir}}$, where $R_{1/2}$ is the radius that contains half the stellar mass of the galaxy and roughly corresponds to observed effective radii. This is done to account for the fact that, for a given mass, disk galaxies have a larger effective radius than spheroids (Shen et al., 2003), and to better resemble the radius ranges studied in FR13. The left panel shows the $M_{\text{star}}-j_{\text{star}}$ -plane for our galaxies classified as spheroids (red circles), including the 23 elliptical galaxies (orange circles) presented in FR13 (their Figure 2). In the right panel the same is shown for our disk galaxies (blue diamonds) in comparison to the 57 spiral galaxies (purple diamonds) from FR13. In general, our simulated galaxies are in good agreement with the observations. This result has already been shown for a subset of our galaxies at $z = 0$ with a rather crude classification criterion in Remus et al. (2015), and we find an even better agreement with observations with our more advanced classification scheme. Recently, Genel et al. (2015) have shown a comparison of the galaxies in the Illustris simulation with those observations, which are also in good agreement when a similar feedback mechanism is used.

To understand the impact of the choice of radius used to calculate the angular momentum and the stellar mass, we included the values for all galaxies evaluated within 10% of the virial radius, as previously shown in Fig. 3.2.1. For the spheroidal galaxies the effect is much stronger, and we clearly see that the angular momentum is larger for larger radii. The radius dependence is shown in more detail in the right panel of Fig. 3.5.4 in Section 3.5, where we show that the angular momentum of spheroids increases with radius and that there is a significant contribution to the specific angular momentum from large radii. For disk galaxies the exact radius is less important, as most of the angular momentum is contained within the disk at relatively small radii. The same holds true for the b -value, which more strongly depends on the considered radius for spheroids than for disks, which can be seen in Fig. 3.5.5 in Section 3.5.

Note that we compare here the specific angular momentum directly measured from the total stellar component from the simulations (Equation 3.2), while the observations are inferred from the projected measurements. We also do not resolve galaxies with stellar masses smaller than $\approx 10^{10}M_{\odot}$, while the observations include some objects with smaller masses.

3.3.3 The Simulated Stellar Specific Angular Momentum at $z = 2$

The content of this subsection has been published in Teklu et al. (2016)

In order to see if this split-up is already present at higher redshift, we show in Fig. 3.3.2 the $M_{\text{star}} - j_{\text{star}}$ -relation for redshift $z = 2$ for our simulated galaxies. We find that the galaxies, in general, have a lower stellar specific angular momentum than the galaxy population at redshift $z = 0$, and it is more pronounced for disk galaxies. This is in good agreement with recent theoretical approaches by Obreschkow et al. (2015).

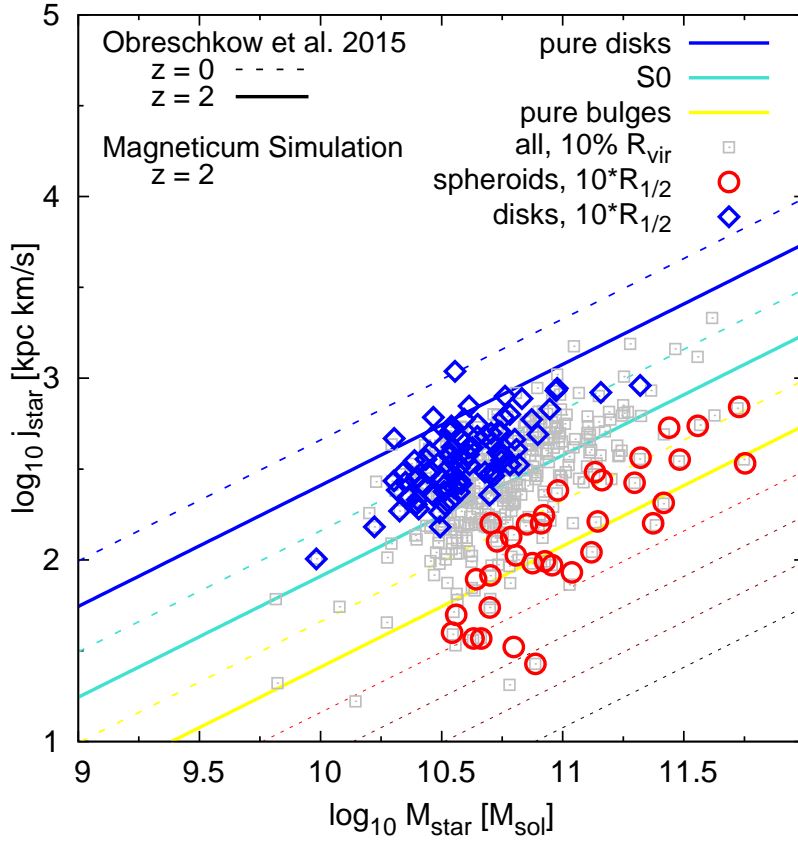


Figure 3.3.2: Simulated galaxies within the stellar-mass–specific-angular-momentum plane at $z = 2$. Dashed and solid lines are the predicted scalings from [Obreschkow et al. \(2015\)](#) for $z = 0$ and $z = 2$, respectively.

3.3.4 The Gas and Stellar Specific Angular Momentum in Simulations and Observations

We also compare the specific angular momentum of the gas with that of the stars for all classified galaxies in our simulations. Fig. 3.3.3 shows the relations for all four redshifts as indicated in the plots. At redshift $z = 0.1$ we include the observational data taken from the THINGS (The HI Nearby Galaxy Survey, [Walter et al., 2008](#)) sample, which consists of 16 spiral galaxies in the local Universe, for which surface densities of stars and cold gas are available ([Leroy et al., 2008](#)). Specific angular momenta for the gas and stellar components of those galaxies were presented by [Obreschkow and Glazebrook \(2014\)](#).

For the disk galaxies, we find that the specific angular momentum of all stars in the central region is slightly smaller than that of the gas (blue diamonds), in agreement with the observations (purple symbols). This, most likely, originates from the fact that the specific angular momentum of the gas is constantly replenished by freshly accreted gas, which transports larger angular momentum from the outer parts of the halo to the center.

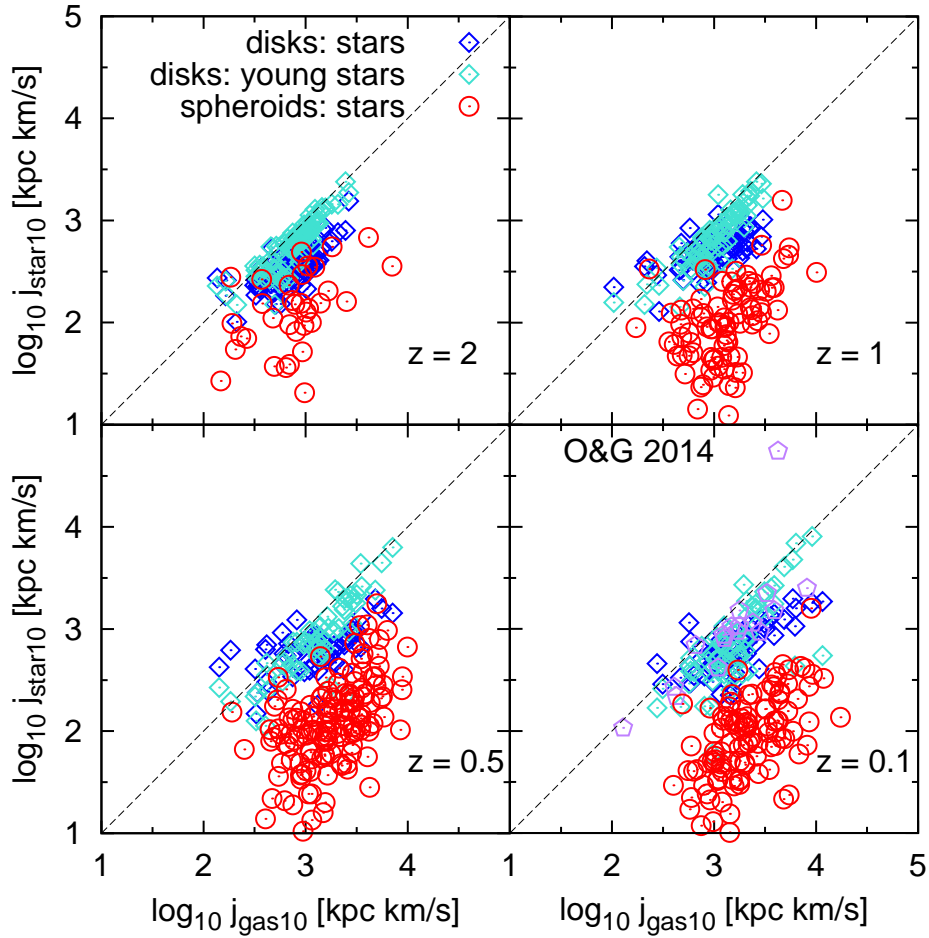


Figure 3.3.3: Specific angular momentum of the gas against the specific angular momentum of stars, both within 10% of the virial radius for galaxies which are classified as disks (blue diamonds) at four redshifts as indicated in the plots. Additionally, we show the relation also considering only young stars (turquoise diamonds). At $z = 0.1$ we overplot observational data points calculated by [Obreschkow and Glazebrook \(2014\)](#) (purple pentagons). The values agree well with the observations, and we note an overall spin-up with cosmic time.

This becomes more evident by looking at the newly formed stars (turquoise diamonds) in our simulations. We consider a star to be young if its formation happened not more than $\Delta z = 0.05 \times 1/(1+z)$ ago at a given redshift z , which corresponds to a stellar age of 0.2Gyr at $z = 2$, 0.4Gyr at $z = 1$, 0.5Gyr at $z = 0.5$, and 0.7Gyr at $z = 0.1$. If we only take the young stars into account, we find almost an equality (dotted line) with the specific angular momentum of the gas. At a lower redshift (lower right panel) the values of the specific angular momentum of the gas are slightly larger than at higher redshift (upper left panel). This behavior reflects the spin-up of the cold gas with time, as already seen before. Hence, also the young stars have higher specific angular momentum. This appears in a slight trend for a separation of the young stars and the total stellar component, which have lower specific angular momentum than the gas.

The spheroids (red circles in Fig. 3.3.3), however, have a significantly lower specific stellar angular momentum compared to that of their gas. This suggests that, especially at high z , most gas in spheroids originates from the accretion of material from large radii (cold streams or infalling substructures) and hence transports the higher angular momentum from the outer parts into the center.

We can clearly see that the spheroids and the disk galaxies show a different behavior in the relation between the angular momentum of the gas and stars. We also have seen that the gas gains angular momentum over time, especially in disk galaxies. In disk galaxies, stars have slightly smaller specific angular momentum than the gas, and they also show a mild difference between the specific angular momentum of stellar components with different ages. Here the young stars have slightly larger specific angular momentum, basically reflecting the angular momentum of the gas from which they form.

All in all, the results from the simulations fit well with the observational data. In particular, we are in agreement with Fall (1983), who find that the specific angular momentum of the galaxies increases with the disk-to-bulge ratio for a given mass.

We note that the evaluation of this quantity for spheroids especially at lower redshifts might be fault-prone since, owing to the selection criterion, there is only a small amount of cold gas within the chosen radial range.

3.3.5 Comparison of the Gas and DM Specific Angular Momenta

Finally, we compare the specific angular momenta of DM and gas. In particular, we are interested in the scaling relations of the corresponding individual specific angular momenta of baryonic and nonbaryonic matter. Previous studies (e.g. Fall, 1983; Mo et al., 1998) suggest an equality between the angular momentum of the total DM halo and that of the central gas component of disk galaxies.

The relation between the specific angular momentum of the cold gas of the galaxy, which resides within the innermost 10% of the virial radius, and that of the total DM halo is shown in Fig. 3.3.4 for different redshifts. In general, we find the specific angular momentum of the DM to exceed (by a factor of ≈ 2) the specific angular momentum of the cold gas. Interestingly, the cold gas in disk and spheroidal galaxies does behave in the same way. This is due to the fact that cold gas always settles in disk-like structures, even in elliptical galaxies (e.g. Lees et al., 1991; Young et al., 2011). We plot all disks above the redshift-dependent $M_{\text{cold}}/M_{\text{star}}$ -cut (blue diamonds). Additionally, we fit a line parallel to the 1:1 relation (blue dotted) to the data, in order to see the offset. For all shown redshifts we find values of the y -intercept between 0.33 and 0.41 in log space, which is between 2.14 kpc km/s and 2.57 kpc km/s in normal space. However, the scatter around this fit curve is very large. The yellow diamonds show the value for one simulated galaxy at different redshifts as presented in Kimm et al. (2011). Their disk galaxy has only slightly higher specific angular momentum in the gas component compared to the DM halo, but sits within the

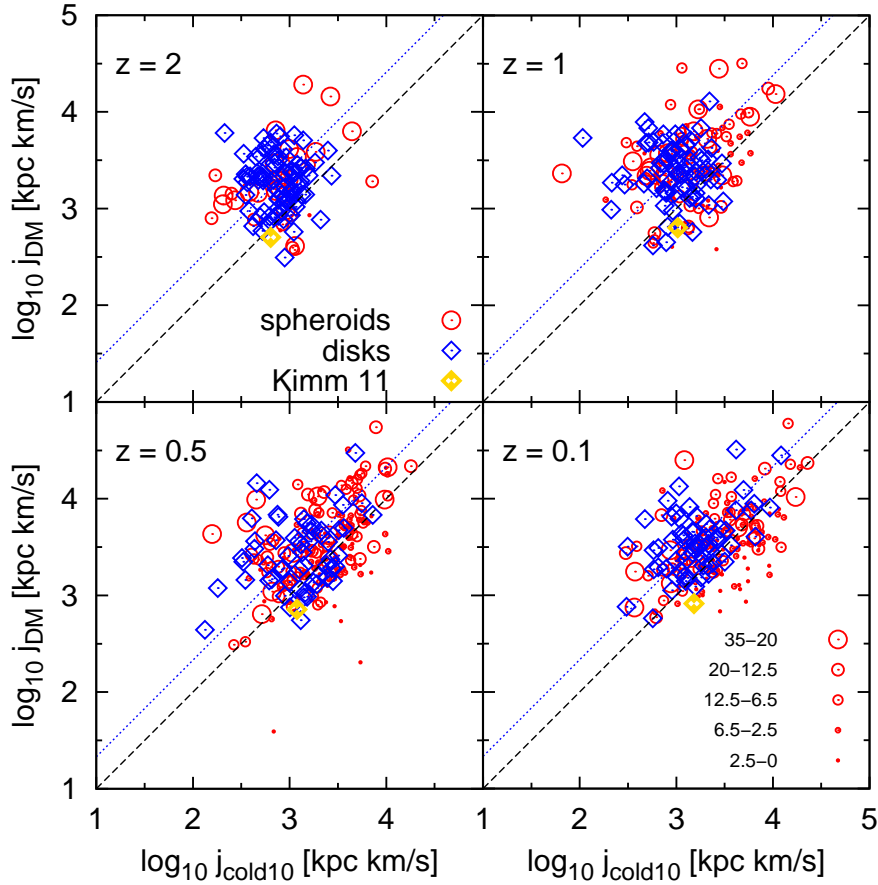


Figure 3.3.4: Specific angular momentum of the cold gas within 10% of the virial radius against the specific angular momentum of DM within the entire virial radius. The blue diamonds show the disks and the red circles the spheroidal galaxies, where the size of the circles reflects the fraction of the cold gas mass with respect to the stellar mass. The blue dotted line shows the fit for the disk galaxies. The 1:1 relation is represented by the black dashed line. For comparison, we add the results obtained by [Kimm et al. \(2011\)](#) (yellow diamonds).

distribution of values we find in our simulation for different galaxies. Our values are also broadly in line with the results of [Danovich et al. \(2015\)](#), who find that the spin of the disk is comparable to that of the DM halo. The size of the symbols of the spheroids (red circles) is plotted according to their fraction of cold gas mass with respect to the stellar mass. For completeness we plot all spheroids with a cold gas mass fraction lower than 35% for all redshifts. At higher redshift most spheroids have a large amount of cold gas. At the lowest redshift there are still some objects that were classified as spheroids with the $\varepsilon_{\text{star}}$ -criterion but have a high cold gas mass fraction. Interestingly, there are some spheroids with high specific cold gas angular momentum, which might be due to individual infalling clumps and small substructures, as these are spheroidal galaxies that have extremely small cold gas fractions. However, in such cases we cannot relate the specific angular momentum of these individual structures to the specific angular momentum of the halo.

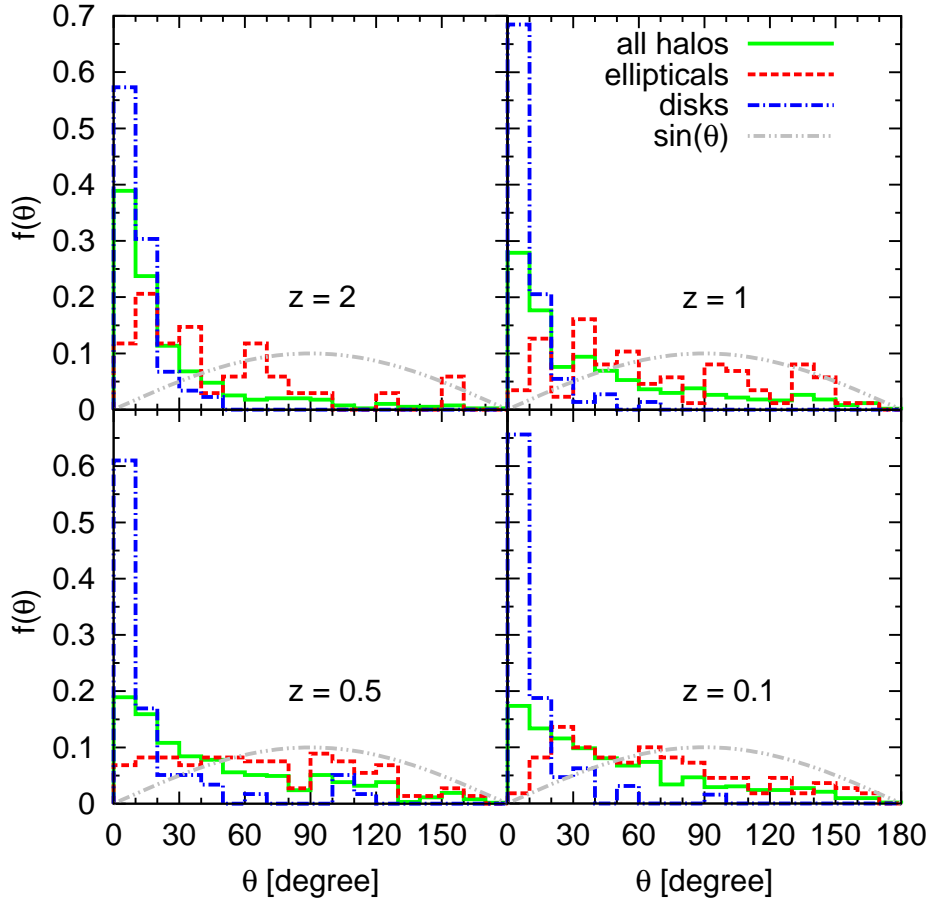


Figure 3.3.5: Angle between the angular momentum vector of gas and stars, both within the innermost 10% of the virial radius. At all redshifts the disks (blue dot-dashed) are well aligned. In contrast, the spheroids (red dashed) are randomly distributed. The overall distribution (green solid) gets worse aligned with decreasing redshift.

3.3.6 Misalignment Angles

As seen before, another indicator for the different evolutionary states reflected by the stars, DM, and gas are the misalignment angles between these three components. We now investigate their behavior by focusing on our selected disk and spheroidal galaxies.

The Angle between Gas and Stars

At first, we investigate whether we find a correlation between the morphological type and the angles between the angular momenta of the gas and the stars, both within the innermost 10% of the virial radius. Fig. 3.3.5 shows the angle for four different redshifts. The disk galaxies (blue dot-dashed histograms) have very well aligned gas and stellar angular momentum vectors with median values of 7.8° at redshifts $z = 2$ and $z = 0.1$ and

Table 3.3: Median Misalignment Angles between the Baryons in the Center

Redshift	All Halos	Disks	Spheroids
2	13.4	7.8	37.4
1	24.4	6.3	56.5
0.5	35.8	7.6	65.5
0.1	37.6	7.8	60.4

The median misalignment angles between the angular momentum vectors of gas and stars, both within the inner 10% of the virial radius ($\theta_{\text{gas10-stars10}}$).

median values of 6.3° and 7.6° at redshifts $z = 1$ and $z = 0.5$, respectively. This is in good agreement with [Hahn et al. \(2010\)](#), who found median angles of about 8° for their disks at $z = 1$ and a median of 7° at redshifts $z = 0.5$ and $z = 0$. It demonstrates that the stellar and gaseous disks in disk galaxies are very well aligned, which is what we expect, since the stars form out of the gas and thus maintain the same orientation.

The spheroids have a random distribution with a median value of 60.4° , i.e., the gas and stellar components in spheroidal galaxies are often misaligned. In summary, the gas and star components of spheroids become less aligned with decreasing redshift, while there is no change for disk galaxies (see [Table 3.3](#)). The overall trend for all halos in the simulation shows the same behavior as the spheroids, in agreement with [Fig. 3.2.5](#).

The Angle between DM and Baryons

Since we see a clear difference in the alignment between the angular momenta of the stars and gas for spheroids and disks, we want to test whether this is reflected in the relation between the angular momentum of the baryonic components and DM. The left panel of [Fig. 3.3.6](#) shows the misalignment angle between the angular momentum of the total DM halo and the gas within the inner 10% of the virial radius at redshift $z = 0.1$. Again, the gray dashed line is the expected distribution if the angles were spread randomly. We clearly see that the median misalignment found for all halos (green solid lines) is $\approx 49^\circ$, for the disks $\approx 45^\circ$, and for the spheroids $\approx 47^\circ$. This is slightly larger than the results of [Sharma et al. \(2012\)](#), who found a median misalignment angle of about 30° for the gas within the innermost 10% of the virial radius compared to the total angular momentum vector of all halos. On the other hand, [Hahn et al. \(2010\)](#) compared the angular momentum of the gas component of the disk to the total angular momentum and obtained about 49° at $z = 0$, well in line with our results.

We now want to see under which circumstances the orientation of the angular momentum vectors of the total DM halo is reflected in that of the stellar component, since we have seen in [Fig. 3.3.5](#) that the angular momentum vectors of the gas and that of the stars are very well aligned in the inner part of the halo for disk galaxies and poorly aligned for

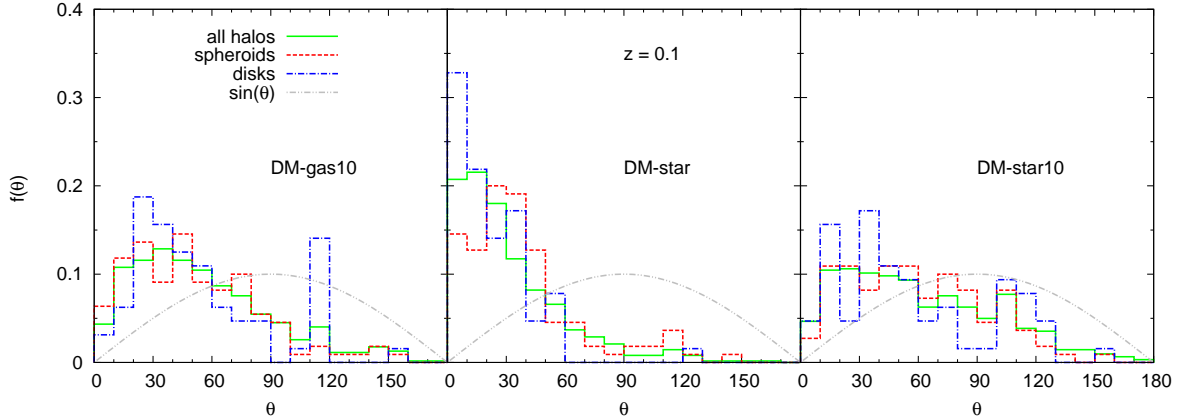


Figure 3.3.6: *Left:* angle between the total angular momentum vector of DM in R_{vir} and the gas within the innermost 10% of R_{vir} . The overall alignment is poor. *Middle:* The angle between the total angular momentum vectors of the DM and stars within R_{vir} . The disk galaxies (blue dot-dashed lines) seem significantly better aligned than the spheroids (red dot-dashed lines). *Right:* angle between the total angular momentum vector of the DM in R_{vir} and the stars within the innermost 10% of the virial radius. For all shown distributions the alignment is very poor, almost random.

spheroids. The angle between the angular momentum vectors of the DM and that of the stars within the virial radius is shown in the middle panel of Fig. 3.3.6. In general, there is an alignment of the two components. The disk galaxies are slightly better aligned with a median angle of $\approx 18^\circ$ compared to the spheroids that have a median angle of $\approx 31^\circ$. As a median value for all halos we find $\approx 24^\circ$ at redshift $z = 0.1$ and a similar value for $z = 1$, namely, $\approx 22^\circ$, which is not shown here.

The right panel of Fig. 3.3.6 shows the angle between the angular momentum vector of the stars within the inner 10% of the virial radius and the DM within the entire virial radius. The distribution of the alignment angles looks similar to that of the gas (left panel of Fig. 3.3.6) for all galaxies. The alignment seems poor, with median angles of $\approx 55^\circ$ for all halos, $\approx 46^\circ$ for disks, and $\approx 57^\circ$ for spheroidal galaxies. This agrees well with Hahn et al. (2010), who calculated a median angle of the stellar component and the total halo content of about $\approx 49^\circ$ at $z = 0$ for disk galaxies, similar to Croft et al. (2009) reporting a median angle of $\approx 44^\circ$ at redshift $z = 1$. Bett et al. (2010) found slightly smaller angles of $\approx 34^\circ$ for the alignment of the galaxies with respect to the hosting total DM halo. The galaxies at $z = 1.2$ investigated by Codis et al. (2015), using the Horizon-AGN simulation, are slightly less aligned with their DM halos than our simulated galaxies (see also the right panel of Fig. 3.5.2 of Section 3.5). Deason et al. (2011) reported that 41% of their disk galaxies had misalignment angles larger than 45° with their DM halo. In addition, they found that the disk galaxies are better aligned with the DM in the innermost 10% of the r_{200} . Though we do not show this, here we obtained a median angle of $\approx 9^\circ$ for the angular momentum vectors of the stellar and DM components in the innermost 10% for our disk galaxies at $z = 0.1$, and thus we can confirm this trend. It also agrees well with Hahn

Table 3.4: Median Misalignment Angles of the DM at Different Radii

Redshift	All Halos	Disks	Spheroids	DMO
2	56.7	54.8	57.2	66.6
1	54.9	51.2	61.3	—
0.5	48.3	53.1	48.8	53.5
0.1	47.4	42.2	50.6	51.3

The median misalignment angles between the angular momentum vectors of the DM within 10% and that of the total DM halo ($\theta_{\text{DM-DM10}}$) for the hydrodynamical run as well as for the run with only DM (DMO).

[et al. \(2010\)](#), who find a median value of $\approx 15^\circ$ for the angle between the DM and stellar components of the galactic disks. For the DM and the gaseous components of their disks they obtain a median value of $\approx 18^\circ$, which is in line with the median value of $\approx 12^\circ$ for our disk galaxies.

3.4 The Host Halos of Different Galaxy Types

So far we have seen the intrinsic difference of the baryonic components and how they reflect global halo properties for galaxies classified as either disk or spheroidal galaxies. We now want to study whether there are underlying differences in the DM halo contributing to the formation of these two classes of galaxies.

3.4.1 The Alignment of the Host Halos with Their Centers

One interesting question is if there are signatures of differences in the internal structure of the angular momentum in the DM component for disk galaxies and spheroidal galaxies. Therefore, we compare the angular momentum of the DM within the whole halo with the one within 10% of the virial radius. Fig. 3.4.1 shows the cumulative distributions of the angle between the DM angular momentum vector of the whole halo and that of the inner part of the halo. At $z = 2$, $z = 0.5$, and $z = 0.1$ we include the corresponding distribution of the DM-only run ⁴. The alignment is generally better for disks than for spheroids (see also Table 3.4), as already speculated in [Bullock et al. \(2001\)](#). Interestingly, the relative difference between the alignments for disk and spheroidal galaxies is largest at $z = 1$, which corresponds to a typical formation redshift of spiral galaxies. Overall, the misalignment grows with redshift for all halos. At redshift $z = 0.1$ we calculate median values for all halos of $\approx 47^\circ$, which agrees well with [Hahn et al. \(2010\)](#), reporting a value of 45° .

⁴For technical reasons there were no data available at $z = 1$ from the DM-only run.

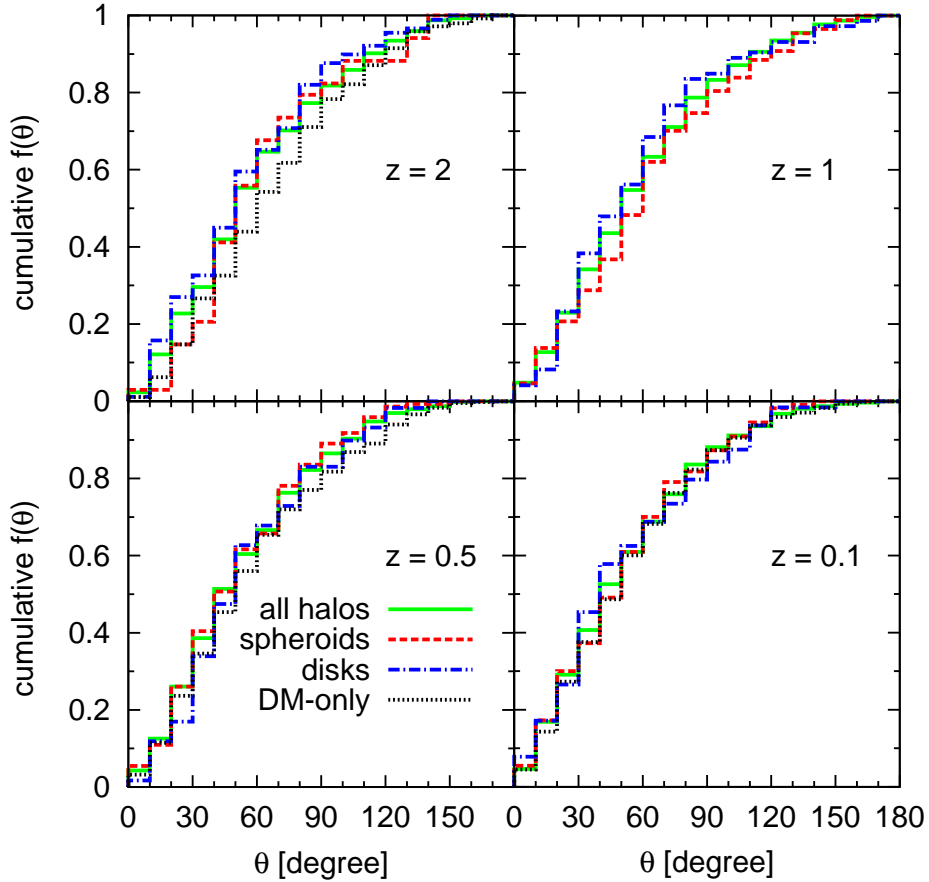


Figure 3.4.1: Angle between the total angular momentum vector of the DM in R_{vir} and that of the DM within the innermost 10% of the virial radius. At redshifts $z = 2$, $z = 0.5$, and $z = 0.1$ we overplot the distribution of the DM-only run (black dotted).

In contrast, in the DM-only run the values are slightly higher at all redshifts, with median misalignment angle of $\approx 51^\circ$ at $z = 0.1$. This tendency was also seen by [Bett et al. \(2010\)](#), who found that in their run with baryons the vectors were slightly more aligned than in the DM-only case. The misalignment angle in our analysis is higher than their median angles of $15^\circ - 30^\circ$ for their run with baryons. This could be due to the fact that we only consider the inner 10% instead of 25%, as in their study. This is expected, since [Bailin and Steinmetz \(2005\)](#) found that the alignment becomes worse when the radii are further separated.

A possible interpretation of the above findings could be that disk galaxies preferentially reside in halos, where the core is better aligned with the outer parts of the halo (see also [Bullock et al., 2001](#)). It might well be that in such halos the angular momentum can be transported more effectively by the cooling of gas from the outer parts into the central parts. Another possibility could be that disk galaxies survive merger events longer, when consecutive infall is aligned with the angular momentum of the galaxy. Interest-

ingly, spheroidal galaxies (especially at $z \approx 1$) show exactly the opposite behavior. The inner and outer parts of their DM halos are less aligned, indicating that major merging events are contributing to the buildup of spheroidal galaxies. This is in line with previous studies showing that major mergers with misaligned spins can be responsible for angular momentum misalignments (Sharma et al., 2012).

In addition, Welker et al. (2014) proposed that anisotropic cold streams realign the galaxy with its hosting filament. However, Sales et al. (2012) suggested that disks form out of gas having similar angular momentum directions, which would favor the spherical hot accretion mode, while the accretion along cold flows that are mainly misaligned tends to build a spheroid. To answer this question in detail, further investigation is needed to trace back disk galaxies and see whether the primordial alignment causes the inflowing matter to become a spiral or whether it is the other way around, i.e., if the galaxy type over cosmic time induces the alignment. We suspect that the environment has a significant impact on the formation of disk galaxies. In less dense environments, where the halos can evolve relatively undisturbed, the angular momentum of the galaxy preferably remains aligned with that of its host halo, and thus a disk can form.

3.4.2 The Spin Parameter λ of the Host Halos

In the following section we finally return to the spin parameter λ , evaluated for the whole halo. In Fig. 3.4.2 we show the distribution of the λ -parameter for the total matter distribution within our halos for different redshifts. The histograms and lognormal fit curves (see Equation 3.6) are each normalized to the number of the halos. The distribution of λ for all 396 halos at $z = 2$ (upper left), 606 halos at $z = 1$ (upper right), 629 halos at $z = 0.5$ (lower left), and 621 halos at $z = 0.1$ (lower right) is shown in green. We also plot the distribution of the spheroidal (red dashed) and disk (blue dot-dashed) galaxies. The spheroids, which have only little rotation in the stellar component, tend to have lower λ -values. The disk galaxies have their median at higher values. This bimodality of the two galaxy types is seen at all four redshifts, as already shown in Teklu et al. (2015). The spheroids have always lower median values than the disk galaxies (see also Table 3.5 for the fitting parameters). Observationally, Hernandez et al. (2007) also found that the spiral galaxies on average have larger λ -values than the ellipticals of their sample. However, this was not seen in previous studies by Sales et al. (2012) and Scannapieco et al. (2009), who did not find a correlation between galaxy type and the spin parameter.

The λ -distribution for all halos seems to be relatively constant with time, i.e., independent of redshift, which is in agreement with Peirani et al. (2004).

To verify the statistical significance of the differences, we show in Fig. 3.4.3 the cumulative distributions for the λ -values, again splitting the halos according to the different galaxy types they host. This illustrates the distances between the two distributions, where the curve for the halos of the spheroidal galaxies is always left of the curve for all halos and the

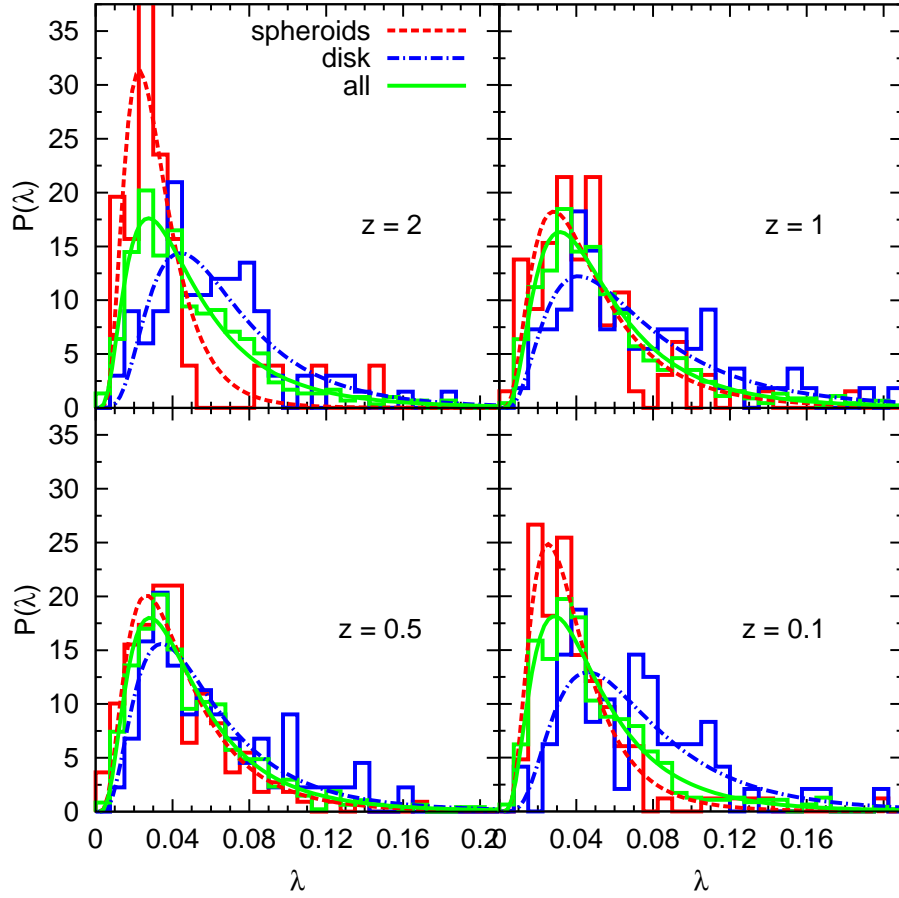


Figure 3.4.2: The λ -distribution calculated with formula (3.3) for the different redshifts as indicated in the plots. Green takes all halos into account. The distributions of the spheroids are the red dashed histograms, and those of the disks are blue dot-dashed histograms. The curves are the fits given by equation (3.6). At all redshifts a split-up of the two different galaxy types is present. The spheroids have their median at the lower λ -values, while the disks have higher values.

curve of the disk galaxies stays always to the right. The differences are more pronounced for small spins. To quantify the statistical significance of differences in the distributions for the disk and spheroidal galaxies, we apply a Kolmogorov-Smirnov (K-S) test. This test is applied to the two unbinned distributions for the disks and the spheroids. Table 3.6 shows the calculated values for the maximum distance D and the probability. With the exception of the results⁵ at $z = 0.5$, this confirms that the spin distributions of the halos hosting disk galaxies are statistically significantly different from the halos hosting spheroidal galaxies.

In this section we have seen that there is a statistical correlation between the morphological type and the overall distribution of the spin parameter λ . We thus conclude that the total

⁵Although unlikely, the value obtained at $z = 0.5$ does not allow to exclude the same origin of the two distributions.

Table 3.5: Calculated Median Values and the Fit Values of the λ -Distributions

Redshift	All Halos
2	$\lambda_{\text{med}} = 0.043, \lambda_0 = 0.043, \sigma = 0.662$
1	$\lambda_{\text{med}} = 0.046, \lambda_0 = 0.047, \sigma = 0.635$
0.5	$\lambda_{\text{med}} = 0.041, \lambda_0 = 0.042, \sigma = 0.640$
0.1	$\lambda_{\text{med}} = 0.042, \lambda_0 = 0.043, \sigma = 0.630$
Redshift	Disks
2	$\lambda_{\text{med}} = 0.058, \lambda_0 = 0.059, \sigma = 0.543$
1	$\lambda_{\text{med}} = 0.060, \lambda_0 = 0.062, \sigma = 0.644$
0.5	$\lambda_{\text{med}} = 0.051, \lambda_0 = 0.050, \sigma = 0.617$
0.1	$\lambda_{\text{med}} = 0.069, \lambda_0 = 0.064, \sigma = 0.570$
Redshift	Spheroids
2	$\lambda_{\text{med}} = 0.028, \lambda_0 = 0.029, \sigma = 0.497$
1	$\lambda_{\text{med}} = 0.042, \lambda_0 = 0.042, \sigma = 0.633$
0.5	$\lambda_{\text{med}} = 0.037, \lambda_0 = 0.039, \sigma = 0.620$
0.1	$\lambda_{\text{med}} = 0.034, \lambda_0 = 0.034, \sigma = 0.546$

The calculated median values λ_{med} and the fit values λ_0 and σ of the λ -distributions at different redshifts for our sample of galaxies.

Table 3.6: K-S Test for the λ -Distributions

Redshift	D	Probability
2	0.563	$1.41 \cdot 10^{-7}$
1	0.319	$4.45 \cdot 10^{-4}$
0.5	0.237	$1.45 \cdot 10^{-2}$
0.1	0.421	$6.31 \cdot 10^{-7}$

The maximum distance D and the significance level (probability) resulting from the K-S test that the λ -distributions for disks and spheroids at different redshifts for our sample of galaxies are from the same distribution.

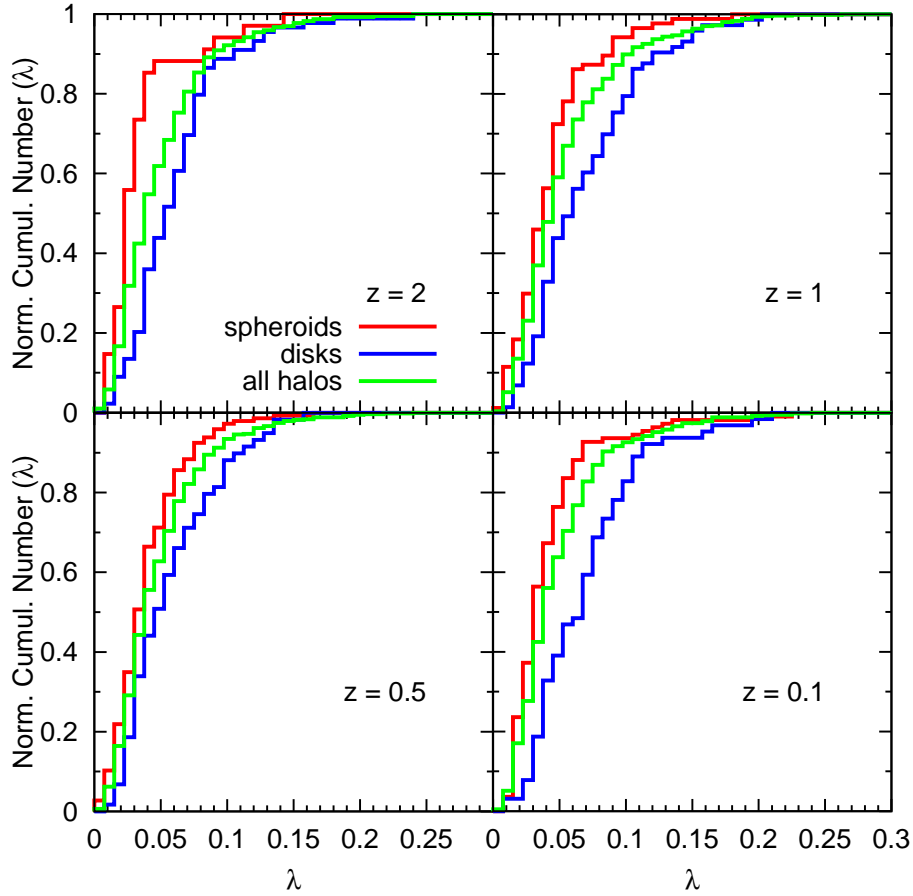


Figure 3.4.3: The λ -parameter plotted against the normalized cumulative number of halos. Green takes all halos into account, red the spheroidal galaxies, and blue the disk galaxies. The distributions of the disks and the spheroids do not overlap (besides at $z = 0.1$ at the higher end). The disks are on the right side, i.e., at higher values, of the distribution for all halos, while the spheroids are on the left, i.e., at lower values.

DM halo somehow “knows” about the morphology of the galaxy at its center. At all four considered redshifts the distributions for the spheroids have lower median λ -values than those of the disks. According to the K-S test, there is a strong indication that they do not originate from the same distribution. On the other hand, we have also found that there are spheroids with even higher λ -values than disk galaxies.

To verify that these differences are intrinsic to the halo and not caused by the contributions of the baryonic component to the spin parameter, we calculated the spin parameter λ_{DM} for the DM component of the halos. Fig. 3.4.4 shows the λ_{DM} -distribution for the baryon run for the four redshifts as indicated in the plots. The green histogram shows λ_{DM} for all halos, the red one stands for the spheroids, and the blue one for disk galaxies. Here again, most prominently visible at redshifts $z = 2$ and $z = 0.1$, there is a splitting of the two different galaxy types, the distribution of the spheroids peaks at lower values, and that of

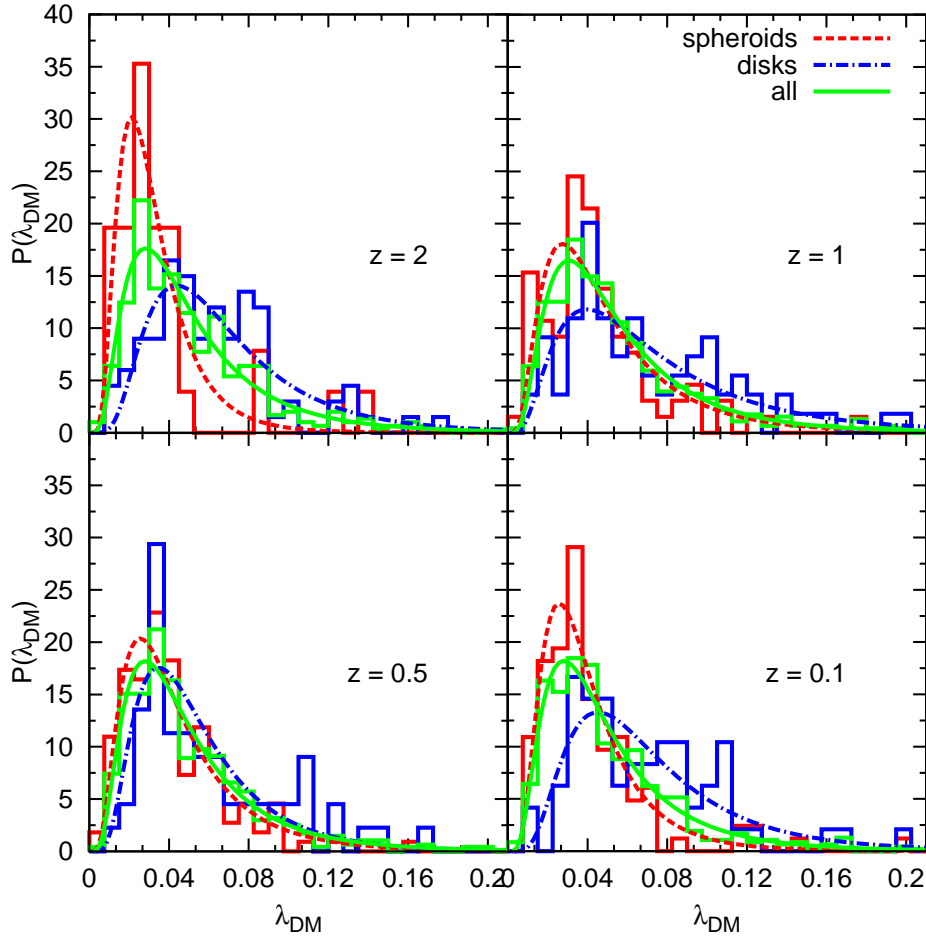


Figure 3.4.4: The λ -parameter for the DM component within R_{vir} ; also in the DM component of all halos (green) there is a broad distribution, which splits into spheroids (red) at lower values, while disks (blue) peak at higher values.

the disks at higher values. We also perform a K-S test on the two distributions (see Table 3.7). The values are similar to that of the general λ -distribution (Table 3.6).

In Section 3.5 we show that this split-up of the galaxy types is also reflected in the spin parameter λ of the stellar component.

In order to see whether the differences originate from differences within the DM halo or if they are caused by the interplay between the DM and the baryonic component, we finally compare the run with the baryons to the DM-only control run. We thereto cross-identify the halos of the DM-only run with those of the hydrodynamical run. We search for the corresponding halos in the DM run, allowing the center of the halo to be in a range of 200 kpc around its position in the simulation with baryons, and additionally restrict to halo pairs that only differ by up to 30% in their virial masses. At redshift $z = 2$ we found 364 halos in the baryon run that match with the DM-only run, at $z = 0.5$ we could assign 609

Table 3.7: K-S Test for the λ_{DM} -Distributions

Redshift	D	Probability	D_{DMO}	Probability _{DMO}
2	0.537	$5.92 \cdot 10^{-7}$	0.590	$8.14 \cdot 10^{-8}$
1	0.319	$4.45 \cdot 10^{-4}$	—	—
0.5	0.234	$1.65 \cdot 10^{-2}$	0.285	$2.3 \cdot 10^{-3}$
0.1	0.390	$4.60 \cdot 10^{-6}$	0.370	$9.84 \cdot 10^{-5}$

The maximum distance D and the significance level (probability) resulting from the K-S test that the λ_{DM} -distributions for disks and spheroids at different redshifts originate from the same distribution for the baryon run and the DM-only (DMO) run.

halos, and at $z = 0.1$ we cross-matched 575 halos. We find that the λ_{DM} -values of each halo identified in both runs are very similar (see Fig. 3.5.4 of Section 3.5). Since baryons have an effect on the DM, in the two runs the evolution of some of the halos can be quite different, as also discussed in Bett et al. (2010). Therefore, we cannot match every halo.

Fig. 3.4.5 shows the λ -distribution for the DM component at three different redshifts. The overall distribution is shown in black. The fit values λ_0 for the DM-only run are slightly lower than for the run with baryons. When we split the halos in the DM-only run according to their galaxy type assigned in the run with baryons, we find a similar split in the distributions as in the run with baryons. At redshift $z = 2$ we could use 76 disks and 33 spheroids, at $z = 0.5$ there are 55 disks and 143 spheroids, and at $z = 0.1$ we cross-matched 53 disks and 99 spheroids. The results of the K-S test (see Table 3.7) show that these two distributions are unlikely to originate from the same one. It is striking that even in the run without baryons, the split-up of the spin parameter for the different galaxy types is clearly visible. This suggests that the hosting DM halo and, connected with that, the formation history and environment play an important role for the morphology of the resulting galaxy.

3.5 Further Details and Tests

In the following section we provide further details and present tests that we have performed. This supplementary information underlines the previously found results.

3.5.1 Details on the Classification

In order to illustrate the choice of the cuts in $\varepsilon_{\text{star}}$ used for the classification of our galaxies, we show the cumulative circularity distribution for spheroids (left panels) and the ‘anti-’cumulative distribution for disk galaxies (right panels) in Fig. 3.5.1. For the spheroids we sum up the fractions from $-\varepsilon$ to ε of the distributions shown in Fig. 3.2.2, $f(x) =$

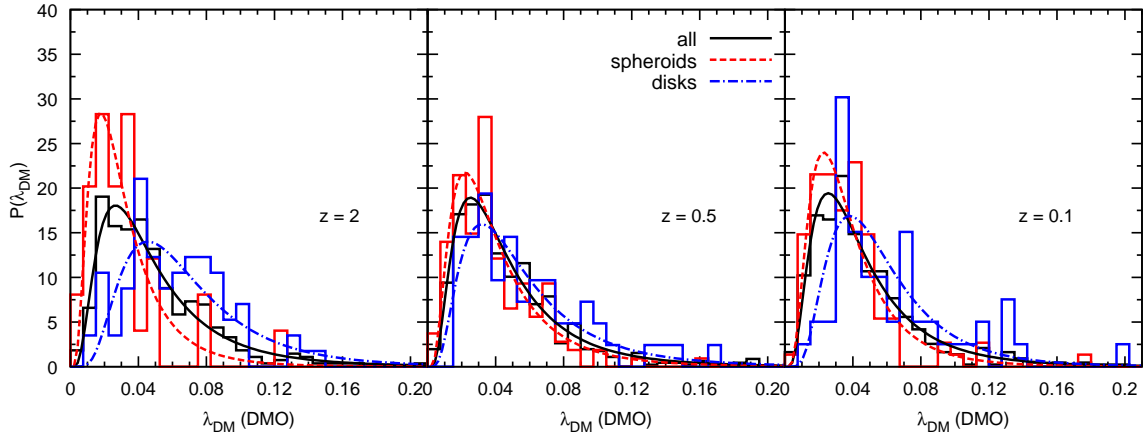


Figure 3.4.5: The λ -parameter for the DM component for the DM-only run (black) at three redshifts. The red curves show the distribution for halos that were identified in the baryon run and classified as spheroids, while the blue curves show the halos classified as disks in the baryon run. There is a split-up of the galaxy types, which suggests that the morphology could be a result of the formation history.

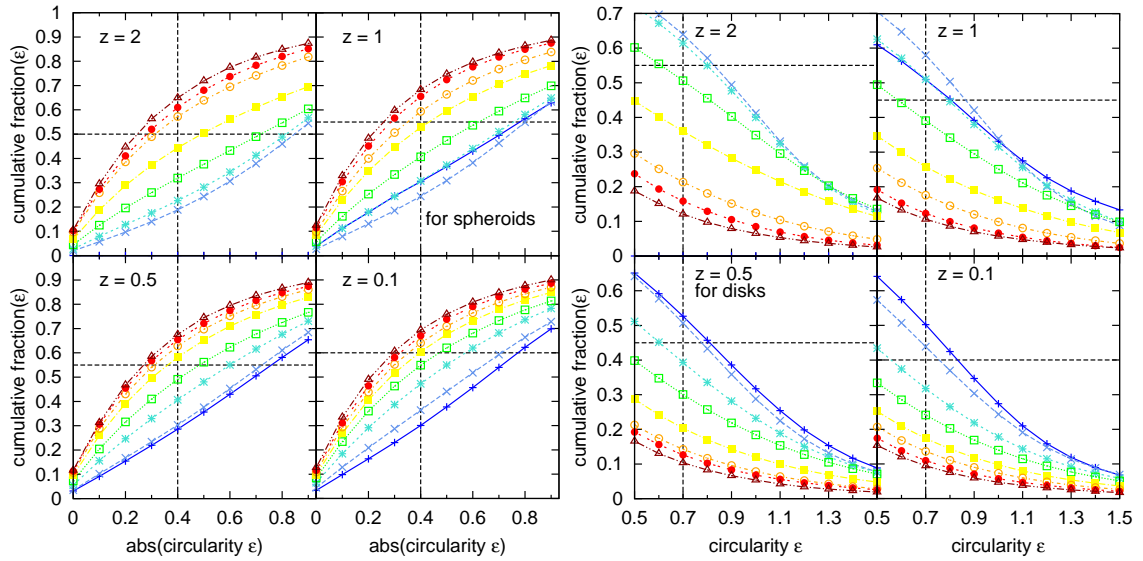


Figure 3.5.1: *Left:* cumulative fraction of all galaxies in dependency of the circularity ε of the stars for all four redshifts. The colors reflect the different b -value bins, as in Fig. 3.2.2. From this we estimate the cut for the determination of the spheroidal part of a galaxy. This cut differs for each redshift. *Right:* cumulative fraction in order to determine the disk part of a galaxy. The values on the y -axis are the cumulative values from the corresponding point on the x -axis up to an ε -value of 3.

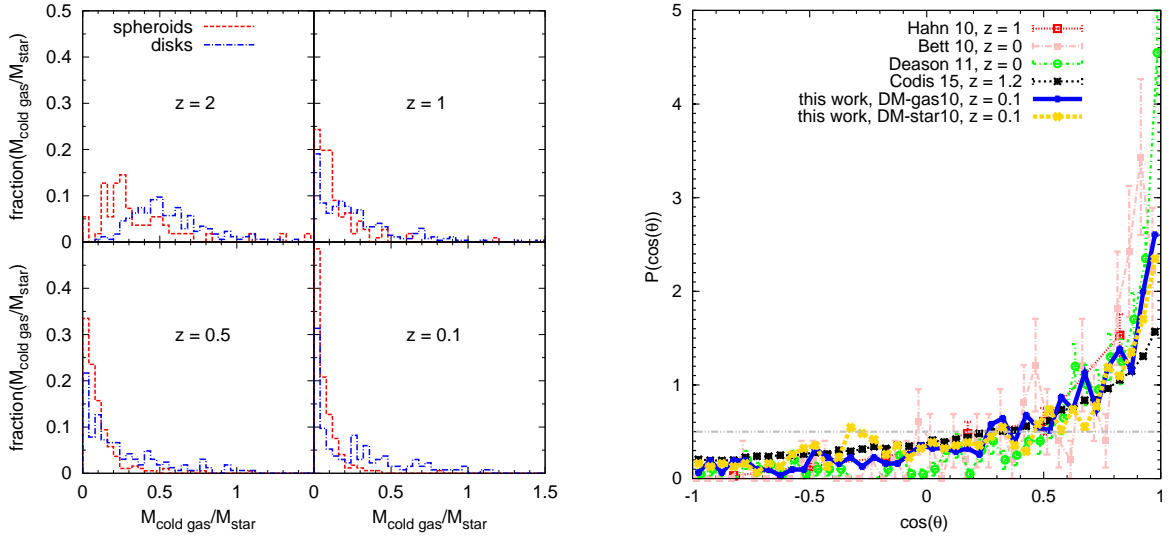


Figure 3.5.2: *Left:* fraction of the mass of the cold gas with respect to the stellar mass, both within the inner 10% of the virial radius. The cold gas fraction decreases continuously with decreasing redshift, for spheroids faster than for disk galaxies. Note that at $z = 2$ most spheroidal galaxies have a mass fraction larger than 10%. At $z = 0.1$ the disk galaxies are divided into two populations, one with a fraction higher than 30% and the other having less than 10%. We suggest that the second population comprises lenticular galaxies. *Right:* probability distribution function of the alignment of the galaxies compared to their DM halo in comparison with previous studies, as indicated in the plot.

$\sum_{-x}^x fraction(\varepsilon)$. The cut is drawn between the halos of the b -value-bin that show a clear behavior of spheroids at the corresponding redshift. The same is done for the disk galaxies, besides that here we sum up the fraction from ε to 3, $f(x) = \sum_x^3 fraction(\varepsilon)$.

In the left panels of Fig. 3.5.2 we show that at high redshift there are many spheroidal galaxies (red histograms, classified with $\varepsilon_{\text{star}}$) with a high fraction of cold gas mass with respect to the stars. This fraction decreases very fast with decreasing redshift. Disk galaxies (blue) have a higher amount of cold gas at all times, especially at high redshift. Still, at low redshift there are many disk galaxies that have less than 10% cold gas. Those galaxies actually resemble S0 properties and are not classical “disks.”

In Table 3.8 we list the values of the cuts for the classification criteria. The values for the spheroids should be understood as an upper limit, while for the disks they represent a lower limit.

3.5.2 The Alignment of the Galaxy with Its DM Halo

The right panel of Fig. 3.5.2 shows the probability distribution function of the cosine of the angles between the innermost 10% of the virial radius of our disk galaxies and the hosting

Table 3.8: Upper/Lower Limits for the Classification Criteria

Redshift	$\varepsilon_{\text{star}, d}$	$\varepsilon_{\text{star}, s}$	$M_{\text{cold}}/M_{\text{star}, d}$	$M_{\text{cold}}/M_{\text{star}, s}$
2	0.55	0.5	0.5	0.35
1	0.45	0.55	0.35	0.2
0.5	0.45	0.55	0.275	0.125
0.1	0.4	0.6	0.215	0.065

The values for the classification depending on redshift. We list the lower limit for the $\varepsilon_{\text{star}}$ for disks (d) as well as spheroids (s). For the disks the $M_{\text{cold}}/M_{\text{star}}$ is a lower limit, while the spheroids have to have less than the given value.

DM halo. The solid blue line stands for the gaseous component, and the yellow dashed line for the stellar component. We extracted the other data points from [Codis et al. \(2015\)](#) for an easier comparison with previous works. Overall, our results are in good agreement with previous studies. We find that our disk galaxies have a slightly weaker alignment than those of [Bett et al. \(2010\)](#) and [Deason et al. \(2011\)](#). Our results agree well with [Hahn et al. \(2010\)](#). [Codis et al. \(2015\)](#) report slightly less aligned galaxies.

3.5.3 The Spin Parameter λ

The left panels of Fig. 3.5.3 show the λ -parameter of the stellar component within the innermost 10% of the virial radius against that of the total DM halo for individual halos classified as spheroids (red circles) and disks (blue diamonds). We can clearly see the split-up of the two populations, where disk galaxies have a higher stellar spin than the spheroids.

On the right side of Fig. 3.5.3 we show the λ -distribution for the stellar component within the total virial radius. We also see a split-up of the spheroidal (red) and disk (blue) galaxies. The stars in disk galaxies have a higher spin than in spheroids. This seems plausible, since most stars in disk galaxies are found in the disk while most stars in spheroidal galaxies are found in the dominant bulge and thus are more spherically distributed. Hence, they have a net spin that is lower than that in disk galaxies, where the stars sum up their spin. This also shows that the stars trace the formation history of the galaxies. The stars in disks form out of the fresh gas with high angular momentum, while in spheroids many stars are accreted (via minor/major mergers).

In Table 3.9 we show the results from the K-S test for the λ_{star} -distribution. The two distributions for the disks and spheroids do not originate from the same distribution.

In order to see how the λ -parameter behaves for individual halos in the baryon and the DM-only runs, we identified the same halos in the baryonic and the DM-only run (as described earlier). The left panels of the left figure of Fig. 3.5.4 show the λ -parameter of the DM component against the λ -parameter of the DM-only run in logarithmic scaling for

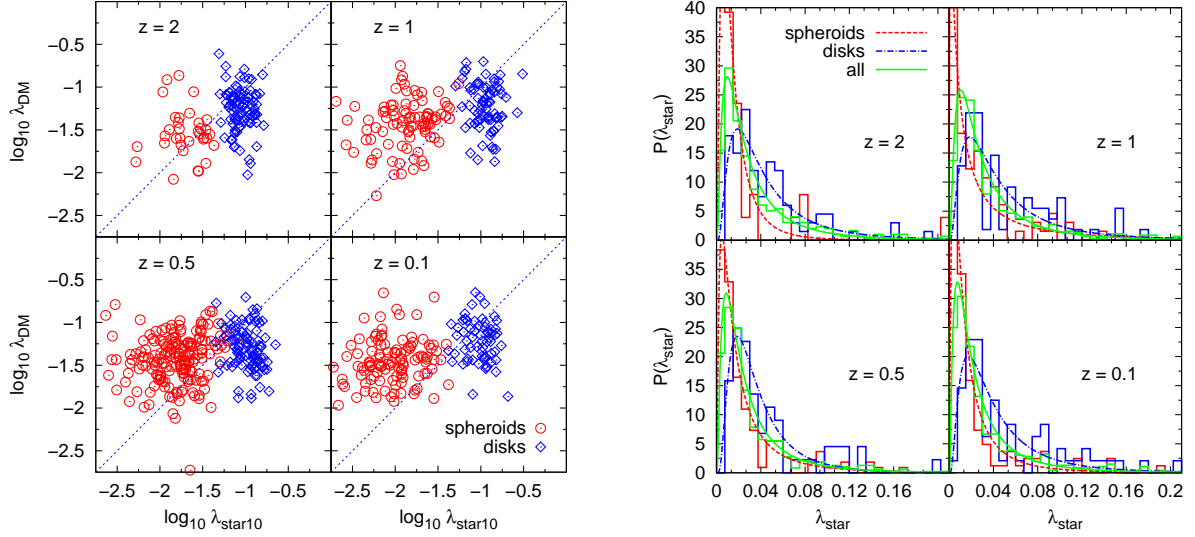


Figure 3.5.3: *Left:* λ -parameter for the stellar component in the innermost 10% against that of the DM of the entire DM halo, at four different redshifts, divided into spheroidal (red circles) and disk (blue diamonds) galaxies. *Right:* λ -distribution for the stellar component at four different redshifts, divided into spheroidal (red dashed) and disk (blue dot-dashed) galaxies. The stellar component of spheroids has a very low median value, whereas the disk galaxies have a higher one at all shown redshifts.

Table 3.9: K-S Test for the λ_{star} -Distributions

Redshift	D	Probability
2	0.558	$1.81 \cdot 10^{-7}$
1	0.364	$3.42 \cdot 10^{-5}$
0.5	0.443	$6.62 \cdot 10^{-8}$
0.1	0.493	$2.40 \cdot 10^{-9}$

The maximum distance D and the significance level (probability) resulting from the K-S test that the λ_{star} -distributions for disks and spheroids at different redshifts are drawn from the same distribution.

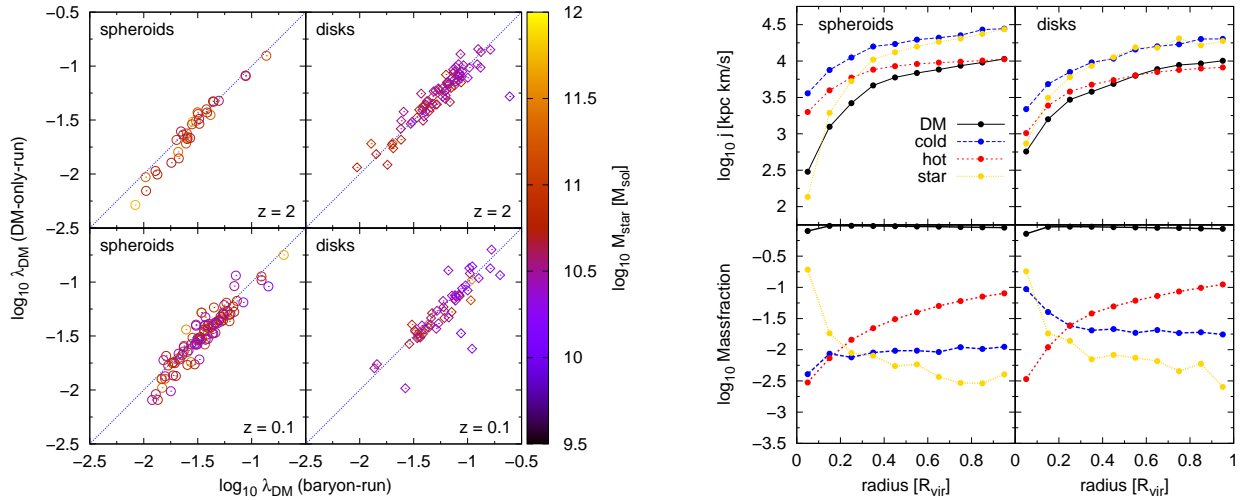


Figure 3.5.4: *Left:* λ -parameter plotted logarithmically for the DM component, on the x -axis the λ for the baryon run and on the y -axis for the DM-only run; the color codes the stellar mass within the inner 10% of the virial radius. On the left panels are the spheroids and on the right panels the disks. The upper panels show redshift $z = 2$ and the lower ones $z = 0.1$. *Right:* specific angular momentum (top panels) and the mass fractions (bottom panels) against distance from the center for the cold gas (blue), hot gas (red), stars (yellow), and DM (black) of our sample of galaxies at $z = 0.1$. On each left-hand side we show the analysis for the spheroidal galaxies, and on each right-hand side that for the disks.

spheroids at redshifts $z = 2$ (upper panel) and $z = 0.1$ (lower panel). The values of the λ -parameter of the corresponding halos in both runs are similar. The stellar mass within 10% of the virial radius of the baryon run is color-coded. On the right panels we find the λ_{DM} -values for the disks. At redshift $z = 2$ (upper panel) we note a slight tendency for the λ_{DM} to decrease with increasing stellar mass. The less massive disks tend to have higher λ -values. This is in agreement with [Berta et al. \(2008\)](#), who computed the DM spin parameter of $\approx 52,000$ disk galaxies from the SDSS (for details of the sample see references in [Berta et al. \(2008\)](#)). They found a clear anticorrelation between the DM spin and the stellar mass, i.e., that galaxies with a low mass in general have higher DM spins. For the spheroidal galaxies we do not see this trend. In addition, this figure demonstrates that a high λ does not automatically lead to a disk galaxy and a small λ is no guarantee for a spheroidal galaxy. The scatter is equal for both galaxy types. The fact that λ_{DM} in the whole virial radius is similar in the DM-only and the baryon run is in good agreement with [Bryan et al. \(2013\)](#).

3.5.4 The Radial Specific Angular Momentum Profiles

In order to illustrate the behavior of the specific angular momentum of the different components, we show on the right-hand side of [Fig. 3.5.4](#) the mean of our sample of spheroidal

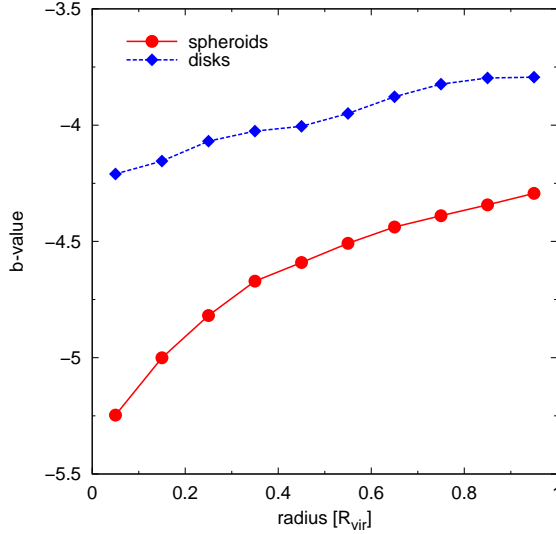


Figure 3.5.5: The radial profile of the b -value averaged over spheroids (red circles) and disks (blue diamonds).

(left panel) and disk galaxies (right panel) at $z = 0.1$. In the upper panels we plot the differential specific angular momenta of the different components against radius, and in the lower panels we plot the individual mass fractions of the corresponding components against radius. The x -axis is linearly binned with a bin size of 10% of the virial radius of a halo. The specific angular momentum of the two galaxy types increases from the center of the halo up to the virial radius. On the outer parts the specific angular momentum of the hot gas follows the DM, while the specific angular momentum of the stars follows that of the cold gas. This might be due to the infalling substructures, which mostly consist of small gas clumps with stars that formed out of it. The main difference of the two galaxy types becomes clear in the center: the angular momentum of the stars drops dramatically in spheroidal galaxies, while in disk galaxies it remains higher than that of the DM. With respect to the baryons, the outer region is dominated by the hot gas, which behaves similarly for spheroids and disks.

Fig. 3.5.5 shows the radial profile of the b -value. Therefore, we calculated

$$b = \log_{10} \left(\frac{j_{\text{star}}(\leq r)}{\text{kpc km/s}} \right) - \frac{2}{3} \log_{10} \left(\frac{M_{\text{star}}(\leq r)}{M_{\odot}} \right), \quad (3.10)$$

averaged over the spheroids and disks. The slope is steeper for the spheroids than for the disk galaxies. This illustrates that the measurement of the kinematic properties is more sensitive to the radius for spheroidal than for disk galaxies.

3.6 Discussion and Conclusions

We extracted between 400 and 630 halos with total halo masses above $5 \cdot 10^{11} M_{\odot}$ at four different redshifts from the hydrodynamical, cosmological state-of-the-art simulation Magneticum Pathfinder, which includes detailed treatment of star formation, chemical enrichment, and evolution of supermassive BHs. We investigated the distribution of the spin parameter λ_k of the different components (DM, stars, hot and cold gas) and the alignment of the angular momentum vectors of those components within the entire halo, as well as within the central 10% of the virial radius. To classify the galaxies according to their morphology, we rotate them such that their angular momentum vector is oriented along the z -axis. For this orientation we calculate the circularity parameter ε , which allows a classification based on their circularity distribution. This allows us to define the subset of galaxies clearly identified as spheroidal or disk galaxies and to compare their properties to observations. We additionally performed and analyzed a DM control simulation to test the effect of the baryonic processes and the formation history on the angular momentum within the halos. We summarize our findings as follows:

- For all our halos, the stellar component generally has a lower spin than the DM component, while the gas shows a significantly higher spin parameter, especially the cold gas component that dominates the overall spin parameter of the gas. While the distribution of the spin parameters of stars and DM does not show a significant evolution with time, the spin distribution of the gas component significantly evolves toward larger spin values with decreasing redshift.
- In general, the angular momentum vectors of the baryonic components and the DM are well aligned. There is an evolution within these alignments, where at high redshifts the alignment between gas and stars is better than their alignment with the DM component, while at low redshift stars and DM tend to be better aligned.
- When classifying galaxies according to their position within the stellar-mass-specific-angular-momentum plane, we demonstrate that various galaxy properties show smooth transitions, as expected when going from rotation-dominated systems to dispersion-dominated systems. This is most prominently found for the circularity distribution of stars and gas, the cold gas fraction, but also for the spin parameter distribution and the alignments of the angular momenta. Rotation-dominated galaxies have generally larger spin parameters, and the angular momentum vectors of the stars and gas components are aligned. On the contrary, dispersion-dominated galaxies generally have smaller spin parameters and show almost no alignment between the angular momentum vectors of stars and the (however small) gas components.
- Alternatively, when classifying our galaxies according to their circularity distribution in combination with the cold gas content into disk galaxies and spheroidal galaxies, they populate clearly distinguishable regions within the stellar-mass-specific-angular-momentum plane. Using that classification, we lose a significant number of galaxies

that cannot be classified within this scheme. Nevertheless, for those galaxies that can be classified the results are in excellent agreement with observations for both spheroidal and disk galaxies.

- In disk galaxies the specific angular momentum of the gas is slightly higher than that of the stars, which is in good agreement with recent observations (Obreschkow and Glazebrook, 2014). This is due to the fact that the gas component has contributions from freshly accreted gas with higher specific angular momentum, which will be turned into stars later. This is also reflected in our result that the specific angular momentum of the young stars is slightly larger compared to that of all stars.
- In general, the specific angular momentum of the total halo is higher than the specific angular momentum of the gas in the galaxy. For disk galaxies it accounts for roughly 43% of the value found for the total halo, with no significant redshift evolution.
- Overall, the angular momentum of the total halo is only weakly aligned with the angular momentum of the central part. Here the simulation including baryons shows slightly more alignment than the DM-only simulation. However, we found that in general the halos hosting disk galaxies (in comparison with halos with spheroidal galaxies at their centers) show a better alignment of the angular momentum vectors of the total halo and the central part for the DM component. This is most pronounced at redshift $z \approx 1$, where most disk galaxies are forming.
- The splitting of the galaxies into disk and spheroidal galaxies reveals also a dichotomy in general halo properties: the halos hosting disk galaxies have a slightly larger spin than the halos hosting galaxies classified as spheroidal galaxies. This dichotomy is even reflected in the distribution of the spin parameters in the DM control run, where we cross-identified the halos which in the hydrodynamical simulation host galaxies of different types. This indicates that the formation history of the DM halo plays an important role for defining the morphology of the galaxies.

Our results are based on the classification of galaxies obtained from the circularity of the stellar component ($\varepsilon_{\text{star}}$) in combination with the fraction of cold gas with respect to the stellar mass within the central part of the halo, where the galaxies form. This allows us to select classical disk and spheroidal galaxies, which show very distinct dynamical properties, reflected in their circularity distribution, cold gas fractions, specific angular momentum, and spin and angular momentum vector alignments. They therefore shed light on the main formation mechanism of these galaxies within the cosmological framework.

While our current classification focuses on a selection of galaxies whose properties resemble those of classical spiral and elliptical galaxies, the lion's share of the galaxies in our simulation cannot be classified as poster child disk or spheroidal galaxies. This again reflects observational facts, since at present day many galaxies exhibit signs of distortions, ongoing merger events, peculiar structures, or other irregularities. For our unclassified galaxies, we clearly see that their properties show a smooth transition between the poster child disks and spheroids, and to understand those transition processes, more complex classification

schemes are needed. We suggest that those schemes should consider a differentiation between young and old stellar components, as well as the general distribution of the diverse gas phases in different parts of the galaxies.

Additionally, when comparing to observations, more emphasis needs to be placed on how observational quantities are obtained and how this is mimicked when analyzing simulations. Classifications of galaxy morphologies in cosmological simulations also allow the interpretation of cosmological simulations in various new ways, as already proven in this work, not only for studying the formation and evolution of galaxies but also for studying the relation of AGNs with their host galaxies, as well as for cosmological studies, where the bias of the measurements depends on the morphologies of the galaxies. Therefore, the good agreement of the intrinsic dynamical properties for our classified galaxies with respect to current observations can be seen as a first step to promote cosmological, hydrodynamical simulations for future cosmological studies.

Chapter 4

The Morphology-Density Relation: Impact on the Satellite Fraction

This chapter has been published in [Teklu et al. \(2017\)](#)

Abstract

In the past years several authors studied the abundance of satellites around galaxies in order to better estimate the halo masses of host galaxies. To investigate this connection, we analyze galaxies with $M_{\text{star}} \geq 10^{10} M_{\odot}$ from the hydrodynamical cosmological simulation Magneticum. We find that the satellite fraction of centrals is independent of their morphology. With the exception of very massive galaxies at low redshift, our results do not support the assumption that the dark matter (DM) halos of spheroidal galaxies are significantly more massive than those of disk galaxies at fixed M_{star} . We show that the morphology-density relation starts to build up at $z \sim 2$ and is independent of the star formation properties of central galaxies. We conclude that environmental quenching is more important for satellites than for centrals. Our simulations indicate that conformity is already in place at $z = 2$, where formation redshift and current star formation rate (SFR) of central and satellite galaxies correlate. Centrals with low SFRs have formed earlier (at fixed M_{star}) while centrals with high SFR formed later, with typical formation redshifts well in agreement with observations. However, we confirm the recent observations that the apparent number of satellites of spheroidal galaxies is significantly larger than for disk galaxies. This difference completely originates from the inclusion of companion galaxies, i.e. galaxies that do not sit in the potential minimum of a DM halo. Thus, due to the density-morphological-relation

the number of satellites is not a good tracer for the halo mass, unless samples are restricted to the central galaxies of DM halos.

4.1 Classification of Simulated Galaxies

From our data set we extract all galaxies with stellar masses higher than $10^{10}M_{\odot}$ from the simulation, regardless if they are the central galaxy or a satellite of a larger halo. This limit was chosen to ensure a sufficient resolution of the stellar content. This leads to a total number of 2112 galaxies at $z = 0$, see Table 4.1. We calculate the stellar specific angular momentum j for all galaxies, including all stars within a radius of $5 \cdot R_{1/2}$. We choose $R_{1/2}$ to be the stellar half-mass radius of all stars bound in the according subhalo.

For a relatively simple but still efficient classification of the galaxies we utilize the stellar mass vs. stellar angular momentum plane of galaxies. The position of galaxies on this plane was shown from both observation (e.g. Fall, 1983; Romanowsky and Fall, 2012) and simulations (Teklu et al., 2015) to be a good indicator for the galaxy type.

Following Teklu et al. (2015), for each galaxy we calculate the b -value

$$b = \log_{10} \left(\frac{j}{\text{kpc km/s}} \right) - \frac{2}{3} \log_{10} \left(\frac{M}{M_{\odot}} \right), \quad (4.1)$$

which is the y -intercept of the linear relation $f(x) = ax + b$ in the log-log of the stellar mass vs. stellar angular momentum plane. At $z = 0$, galaxies with $b > -4.35$ are classified as disk galaxies, while galaxies with $b < -4.73$ are classified as ellipticals. Everything in between are labeled as intermediates. For higher redshifts, we adopt the theoretically expected scaling derived by Obreschkow et al. (2015), which was shown to be an excellent match for both disk and elliptical galaxies in the simulations at $z = 2$ by Teklu et al. (2016).

In Table 4.1 we list the resulting number of galaxies classified into spheroids, intermediates, and disks at four different redshifts ($z = 0$, $z = 0.5$, $z = 1$ and $z = 2$). While clear spheroids are getting less frequent at higher redshift, the fractions of disk and intermediate galaxies increase with higher redshift.

Table 4.1: The number of all host galaxies with stellar masses higher than $10^{10}M_{\odot}$ at four different redshifts

redshift	N_{spheroid}	$N_{\text{interm.}}$	N_{disk}	$N_{\text{quiescent}}$	N_{SF}
0	656	760	696	1763	349
0.5	549	861	815	1697	528
1	419	934	857	1374	836
2	246	869	605	180	1440

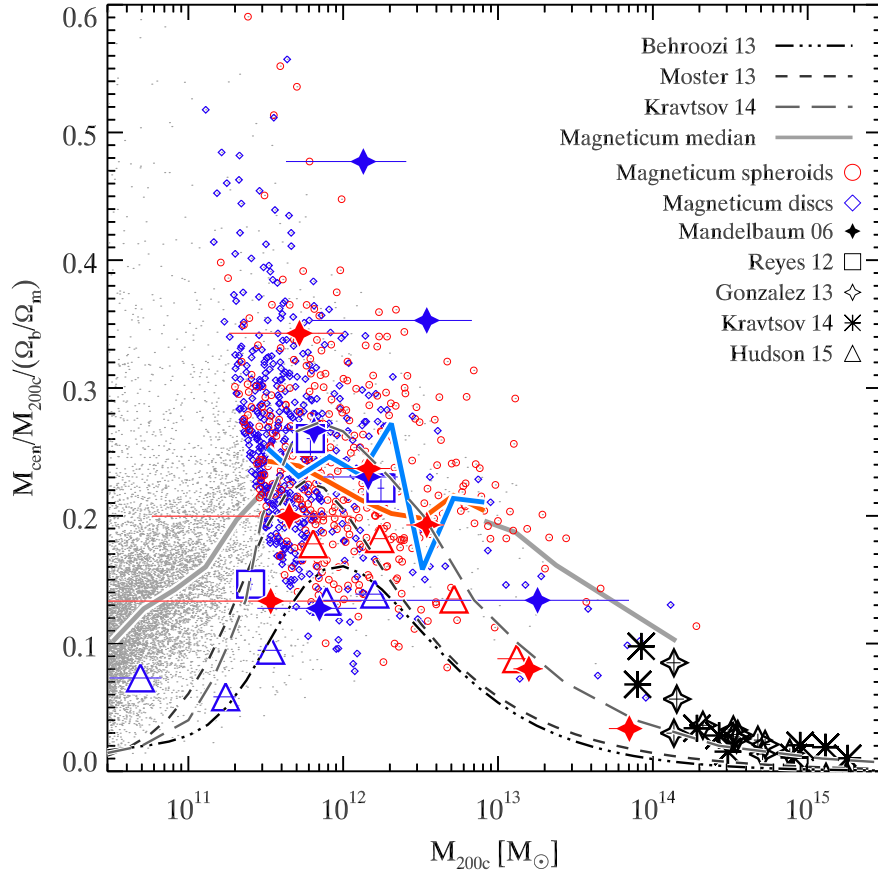


Figure 4.2.1: The stellar mass fraction of central galaxies with respect to critical halo mass M_{200c} normalized by the global, cosmological baryon fraction Ω_b/Ω_m , as a function of the halo mass M_{200c} . There is no difference between spheroids (red circles) and disks (blue diamonds).

As observations often utilize the specific star formation rate (sSFR) as an indicator for the morphology of galaxies, we also split our sample into quiescent and star forming galaxies. Following the classification by [Franx et al. \(2008\)](#), we define quiescent galaxies to have a sSFR smaller than $0.3/t_{\text{Hubble}}$, where $t_{\text{Hubble}} = 1/H(z)$ is the Hubble time, while the rest is classified as star-forming. The resulting number of quiescent and star-forming galaxies for different redshifts is listed in [Table 4.1](#).

4.2 The Relation between the Stellar and Halo Mass of Central Galaxies

Over the past years several studies investigated the stellar-to-halo-mass relation (e.g. [Behroozi et al., 2010](#); [Brook et al., 2014](#); [Dutton et al., 2010](#); [Kravtsov et al., 2018](#); [Mandelbaum et al., 2006](#); [Moster et al., 2010](#); [Munshi et al., 2013](#); [Rodríguez-Puebla et al., 2015](#);

Shankar et al., 2014; Tinker et al., 2017; van Uitert et al., 2016; Wake et al., 2011). This relation, applicable only for galaxies at the center of the underlying dark matter halo, can give important insights into the galaxy formation process. One interesting question is, for example, if galaxies of identical stellar mass but different morphological type are hosted by dark matter halos of different masses. Another interesting aspect is, that the efficiency with which galaxies are converting their cosmological baryon reservoir into stars, turned out to depend on halo mass, where galaxies residing in dark matter halos of approximately $10^{12}M_{\odot}$ appear to be most efficient.

To investigate this aspect, we show the baryon conversion efficiency as function of halo mass for our central galaxies in Fig. 4.2.1, where we show the elliptical galaxies as red circles and the disk galaxies as blue diamonds. Intermediate galaxies and galaxies below our mass cut are shown as gray dots. The gray solid lines mark the median of all galaxies, while the red and blue solid lines show the median of the ellipticals and disks, respectively. For comparison, we overplot data points from observations by Mandelbaum et al. (2006) (filled stars), Reyes et al. (2012) (squares), Gonzalez et al. (2013) (open stars), Kravtsov et al. (2018) (asterisks) and Hudson et al. (2015) (triangles), where the colors red and blue represent samples of elliptical/ETGs and disk/LTGs, respectively. Our simulated galaxies agree qualitatively with the different observations, which show a wide spread. In both simulations and observations the differences for different galaxy types are only marginal. The differences between our simulations and the observations are most prominent at the low and very high-mass end. They are driven by too inefficient stellar feedback for the low-mass halos and too inefficient black hole feedback at the high-mass end.

Only at the very high-mass end, X-ray observations allow to infer unambiguously the underlying dark matter potential of individual galaxies (Gonzalez et al., 2013; Kravtsov et al., 2018). In addition, the outer stellar components of these massive galaxies can be measured and their total stellar mass can be inferred, pushing the observations closer to our simulation result. We also plot the curves obtained with abundance matching by Moster et al. (2013) (dashed line), Behroozi et al. (2013) (dash-dotted line), and Kravtsov et al. (2018) (solid line). Especially, the results obtained by Kravtsov et al. (2018) resemble very closely the simulation result.

A direct comparison between the total mass of the halo and the stellar mass of the central galaxy and its evolution with time is shown in Fig. 4.2.2. Red, blue and green lines represent the relation for the ellipticals, disks, and intermediates in the simulation, respectively. At redshift $z = 0$ (upper left panel) we add data points from Mandelbaum et al. (2006), Conroy et al. (2007), More et al. (2011), Gonzalez et al. (2013), Kravtsov et al. (2018), Velander et al. (2014), Mandelbaum et al. (2016) and Wang et al. (2016). Black symbols represent those studies that do not distinguish between galaxy types, while red symbols represent elliptical/red/ETG samples and blue symbols represent spiral/blue/LTG samples.

At masses below $2 \times 10^{11}M_{\odot}$ the simulations overall lie within the large spread covered by the observations. Although the simulations best resemble the results by Mandelbaum

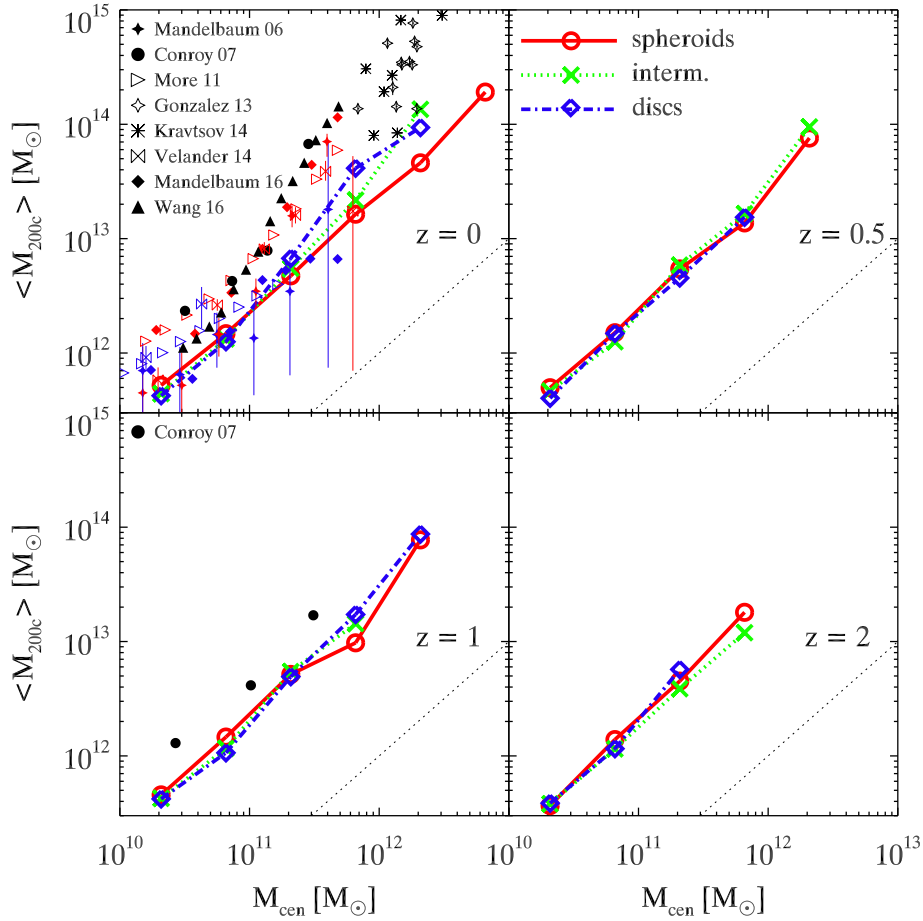


Figure 4.2.2: The average critical halo mass M_{200c} of a halo as a function of the stellar mass of the central galaxy for different redshifts.

et al. (2006, 2016), they generally predict slightly higher stellar mass at given halo masses than most observations. This difference increases with stellar mass. However, at the very high-mass end, where observations can properly include the outermost parts of the galaxies in form of the intracluster light (ICL) component (Gonzalez et al., 2013; Kravtsov et al., 2018), the observations lie again closer to our results. Therefore, this systematic upturn seen in the observations could be related to the effect of the contribution of the outer halo to the total stellar mass.

Using observational data from the SDSS Mandelbaum et al. (2006) and More et al. (2011) concluded that the halo mass is independent of the morphology at a fixed stellar mass below 10^{11} and $2 \cdot 10^{10.5} M_{\odot}$, respectively, while both found that red/elliptical galaxies reside in more massive halos at higher stellar masses. They argue that this halo mass is likely to reflect the mass of the cluster/group in which more massive ETGs live in. Mandelbaum et al. (2016) find that passive galaxies with stellar masses between $10^{10.3}$ and $10^{11.6} M_{\odot}$ reside in more massive halos than their star-forming counterparts. While our simulations

also do not show any differences for the host halo masses at low stellar masses for ellipticals and disks, we cannot support this conclusion that dark matter halos of spheroids are more massive than those of disk galaxies with comparable stellar masses. In contrast, we even find that disk galaxies with stellar masses above $2 \times 10^{11} M_{\odot}$ live in more massive halos than spheroids of the same stellar mass, however, this could be due to low number statistics, since at high stellar masses there are only few disks in our simulation.

This discrepancy vanishes at higher redshift, where we do not find any differences between the ellipticals and disks, even at large stellar masses. Furthermore, we do not find any evolution of the stellar-to-halo-mass relation with redshift at all, in agreement with observations using satellite kinematics by [Conroy et al. \(2007\)](#), who find that the stellar to halo mass ratio does not evolve between $z \sim 0$ and $z \sim 1$ for their sample of observed host galaxies below $M_{\text{star}} \approx 1.5 \times 10^{11} M_{\odot}$. This is partly in agreement with [Hudson et al. \(2015\)](#) who find no significant redshift evolution for their sample of blue galaxies. However, they observe a time evolution of the relation for their red galaxies.

In [Fig. 4.2.3](#) we take a closer look at the stellar-to-halo-mass relation at a fixed stellar and virial mass regarding the different classifications, i.e. the classification according to the kinematical b -value and that according to the sSFR, of the central galaxies at $z = 0$. The upper left panel shows the relation for individual central galaxies color-coded by the dynamical classification parameter b -value. There is no observable trend with the b -value. The upper right panel shows the distribution of the virial masses of the centrals with stellar masses in the small range between $2.7 \cdot 10^{10} M_{\odot}$ and $3.3 \cdot 10^{10} M_{\odot}$. In agreement with [Fig. 4.2.2](#), we find that the spheroidal galaxies peak at higher virial masses than the disks. When looking at the distributions of centrals of virial masses in the range between $7.8 \cdot 10^{11} M_{\odot}$ and $9.5 \cdot 10^{11} M_{\odot}$ (middle left panel) we do not find a difference in the distribution.

The right bottom panel shows the relation for the galaxies color-coded by the SFR, where centrals with SFRs $< 1 M_{\odot}/\text{yr}$ are red. As on the upper left panel there is no visible trend between the two quantities and the SFR. In contrast to the result where we have taken the b -value (upper right), the same galaxy population in the same small stellar mass bin shows no difference in the distribution in the virial masses of quiescent and star-forming centrals (bottom left). There is also no difference in the distribution of the stellar masses at fixed virial mass (middle right panel), which is in agreement with the results from the b -value classification.

This result demonstrates that different classifications can lead to different conclusions regarding the relation between the virial mass and the stellar mass and the morphology. Furthermore, we find a dependence on the mass range: as shown in [Fig. 4.2.2](#), at higher mass this trend even reverses. Additionally, we clearly see that a different behavior occurs if the distribution at fixed stellar mass (where in this case we see a different behavior) is considered, or the distribution at fixed virial mass (where in this case we do not see a different behavior) is taken.

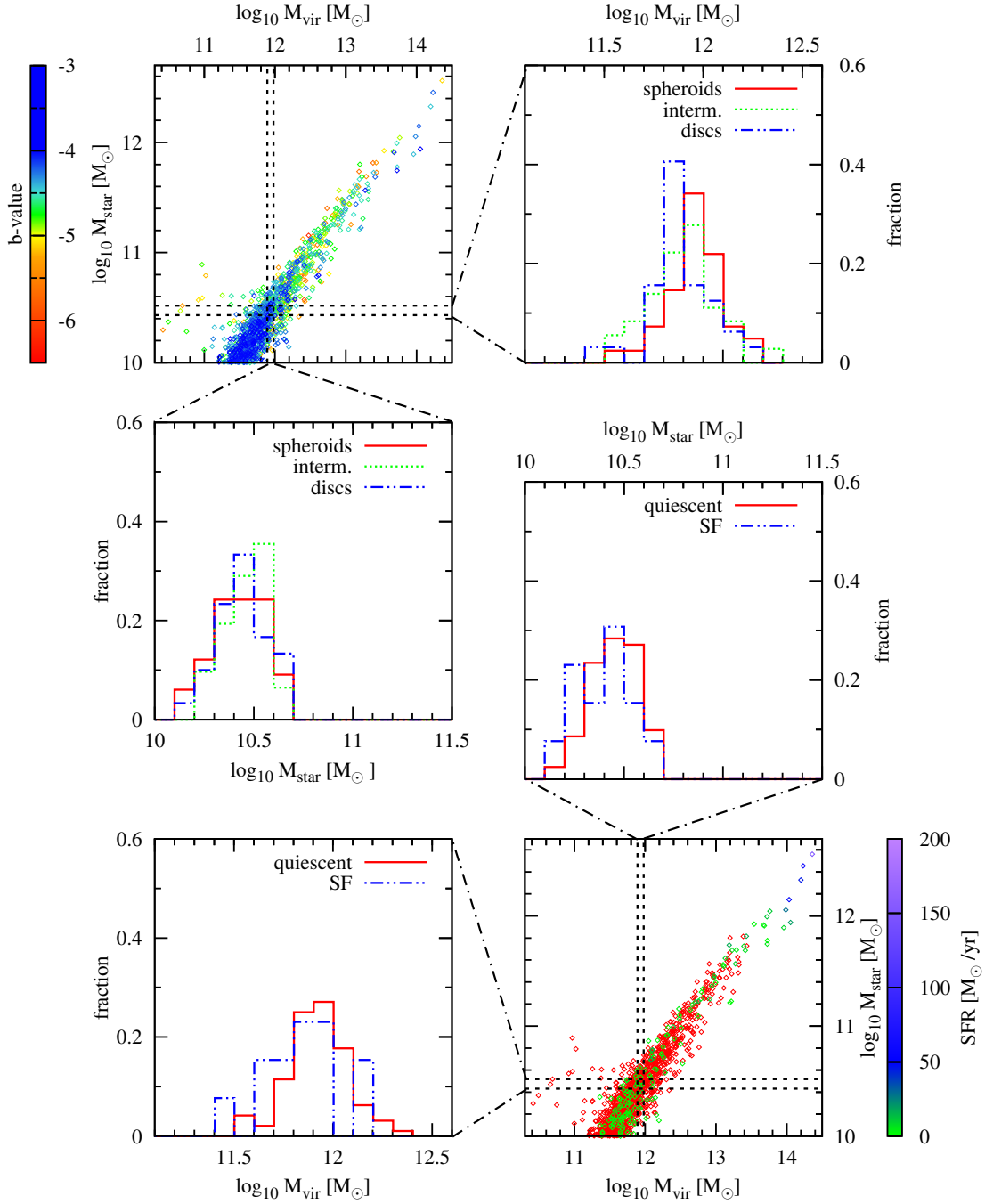


Figure 4.2.3: The stellar to halo mass relation for the centrals in *Box4* at redshift $z = 0$. *Top left:* the virial mass against the stellar mass of individual centrals, color-coded by the b -value; *top right:* the fraction of centrals with $M_{\text{star}} \in [2.7 \cdot 10^{10}, 3.3 \cdot 10^{10}]$ in bins of M_{vir} , divided into spheroids, intermediates and disks; *middle left:* the fraction of centrals with $M_{\text{vir}} \in [7.8 \cdot 10^{11}, 9.5 \cdot 10^{11}]$ in bins of M_{star} . *Bottom right:* the virial mass against the stellar mass of individual centrals, color-coded by the SFR; *bottom right:* the fraction of centrals with $M_{\text{star}} \in [2.7 \cdot 10^{10}, 3.3 \cdot 10^{10}]$ in bins of M_{vir} divided into quiescent and star-forming; *middle right:* the fraction of centrals with $M_{\text{vir}} \in [7.8 \cdot 10^{11}, 9.5 \cdot 10^{11}]$ in bins of M_{star} .

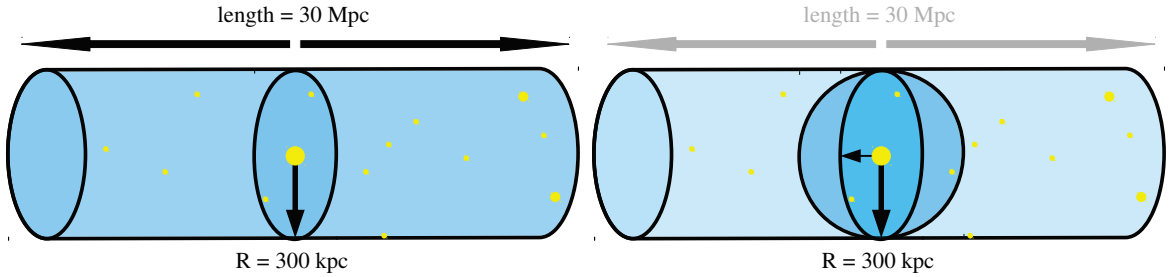


Figure 4.2.4: Selecting galaxies in different ways: the upper figure illustrates Method 1, where we select satellites within a cylinder of radius $r = 300\text{kpc}$ and a length of 30 Mpc. The lower figure illustrates the second method, where we select all satellites within a sphere of 300kpc.

4.3 The Abundance of Satellites

In a recent observational study, [Ruiz et al. \(2015\)](#) tried to infer the dark matter halo masses of galaxies based on the abundance of their satellites. They found a systematically decreasing number of satellites around galaxies along the Hubble sequence. As in the observations, we target all galaxies above a given mass threshold in our simulations, regardless of them being centrals or not, and assign all surrounding galaxies within a mass ratio of $M_{\text{sat}}/M_{\text{host}} \in [0.01, 1]$ to be their apparent satellite galaxies. Generally, we do not apply any additional isolation criterion for choosing host galaxies, which – depending on the different selection criteria – can lead to double counting of satellite galaxies. However, galaxies that clearly interact are not counted as host and satellite but are treated as one single central galaxy and are never classified as disk or spheroidal but always as intermediates.

By different ways of counting, as shown in Fig. 4.2.4, we can estimate the contribution of projection effects by performing our selection in two different ways: first, we select apparent satellite galaxies within a cylinder of radius r and with a length l , as usually done in observations; Second, we select apparent satellite galaxies within a sphere of radius r around a target galaxy. With these different search criteria we aim to show the difference between the intrinsic signal and effects induced by the projections and the background. We have additionally checked that a direct correction for the background galaxies as done in the observations does not change the results qualitatively.

To obtain a meaningfully statistical number of galaxies we had to choose a mass threshold of $M_{\text{star}} \geq 10^{10} M_{\odot}$, which is lower than the one used by [Ruiz et al. \(2015\)](#). However, in respect to r and l we follow the observations by [Wang and White \(2012\)](#) and [Ruiz et al. \(2015\)](#), namely by choosing a radius $r = 300\text{kpc}$ and a length $l = +/ - 15\text{Mpc}$ along the line of sight, which correspond to the redshift interval of $|\Delta z| < 1000\text{kms}^{-1}$.

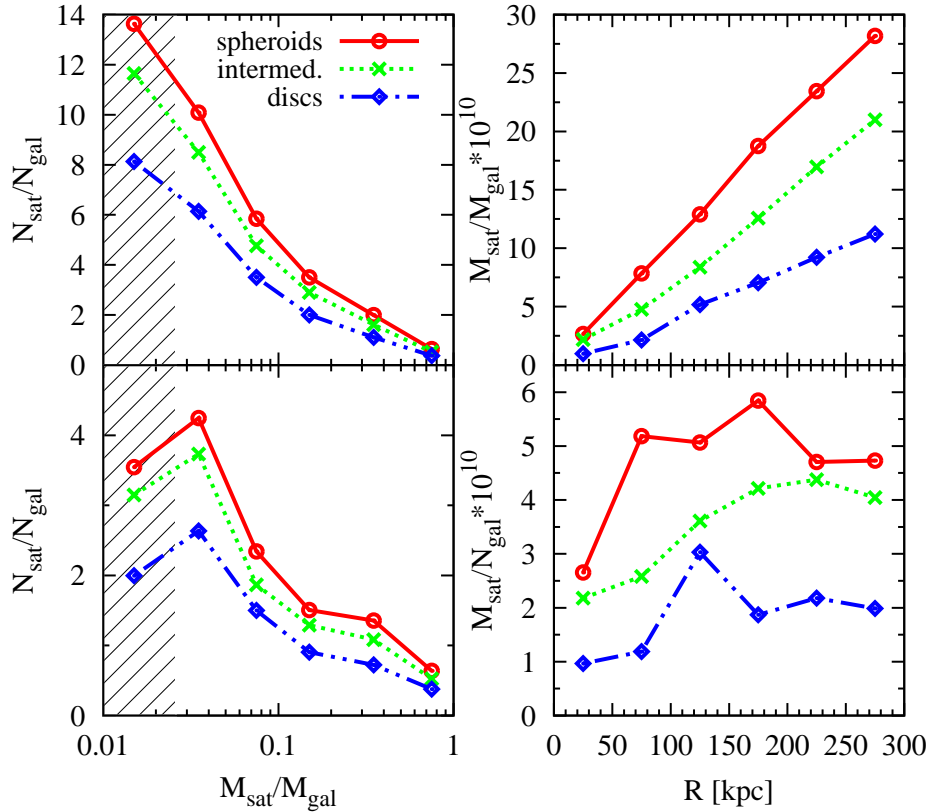


Figure 4.3.1: *Upper Left:* the mass fraction of satellites with respect to the stellar mass of the host galaxies against the cumulative number of satellites per host galaxy in a cylinder of radius $r = 300\text{kpc}$ and a length of 30Mpc . *Lower left:* the differential number of satellites per host galaxy. *Upper right:* the cumulative radial distribution of the satellite mass around host galaxies. *Lower right:* the differential distribution of the satellite mass along the radius.

4.3.1 Comparison of the Satellite Number with Recent Observations

In the following section we compare the abundance of inferred satellites around the selected sample of galaxies in our simulation with the results from [Ruiz et al. \(2015\)](#). Therefore, we use the first selection method, where the apparent satellites are counted within a cylinder to calculate the number of inferred satellites around massive galaxies.

In the left panels of Fig. 4.3.1 we show the mean number of inferred satellites as function of their stellar mass ratio to the host galaxy at $z = 0$. The upper panel shows the (anti)cumulative fraction, while on the lower panel the differential fraction is shown. The shaded area indicates the completeness of our sample, assuming that galaxies with more than 100 star particles are always numerically resolved. The number of satellites for spheroidal host galaxies is shown in red, while the according numbers for disk host galaxies are shown in blue. In agreement with observations by [Ruiz et al. \(2015\)](#) (see also

e.g., Wang et al. (2014)), we find that spheroidal host galaxies have more inferred satellites than disk galaxies.¹

The radial distribution of the apparent satellite mass around the host at redshift $z = 0$ is shown in the right panels of Fig. 4.3.1, where the upper one shows the cumulative number, while the lower one shows the differential mass distribution. For all galaxy types the mass in inferred satellites rises towards the outer regions. We find that spheroids are surrounded by $\propto 3$ times the mass in inferred satellites compared to disks and $\propto 1.5$ times compared to intermediates. This tendency agrees qualitatively well with the observations by Ruiz et al. (2015).

4.3.2 Abundance of Satellites for $z > 0$

A more reasonable selection (which obviously is not possible in observations) is the second selection method, where the apparent satellites are counted within a sphere around the host galaxy, which is more closely related to the physical satellite population and in principal better allows to study the evolution of the satellite population. As shown in Fig. 4.3.2, the different number of inferred satellite galaxies around spheroidal galaxies compared to disk galaxies is already present at higher redshift, independent of the counting method. Interestingly, the relative strength of the signal is even larger when counting apparent satellite galaxies within spheres compared to cylinders, indicating that the immediate environment contributes the most.

The difference of the number of inferred satellites between the spheroids and disks becomes smaller with increasing redshift, due to the decreasing number of inferred satellites around spheroids, while the number of inferred satellites stays constant for disk galaxies. Our results are in agreement with studies by Mármol-Queraltó et al. (2012), Nierenberg et al. (2012) and Nierenberg et al. (2016), who find no significant redshift evolution of the number of apparent satellites for the redshift range between $0.2 < z < 2$, $0.1 < z < 0.8$ and $0.1 < z < 1.5$, respectively. They also mention that the difference in the abundance of inferred satellites between spheroids and disk-like galaxies is more prominent at lower redshift; This likely is an effect of clustering of spheroidal galaxies, which is more important at lower redshifts (see Mármol-Queraltó et al., 2012).

In this context, we want to mention that it is important to keep in mind, in which units the distances are measured, i.e. in physical or comoving, which becomes more and more important with increasing redshift.

Since it is common to use physical units in observations, we show the result for redshift $z = 2$ with physical units in Fig. 4.5.1 in Section 4.5. However, throughout this study we

¹The differences in the absolute number of apparent satellites between the simulations and the observations is driven by the different masses in the two samples.

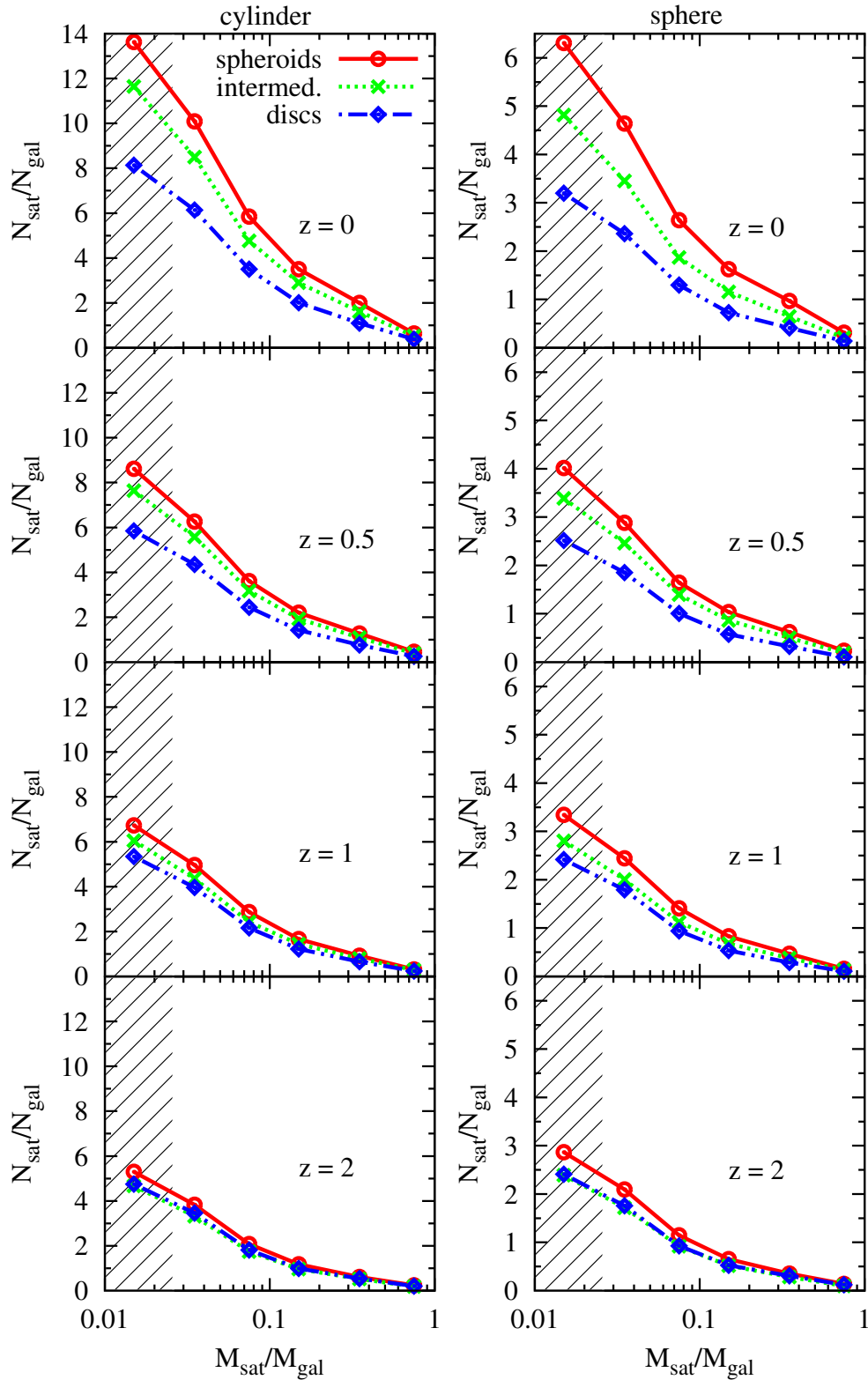


Figure 4.3.2: The cumulative number of satellites per host galaxy at different redshifts for all host galaxies. The *left* column shows the results for a cylinder, while for the *right* column we collect satellites within a sphere of $r = 300\text{kpc}$ (comoving). The split-up of the distribution is visible for all redshifts, but it becomes smaller with increasing redshift. Be aware: y -axes have different scales!

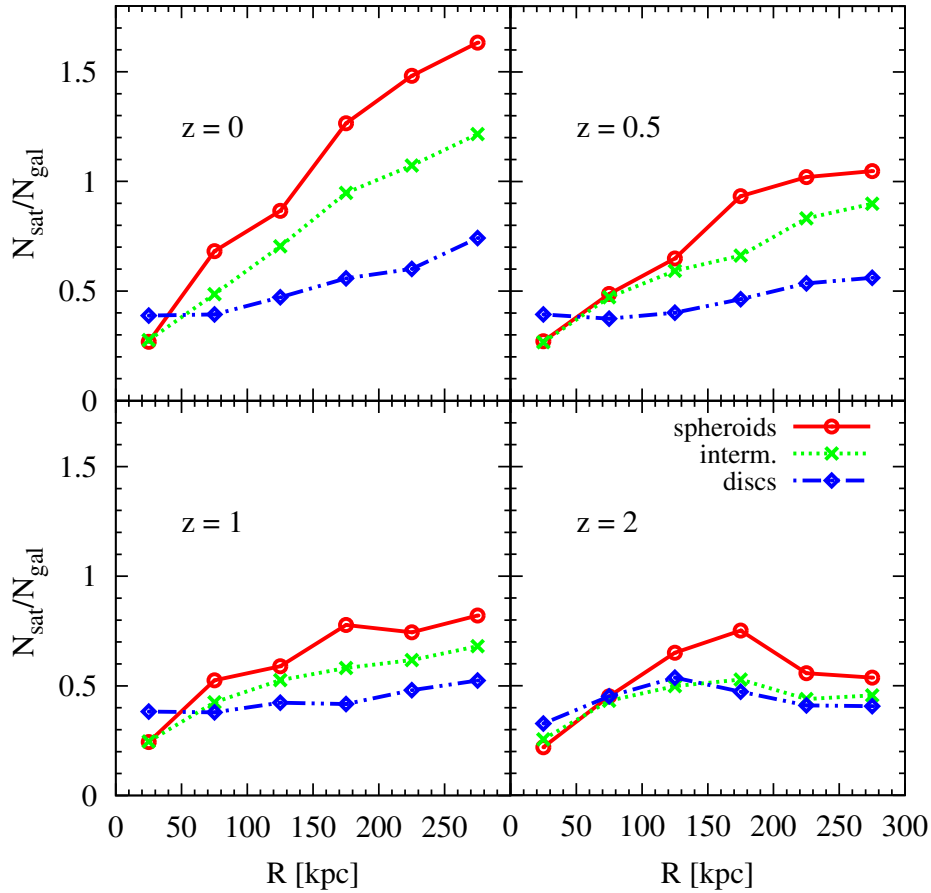


Figure 4.3.3: The differential number of satellites per host galaxy depending on the radius of the host galaxies for different redshifts in comoving units. With increasing redshift the number of satellites decreases, especially for the spheroids.

use comoving units to separate between the expansion of the universe and the real growth of structures.

4.3.3 Radial Distribution of Satellites

In Fig. 4.3.3 we study how many inferred satellites within a sphere are located in different bins of the radius for four different redshifts. We clearly see that spheroidal galaxies (red circles) have more apparent satellites at all radii than disk galaxies (blue diamonds), except for the inner most region. This is in agreement with studies by Wang et al. (2014) who find similar results for different mass ranges of isolated galaxies from the SDSS. At low redshift (upper left) there is an almost linear distribution of inferred satellites surrounding spheroids, increasing from inside out. While in the inner parts the number of inferred satellites is relatively constant towards higher redshifts, in the outer region the number of inferred satellites decreases with increasing redshift. For intermediates a similar but

Table 4.2: The number of central and companion galaxies with stellar masses higher than $10^{10} M_{\odot}$ at four different redshifts

centrals			
redshift	N_{spheroid}	$N_{\text{interm.}}$	N_{disk}
0	396	442	481
0.5	344	539	561
1	285	630	629
2	179	663	463
companions			
redshift	N_{spheroid}	$N_{\text{interm.}}$	N_{disk}
0	260	318	215
0.5	205	322	254
1	134	304	228
2	67	206	142

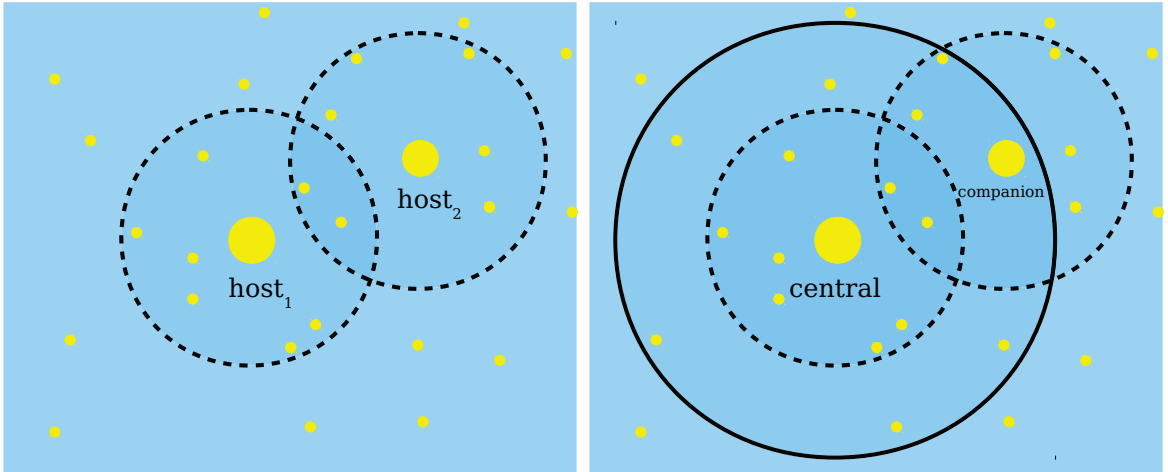


Figure 4.3.4: Selecting host galaxies in different ways. The upper figure illustrates the selection of satellites for “all galaxies”: every galaxy more massive than $10^{10} M_{\text{star}}/M_{\odot}$ is counted as host galaxy. The lower scheme shows the split-up into central and companion galaxies. While host_1 in the upper figure is a central, i.e. the galaxy in the potential minimum of the dark matter halo (black solid circle), host_2 from the upper figure is a companion, i.e. a large satellites within the same dark matter halo.

weaker trend can be seen. In contrast to the spheroids and intermediates, disk galaxies have a shallower slope; the apparent satellites are evenly distributed along the radius and there is no evolution with redshift.

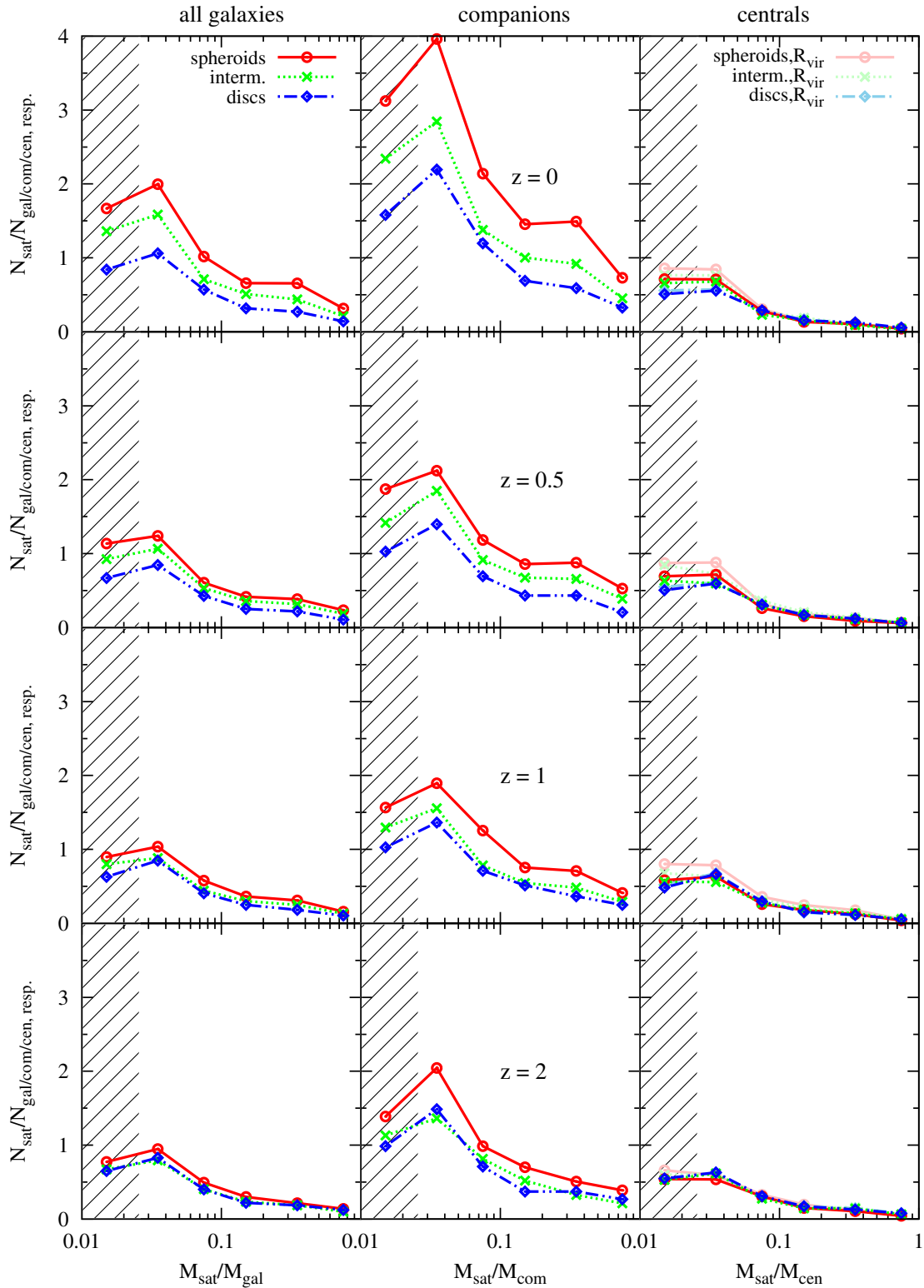


Figure 4.3.5: The differential number of satellites per host galaxy at different redshifts (rows) for all host galaxies (left panels), companions (middle panels) and central galaxies (right panels) in comoving units. The normal colors show satellites within $r = 300\text{kpc}$, and the pale colors show satellites within R_{vir} . The split-up of the distribution is mainly caused by the companions, since the centrals do not exhibit such a split-up. The split-up in the distribution for the companions is present at all redshifts.

4.3.4 Comparison of Companions and Centrals

To better understand the origin of the observed signal, we can now split our sample of target galaxies in *centrals* (which are, as discussed before, at the center of a dark matter halo) and *companions*, which are by themselves already parts of a larger dark matter halo. Therefore, we count every galaxy from the host galaxy sample as a central galaxy if it resides in the potential minimum of a dark matter halo. All remaining galaxies, which sit within the virial radius of a central galaxy, are considered as companions. This different way of counting compared to what was done before is illustrated in Fig. 4.3.4. The resulting number of companion and central galaxies classified into spheroids, intermediates and disks at four different redshifts are listed in Table 4.2.

Fig. 4.3.5 shows the number of satellite galaxies inferred for all host galaxies (left column) compared to the number of satellite galaxies for the sample split into *centrals* (right panel) and *companions* (middle panel). We see a clear difference in the number of apparent satellites: while there is a clear split-up between spheroidal and disk galaxies for the host and companion samples, there is no such difference visible for the centrals. We carefully checked that the signal is not caused by the most massive galaxies within our sample.

Thus, we clearly see that the companions within the sample are responsible for the split-up seen for the sample of all host galaxies. This can be explained by the fact that *companions* are by definition in dense regions and due to the morphology-density relation preferentially are spheroidal galaxies. Therefore, we conclude that the observed difference in the apparent number of inferred satellite galaxies around spheroidal and disk galaxies is entirely driven by the morphology-density relation and not by different underlying halo masses.

This also explains the weakening of the signal with increasing redshift, as shown in the lower panels of Fig. 4.3.5 and in Fig. 4.3.2. This is caused by the lack of massive companion galaxies at higher redshifts as can clearly be seen from Table 4.2 and the middle and right panels of Fig. 4.3.5. Thus, the split-up of the distributions of companions is visible at all redshifts but less pronounced at higher redshift.

This is also supported by the radial distribution of satellites as previously shown in Fig. 4.3.3. Fig. 4.3.6 confirms that this difference in the radial distribution also originates purely from the companions (right panel), while the signal completely disappears for the central galaxies (left panel), as expected. This clearly shows that the spheroidal host galaxies have more satellites than the disks and the number of these satellites increases towards larger radii, again pointing towards the morphology-density relation as origin of the split-up.

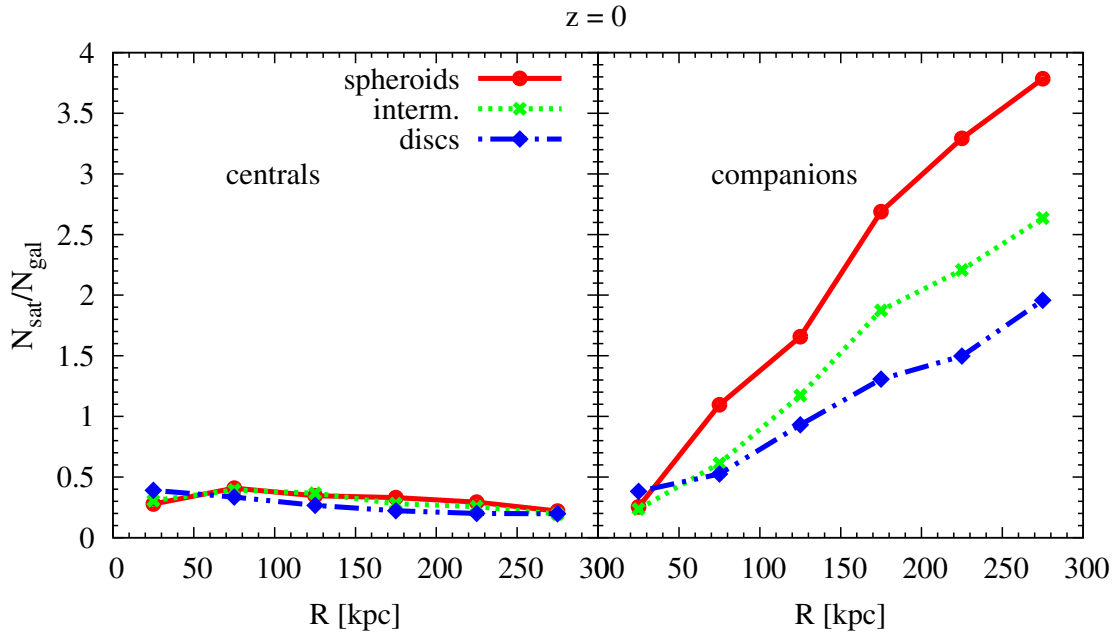


Figure 4.3.6: The differential radial distribution of satellites per host galaxy at redshift $z = 0$ for centrals (left) and companions (right).

4.3.5 Average Number of Satellites in Dependence of the Virial Mass

In order to see if one can directly infer the halo mass of a central galaxy from the number of the satellites, we show in Fig. 4.3.7 the number of satellites averaged for the central galaxies according to their virial mass. Here, we include all satellites with stellar masses higher than $10^8 M_\odot$ that reside within the virial radius of their central galaxy. We find that the number of satellites is directly proportional to the virial mass of the central galaxy, where the central galaxies which reside in halos with higher masses have more satellites than those residing in low-mass halos. There is no difference for galaxies with different morphological types. In addition, we do not find an evolution with redshift.

The independence of the number of satellites of the central’s morphology and the redshift is also shown in Fig. 4.3.5, where we included the satellite counts within R_{vir} in pale colors in the right panels. The change compared to the number of satellites within $r = 300\text{kpc}$ is only marginal, since the average virial radius of the central galaxies has about the same size as the considered sphere.

We conclude that counting the satellites of galaxies without distinguishing between central galaxies and companions, i.e. large satellites, just reflects the environment they live in. The number of satellites within the virial radius of *centrals*, however, remains almost constant with increasing redshift and therefore traces the underlying dark matter halo.

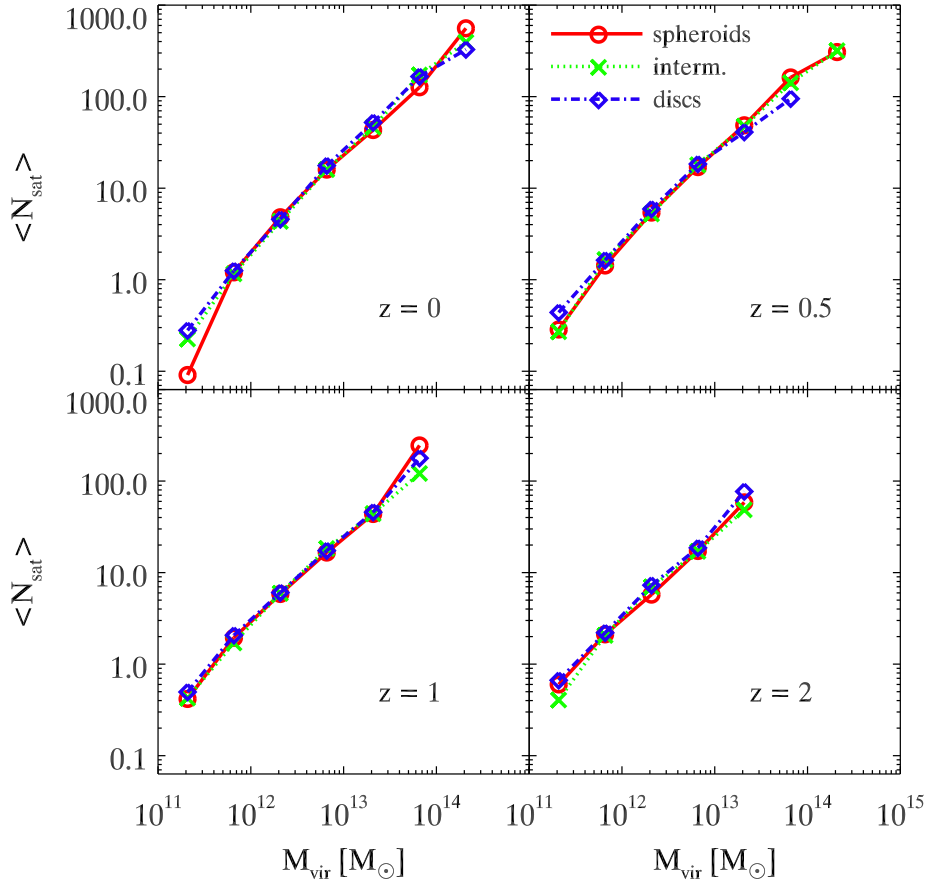


Figure 4.3.7: The average number of satellites with stellar masses larger than $10^8 M_{\odot}$ around centrals, within the virial radius in bins of the virial mass for different redshifts.

4.3.6 Massive Galaxies at High Redshift

In order to test the signal for massive galaxies in more detail by choosing a very narrow mass range of $10^{11} M_{\odot}$ and $2 \cdot 10^{11} M_{\odot}$, as done in the observations by Ruiz et al. (2015), we now select galaxies from the larger volume simulation *Box3*. This large volume simulation was so far only evolved down to a redshift of $z = 2$. This simulation has the same resolution as the simulation used before, and we find the same results for the satellite fractions using the full mass range. This volume is actually large enough to obtain several hundreds of galaxies, even within such a narrow mass range, which we can split into companion and central galaxies and classify them as spheroids, intermediates, and disks, as reported in Table 4.3. Note that the underlying AGN feedback in this new, larger volume simulation has slightly different parameters, which generally leads to a fraction of passive galaxies even closer to the observed one, as shown in Steinborn et al. (2015).

In Fig. 4.3.8 we plot the mass fraction of the satellites against the number per host galaxy as in Fig. 4.3.5 but for the narrow mass range of $10^{11} M_{\odot}$ and $2 \cdot 10^{11} M_{\odot}$, where

Table 4.3: The number of all host galaxies with stellar masses higher between $10^{11} M_{\odot}$ and $2 \cdot 10^{11} M_{\odot}$ at $z = 2$ in *Box3/ubr*

galaxy type	N_{spheroid}	$N_{\text{interm.}}$	N_{disk}
all galaxies	156	209	180
companion	10	23	15
central	146	186	165

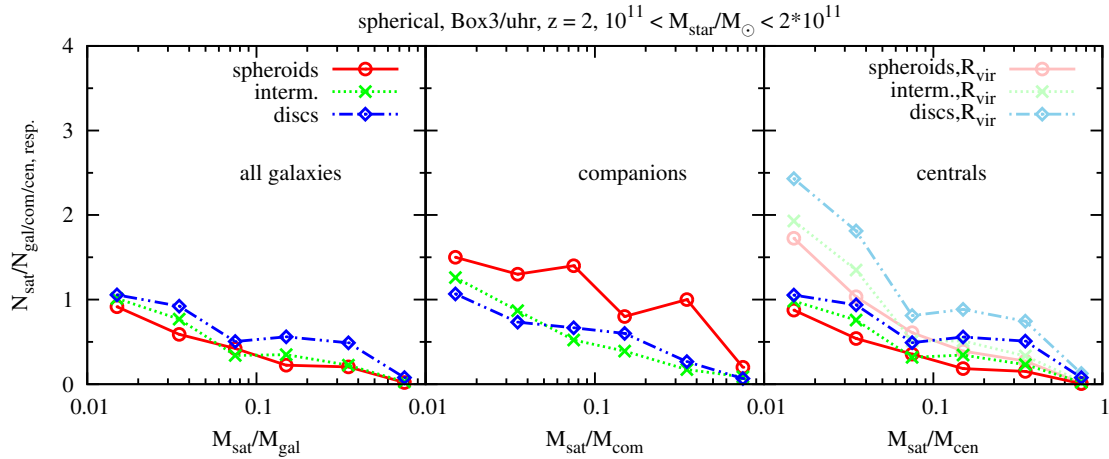


Figure 4.3.8: *From left to right:* same as Fig. 4.3.5 but in the larger *Box3* with the same resolution at $z = 2$. There is no split-up of the distribution for all host galaxies (left panel), since the number of companions is very small in this mass range at $z = 2$ and thus the distribution for all galaxies is reflecting that of the centrals (right panel). The distribution of the companions exhibits again the split-up (middle panel).

our simulation resolves the complete mass range of the satellite galaxies. We still see the increased number of satellites for elliptical companions, and no increased number for centrals. As shown before, at this high mass range, the signal for the centrals even slightly reverses. The pale curves again show the satellite number per central within the virial radius. From this we conclude that our key result, namely that the split-up is caused by the companion galaxies, is not biased by a mass selection effect, since we find this split-up in both galaxy samples despite the different mass ranges.

4.4 Relation between Host and Satellite Properties

Until now we have only considered the number of satellites for centrals of different morphology. However, at high redshift morphology (traced via kinematic properties like the b -value) and starforming activity can mean different things, as shown before (see also Teklu et al., 2015). Additionally, the relation between satellites and their centrals seems to be more complex. Therefore, it is important to understand the connection between properties

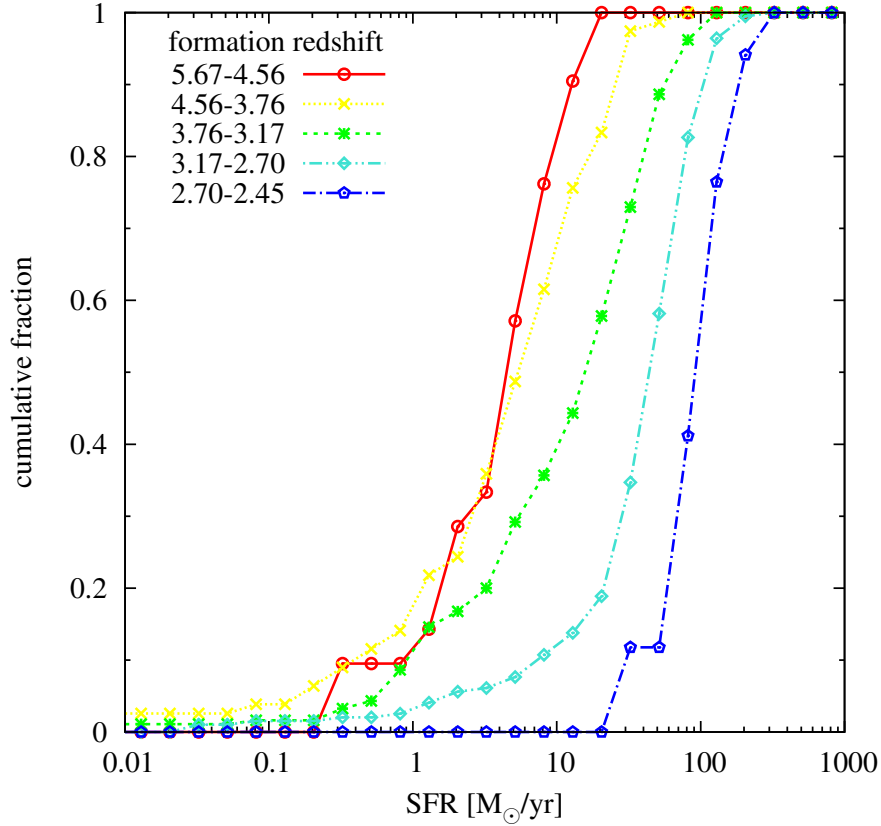


Figure 4.4.1: The cumulative fraction of centrals binned according to their SFR in *Box3* at $z = 2$. The formation redshift of the centrals is color-coded, where younger centrals are blue and older ones are red. There is a trend that young centrals have a higher SFR than older ones.

of host and satellite galaxies in more detail. In the following section we will take a closer look at the relations between host and satellite galaxies with respect to their star formation rates (SFRs), formation redshifts, and dynamical properties.

4.4.1 SFR and Formation Redshift of Satellites and Central Galaxies

In Fig. 4.4.1 we show, how the current star formation rate is reflected in the formation redshift (z_{form}). To avoid bias from possible mass-dependence effects, we therefore again analyze the centrals from the narrow mass range $[10^{11}, 2 \cdot 10^{11}]M_{\odot}$. Here we show the cumulative fraction of centrals according to their SFR at $z = 2$, where the colors represent the average redshift, where the stars of a given galaxy were formed. As expected, we clearly find a smooth, continuous tendency for older (red) centrals to have lower SFRs at current time (e.g. $z = 2$), and therefore older centrals are more quenched than younger (blue) centrals.

In the following we want to verify if and how the b -value (i.e., the morphology), the SFR, and the formation redshift of the central galaxies correlate with the formation redshift and the star formation of their satellite galaxies (within the virial radius).

The left column of Fig. 4.4.2 always shows the cumulative fraction of the star formation of the satellite galaxies, while the right column always shows the cumulative fraction of the formation redshift of the satellite galaxies. The different colors in the rows reflect different selection criteria of the underlying central galaxies as follows:

The upper row shows the sample of host galaxies split into the different morphological types (e.g. spheroids, intermediates and disks classified via low, medium and high b -values, respectively). For all host morphologies, the majority of satellite galaxies are already quenched and do not show any differences in their formation time. The curves for the SFRs for satellites of the disk-like and spheroidal centrals are indistinguishable above $0.1M_{\odot}/yr$, and a K-S test gives a probability of $5.36 \cdot 10^{-1}$ that the overall distributions (red and blue curve) are the same.

In the middle panels we check how the star formation of the centrals is related to the star formation and the formation redshift of their satellites. The left panel shows that centrals with almost no star formation (red curve) are mainly surrounded by satellites which themselves have no star formation, while star-forming centrals have a larger fraction of satellites with significant star formation. This suggests that the environment provides the star-forming centrals as well as their satellites continuously with gas. Additionally, we see an indication for a weak correlation between the star formation of the centrals and the formation redshift of their satellites (right panel). Here, the K-S test gives a probability of $2.14 \cdot 10^{-2}$ that the two distributions of non-star-forming (red curve) and highly star-forming (purple curve) centrals have the same underlying distribution.

In the lower row we color-code the distributions according to the formation redshift of the centrals. On the left panel we note a slight correlation between the star formation of the satellites and the formation redshift of the centrals: Older central galaxies have a larger fraction of quiescent satellites, younger centrals have a larger fraction of star-forming satellites, except for the bin with the youngest centrals (blue curve) which, however, is based on low number statistics. On the right panel we find a correlation between the formation redshift of the satellites and the formation redshift of their centrals. The older centrals (red curve) have older satellites, while the younger centrals (blue curve) tend to have younger satellites, which is confirmed by the K-S test with a probability of $1.85 \cdot 10^{-6}$.

We conclude that the morphology of the central galaxy does not relate to the star formation and the formation redshift of its satellites at $z = 2$. Nevertheless, we find a significant correlation between the star formation and the formation redshift of the centrals themselves with the star formation and the formation redshift of their satellites, reflecting the so-called conformity (see e.g. Tinker et al., 2018). The fact that there is neither a correlation between the b -value of the central and the star formation and formation redshift of the satellites nor a correlation between the b -value and the number of satellites suggests that the environment

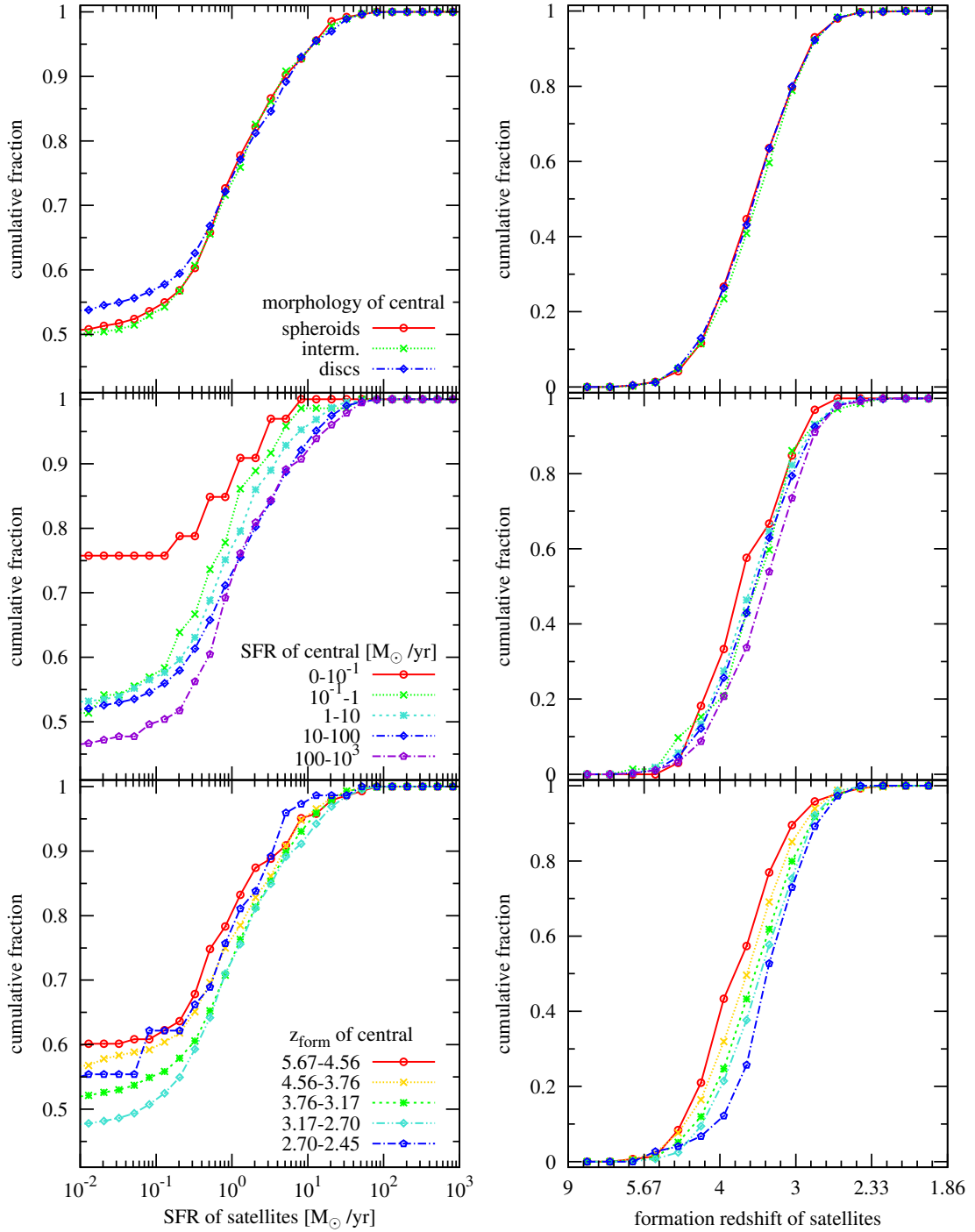


Figure 4.4.2: *Left:* the cumulative fraction of satellites within the virial radii of centrals binned according to their SFR. *Right:* the cumulative fraction of satellites according to their formation redshift. In the upper row the color encodes the b -value of the centrals of the satellites, the middle row divides the centrals according to the SFR and the lower panels show the satellite population split according to the formation redshift of their central, for galaxies in *Box3* at $z = 2$.

is the main mechanism that controls the global star formation properties and thus links the formation redshift of both centrals and satellites.

4.4.2 Evolution of the SFR- z_{form} relation

The evolution of the relation between the SFR and the formation redshift of the central galaxies is shown in Fig 4.4.3. Here all panels show a scatter plot of the SFR as function of formation redshift, colored by the stellar mass of the central. The left and middle panels present the $z = 2$ results for the narrow mass range sample from *Box3* (left) and the full sample from the smaller *Box4* simulation (middle). The right panel shows the according result from *Box4* at $z = 0$. The green diamonds are the averaged SFR, binned for different formation redshifts. Centrals with SFRs lower than $0.01 M_{\odot}/\text{yr}$ are plotted on the lowest displayed value of the y -axis.

We find a clear trend of the median SFR with the formation redshift at $z = 2$, in agreement with our previous finding that old centrals tend to have a lower SFR, while young centrals on average have a higher SFR. A part of this relation is expected, as more massive galaxies are expected to have higher SFRs and also form earlier. However, this relation holds even at fixed stellar mass, as shown by the narrow mass range sample (left panel in Fig. 4.4.3). This means that galaxies with already quenched star formation usually have formed earlier, in line with previous studies by e.g. Feldmann et al. (2016). At $z = 2$ we find a median formation redshift for star-forming galaxies to be 3.36, which is in line with recent observations by Thomas et al. (2017), who evaluate a median formation redshift of ~ 3.22 for their galaxy sample observed at $2 < z < 6.5$ when using a formation redshift based on mean stellar ages similar to ours.

At redshift $z = 0$ (right panel), we still find this correlation between the formation redshift

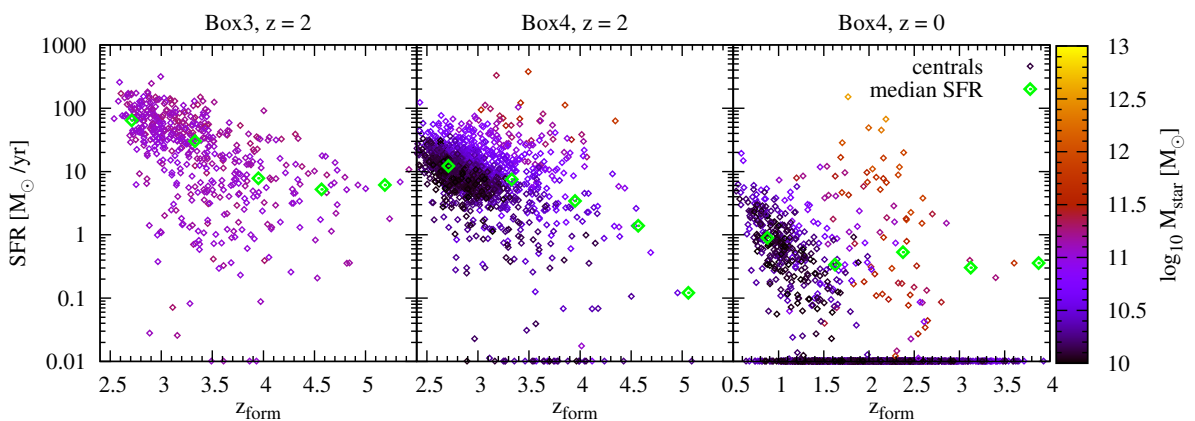


Figure 4.4.3: The formation redshift z_{form} against the current SFR for centrals with stellar masses between 10^{11} and $2 \cdot 10^{11} M_{\odot}$ in *Box3* at $z = 2$ (left) and centrals with stellar masses above $10^{10} M_{\odot}$ in *Box4* at $z = 2$ (middle) and at $z = 0$ (right).

Table 4.4: The number of centrals and companions with $M_{\text{star}} > 10^{10} M_{\odot}$ divided into quiescent and star-forming at four different redshifts

redshift	centrals		companions	
	$N_{\text{quiescent}}$	N_{SF}	$N_{\text{quiescent}}$	N_{SF}
0	1069	250	694	99
0.5	1064	380	633	148
1	908	636	466	200
2	107	1198	73	242

z_{form} and the SFR for low-mass galaxies, while high-mass galaxies show no clear trend anymore. These massive galaxies live in very dense environments like galaxy groups and clusters in which star formation can continue, fed by cooling from the halo, even for systems with early formation times. Such massive galaxies at $z = 0$ all have formed at early times, typically with a formation redshift between $z = 1.5$ and $z = 2.5$.

4.4.3 The Relation between the Environment and the SFR

To investigate how the environment is affecting the SFR of galaxies, we characterize the environment of galaxies by their neighbor counts. Therefore, we count all galaxies with stellar masses above $10^8 M_{\odot}$ within a sphere of radius $r = 5$ Mpc around our centrals. We define the environmental density as

$$\rho_{\text{env}} = \frac{N_{\text{gal}}(5\text{Mpc})}{4/3 \cdot \pi \cdot r^3}. \quad (4.2)$$

Here, following [Treu et al. \(2003\)](#), the radius was chosen to include all potential cluster members. Accordingly, using the distance to the 10th neighbor results in a similar median value (see [Cappellari et al., 2011b](#)).

[Fig. 4.4.4](#) shows the build-up of the morphology-density relation (e.g. [Dressler, 1980](#)) with cosmic time. The different panels show the dependence of the morphology-density relation on the star formation properties of the central galaxies: the left panels show the quiescent centrals, while the right panels show the star-forming centrals. [Table 4.4](#) lists the sample sizes at the different redshifts.

We do not find evidence for a morphology-density relation at high redshift ($z > 2$), for neither of the two galaxy types. Generally, we see a clear evolution with decreasing redshift, and the build-up of the morphology-density relation starts at around $z = 2$. At this redshift the trend appears that centrals that live in overdense regions have a high fraction of quiescent neighbors, while galaxies in lower density environments have on average a lower fraction of quiescent neighbors. This trend is in good agreement with observations by [Darvish et al. \(2016\)](#), who also find that at higher redshift the fraction of quiescent

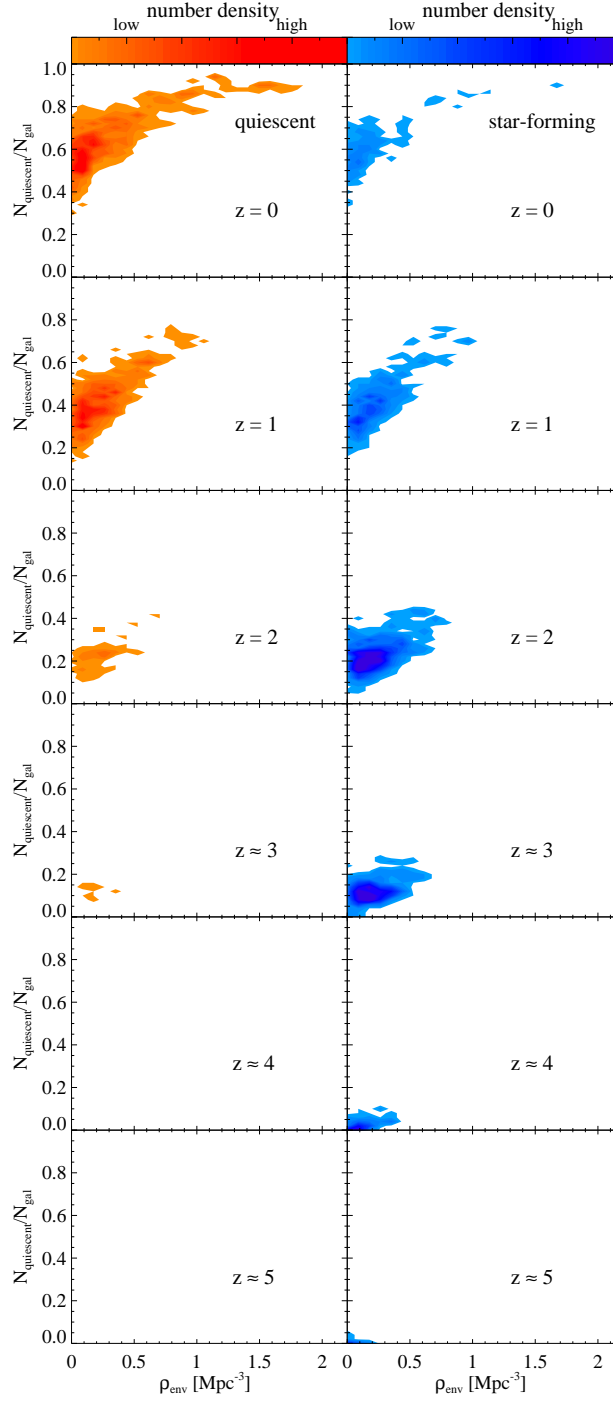


Figure 4.4.4: The fraction of quiescent galaxies more massive than $10^8 M_{\odot}$ within a sphere of radius 5 Mpc (comoving) around quiescent (left panels) and star-forming (right panels) centrals with stellar masses above $10^{10} M_{\odot}$ in *Box4* at different redshifts. There is a clear build-up of the morphology-density relation starting at around $z = 2$; while at high redshift the fraction of quiescent galaxies does not depend on the number of neighboring galaxies, i.e. the environment, with decreasing redshift the environment becomes more and more important for the quiescent fraction. The distribution looks very similar for quiescent and star-forming galaxies.

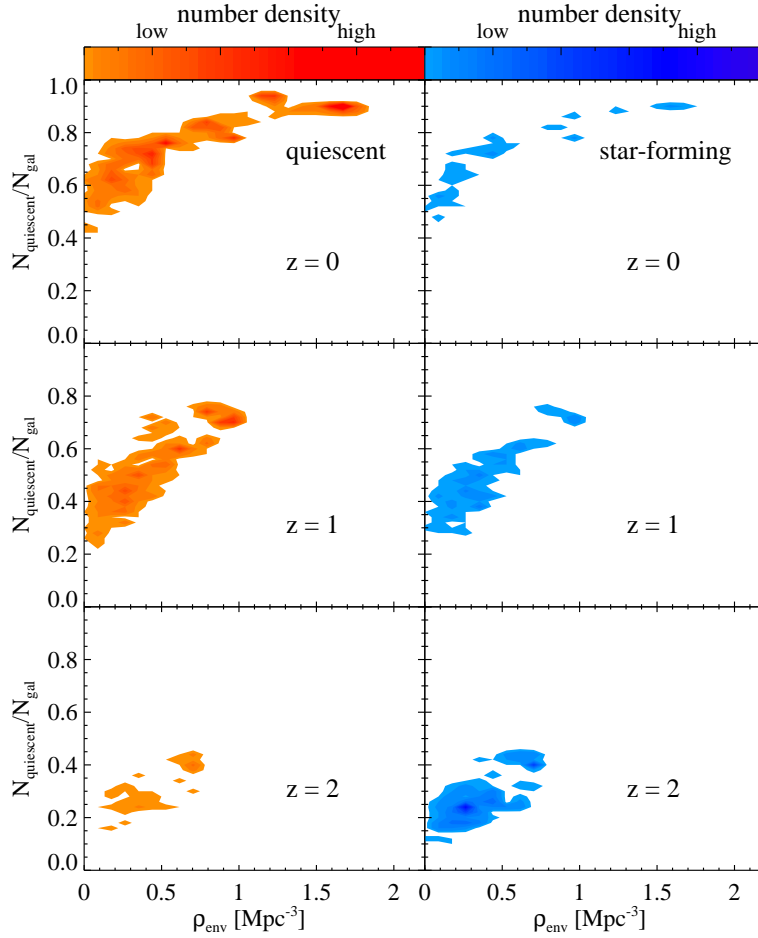


Figure 4.4.5: The same as in Fig. 4.4.4, but for companions. As seen for the centrals, there is a built-up of the morphology-density relation, where there is no difference between quiescent and star-forming companions.

galaxies does not depend on the environment, while it does at low redshift. Interestingly, it does not make a difference if the central is quiescent or star-forming itself: there are for example quiescent centrals in low-density environments that have a very low fraction of quiescent galaxies around them and vice versa, star-forming centrals in high-density environments with a high fraction of quiescent galaxies.

Several studies (e.g., Peng et al. (2010), Lee et al. (2015) and Hirschmann et al. (2016)) find that this environmental quenching is important especially for low-mass satellite galaxies. For completeness, we show in Fig. 4.5.2 of Section 4.5 the morphology-density relation for centrals in physical units.

In Fig. 4.4.5 we show the morphology-density relation for the companion galaxies for redshifts $z = 0$ to $z = 2$, as there are too few companions at higher redshifts. The shape of the morphology-density relation for the companion galaxies is the same as for the central

galaxies (see Fig. 4.4.4). Similarly, it does not make a difference for the fraction of quiescent neighboring galaxies if the companion galaxy itself is quiescent or star-forming. While the number density of the quiescent central galaxies peaks in the low-density environments, the number density of the quiescent companions is more shifted towards denser environment. In contrast, the distribution of the number densities in the morphology-density relation of star-forming centrals and satellites does not differ. This clearly demonstrates that environmental quenching is more important for satellite galaxies than for centrals. Since our satellite galaxies on average are low-mass galaxies this supports earlier studies by Hirschmann et al. (2016), who concluded that the fraction of quiescent galaxies is mainly determined by internal processes, while the environment becomes important at lower masses.

4.5 The World in Physical Units

Since it is common to use physical units in observations, we show some of our results in physical units, where we take the expansion of the Universe into account. The difference to the comoving units, which capture the real growth of a structure, becomes more and more important with increasing redshift.

4.5.1 Satellite Fraction in Physical Units

In Fig. 4.3.5 we showed the abundance of satellites per host galaxy binned by the mass ratio with respect to their host, for all potential host galaxies (left panel) and split into companion (middle panel) and central (right panel). Fig. 4.5.1 shows the same for redshift $z = 2$ in physical units. Compared to the bottom panels in Fig. 4.3.5, the number of satellite galaxies is higher. It is also higher than at $z = 0$, which is not surprising when comparing volume-limited samples at different redshifts (see also discussion in Conroy et al. (2007)). This demonstrates that careful choice of distance scale is important, especially at high redshift.

4.5.2 Morphology-Density Relation in Physical Units

The influence of the choice of distance scale becomes especially prominent for the morphology-density relation. Comparing Fig. 4.4.4, which illustrates the morphology-density relation for centrals in comoving units, with Fig. 4.5.2, which is the same relation in physical units, the shape and its evolution look strikingly different. When taking a sphere in physical units, the induced change in the distance scale masks the presence of the density morphology relation at $z \geq 1$, resulting in a later and steeper increase of the morphology-density relation. This is due to the fact that in physical units the search radius becomes larger

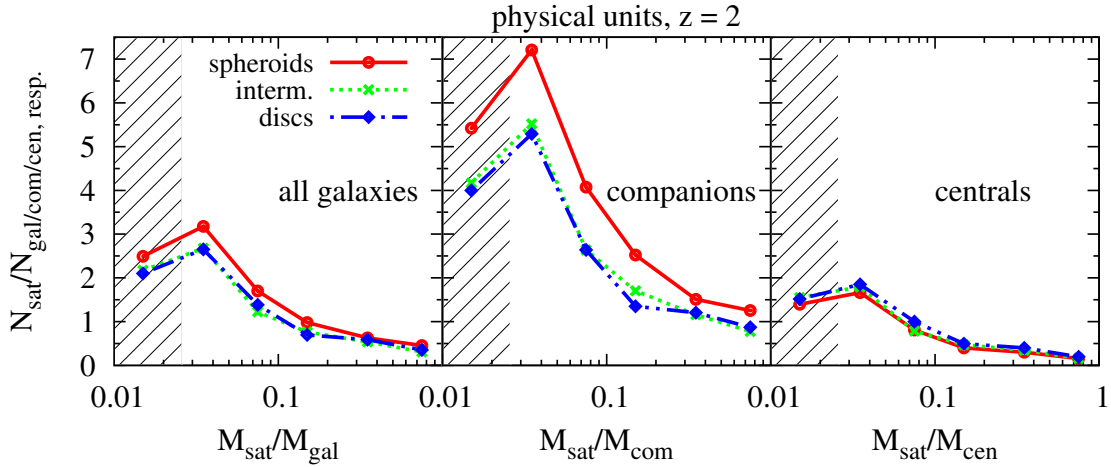


Figure 4.5.1: The differential number of satellites per host galaxy at redshift $z = 2$ for all host galaxies (left), companions (middle) and central galaxies (right) within a sphere of 300 kpc in physical units, binned according to their mass ratio.

compared to the central galaxies with increasing redshift and we thus go farther outside of the “local” environment to the “global” environment. In the “local” environment we find a higher number of quiescent neighboring galaxies than in the “global” environment, emphasizing the importance of the “local” environment for the satellite quenching.

4.6 Discussion and Conclusions

We use galaxies extracted from the high resolution cosmological simulation suite Magneticum to investigate the relation between the dark matter halo mass and the internal properties of galaxies as well as the environmental imprint on the star formation properties. Especially, we want to test whether the morphological type of a galaxy depends on the dark matter halo mass, as recently concluded from the observed differences in the abundance of satellites around galaxies of different morphological types by Ruiz et al. (2015). We select all galaxies with stellar masses above $10^{10} M_{\odot}$ and use a dynamical parameter, the so-called b -value (see Teklu et al., 2015), as indicator of morphological type. We find that:

- When applying the observed strategy of counting satellite galaxies around all massive galaxies we clearly reproduce the observed signal of more satellites around spheroidal galaxies compared to disk galaxies for both the total numbers for different mass ratios as well as for the radial abundance profile.
- This signal does not depend on (and therefore is not produced by) the way of defining the volume in which the satellites are counted. We find that the signal even holds if we use spherical volumes around the galaxies instead of a cylinder defined by a redshift range as observers have to rely on.

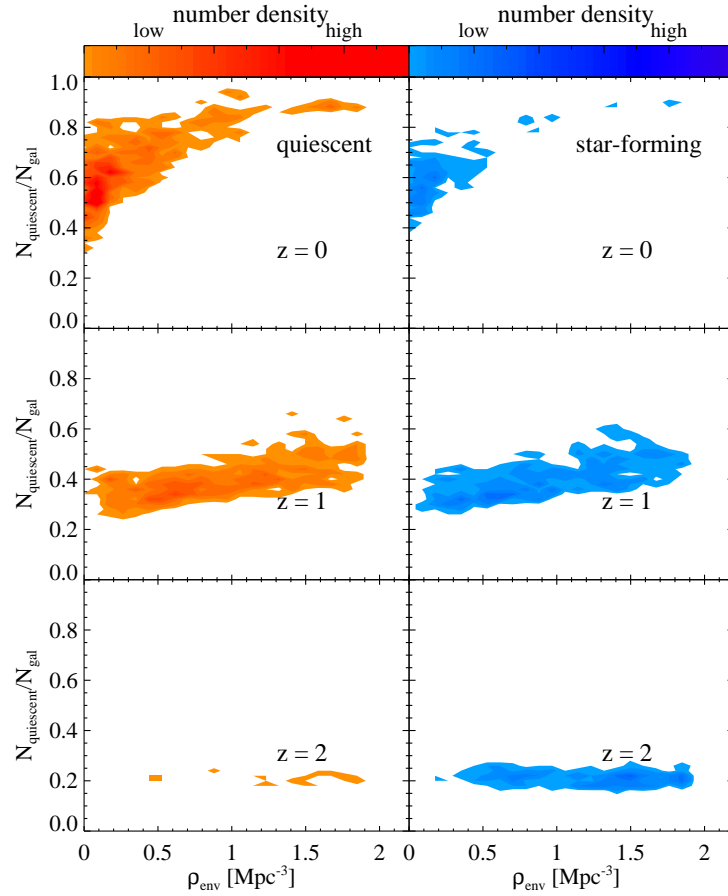


Figure 4.5.2: The fraction of quiescent galaxies more massive than $10^8 M_{\odot}$ within a sphere of radius 5 Mpc (physical) around quiescent (left panels) and star-forming (right panels) centrals with stellar masses above $10^{10} M_{\odot}$ in *Box4* at different redshifts.

- However, when splitting the sample of massive galaxies into galaxies at the center of their dark matter halo (i.e. centrals) and companion galaxies (which are only large satellites of other massive galaxies within a common dark matter potential), we find that the signal is exclusively caused by the companion galaxies. If only the central galaxies are considered, the signal completely disappears.
- This result is found to hold true even at higher redshifts up to $z = 2$. However, when considering all galaxies (centrals and companions), the difference in the satellite number between spheroids and disks becomes smaller with increasing redshift due to the lower number of companions at higher redshift.
- This is also supported by the fact that the baryon conversion efficiency of our galaxies does not show any significant trend with the inferred morphological type.

We therefore conclude that the observed differences in the abundance of satellites around massive galaxies of different morphological types is only driven by the different environ-

ments, in which spheroid and disk galaxies are typically living, and that they are not related to differences in the baryon conversion efficiency of galaxies with different morphological types. This is supported by observational results from [Guo et al. \(2015\)](#) that isolated primaries in a filamentary environment have more satellites than those outside of filaments.

We investigate in more detail the relation between the quenching of star formation and our morphological classification based on the b -value for galaxies at high redshift (i.e. $z = 2$). Selecting a large number of galaxies (≈ 500) within a very narrow mass range (i.e. $10^{11} M_{\odot} < M_{\text{star}} < 2 \cdot 10^{11} M_{\odot}$), allows us to exclude any mass dependencies. We find that:

- In contrast to galaxies at $z = 0$, the galaxies which are already quenched at $z = 2$ do not show a relation to their morphological type.
- Quenched galaxies at $z = 2$ have on average formed earlier than their starforming counterparts, as suggested in previous studies (e.g. [Feldmann et al., 2016](#)).
- Satellites of quenched galaxies at $z = 2$ have typically formed earlier and show on average less star formation activity compared to satellites of star-forming galaxies, as suggested in earlier studies (e.g. [Feldmann et al., 2016](#)).

Our simulations furthermore show that at redshifts of $z = 2$, in contrast to present time, the dynamical classification of galaxies based on morphology results in a different selection than the classification based on star formation. Our results are broadly in agreement with the picture that was pointed out in previous studies (e.g. [Hirschmann et al., 2016](#); [Huertas-Company et al., 2016](#); [Peng et al., 2010](#)) that the environment is effective in quenching star formation of lower mass galaxies, while at higher masses and redshifts $z > 1$ other (internal) effects are the dominant drivers.

Additionally, we study the connection between the environment and the star formation rate evaluating the environment density ρ_{env} . From the evolution of the morphology-density relation between $z \approx 5$ and $z = 0$ we conclude that:

- At high redshifts ($z \geq 3$) there is no signature of a morphology-density relation for central galaxies. The built-up of the morphology-density relation starts at around $z \approx 2$.
- The morphology-density relation for quiescent and starforming centrals is similar, indicating a negligible influence of the environment on the star-forming properties of the central galaxies.
- The shape of the morphology-density relation for the companion galaxies is the same as for the central galaxies.
- The quiescent fraction of companion galaxies is comparable to that of the central galaxies.

- The number density of the quiescent central galaxies peaks in the low-density environments, while the number density of the quiescent companions peaks at denser environments.
- The distribution of the number densities in the morphology-density relation of star-forming centrals and satellites does not differ.

We conclude that environmental quenching is more important for satellite galaxies than for centrals.

Chapter 5

The Kinematics of the Different Stellar Populations in Galaxies with Different Morphology

This chapter is based on a paper, Teklu et al., to be submitted (hopefully soon)

Abstract

In recent years IFU surveys have delivered new insights into the stellar kinematics and stellar populations of galaxies. In order to study the connection between the age of the stellar populations and kinematics of galaxies of different morphologies via the b -value, we use galaxies extracted from the cosmological hydrodynamical *Magneticum Pathfinder* simulations. We find that the old stars dominate the overall rotation, i.e. the old stellar populations in disks have a high b -value, while those of spheroids show less rotational support. The different stellar populations in disks have similar b -values, which suggests a relatively quiet evolution. On the other hand, the different stellar populations within spheroids differ from each other, which points to different origins of the various components. When subclassifying the early-type galaxies (ETGs) according to features in their velocity maps, we find that galaxies with distinct cores represent a special class; they have, on average, more young and middle-aged stars than the other subclasses of ETGs. This implies that the populations of different subclasses of ETGs have formed via different formation channels.

5.1 Classification of Simulated Galaxies

From our simulations we extract central galaxies with stellar masses higher than $10^{10} M_{\odot}$ at redshift $z = 0$. This limit was chosen to ensure a sufficient resolution of the stellar content. This leads to a total number of 1319 galaxies. In order to see if the classification qualitatively influences the results, for our studies we will use different classifications, which are briefly introduced in the following.

- In order to classify **poster child disk** and **poster child spheroidal** galaxies we use the circularity parameter ε , defined as $\varepsilon = j_z/j_{\text{circ}}$, which was discussed and used in Chapter 3. Applying this approach we find 15 poster child disk galaxies and 61 poster child spheroidal galaxies.
- For the separation into **disks**, **spheroidal** and **intermediate** galaxies we use a relatively simple but still efficient classification of the galaxies, utilizing the stellar mass vs. stellar angular momentum plane of galaxies, i.e. the b -value, which was explained and used to classify the galaxies for our studies in Chapter 4. Employing this method, we end up with 466 disks, 441 intermediates and 412 spheroidal galaxies.

5.1.1 Subclasses of Early-Type Galaxies

As already mentioned in the Introduction (Chapter 1), the classical picture of ETGs has changed dramatically over the past decade. This is owing to the improvement of observational instruments, so that the integral field surveys like, e.g., ATLAS^{3D} (Cappellari et al., 2011a), CALIFA (Sánchez et al., 2012), MaNGA (Bundy et al., 2015) or SAMI (Bryant et al., 2015; Croom et al., 2012), could resolve the kinematical structures of ETGs by providing spatially resolved 2D maps of stellar properties, including stellar kinematics and stellar ages. It became obvious that ETGs were not all the same, but they exhibit substructures like disks and rings (see e.g. Cappellari, 2016; Emsellem et al., 2011; Guérou et al., 2016; Krajnović et al., 2011). According to their different properties the ETGs could be further divided into subgroups according to their kinematics. Therefore, for the third and fourth classification we focus on ETGs. The classifications are taken from Schulze et al. (2018). In the following, we will briefly sketch the methodology of the classifications (for a detailed description, see Schulze et al. (2018)).

A simple preselection is used in order to exclude galaxies with cold gas reservoirs and select ETGs: we first select galaxies that have a cold gas fraction compared to the stellar mass which is lower than 0.1 (see Schulze et al., 2018). Furthermore, we exclude galaxies with $R_{1/2} < 2$ kpc, which is equivalent to two times the softening length, to ensure a proper spatial resolution.

For the third classification we use the kinematical so-called λ_R -parameter (Emsellem et al., 2007) and the morphological ellipticity parameter ϵ (Cappellari et al., 2007), which have

been shown to be a helpful tool for gaining better insights on the nature of ETGs (e.g. Emsellem et al., 2007; Schulze et al., 2018). λ_R is a proxy for the observed projected stellar specific angular momentum and for an observed 2D kinematical map it is defined as

$$\lambda_R = \frac{\langle R|V| \rangle}{\langle R\sqrt{V^2 + \sigma^2} \rangle}, \quad (5.1)$$

where R is the observed distance to the center of the galaxy, V the line-of-sight velocity and σ the projected velocity dispersion. In order to be able to apply the parameter to simulated galaxies it has to be adapted. Following previous theoretical studies (e.g. Naab et al., 2014; Schulze et al., 2018), λ_R is given by

$$\lambda_R = \frac{\sum_{i=1}^{N_p} M_i R_i |\bar{V}_i|}{\sum_{i=1}^{N_p} M_i R_i \sqrt{\bar{V}_i^2 + \sigma_i^2}}, \quad (5.2)$$

where the sum runs over all pixels of the velocity map and M_i , R_i , $|\bar{V}_i|$ and σ_i are the stellar masses, the projected distance to the center of the galaxy, the mean stellar velocity and the velocity dispersion of the i^{th} photometric bin. The ellipticity parameter ϵ is calculated by iteratively diagonalizing the moment of inertia tensor.

After having calculated the two parameters, the galaxies are divided into slow and fast rotators, following Emsellem et al. (2007); galaxies that fulfill the condition $\lambda_{R_e} > 0.31 \sqrt{\epsilon_{R_{1/2}}}$ are classified as **fast rotators** and those with $\lambda_{R_e} \leq 0.31 \sqrt{\epsilon_{R_{1/2}}}$ are classified as **slow rotators**. Here, we find 563 fast rotators and 189 slow rotators.

For the fourth classification we divide the ETGs into four kinematical groups, using the classification presented in Schulze et al. (2018) (see also Krajnović et al., 2011), which is based on a visual inspection of the line-of-sight velocity maps in the edge-on projection. Galaxies with velocity maps showing ordered rotation around the minor axis and no distinct kinematical features, are classified as **regular rotators**. If the velocity maps show low-level velocities or no distinct kinematical features, the galaxies are **non-rotators**. Galaxies are classified as **distinct cores** if the maps exhibit low-level velocities in the outskirts and a central rotating component. If the velocity map shows ordered rotation around the major axis, the galaxies are classified as **prolate rotators**. We identify 329 regular rotators, 78 non-rotators, 16 galaxies with distinct cores, and 11 prolate rotators.

5.2 Stellar Populations in Galaxies of Different Types

The age of a galaxy, in particular the contribution and distribution of the stars of different ages, gives valuable insights into the formation and assembly history of a galaxy (Guérou et al., 2016). In particular, their kinematics can provide helpful information, as different mechanisms during the formation leave different imprints on the rotational pattern. In

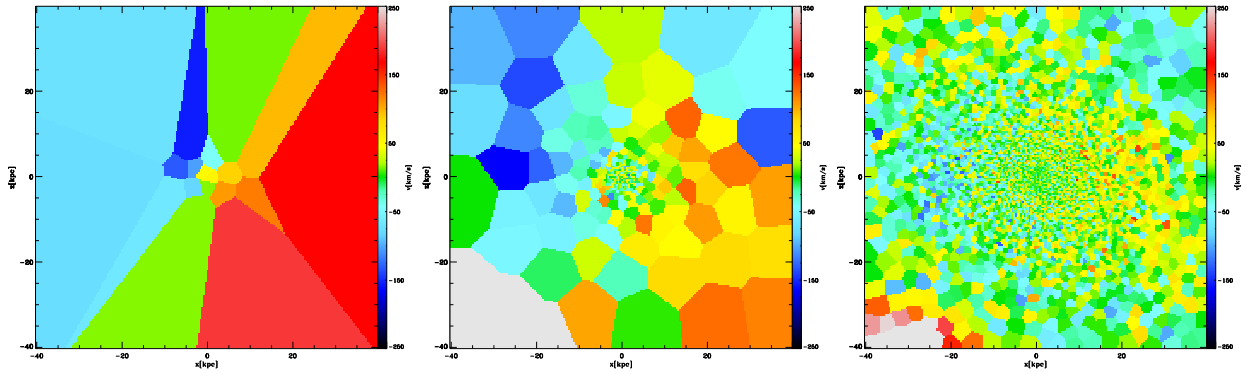


Figure 5.2.1: The voronoi-binned line-of-sight velocity maps for a poster child spheroidal galaxy divided into stellar populations of different age. *Left:* Only young stars are illustrated. This small population of young stars exhibits a rotation. *Center:* Only middle-aged stars are shown. They also show a slight rotation. *Right:* In the old stellar component there is no ordered motion.

order to gain a general impression of the behavior of the different stellar populations we divide the stars according to their age. For this, we consider all stars that are younger than 2 Gyrs as young, those that are between 2 and 8 Gyrs as middle-aged and all stars older than 8 Gyrs as old. In the following subsections we will analyze the behavior of these different stellar populations and try to connect it to the morphology and kinematical properties of the galaxies.

5.2.1 Stellar Populations in Poster Child Disks and Spheroids

For the first study we will focus on the poster child disk and spheroidal galaxies, which we classify using the circularity parameter ε and, in addition, a criterion based on the mass fraction of the cold gas, as described in Sec. 5.1 and 3.3.

Fig. 5.2.1 displays the voronoi-binned line-of-sight velocity maps of one of the poster child spheroidal galaxies; on the left panel only young stars are shown, in the center only middle-aged stars, and on the right panel only old stars. In order to reduce the statistical error on the velocities, the cells contain a minimum of 100 particles. As one can see from the bin sizes there are very few young stars. Still, a rotation of this population is visible. This young rotating component has very likely formed out of a small gas disk. In the motion of the middle-aged stars only a slight rotation is noticeable. The old stellar component is apparently nonrotating. This fits well in the general picture of a spheroidal galaxy, which has a dominant old stellar population, and generally assembled through (multiple) merger events leading to a dispersion-dominated system. This difference in the rotational pattern of the different stellar populations is a first hint that the populations have different origins.

Fig. 5.2.2 shows the velocity map for one of the poster child disk galaxies. As expected, the young stars (left) lie in a relatively thin disk and have a highly ordered motion. The

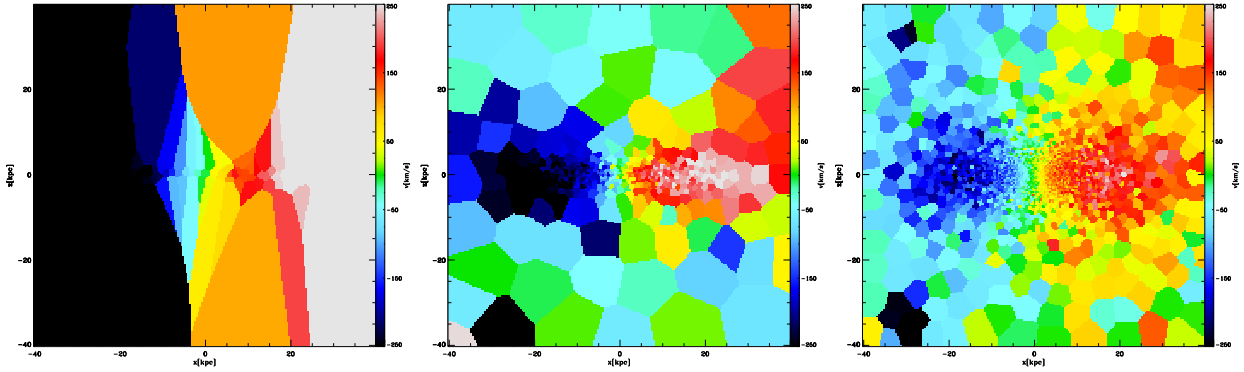


Figure 5.2.2: The same as in Fig. 5.2.1, but for a poster child disk galaxy. *Left:* There is a relatively thin disk of rotating young stars. *Center:* The middle-aged stars have a disk-like appearance and are rotating. *Right:* Also in the old stellar component we find a highly ordered motion.

middle-aged stars (center) also reside in a rotating disk. Even the old stellar population (right), although distributed more spherically, shows a highly ordered motion.

Since the b -value is a good tracer of the morphological type of the whole galaxy, we want to investigate how the galaxy type is reflected in the b -value of the different stellar populations. For this, the b -value is calculated for each population by using the specific angular momentum of the respective population and the whole stellar mass of the galaxy. Similarly, Romanowsky and Fall (2012) have calculated of the angular momentum of the disk and bulge component separately, where they found the bulges of spiral galaxies to follow a similar $M_* - j_*$ relation compared to the elliptical galaxies.

The left panel of Fig. 5.2.3 shows the distribution of the mean b -value per galaxy of the young stars in disks (blue histograms) and spheroids (red histograms). Interestingly, the distributions along the x -axis do not look very different; the young stars of both galaxy types cover a broad range, however, from the height of the histograms, which are normalized by the according number of galaxies of that type (i.e. they do not integrate to unity), we can see that there are spheroidal galaxies that do not have any young stars. It seems that there are two populations of disk galaxies; one that mainly has young stars having a higher rotation with b -values higher than -4.25 , and another one whose young stars rotate slower with b -values lower than -4.25 .

The distribution of the middle-aged stars (middle panel) looks different for spheroids and disks. While the spheroids have a broad distribution, the middle-aged stars in disks mainly have a higher rotational support.

In the old stellar components (right panel) this becomes even more obvious. Here, the two distributions show a clear dichotomy.

In order to better understand the behavior of the different stellar populations within the two galaxy populations, Fig. 5.2.4 shows the same histograms as Fig. 5.2.3 but arranged

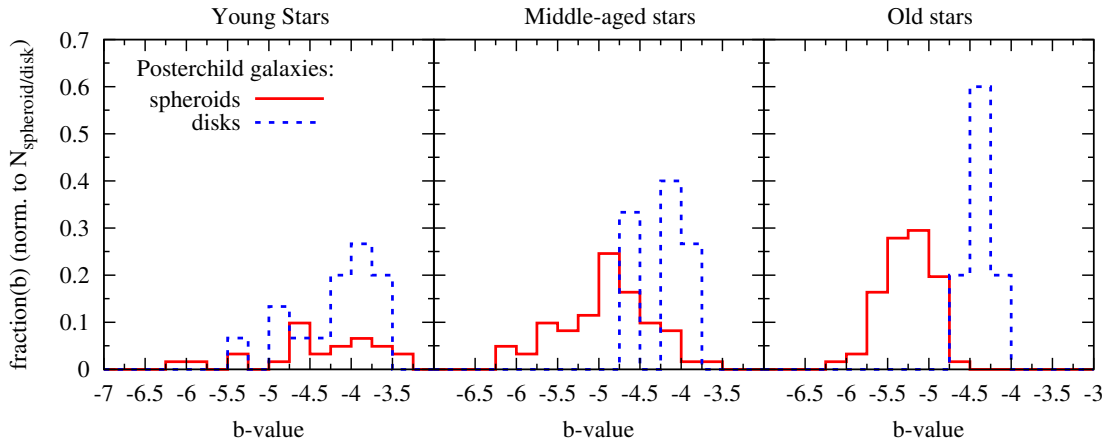


Figure 5.2.3: Shown are the binned b -value distributions of young stars (left), the middle-aged stars (center), and the old stellar population (right). They are normalized to the number of the according galaxy type, where red histograms represent the poster child spheroids, while the blue ones represent the disk galaxies. Interestingly, the distribution of the young stars looks similar for disks and spheroids. While the middle-aged stars in spheroids have a broad distribution, in disks they tend to higher b -values. In the old stellar populations we clearly see a split-up, where in disks the old stars have higher values, while in spheroidal galaxies they have lower values.

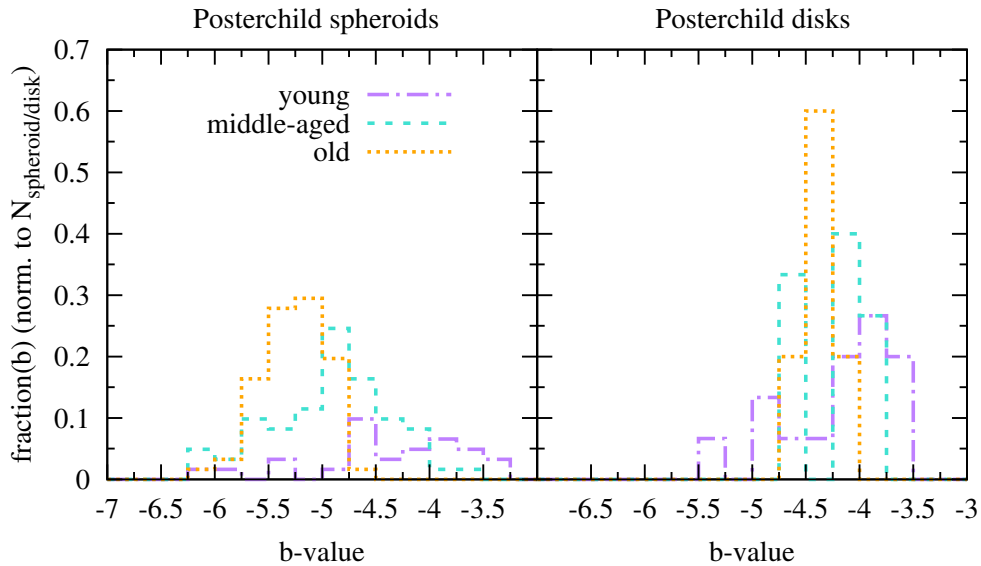


Figure 5.2.4: Similar to Fig. 5.2.3, but now each panel shows the distributions of separate galaxy types, left are the poster child spheroids and right are the poster child disk galaxies. The colors encode the stellar population, where young stars are purple, middle-aged stars are turquoise and old stars are orange. In disk galaxies the distributions of the different stellar populations are more similar than in spheroidal galaxies.

separately for spheroids (left) and disks (right). The colors encode the stellar populations, where young stars are represented by purple lines, middle-aged stars by cyan lines and old stars by orange lines. In disk galaxies the distributions of the b -values of the different populations are relatively uniform, i.e. all stellar populations tend to have a high rotational support. In contrast, the populations in spheroidal galaxies show different distributions; while the old stars have low b -values, the young stars tend to have high b -values. The middle-aged stars cover the whole range of the b -values but peak at a similar value compared to the old stars.

This difference in the distributions between spheroids and disks is likely to be linked to their different formation histories. This fits in the general picture that disk galaxies mostly can evolve undisturbed, so they can continuously form stars. In contrast, the spheroidal galaxies live in more disturbed environments. Thus, spheroidal galaxies experience more encounters with other galaxies, whereby they directly accrete their young stellar components or accrete fresh gas, which then forms new stars. If these galaxies come from different directions, and/or have specific orbital configurations, they can bring in misaligned angular momenta, which lowers the overall rotation (see e.g. [Lagos et al., 2017](#); [Moody et al., 2014](#); [Naab et al., 2014](#)).

In order to see how much the different populations contribute to the dynamics of the galaxy, in [Fig. 5.2.5](#) we show their mass fractions averaged over spheroids (left) and disks (right). It is obvious that the spheroidal galaxies are on average older than the disk galaxies, which is in agreement with other studies, e.g. [González Delgado et al. \(2015\)](#). The spheroidal galaxies have 90 percent of their stellar mass in old stars (orange) and about 10 percent in middle-aged stars (turquoise), while they have a negligible amount of young stars. The disk galaxies on average consist of $\simeq 62$ percent of old stars, of $\simeq 31$ percent of middle-aged stars and of $\simeq 7$ percent of young stars. This shows that the overall dynamical behavior of spheroids and disks, e.g. the total b -value, is dominated by the old stellar population.

These results and the dichotomy seen in the right panel of [Fig. 5.2.3](#) are consistent with the findings of [Teklu et al. \(2015\)](#), i.e. the b -value is a good tracer of the morphology of the galaxy.

5.2.2 Stellar Populations in Disks, Intermediates and Spheroids

Since the b -value is a good tracer of the morphological type of the whole galaxy, we want to directly test how the total b -value is reflected in the b -value of the different stellar populations.

[Fig. 5.2.6](#) shows the mean b -value distributions of young stars (left), middle-aged stars (center), and the old stellar population (right) within the respective galaxy class. The different rows show the distributions at different radii, where the upper row shows the results at $5R_{1/2}$, the middle row at $3R_{1/2}$, and the lower row at $R_{1/2}$. The galaxies are divided into spheroids (red), intermediate galaxies (green) and disk galaxies (blue), according to the

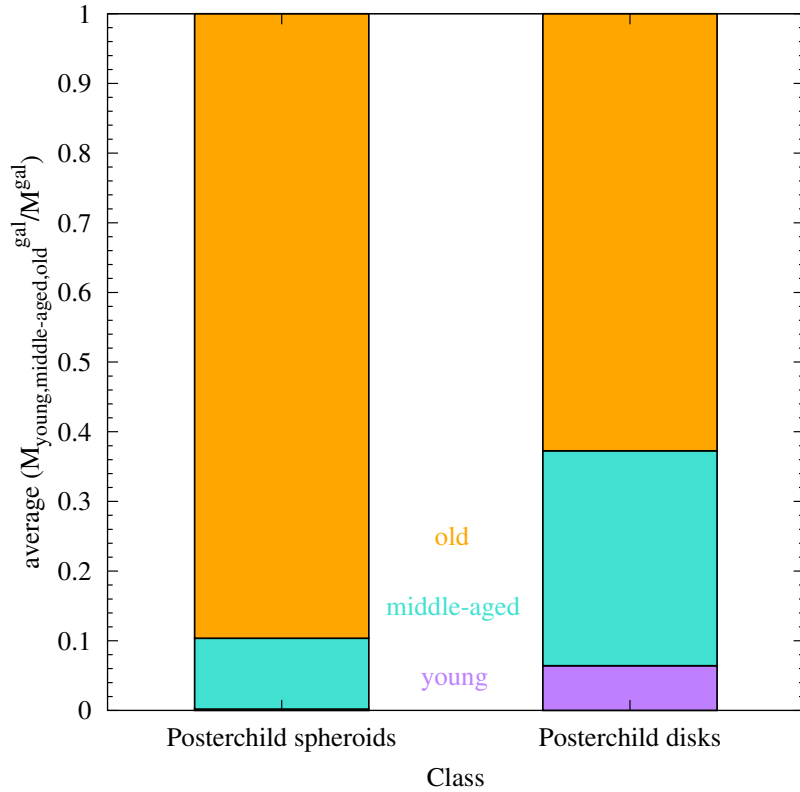


Figure 5.2.5: Average mass fractions of the stellar populations for spheroids (left) and disks (right). On average, the disk galaxies have around 7 percent young stars (purple), 31 percent middle-aged stars (turquoise) and 62 percent old stars (orange). The spheroidal galaxies consist of 90 percent of old stars, and 10 percent of middle-aged stars, while on average they have a negligible number of young stars.

total b -value at the respective radius. For spheroids and intermediates the distributions of the young stars look similarly broad at large radii. Interestingly, on a scale of $R_{1/2}$ the distribution for the young stars of intermediates looks similar to that of the disks, while the distribution for spheroids shows only a minor shift towards larger b -values. This indicates that the young stars close to the center have a higher rotational support than those outside.

The middle-aged stars in spheroids have a broad distribution, whereas in disks they have higher b -values. For the intermediates the distribution of middle-aged stars peaks between that of the spheroids and that of the disks.

In the old stellar populations there is a split-up, where the old stars of disks have high values, while in spheroidal galaxies they have low values. The intermediates, again, lie in between.

In order to directly see how the stellar populations behave within the populations of the different galaxy types, in Fig. 5.2.7 we show the same histograms as Fig. 5.2.6 but this

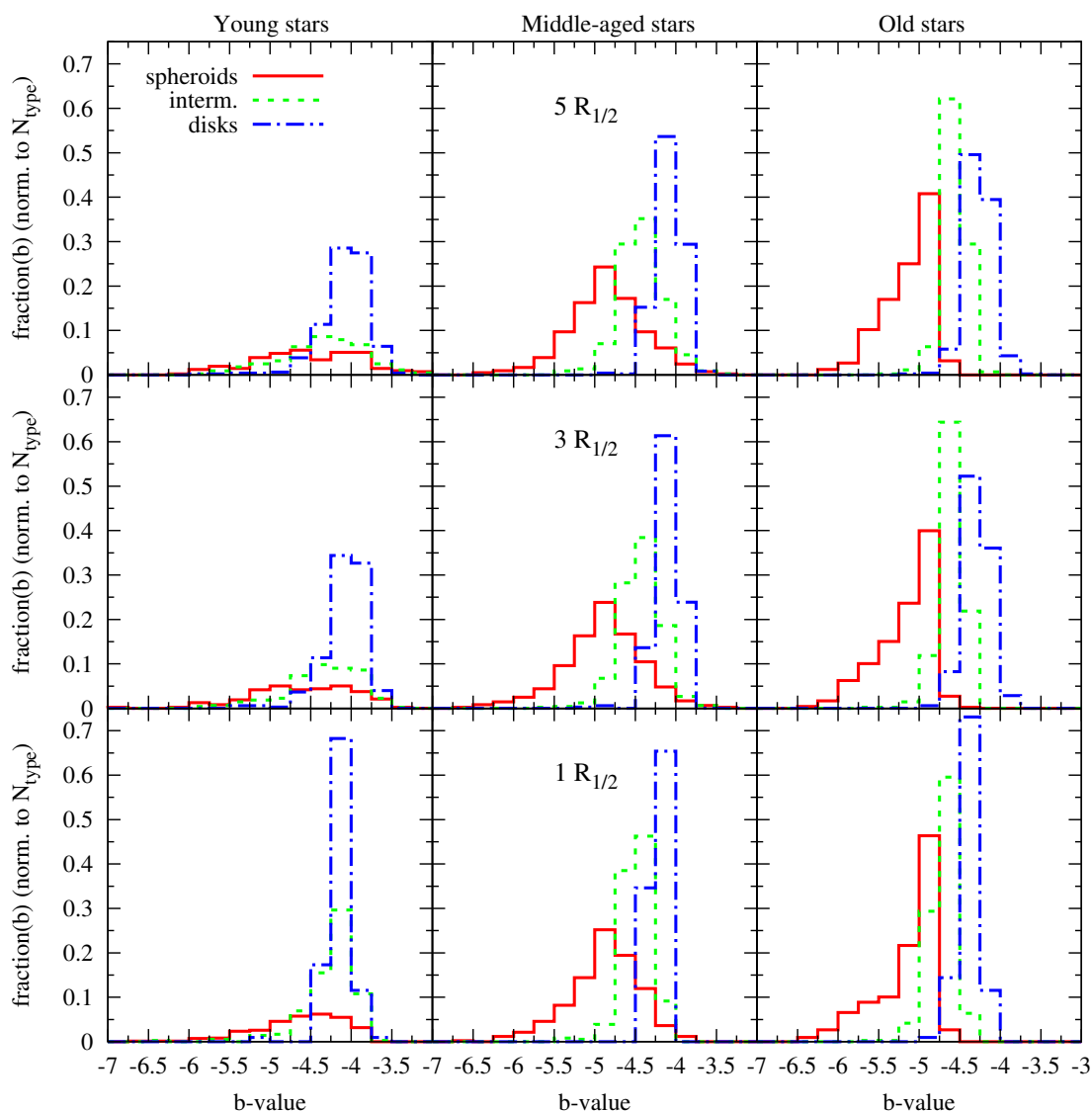


Figure 5.2.6: The b -value distributions of young stars (left), middle-aged stars (center), and the old stellar population (right). The upper row shows the results at $5R_{1/2}$, the middle row at $3R_{1/2}$, and the lower row at $R_{1/2}$. According to the total b -value, the galaxies are divided into spheroids (red), intermediate galaxies (green) and disk galaxies (blue). The distribution of the young stars for spheroids and intermediates looks similar, while the young stars in disk galaxies have higher b -values. While the middle-aged stars in spheroids have a broad distribution, in disks they have higher b -values. The peak of the middle-aged stars of the intermediates is between the spheroids and the disks. In the old stellar populations we clearly see a split-up, where the old stars of disks have higher values, and in spheroidal galaxies they have lower values. The peaks of the distributions become sharper for smaller radii, especially for disks.

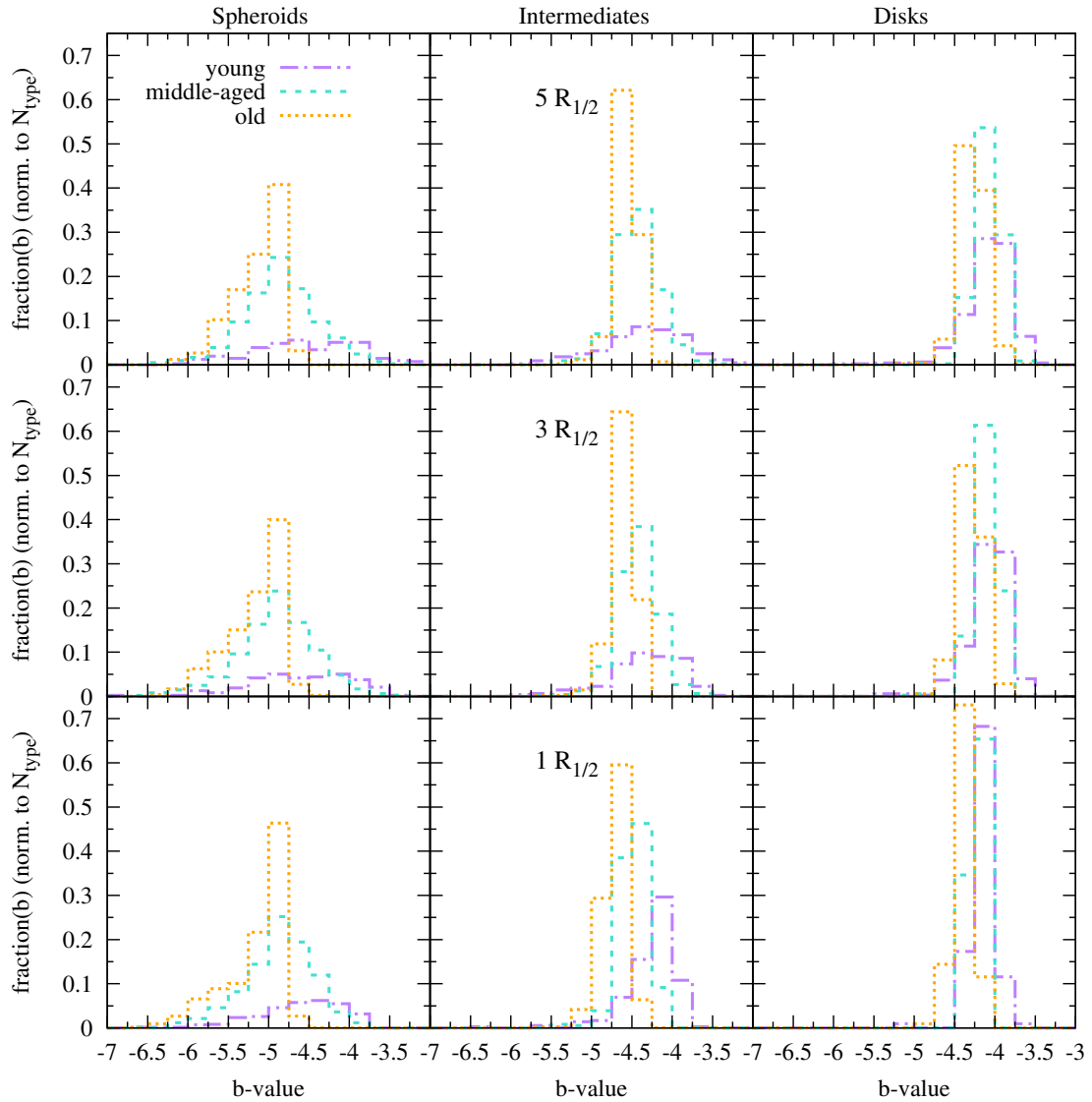


Figure 5.2.7: Similar to Fig. 5.2.6, but each column shows the distributions of one galaxy type, left are the spheroids, in the center the intermediates, and right are the disks. The colors encode the stellar population, where young stars are purple, middle-aged stars are turquoise and old stars are orange. In disk galaxies the distributions of the different stellar populations are very similar to each other, while in spheroidal galaxies they are different.

time separately for spheroids (left), intermediates (middle) and disks (right). The young stars are illustrated by the purple lines, middle-aged stars by cyan lines and old stars by orange lines. In this arrangement we clearly see that in disk galaxies the distributions of the different stellar populations are very similar to each other out to large radii. This is due to the fact that disk galaxies can form relatively undisturbed and continuously form stars out of their gas, which is smoothly accreted. In this way the stars all have similar angular momentum directions, which results in similar high b -values.

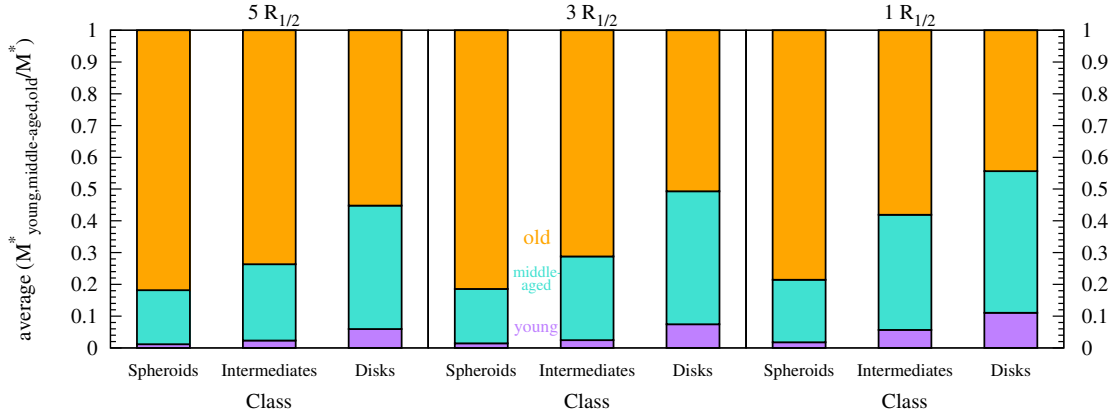


Figure 5.2.8: Average mass fraction of the stellar populations within at different radii, where the left panel shows $5R_{1/2}$, the middle panel $3R_{1/2}$, and the right panel $R_{1/2}$. When going to smaller radii, the mass fraction of the old stellar component (orange) decreases, while the fraction of the middle-aged (turquoise) and the young stars (purple) increases, especially for disk and intermediate galaxies.

In contrast to that, in spheroidal galaxies the b -values of the different star populations are different. The old stars might be a mixture of stars with different angular momenta, which accumulated via (major) mergers or have formed in-situ before the mergers. The young stars could have formed out of small disks of freshly accreted gas, e.g. from small gaseous satellites. Another possibility is that the young stars recently could have been directly accreted in the form of small young satellite galaxies. Another interesting aspect is that, when going from larger to smaller radii, the peaks of the distributions for the disk galaxies become narrower. In spheroidal galaxies, the amount of old stars with low b -values increases towards larger radii, while the middle-aged stars are almost identical at all radii.

In the inner parts of the intermediates, the young stars tend to have high b -values. This indicates the presence of small disks, which might be in the process of growing, in many of the intermediates. The growth of these disks is depending on the implemented feedback model. As shown by Valentini et al. (2017), the size of the stellar disk at low redshift is sensitive to the galactic outflow model. Thus, the question arises if these small disks would grow into more extended ones with a different feedback model. However, answering this question is beyond the scope of this work.

In Fig. 5.2.8 we show the average mass fractions of the different stellar populations for the different galaxy types at different radii, in the left panel for $5R_{1/2}$, in the middle panel for $3R_{1/2}$, and in the right panel for $R_{1/2}$. When going from spheroidal galaxies over intermediates to disk galaxies, the mass fractions of the young and middle-aged stars increase, at all radii. In addition, we find that for intermediate and disk galaxies the mass fractions of young and middle-aged stars increases towards the center.

As shown in Teklu et al. (2015), there is a tendency that at smaller radii the b -value is lower. However, for disk galaxies, this does not play a major role, since all the stellar

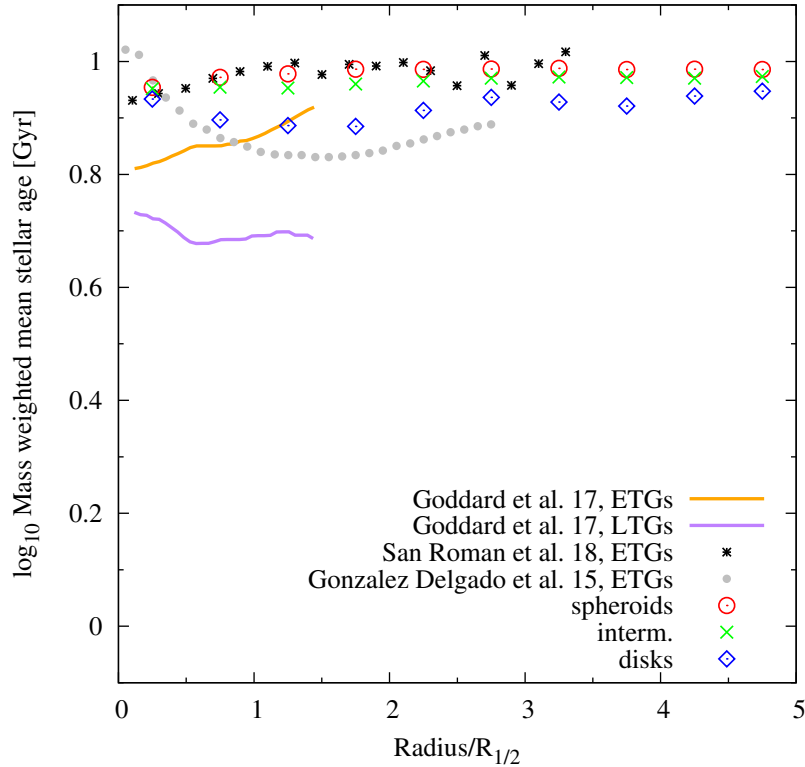


Figure 5.2.9: The mass weighted mean stellar age of the stars at all radii. We add the median mass weighted stellar ages by [Goddard et al. \(2017\)](#), (orange line: ETGs, purple line: LTGs), the mean mass weighted stellar ages by [San Roman et al. \(2018\)](#), (black stars: ETGs) and [González Delgado et al. \(2015\)](#), (gray dots, ETGs). The profiles for our galaxies are relatively flat. However, for spheroids (red circles) in the inner parts, the stars are slightly younger. The disks (blue diamonds) are younger than the spheroids at all radii.

populations have similar b -values. Still, this shows that it is not straightforward which radius to choose for the evaluation of the b -value. For the following studies, we will use $3R_{1/2}$, where not specified otherwise.

In order to better understand the distribution of the different populations within the galaxy, in Fig. 5.2.9 we show the mass weighted mean stellar age of the whole stellar population at all radii. We add observational data by [Goddard et al. \(2017\)](#), (orange line: ETGs, purple line: LTGs), [San Roman et al. \(2018\)](#), (black stars: ETGs) and [González Delgado et al. \(2015\)](#), (gray dots, ETGs). For the comparison with [Goddard et al. \(2017\)](#), we chose their stellar mass bin of $9.935 < \log_{10}/M_{\odot} < 10.552$, as most of our galaxies lie in this mass range. In general, the radial profiles of our galaxies are relatively flat, independent of galaxy type. However, the spheroidal galaxies (red circles) have slightly positive age gradients, which is also seen by [Goddard et al. \(2017\)](#) and [San Roman et al. \(2018\)](#); this indicates an “outside-in” formation, where the star formation has ceased in the outer region, while it continues in the galaxy center ([Bedregal et al., 2011](#)). In contrast to that, the disk galaxies (blue diamonds) have negative age gradients in the inner parts ($r < 2R_{1/2}$), which agrees

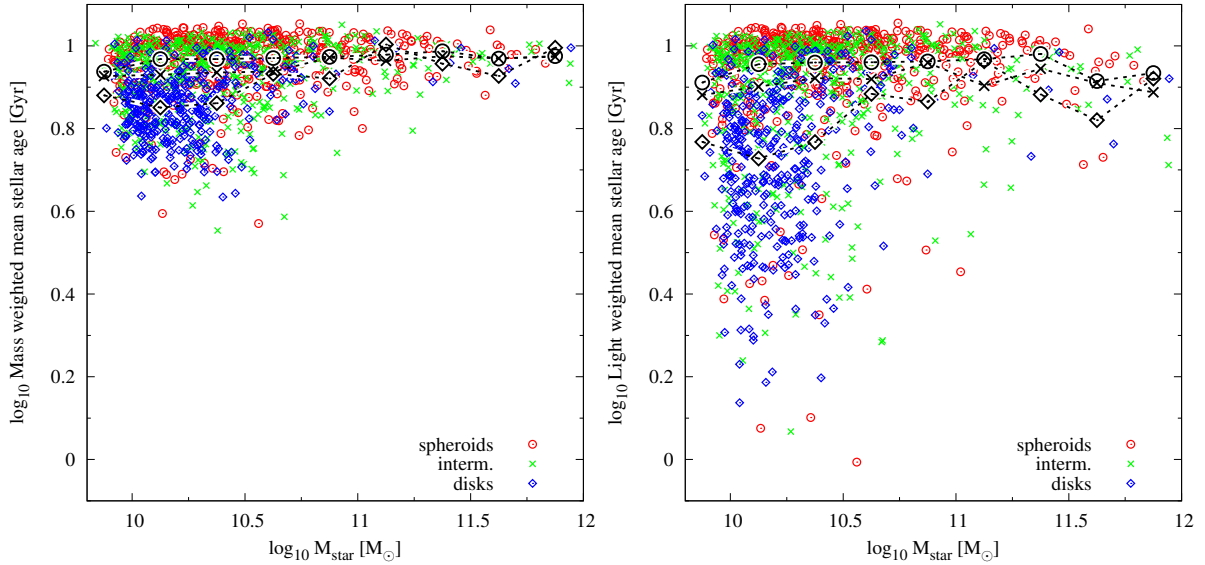


Figure 5.2.10: *Left:* The stellar mass within $3R_{1/2}$ against the mass weighted mean stellar age for individual galaxies. There is a general trend that with higher stellar masses the galaxies are older. On average (black symbols), disks (diamonds) tend to be younger than spheroidal galaxies (circles). *Right:* The same as left but using the light weighted mean stellar age. The general trend is more visible than in the mass weighted case.

with the observations by [Goddard et al. \(2017\)](#). This behavior implies the “inside-out” formation of disks, where the stars in the central region have formed at an earlier epoch, while the galaxies continue to accrete gas from which new stars form. In agreement with the observations by [Goddard et al. \(2017\)](#), the spheroidal galaxies are older than the disk galaxies at all radii. We also note an offset of the curves among the observations, which is based on various factors; on the one hand, the observations use different models to calculate the ages of the stellar populations. As shown by [San Roman et al. \(2018\)](#) this does not change the global trend but shifts the values. [Goddard et al. \(2017\)](#) and [San Roman et al. \(2018\)](#) used the same model. The model used by [González Delgado et al. \(2015\)](#) yields lower stellar ages (see Figs. 14 and 15 in [San Roman et al., 2018](#)).

The total stellar mass of a galaxy is, together with the angular momentum, one of the most important quantities of a galaxy (e.g. [Obreschko and Glazebrook, 2014](#); [Romanowsky and Fall, 2012](#)). Therefore, we study the relation between the total stellar mass, the age and the morphology of the galaxies. The left panel of Fig. 5.2.10 shows the mass weighted mean stellar age as a function of the total stellar mass. At lower stellar masses we see a split-up between the different galaxy types; at fixed mass, the spheroids (red circles), on average (black symbols), are older than the disks (blue diamonds) with a significant overlap (see also [González Delgado et al., 2015](#)). The relation for the spheroidal galaxies is rather flat. [González Delgado et al. \(2015\)](#) noted a flat relation for the early-type spirals (Sa), S0 and ellipticals, and conclude from this that not only mass but also the morphology is an important factor for the star formation history. In agreement with observational studies

by e.g. McDermid et al. (2015); San Roman et al. (2018); van de Sande et al. (2018), we find the general trend, however weak, that the age increases with increasing mass. This is referred to as “downsizing” (Cowie et al., 1996; Gallazzi et al., 2005) and indicates that more massive systems formed earlier.

When considering the light weighted ages (see right panel of Fig. 5.2.10), galaxies appear younger compared to the mass weighted case (see e.g. Boardman et al., 2017; Goddard et al., 2017). This is owing to the fact that young stars are, in general, brighter than old stars and thus, contribute more to the average age. In this representation, the downsizing is more easily visible.

5.3 Stellar Populations in Late-Type Galaxies

Until now, we have studied the behavior of whole populations of different galaxy types and the differences between these types. In the following, we will take a closer look at individual galaxies within the populations of different types, in order to see if they behave equally or can be further subdivided into different types. This can give important hints to different formation channels that still lead to the same morphological type.

First, focusing on LTGs, we analyze individual *poster child* disk galaxies. We have checked the velocity maps for all disk galaxies. Similar to the example disk galaxy in Fig. 5.2.2, we find that the old stellar halos of most disks rotate.

We now test if the mass fractions of the different populations among the disks are a determining quantity for being a disk galaxy. The left panel of Fig. 5.3.1 shows the mass fractions of old (orange), middle-aged (turquoise) and young (purple) stars for individual disk galaxies. Interestingly, there is a large variation in the mass fractions. For example, we find one disk that has a completely negligible amount of young stars (Halo 103), whereas another one has almost 30% young stars (Halo 298). Our poster child disk galaxies with a dominating old component, in general, must have evolved undisturbed so that their high angular momentum is preserved and their disk remains intact.

In the right panel of Fig. 5.3.1 we show the different mass fractions in dependence of the b -value of the young component. The galaxies have one data point each for the young (purple), middle-aged (turquoise) and old (orange) stellar component. There might be a slight trend that galaxies with b -values of the young component which are higher than -4.5 have old star fractions higher than 50%. However, this is statistically not significant, as we have only a few poster child disks. In the future, this aspect should be probed with a larger sample.

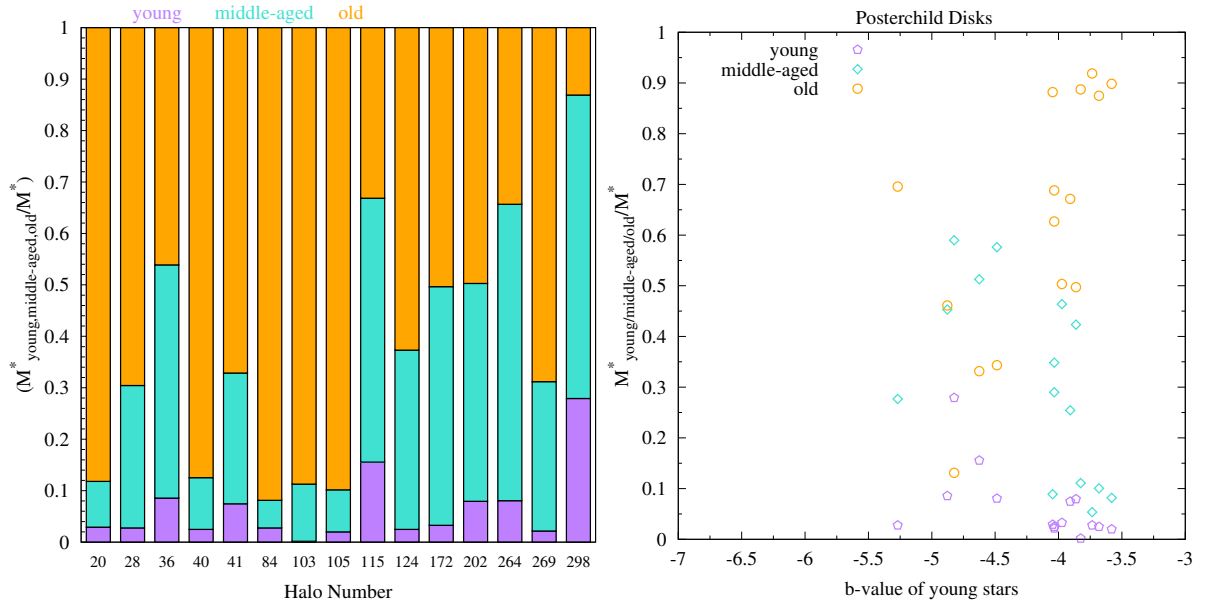


Figure 5.3.1: *Left:* Mass fractions of the stellar populations for individual poster child disk galaxies within $5R_{1/2}$. *Right:* The b -value of the young stellar population against the average mass fraction of the stellar populations for poster child disk galaxies. Note that every galaxy has three data points. There is no correlation between the rotation of the young stars and the different mass fractions.

5.4 Stellar Populations in Early-Type Galaxies

In the following section we will focus on ETGs and check if different types of ETGs behave differently. This might give us important information about possible different formation histories of ETGs. We use two different ways to divide the ETGs, as discussed in Sec. 5.1.1. First we subdivide them into slow and fast rotators and second, we divide them into kinematical groups.

5.4.1 ETGs Divided into Slow and Fast Rotators

As described in Sec. 5.1.1 we first divide the ETGs into slow and fast rotators, where the so-called λ_R -parameter, and the morphological ellipticity parameter ϵ are used as classification criteria. Fig. 5.4.1 shows the distributions of the b -value of the different stellar populations separately for slow (left) and fast rotators (right). The distributions of all populations in slow rotators are relatively broad, especially that of the young component, and show a large overlap. However, there is a slight trend for old stars to have lower b -values than middle-aged stars, and the young stars are mainly found at b -values higher than -5. The fast rotators have narrower distributions and sharper peaks, tending to slightly higher b -values compared to slow rotators. This is what we expect, as Schulze et al. (2018) have

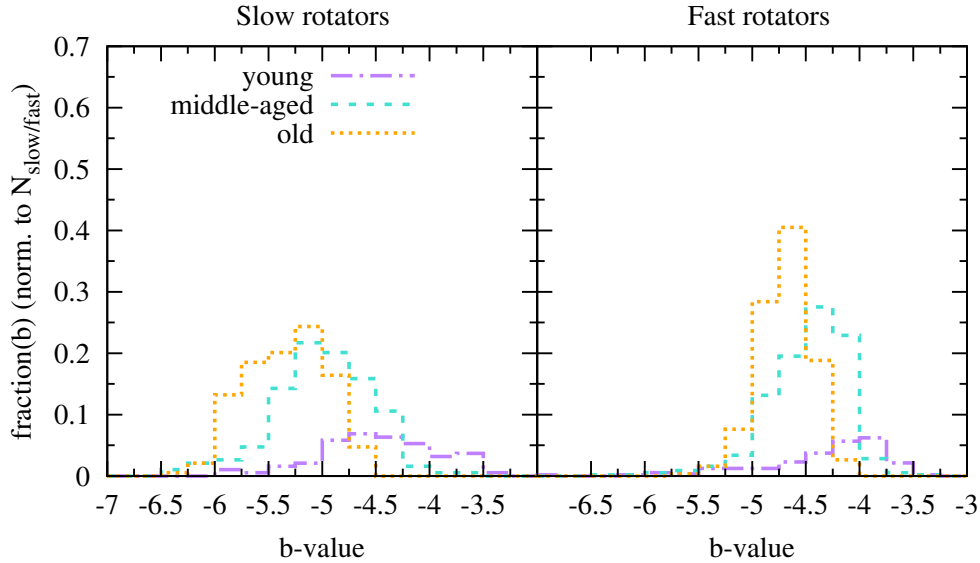


Figure 5.4.1: Shown are the b -value distributions of young stars (purple), middle-aged stars (turquoise), and the old stellar population (orange), for slow rotators (left panel) and fast rotators (right panel). In general, the distributions of the different stellar populations of the fast rotators are narrower and peak at higher b -values than those of the slow rotators.

demonstrated that the b -value is strongly correlated to the position of the galaxy on the λ_R - ϵ -plane, i.e. to the type of ETG in terms of slow and fast rotator.

In Fig. 5.4.2 we check the mass contributions of the different stellar populations. Interestingly, there is no big difference between the two types of rotators. Both have less than one percent mass in young stars. A small difference lies in the mass fraction of middle-aged stars, of which fast rotators have slightly more than slow rotators. Accordingly, fast rotators have slightly fewer old stars than the slow rotators. This is in line with our conclusions from Figs. 5.2.5 and 5.2.8, especially for the spheroids, the old stars account for the major part of the stellar mass.

We now directly relate the b -value of the different stellar populations to their mass fractions. In Fig. 5.4.3 the values for individual slow rotators (left) and fast rotators (right) are shown. Note that all galaxies have one data point each for young (purple), middle-aged (turquoise) and old (orange) stellar populations. The averaged mass fraction seen in Fig. 5.4.2 does not give consideration to the different possible combinations but gives the impression that the fast and slow rotators have the same age distributions.

In this section, we have found hints that the difference in the behavior of these two types of ETG is based on a difference in the contributions of the different stellar populations. We suggest that for the outcome it is important if the angular momenta of the merging objects are aligned. If the galaxy accretes satellites from different directions, the overall angular momentum decreases (see e.g. Vitvitska et al., 2002), which favors the formation of a slow rotating spheroid (see e.g. Bournaud et al., 2007; Guérou et al., 2016; Lagos et al.,

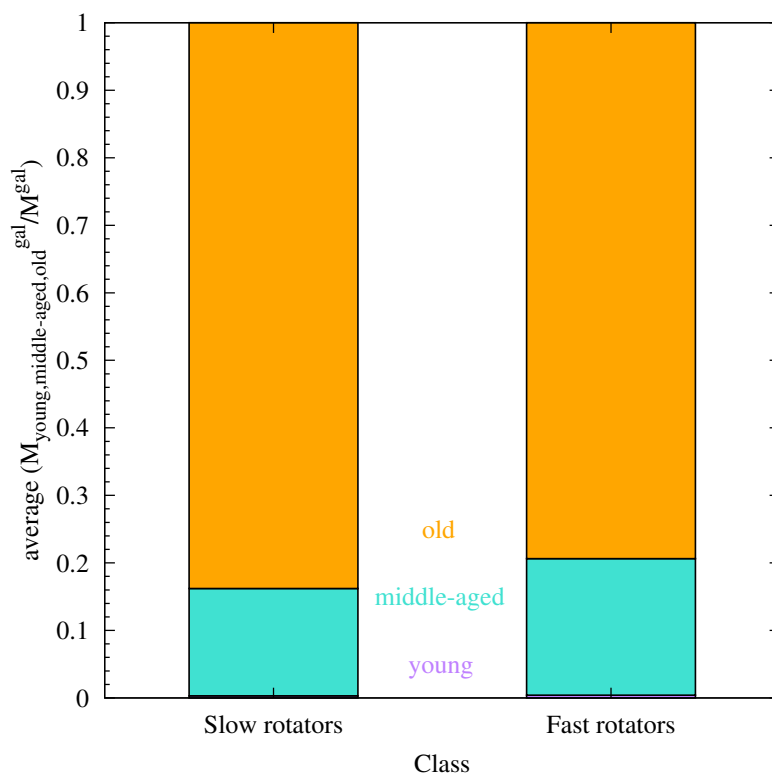


Figure 5.4.2: Average mass fraction of the stellar populations of slow and fast rotators. On average, both galaxy populations have a negligible number of young stars (purple), while the main contribution comes from the old stars (orange).

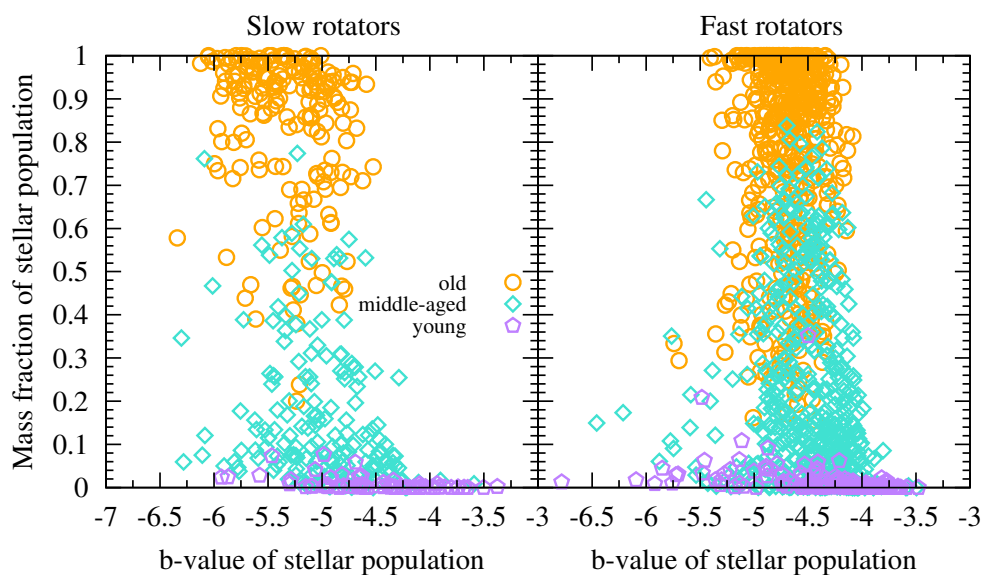


Figure 5.4.3: The mass fraction of the different populations for individual galaxies, on the left panel for slow rotators, and on the right for fast rotators. Note that every galaxy has three data points.

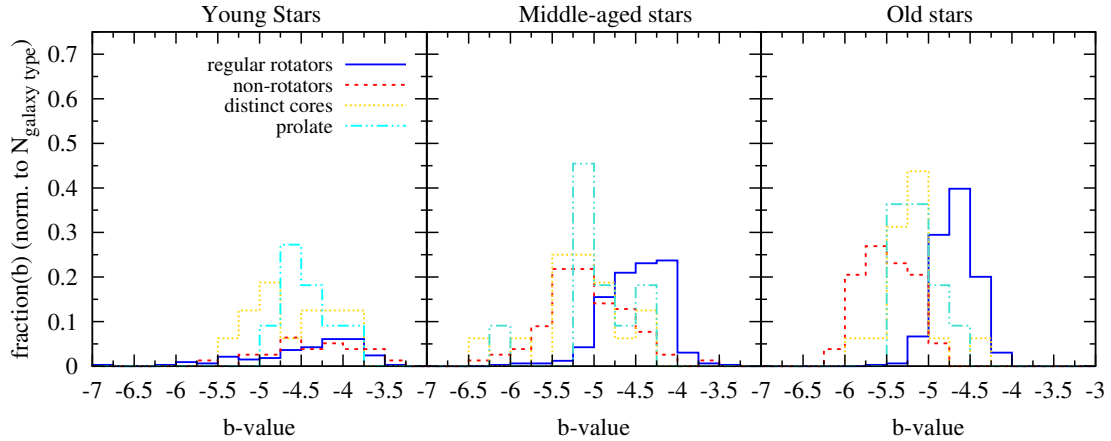


Figure 5.4.4: Shown are the b -value distributions of young stars (left), middle-aged stars (center), and the old stellar population (right), divided into regular rotators (blue), non-rotators (red), galaxies with distinct cores (gold), and prolate rotators (cyan). In the old stellar populations we clearly see a split-up between non-rotators and regular rotators. The other types of ETGs lie in between.

2017, 2018). This is complementary to the studies by Schulze et al. (2018), who found that about 30% of the slow rotators have formed due to a major merger event.

5.4.2 ETGs Divided into Kinematical Groups

Now we use a classification based on the visual inspection of the line-of-sight velocity maps to divide the ETGs into four kinematical groups, namely regular rotators, non-rotators, galaxies with distinct cores, and prolate rotators (see Sec. 5.1.1). We first check if the stellar populations behave differently in the different types of ETGs. Therefore, in Fig. 5.4.4 we present the b -value distributions of the ETGs split into young (left), middle-aged (center) and old stars (right). For regular rotators (blue solid line) and non-rotators (red dashed line) the distributions of the young stars look very similar. They are broad, comparable to those of the spheroidal galaxies (see Fig. 5.2.7), and the slow and fast rotators seen before (see Fig. 5.4.1). The distributions of the middle-aged stars look relatively similar for all types, except for the regular rotators, which are shifted to relatively high b -values, namely, b -values between -5 and -4. In the old stellar components we see a clear split-up between the regular rotators and the non-rotators, where the regular rotators have higher b -values than the non-rotators. The distributions of the remaining types lie in between, for all stellar populations.

Fig. 5.4.5 shows the same as Fig. 5.4.4 but arranged for the different kinematical groups. The distributions of the different stellar populations of the regular rotators looks very similar to those of the fast rotators (right panel of Fig. 5.4.1) and intermediate type galaxies (middle panel of Fig. 5.2.7), while those of the non-rotators are similar to those of the slow

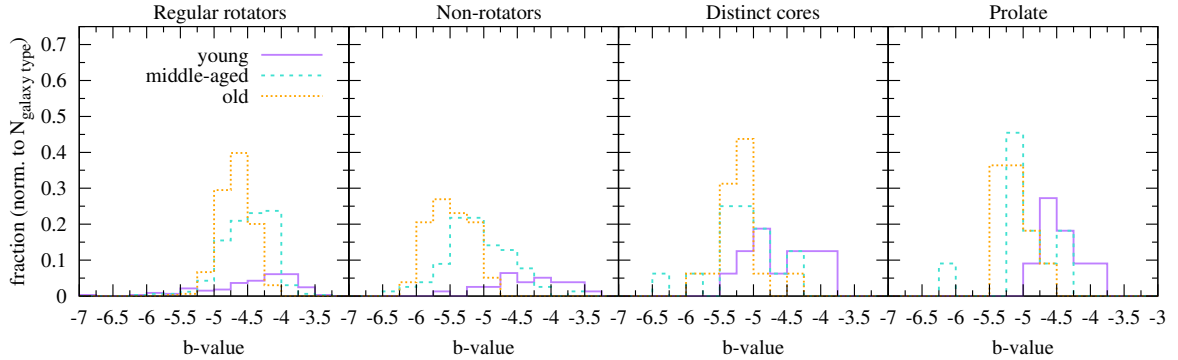


Figure 5.4.5: Shown are the b -value distributions of young stars (purple), middle-aged stars (turquoise), and the old stellar population (orange), for regular rotators, non-rotators, distinct cores, and prolate rotators (from left to right).

rotators (left panel of Fig. 5.4.1) and the poster child spheroids (left panel of Fig. 5.2.4). The different distributions of the distinct cores lie somewhere in between those of the regular rotators and those of the non-rotators. The prolate rotators have a bimodal distribution but we have to keep in mind the low number of these objects.

We now investigate if the similarities of the b -value distributions of the kinematical classes with the other classes, i.e. poster child spheroids/disks, spheroids/intermediates/disks and slow/fast rotators, are affirmed in the mass fractions of the stellar populations. In Fig. 5.4.6 we can clearly see that the distinct cores form a special class among the ETGs. They on average have 60% old stars while all other groups have more than 80%. This is similar to the poster child disks, which, however, have a larger population of young stars. The histogram of the mass fractions of the regular rotators looks identical to that of the fast rotators, as expected. The non-rotators, on average, are older than the regular rotators, which is in agreement with McDermid et al. (2015). Having on average more than 90% old stars and no young stars, they again are reminiscent of the poster child spheroidal galaxies. Apart from the not completely negligible number of young stars, the prolate rotators have similar mass fractions compared to the non-rotators.

We conclude for the ETGs, in general, it makes a difference how we subdivide them. If we group them into slow and fast rotators, they have comparable mass fractions but show differences in the behavior of the b -value. This confirms the findings by Schulze et al. (2018) that the b -value correlates with the $\lambda_R - \epsilon$ -plane. When dividing the ETGs on the basis of the kinematical features we find that the regular rotators show a similar behavior to the fast rotators, in the mass fractions as well as in their b -value distributions. On the other hand, non-rotators in both quantities mimic the poster child spheroidal galaxies. The most interesting group are the galaxies with distinct cores, as they kinematically lie between the regular rotators and the non-rotators but have similar mass fractions compared to the poster child disk galaxies.

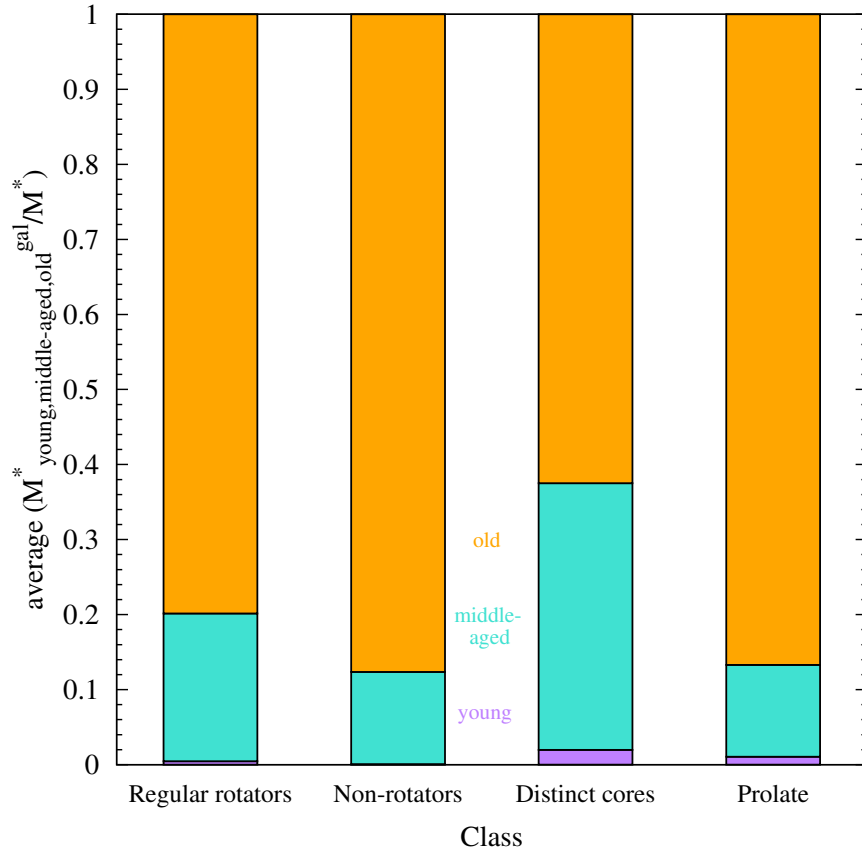


Figure 5.4.6: Average mass fraction of the stellar populations of different kinematic types of ETGs. On average, almost all galaxy populations have a negligible number of young stars (purple) and mass fractions of middle-aged stars (turquoise) below 20 percent. Only the distinct cores have a relatively high fraction of middle-aged stars.

Two Populations of Galaxies with Distinct Cores?

Since the galaxies with distinct cores show a special behavior compared to the other kinematical types of ETGs, we will study them in more detail. In the previous section we have seen that the average mass fractions of the distinct core galaxies look very similar to those of the poster child disk population. In order to see how well these average mass fractions represent the individual distinct core galaxies, in Fig. 5.4.7 we present the mass fractions for each distinct core galaxy. As seen for the poster child disk galaxies (see Fig. 5.3.1), there is a large variation in the mass contributions of the different stellar populations. We find that about half of the distinct core galaxies have less than 50% old stars, while the other half of the galaxies have more than 60%. An interesting aspect here is that this does not depend on the fraction of young stars.

We do not show this here but we have also checked the relation between the b -value of the young stars and the different mass fractions. As seen in Fig. 5.3.1 for the poster child disks,

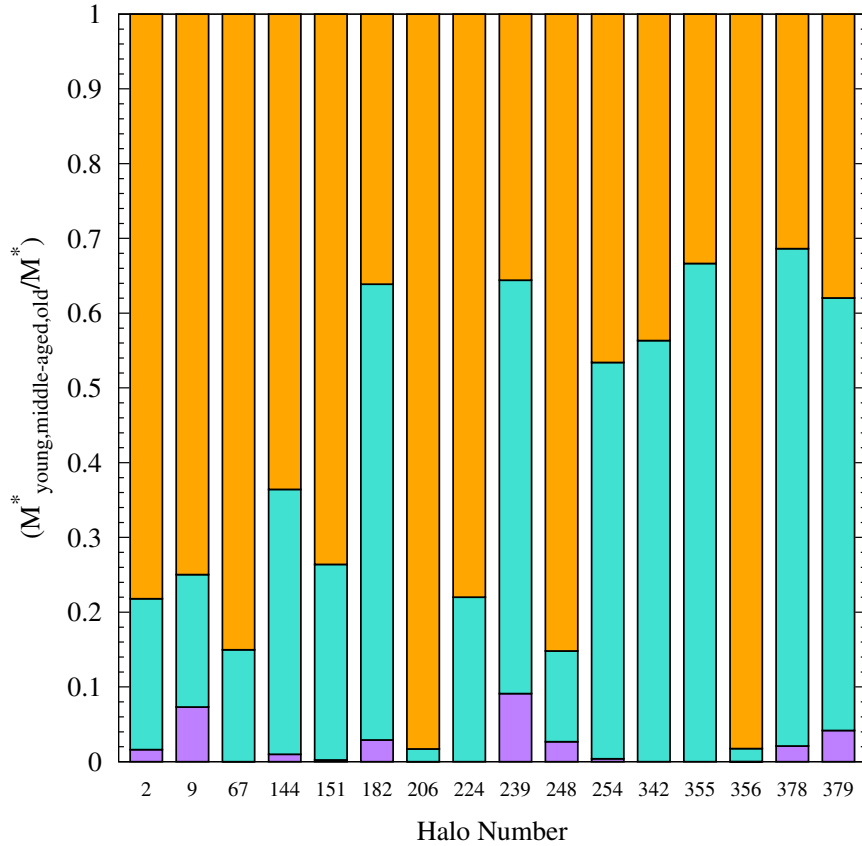


Figure 5.4.7: Mass fractions of young (purple), middle-aged (turquoise) and old stars (orange) for individual galaxies with distinct cores.

the young component does not seem to play a role, i.e. there is no correlation between the b -value of the young stars and any of the different mass fractions of the stellar populations.

In the following we want to investigate the possible connection between the mass fraction of the old stellar component and the core of the galaxy. For this, we inspected the velocity maps (which are not shown here). If a galaxy has many old stars, it tends to have a core in the old component. On the other hand, if there are relatively few old stars, there is no core in the old component but only in the middle-aged component. This is in agreement with observations by [McDermid et al. \(2006\)](#), who propose two different types of distinct cores, which implies that they assembled via different formation channels; one population of distinct core galaxies hosts a core consisting of old stars and has most likely formed by the accretion of old stellar systems or merging at earlier epochs. The other type of distinct core galaxies host a more compact core, which consists of younger stars. However, we note that due to the limited resolution, our young cores are more extended than the observed ones. Merger simulations by [Hoffman et al. \(2010\)](#) and [Schulze et al. \(2017\)](#) showed that these young cores can be the result of a recent major merger with a large amount of gas.

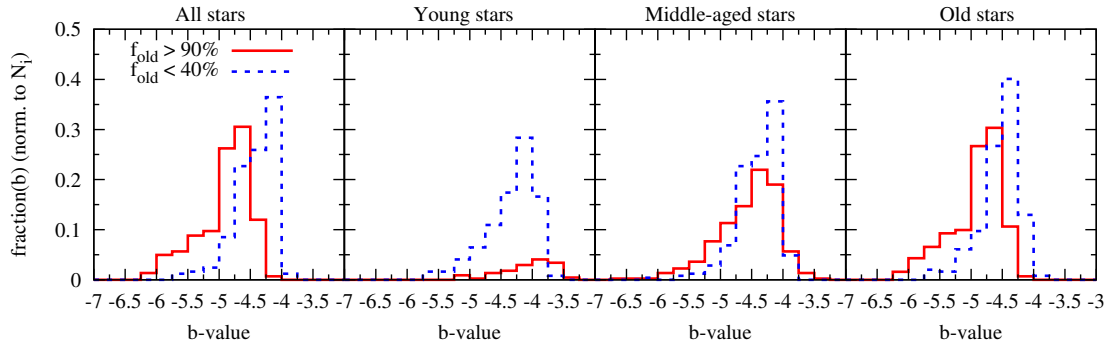


Figure 5.5.1: The b -value distributions of the different components, divided into galaxies with more than 90% old stars (red solid line) and galaxies with less than 40% old stars (blue dashed line). The young (second left) and old (right) stellar populations show a similar behavior to those of the disks and spheroidal galaxies (recall Fig. 5.2.6). The small split-up seen in the old component is reflected in the distribution for the whole stellar population (left).

5.5 Dependence of the Mass of the Old Component on Galaxy Type

In the previous sections we have encountered several times a possible connection between the mass fraction of the old stellar population and the (kinematical) type of the galaxy. In this section we will focus on this aspect.

First, in order to see if there is a general trend, we study the old stellar mass fractions in the whole sample of central galaxies, where we made two groups: One with a fraction of old stars of more than 90%, where we find 442 galaxies, and another with less than 40%, where we end up with 247 galaxies; the remaining galaxies are neglected here. Fig. 5.5.1 shows the b -value distributions of all stars, young, middle-aged and old stars (from left to right) for these two different “types” of galaxies. They look similar to the distributions of the spheroids and disks (see Fig. 5.2.7), where those galaxies with many old stars behave like the spheroids in the young component and have low b -values in the old populations. Those galaxies with few old stars look similar to the disks, i.e. they have similar b -values in all components. Interestingly, in the middle-aged component both types are very similar and we note that, in contrast to the spheroids and disks, which do not overlap in their old component (more or less by construction due to the selection to the overall b -value), they have an overlap in the distributions of the old stellar populations. The galaxies consisting mainly of old stars could experience more mergers, so the orbital configurations of the stellar component is dominated by random motion and thus leads to a low angular momentum. The younger galaxies, on the other hand, most probably had fewer mergers and thus, could evolve relatively undisturbed.

We now want to analyze the different galaxy types divided into these two groups and if we can confirm the previously found similarities between some of the types. Figures 5.5.2 -

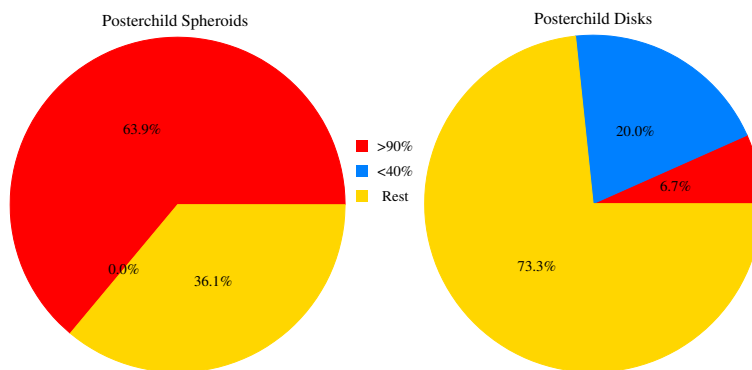


Figure 5.5.2: The fraction of poster child spheroids (left) and disks (right) that have more than 90% old stars (red), less than 40% old stars (blue) and the remaining galaxies (yellow).

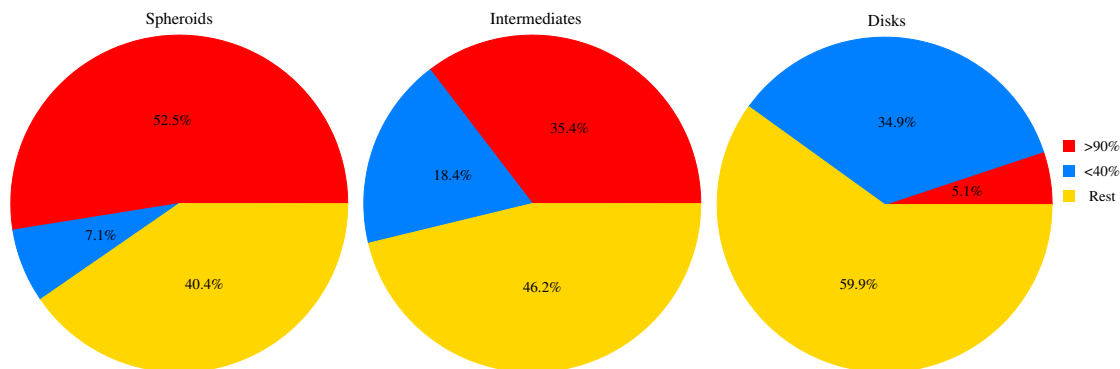


Figure 5.5.3: The fraction of spheroids (left), intermediates (center) and disks (right), classified according to the b -value, that have more than 90% old stars (red), less than 40% old stars (blue) and the remaining galaxies (yellow).

5.5.5 show the pie charts of the different galaxy types divided into galaxies with more than 90% (red) and less than 40% (blue) old stars in mass, those galaxies that have fractions in between are labeled as “rest” (yellow).

Fig. 5.5.2 shows the result for the poster child spheroids (left) and disks (right). Roughly 2/3 of the poster child spheroids have old star fractions above 90% and none of the 61 poster child spheroids have old star fractions of less than 40%. This is what we expect for poster child spheroidal galaxies. Interestingly, about 3/4 of the poster child disks have fractions between 40% and 90%, while only 1/5 have low old star fractions.

The spheroids and disks that are classified according to their b -value (Fig. 5.5.3) show a similar behavior compared to the poster child galaxies (Fig. 5.5.2). However, the spheroid population has a very small fraction of galaxies that have few old stars, while disk galaxies have a small fraction of galaxies with many old stars, i.e. only 5% of the disks are old. As we have seen in the b -value distributions (Fig. 5.2.7) and the average mass fractions (Fig. 5.2.8), the intermediates again lie in between the spheroids and disks.

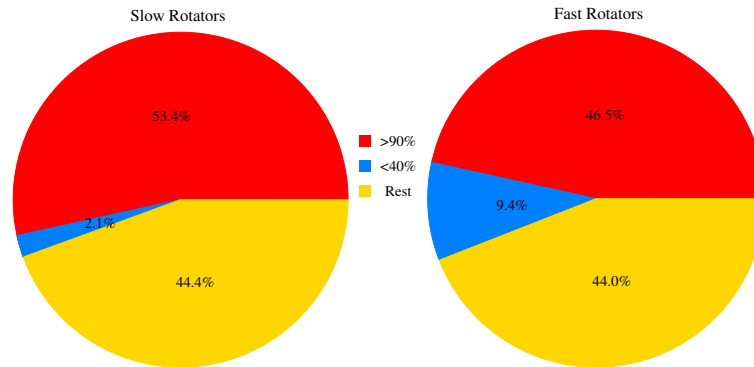


Figure 5.5.4: The fraction of slow rotators (left) and fast rotators (right) that have more than 90% old stars (red), less than 40% old stars (blue) and the remaining galaxies (yellow).

In the subclassification of ETGs in slow and fast rotators (Fig. 5.5.4) we find that the population of slow rotators divides in a similar way compared to the spheroids (left pie chart of Fig. 5.5.3), whereas the behavior of the fast rotators is similar to that of the intermediate galaxies (middle pie chart of Fig. 5.5.3).

The four kinematical groups of ETGs divide differently into the two mass fraction classes, see Fig. 5.5.5. The regular rotators show a bimodal distribution. The majority of the non-rotators has many old stars and only one out of 78 has less than 40% old stars. Around 1/3 of the distinct core galaxies have old star fractions of less than 40%. Again, their behavior is completely different from that of the other types of ETGs, especially regarding their low fraction of galaxies that mainly consist of old stars. Their population splits up similarly to the disk and poster child disk galaxies. A possible explanation for this special behavior could be due to gas rich mergers with retrograde orbital configurations. The gas can form new stars, while the overall stellar angular momentum is lowered. Around 2/3 of the prolate rotators have old star fractions between 40 and 90%, while 1/3 have more than 90% old stars. The fact that there are no prolate rotators with many young stars, favors a formation scenario involving dry mergers, since a gas rich merger probably would

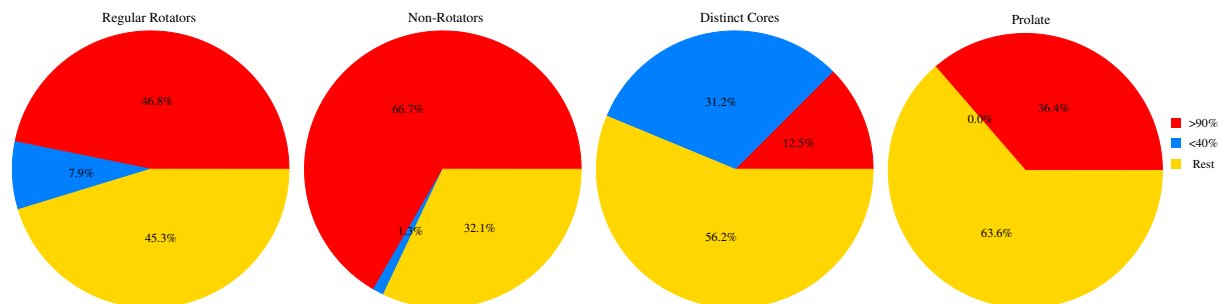


Figure 5.5.5: The fraction of regular rotators, non-rotators, galaxies with distinct cores and prolate rotators (from left to right) that have more than 90% old stars (red), less than 40% old stars (blue) and the remaining galaxies (yellow).

lead to the formation of a newly formed dynamically cold component (see also discussion in [Schulze et al., 2018](#)).

5.6 Discussion and Conclusions

We use galaxies extracted from the high resolution cosmological simulation suite Magneticum to investigate the relation between the kinematical properties of different stellar populations and the morphology of galaxies. We select all galaxies with stellar masses above $10^{10}M_{\odot}$ and use different classification methods. For the classification into poster child disks and poster child spheroids we use the circularity parameter ε , while the so-called b -value (see [Teklu et al., 2015](#)) is used as indicator of the more general morphological types spheroids, intermediates and disks. We find that:

- The old stars in disk galaxies show a high rotation, while those in spheroidal galaxies rotate slower.
- In disk galaxies, all stellar components have similar b -values, which indicates that they have evolved relatively undisturbed. For the spheroidal galaxies, on the other hand, the distributions are different from each other, which suggests that the stellar components have different origins.
- On average, the disk galaxies have a higher fraction of young stars than the spheroidal galaxies (see also e.g. [van de Sande et al., 2018](#)), but within the population of disks the fractions can vary from 0% to 30%.
- On the other hand, the majority of spheroidal galaxies has high fractions of old stars, while most disks have old stellar fractions between 20% and 60%.
- Young stars do not play a role in defining the morphological type, as for the disk galaxies we do not find a connection between the b -value of the young stars and the mass fractions.
- Of importance are the old stars, which dominate the overall rotation, since they make up the majority of the whole stellar population.
- The spheroidal galaxies have on average a positive age gradient, i.e. younger stars in the center, which favors an “outside-in” formation scenario. For the disk galaxies we find a slightly negative age gradient in the inner parts, which supports the “inside-out” growth of disk galaxies.

These findings are important for interpreting observations, as young stars are brighter than old stars and therefore potentially dominate the observable stellar component. Thus, it is crucial to consider the different underlying stellar populations and their associated properties when determining the morphological type of galaxies. Additionally, it has been

shown by [Emsellem et al. \(2011\)](#) that for ETGs the optical morphology is not a good tracer of their properties.

When we divide the ETGs into fast and slow rotators, we find:

- The averaged age distributions of both types look similar. However, the distributions of the b -value differ, where the old stellar component of fast rotators has higher values than that of slow rotators
- The distribution for the different stellar populations of the slow rotators suggests multiple minor mergers as another possible formation channel, besides the formation via major mergers ([Schulze et al., 2018](#)).

When further subdividing the ETGs according to their kinematical features, namely non-rotators, regular rotators, galaxies with distinct cores and prolate rotators, we find:

- The different components of the non-rotators behave like those of the spheroidal galaxies, while the regular rotators more mimic the behavior of the intermediate type galaxies.
- The galaxies with distinct cores represent a special class of ETGs, as they on average have more young and middle-aged stars than the other subclasses of ETGs.
- When dividing the galaxies into galaxy populations with many ($>90\%$) and few ($<40\%$) old stars, the distinct core galaxies split up in a similar way to the (poster child) disks. Kinematically, i.e. in their b -value distributions, the distinct core galaxies behave similarly to the spheroidal galaxies. This supports a formation scenario that involves a gas rich merger with retrograde orbital configurations.
- In the velocity maps of the distinct core galaxies we see that with increasing mass fraction of old stars the galaxy more likely has a core in the old component.

The above results, drawn from the properties of the different stellar populations, confirm the findings from previous studies, particularly from IFUs, that especially ETGs can be formed via various formation channels.

Chapter 6

Declining Rotation Curves at $z = 2$ in Λ CDM Galaxy Formation Simulations

This chapter has been published in [Teklu et al. \(2018\)](#)

Abstract

Selecting disk galaxies from the cosmological, hydrodynamical simulation *Magneticum Pathfinder* we show that almost half of our poster child disk galaxies at $z = 2$ show significantly declining rotation curves and low dark matter fractions, very similar to recently reported observations. These galaxies do not show any anomalous behavior, reside in standard dark matter halos and typically grow significantly in mass until $z = 0$, where they span all morphological classes, including disk galaxies matching present day rotation curves and observed dark matter fractions. Our findings demonstrate that declining rotation curves and low dark matter fractions in rotation dominated galaxies at $z = 2$ appear naturally within the Λ CDM paradigm and reflect the complex baryonic physics, which plays a role at the peak epoch of star formation. In addition, we find some dispersion dominated galaxies at $z = 2$ which host a significant gas disk and exhibit similar shaped rotation curves as the disk galaxy population, rendering it difficult to differentiate between these two populations with currently available observation techniques.

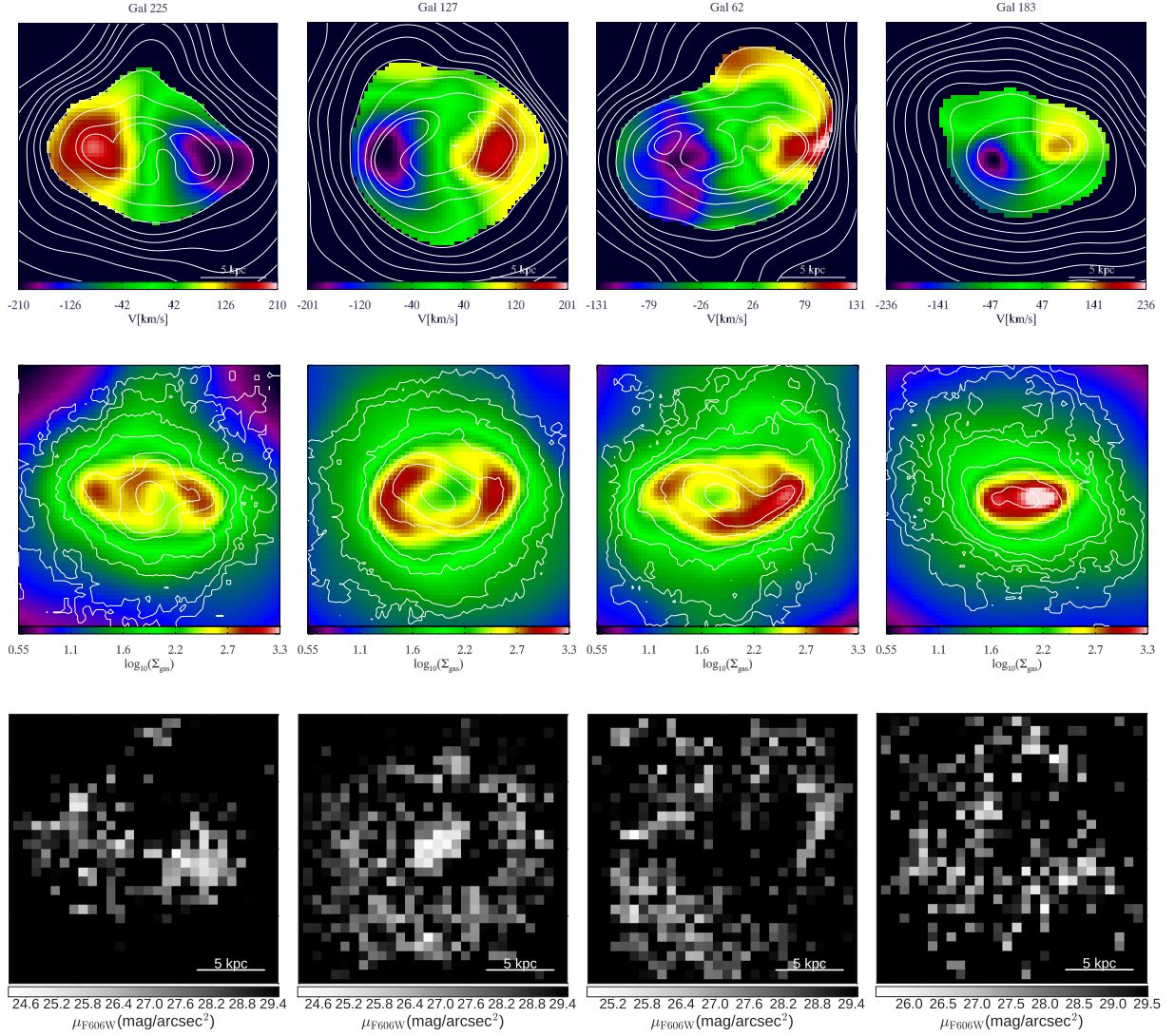


Figure 6.1.1: Example galaxies from the $z = 2$ sample with declining rotation curves (see Fig. 6.2.1), from left to right the three disk galaxies *gal 225*, *gal 127*, and *gal 62*, and the gas-rich spheroidal system *gal 183*, rotated to inclinations (e.g. $i = 60$, $i = 45$, $i = 25$ and $i = 75$, respectively) similar to those of the galaxies presented in Genzel et al. (2017). *Upper row:* Velocity maps of the cold gas component for each galaxy, with contours of the cold gas column density overlaid. *Middle row:* Cold gas column density maps with overlaid stellar column density contours. *Lower row:* Simulated HST broadband F606W images using *GRASIL-3D*.

6.1 Sample of Galaxies

To ensure proper resolution of the inner structure, we only select halos with virial masses above $5 \cdot 10^{11} M_{\odot}$ hosting galaxies with stellar masses above $5 \cdot 10^{10} M_{\odot}$ for this study. These mass ranges are consistent with the observed properties of the high- z galaxy sample of [Genzel et al. \(2017\)](#). This leads to a sample of 212 and 275 halos at $z = 2$ and $z = 0$, respectively. Furthermore, we classify the galaxies based on the distribution of the circularity parameter $\varepsilon = j_z/r\sqrt{GM(r)}/r$ of the stars within the galaxies, where j_z is the z -component of the stars' specific angular momentum (see also [Abadi et al., 2003](#); [Scannapieco et al., 2008](#)). Thus, dispersion-dominated systems represent observed early-type galaxies and are characterized by a broad peak in the distribution at $\varepsilon \simeq 0$, while rotation-supported systems have properties that are characteristic of late-type galaxies and show a broad peak at $\varepsilon \simeq 1$. We define poster child disk galaxies as systems which, in addition to a characteristic peak at $\varepsilon \simeq 1$, have a significant cold gas fraction ($f_{cold} > 0.5$ at $z = 2$ and $f_{cold} > 0.2$ at $z = 0$) with respect to their stellar mass, to distinguish them from transition type systems or ongoing merger events (for details see [Teklu et al., 2015](#)). For our simulations it has been shown that, following this classification scheme, galaxies of these two populations reproduce accordingly the observed stellar-mass–angular-momentum relation ([Teklu et al., 2015](#)) and its evolution ([Teklu et al., 2016](#)), the mass-size relation and its evolution ([Remus et al., 2017b](#)), as well as the fundamental plane distributions ([Remus and Dolag, 2016](#)).

We then rotate the galaxies such that the minor axis of the gas¹ is aligned with the z -axis, so that we can extract the rotation curve without any further modifications.

From the total of 212 (275) galaxies at $z = 2$ ($z = 0$) we classify 26 (15) as poster child disks, which we consider for further analysis. In addition, among our 27 poster child spheroidal galaxies at $z = 2$ we find 5 systems with a large cold gas fraction ($f_{cold} > 0.5$).

[Fig. 6.1.1](#) shows a 20 kpc region for 4 gas-rich example galaxies at $z = 2$, where the upper row displays the line-of-sight velocity maps of the cold gas component, restricted to regions with $\Sigma_{\text{gas}} > 50 \frac{M_{\odot}}{\text{pc}^2}$, with overlaid cold gas column density contours. The gridded data was created using SPHMapper ([Röttgers and Arth, 2018](#)). The middle row shows the cold gas column density maps with overlaid stellar surface density contours. Inclinations and colors were chosen according to the observations presented in [Genzel et al. \(2017\)](#). Each column represents one galaxy, where *gal 225*, *gal 127*, and *gal 62* (from left to right) resemble disk galaxies, while *gal 183* is a gas-rich spheroidal galaxy. Interestingly, all galaxies, even the spheroidal one, show a similar, regular rotation pattern for the cold gas component. This is due to the fact that the gas is in a flattened, centrifugally supported disk, even in the systems where the stars form a spheroid.

The lower panels show mock images of the four galaxies in the HST broadband F606W

¹Note that this is different from the computation for the classification, where the galaxies are rotated into the frame where the angular momentum vector of the stars is aligned with the z -axis.

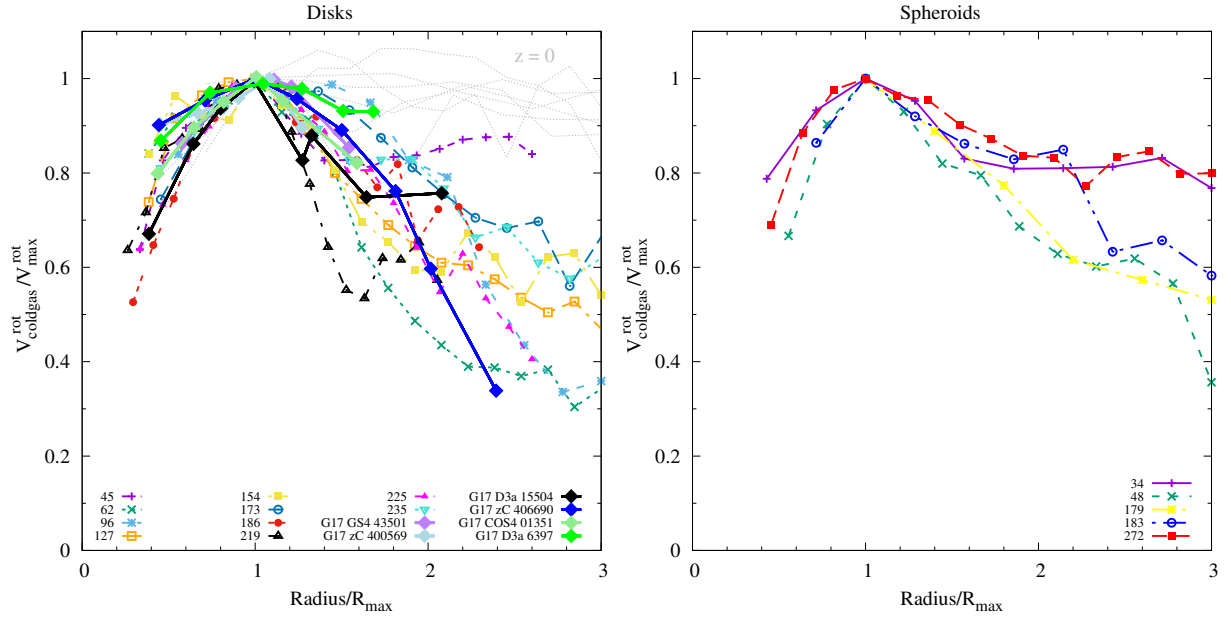


Figure 6.2.1: Rotation curves obtained from the cold gas for 10 out of the 26 poster child disk galaxies which show clearly declining rotation curves (left panel) and for the 5 gas-rich spheroidal galaxies (right panel) at $z = 2$, normalized by $V_{\text{rot_coldgas}}^{\text{rot}}$ at the radius of maximum velocity R_{max} . The thick colored lines in the left panel show the 6 declining rotation curves presented in Genzel et al. (2017), while the gray lines show 7 poster child disk galaxies at $z = 0$, using $\approx 1.4 \cdot R_{1/2}$ as R_{max} .

(4750A-7000A), which corresponds to rest-frame mid-UV. The images have been generated with the radiative transfer code *GRASIL-3D* (Domínguez-Tenreiro et al., 2014). This wavelength range traces the regions of very recent star formation, and the spheroidal galaxy shows a very similar mock image as the disks, hiding the real stellar morphology.

6.2 Rotation Curves at $z = 2$

The rotation curves for our galaxy sample are directly obtained from the averaged velocities (i.e. the circular velocities) of the individual cold gas particles. In order to ensure that only gas within the disk contributes to the rotation curve, only particles within the z -range of $\pm 3\text{kpc}$ are used. While the $z = 0$ disk galaxies show normal rotation curves, 12 out of the 26 poster child disk galaxies at $z = 2$ show a significantly declining rotation profile for their gas disk. However, we further remove 2 of the 12 examples from our detailed analysis, as they show remnants of recent merger activity.

The left panel of Fig. 6.2.1 shows the rotation curves for these 10 poster child disk galaxies at $z = 2$, which exhibit a decline in the rotation curve similar to the observed high- z disk galaxies presented in Genzel et al. (2017) (thick solid lines). Following the observations, we

scaled the individual rotation curves by R_{\max} and V_{\max}^{rot} , where R_{\max} is the radius at which the rotational velocity ($V_{\text{coldgas}}^{\text{rot}}$) has its maximum. We only plot radii larger than two times the gravitational softening of the gas particles, which corresponds to $\simeq 1.33\text{kpc}$ at $z = 2$. As can clearly be seen, the simulated galaxies show the same behavior as the observed ones, with some having an even steeper decline in the rotation curves as the observed galaxies. For comparison, the rotation curves of 7 disk galaxies at $z = 0$ are shown as gray lines. The difference in profile shapes between high- z and present-day galaxies is clearly visible.

Since at high redshift galaxies are in general more gas-rich, we also plot the same curves for the 5 gas-rich spheroidal galaxies from our $z = 2$ sample in the right panel of Fig. 6.2.1. As for the disks, the gas shows a clear rotational pattern (see also example in Fig. 6.1.1), and all of our gas-rich spheroidal galaxies show a declining rotation curve similar to the observed disk galaxies. The only difference here is that the gas disks in the spheroidals are much smaller than the stellar spheroidal bodies, while the sizes are similar in the disk galaxy cases (see Fig. 6.1.1).

The high redshift HST images mainly show young stars, which morphologically closely resemble the gas disks even in the spheroidals (see lower panel of Fig. 6.1.1). This indicates a potential difficulty in distinguishing disk galaxies from gas-rich spheroidals at $z = 2$ observationally. However, this uncertainty should be resolved using the next generation of telescopes which will be able to probe the old stellar component in high redshift systems as well.

6.3 DM Fractions

For spheroidal galaxies it is well known that the DM fraction within the half-mass radius is decreasing at higher redshift, which is commonly interpreted as indication for late growth by dry mergers of such systems. While this trend is qualitatively supported by cosmological simulations independent of the details in the implemented feedback models, the AGN feedback used in our simulation has been shown to produce DM fractions which quantitatively agree well with observations (see Remus et al., 2017b).

The left panel of Fig. 6.3.1 shows the DM fractions within the stellar half-mass radius $R_{1/2}$ for our full galaxy sample (gray dots) compared to observations at $z = 2$. Generally, our galaxies have a tendency for higher average DM fractions with decreasing $V_{\text{coldgas}}^{\text{rot}}$, however, nearly all fractions are well below 30%. Our disk galaxies (blue diamonds) cover the same range of small DM fractions as the observations presented in Genzel et al. (2017) (dark-blue filled circles with error bars)². Interestingly, the DM fractions of the disk systems are almost as small as those of the spheroidal systems. Furthermore, the gas-rich spheroidals cover the same range in DM fractions as the observed and simulated disk galaxies, again

²Note that especially at $z = 2$ the unavoidable differences when inferring the half-mass radius in simulations and observations could lead to noticeable differences.

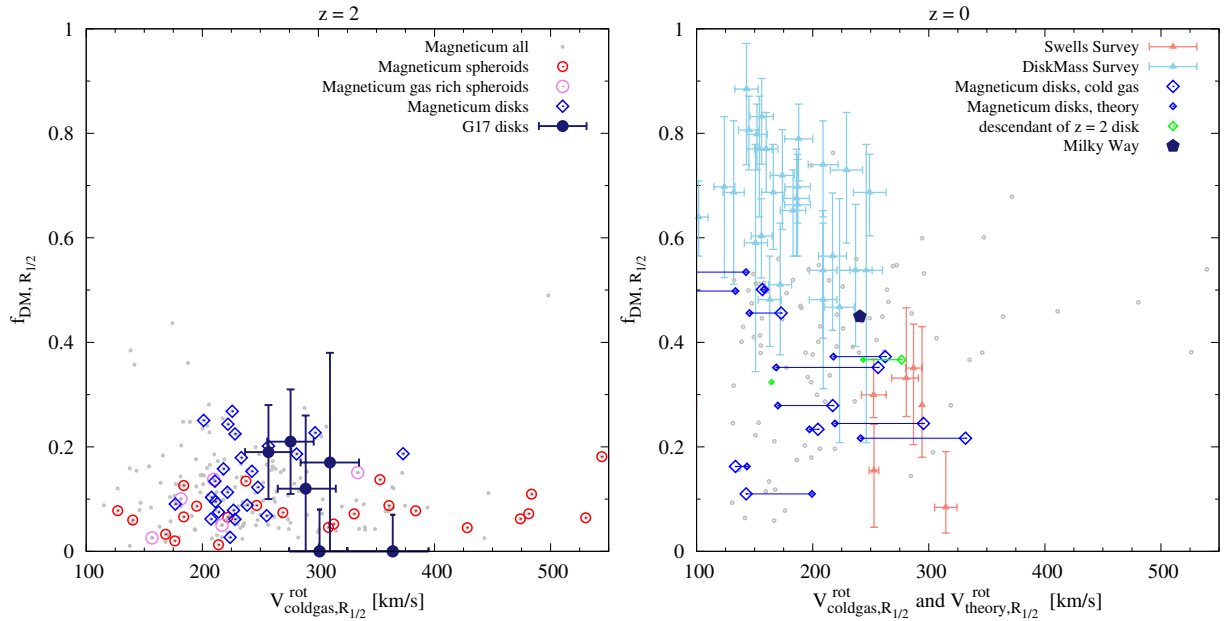


Figure 6.3.1: The DM fraction f_{DM} within the half-mass radius $R_{1/2}$ versus the rotational velocity $V_{\text{rot,coldgas}}^{\text{rot}}$ at $R_{1/2}$ at redshifts $z = 2$ (left) and $z = 0$ (right). At $z = 2$ (left panel), the simulated disks (blue diamonds) and gas-rich spheroidals (pink open circles) are shown together with the gas-poor spheroidals (red open circles). The observations from Genzel et al. (2017) are included as dark-blue points. At $z = 0$ (right panel), we only show the simulated disk galaxies, together with observations as presented in Courteau and Dutton (2015) from the Swells Survey (Barnabè et al., 2012; Dutton et al., 2013) and the DiskMass Survey (Martinsson et al., 2013). The dark-blue filled pentagon shows the Milky Way according to Bland-Hawthorn and Gerhard (2016). To indicate uncertainties involved in inferring $V_{\text{rot,coldgas},R_{1/2}}^{\text{rot}}$ we include for the simulated galaxies both the measured rotational gas velocity at $R_{1/2}$ as well as the theoretical value obtained from the total mass within $R_{1/2}$ and connect both points by lines. We explicitly highlight the data points for those descendants of our $z = 2$ disk galaxies which are still disk galaxies at $z = 0$ (green diamonds).

highlighting the similarities between the gas-rich systems at $z = 2$ independent of their morphologies and demonstrating the difficulty in distinguishing pure rotation-dominated systems from dispersion-dominated systems which host a significant gas disk.

At $z = 0$ the disk galaxies in the simulations show much larger DM fractions which decrease with rotational velocity and agree well with the different measurements for disk galaxies (see right panel of Fig. 6.3.1). To indicate uncertainties involved in inferring $V_{\text{rot,coldgas},R_{1/2}}^{\text{rot}}$ we used both, the measured rotational gas velocity at $R_{1/2}$ as well as the theoretical values obtained by adopting centrifugal equilibrium and taking the total mass within $R_{1/2}$.

6.4 Surface Density, Dispersion and Theoretical Rotation Curve

A detailed look at the four examples from Fig. 6.1.1 shows that the surface density profiles $\Sigma(r)$ of the cold gas disks in the three poster child disk galaxies and the gas-rich spheroidal galaxy follow the expected exponential decline, as shown in the upper panel of Fig. 6.4.1. While the theoretical rotation curves as obtained by the total matter distribution within these halos are flat, as expected, the real measured rotation of the cold gas disk shows a significant decline, as can be seen in the middle panel of Fig. 6.4.1. This decline is a result of the kinetic pressure effect which partly compensates the gravitational force as proposed by Burkert et al. (2010). As expected for a self-gravitating, exponential disk, the maximum of the real rotation curve for the three disk galaxies in the central part, where the baryons dominate over the dark matter halo, is slightly ($\approx 10\text{-}20\%$) above the maximum value for a spherically averaged mass distribution (Binney and Tremaine, 2008). Furthermore, at large distances the real rotational velocity is conspiratorially close to the expected rotational velocity if considering only the cold gas mass. For the gas-rich spheroidal galaxy *gal 183*, the latter holds even across almost all radii, due to its even lower DM fraction and the small size of the disk compared to the stellar body of the galaxy. As a result, the gaseous disk of the spheroidal galaxy *gal 183* is strongly self-gravitating, more compact and shows an even stronger decline. None of our systems with a falling rotation curve shows any significant feature or change in the radial component of the velocity dispersion measured for the cold gas disk which is related to the position at which the rotation curve declines, as shown in the σ_r profiles in the lower panel of Fig. 6.4.1.

6.5 Discussion and Conclusions

Selecting disk galaxies with M_{vir} above $5 \cdot 10^{11} M_{\odot}$ and M_* above $5 \cdot 10^{10} M_{\odot}$ from the cosmological, hydrodynamical simulation *Magneticum Pathfinder* we investigated the rotation curves of disk galaxies at $z = 2$. We find that almost half of our poster child disk galaxies (10 out of 26) show significantly declining rotation curves, very similar to the observations reported in Genzel et al. (2017). Interestingly, the peak of the rotation curve is a fairly good approximation ($\approx 10\%$ larger) of the theoretical value, based on the total mass of the galaxies.

These disk galaxies do not show any significant dynamical features except that the radial dispersion has generally significantly larger values compared to $z = 0$ disks, as expected for dynamically young systems in their assembly phase. Forbes et al. (2012) already presented a model description to explain this temporal evolution, which also quantitatively agrees well with the results of the much higher resolution hydrodynamical simulations *Eris* (Bird et al., 2013), finding ratios of $3 - 4$ between v_{rot} and σ_{gas} for galaxies at $z = 0$ and much smaller σ_{gas} for galaxies at $z = 0$. Furthermore, this is also in line with the observational

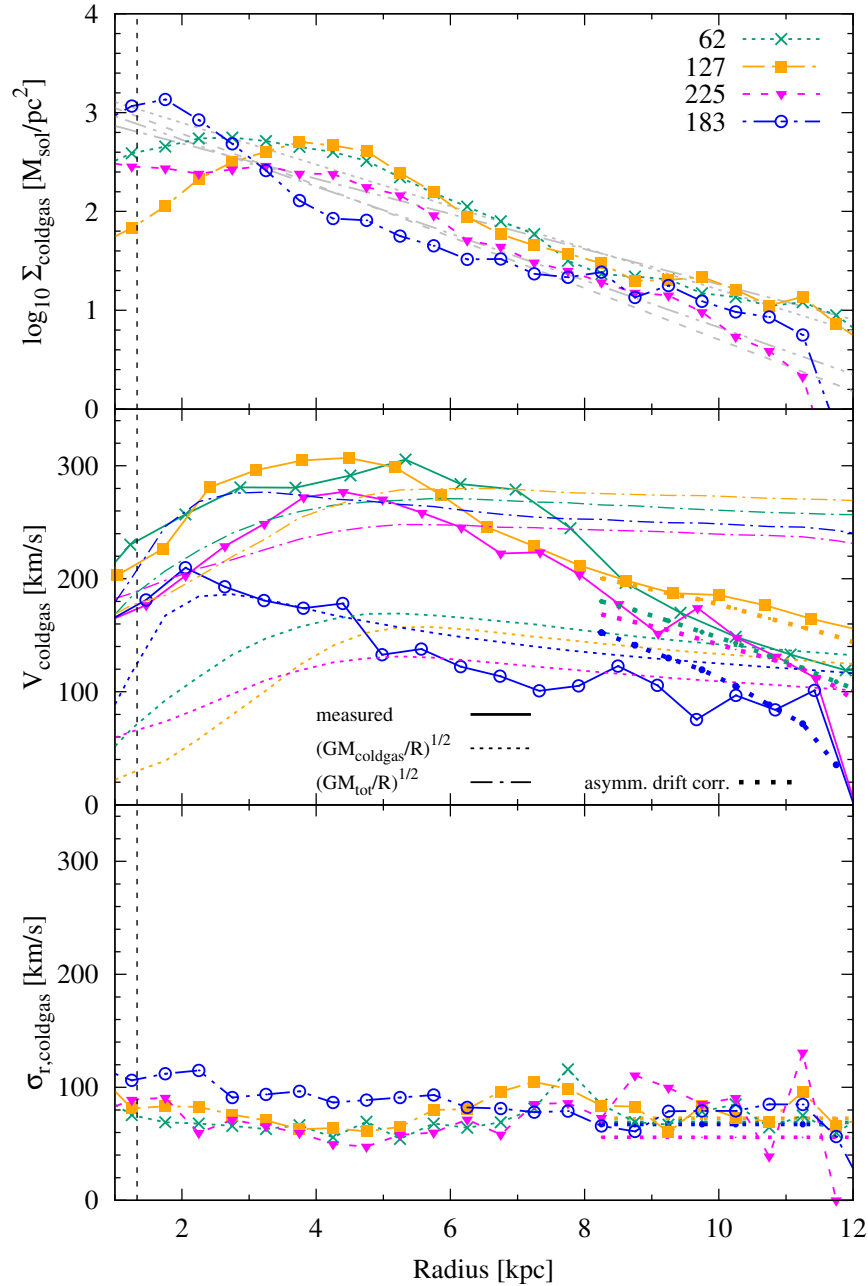


Figure 6.4.1: For the three poster child disks (*gal 62*, *gal 127*, and *gal 225*), and the gas-rich spheroidal galaxy (*gal 183*): *Upper panel:* Surface density Σ of the cold gas. The vertical dashed line indicates four/two times the gravitational softening of the stellar/gas particles at this redshift. The gray lines are fits for an exponential surface density profile for $\Sigma(x) = a \cdot \exp(-x/b)$ with $b \approx 2$ kpc. *Middle panel:* Rotation curves of the cold gas (solid lines) compared to the rotation curves expected from the spherically averaged total mass distribution (dash-dotted lines). Dotted lines show the corresponding cold gas contribution. The thick dotted lines at large radii show the expected theoretical rotation curves when corrected for the asymmetric drift. *Bottom panel:* Radial velocity dispersion σ_r of the cold gas. Thin dotted lines indicate the σ used for the asymmetric drift correction in the middle panel.

findings of [Simons et al. \(2017\)](#), who showed that observed galaxies at $z \sim 2$, independently of their stellar mass, typically have $\sigma_{gas} \sim 60$ km/s, similar to our galaxies shown in [Fig 6.4.1](#). Applying a simple correction

$$v_{rot}^2 = v_{circ}^2 + 2\sigma^2 \times (d\ln\Sigma/d\ln R) = v_{circ}^2 - 2\sigma^2 \times (R/R_d)$$

for the asymmetric drift ([Burkert et al., 2010](#)) based on our measured dispersion profiles onto the theoretical rotation curve results in reduced rotation curves, which qualitatively agree well with our measured ones. Therefore, we conclude that the declining rotation curves of the high redshift galaxies are caused by a relatively thick, turbulent disk, as already discussed in [Genzel et al. \(2017\)](#). We also find that these galaxies show similarly low DM fractions as reported for the observations. The DM halos of these disk galaxies have a mean concentration parameter $c_{vir} \approx 8$ (as expected for these halo masses at $z = 2$) and therefore we can exclude that the low dark matter fractions are caused by especially low concentrations of the underlying halos.

Tracing these galaxies in the simulations until $z = 0$ allows us to infer the present-day appearances of these galaxies. We find that, on average, these galaxies still grow by a factor of ≈ 3.5 both in virial as well as in stellar mass. Two of them resemble present-day disk galaxies with small remaining gas disks, and one ends as a central galaxy of a small group. Three of them become satellite galaxies of small groups, while the rest is mostly classified as transition types. Therefore, we can exclude that the low DM fractions at $z = 2$ imply that these systems have to be the progenitors of today's elliptical galaxies with similar stellar mass and low dark matter fractions.

Interestingly, in our simulations we also find several spheroidal galaxies at $z = 2$ which host a massive cold gas disk with similarly declining rotation curves as the disk galaxies. These gas disks are typically more compact, but as star formation is dominated by the gas disks, these spheroidals appear indistinguishable from the disk galaxies in our mock HST images, highlighting the need for observational instruments that detect the old stellar component even at high redshifts.

In general, we conclude that high-redshift disk galaxies with declining rotation curves and low DM fractions appear naturally within the Λ CDM paradigm, reflecting the complex baryonic physics which plays a role at $z = 2$ and can be found commonly in state-of-the-art, Λ CDM cosmological hydrodynamical simulations.

Chapter 7

Summary and Conclusion

We extracted between 400 and 2000 galaxies in the redshift range $0 < z < 2$ with total stellar masses above $10^{10}M_{\odot}$ from the hydrodynamical, cosmological state-of-the-art simulation *Magneticum Pathfinder*, which includes detailed treatment of star formation, chemical enrichment, and evolution of supermassive BHs. We investigated the connection between the kinematics, the mass, the age, and the morphology of the galaxies. Thereby, we focused on the interplay of the dark matter and the baryonic component. Furthermore, we addressed the question which influence the environment has on the morphology.

For the galaxy classification we applied different methods, depending on the properties that were studied. Qualitatively, the classifications based on the angular momentum, i.e. the circularity parameter ε and the b -value, agree well for the separation of spheroidal and disk galaxies. For detailed studies of kinematical properties, however, we prefer to use the very strict selection criterion of the circularity parameter to ensure that we only include poster child spheroids and disks in our sample. In order to test the effect of the baryonic processes on the angular momentum within the halos and their influence on the formation history, we also performed a DM control run.

In the following we summarize our findings.

The spin parameter of the gas becomes higher with evolving time. In contrast, the spin of dark matter and stars does not show any significant time evolution. The vectors of the angular momentum of stars are better aligned with the gas than with the dark matter at high redshift. However, this changes at low redshift, where the stellar angular momentum vectors tend to be better aligned with those of the dark matter.

On the stellar-mass–stellar-specific-angular-momentum ($M_* - j_*$) plane, the poster child disks and spheroids populate different regions, in very good agreement with observations. In good agreement with observations, we find the specific angular momentum of the (cold) gas in our disk galaxies to be higher than that of the stellar component. When only considering the young stars, the angular momentum is comparable to that of the gas. This

shows that the young stars encode the information of the angular momentum which was accreted recently.

Regarding the question if the specific angular momentum of the gas in the (disk) galaxy is reflecting that of the total halo, we do not find a one-to-one correspondence; the gas only accounts for about 43% of the specific angular momentum value of that of the dark matter halo.

The alignment of the angular momentum vectors of the total dark halo with the inner part is slightly better in the run with baryons compared to the dark matter only run. Furthermore, the halos hosting poster child disk galaxies show better alignment in their angular momentum vectors with the central parts.

In the distribution of the spin parameter λ , which takes into account all components within the halo, we find a dichotomy: the halos hosting disk galaxies tend to have higher spins, while the halos hosting spheroids in their centers tend to have lower spins. This is even reflected in the spin parameter distribution in the dark matter only run, for which we have cross-matched our galaxies. This implies that the formation history is important for the resulting morphology.

We also investigated if the mass of the dark matter halo can be inferred from the abundance of satellites around the host galaxies, as concluded by observational studies. When using all galaxies above a certain mass range, we find the spheroidal host galaxies to have more satellites compared to the disk galaxies. However, when we split the galaxies into central galaxies, i.e. galaxies which reside in the center of the dark matter halo, and companions, which are large satellites, this signal disappears for the central galaxies, but only remains for the companion galaxies. This shows that the difference in the abundance of satellites around ellipticals and spirals is driven by the environment and is just reflecting the morphology-density relation. Thus, one cannot estimate the halo mass from counting the satellites, unless one restricts to central galaxies, which is not straight forward in observations.

We further study the connection between the quenching and morphological type of our galaxies. For this we use a larger box with the same resolution, at redshift $z = 2$, and select galaxies within a narrow mass range in order to exclude effects driven by the mass. Already quenched galaxies do not show any relation to their the morphology and have formed earlier than the star-forming galaxies. Furthermore, we find that, at $z = 2$, the classification based on the kinematics yields different results compared to the classification based on star formation activity.

When studying the connection between the star formation rate and the environment from $z \approx 5$ down to present time, we find that the morphology-density relation starts to build up at $z \approx 2$. The morphology-density relation looks similar for quiescent and star-forming centrals, which indicates a negligible influence of the environment on central galaxies. For quiescent companion galaxies the distribution of the number density peaks at high density environments, while those of quiescent centrals peaks at low density. This leads us to the

conclusion that environmental quenching influences the evolution of satellites rather than central galaxies.

In order to explore the connection of the age distribution in galaxies with the rotational support via the b -value and the morphological type, we divided the stars into young, middle-aged and old stellar populations. We find that the stellar populations of disk galaxies have similarly high b -values, indicating that they generally could evolve without. In contrast, the distributions of the b -value for the different stellar populations of spheroidal galaxies differ from each other, where the old component tends to low values and the young component has a broad distribution. This supports a picture in which these stellar populations have different origins. As the old stars contribute most to the mass and we do not find a connection between the b -value of the young stars and the mass fraction of disks, we conclude that the old stellar component determines the morphological type. Therefore, in observations it is important to consider the different stellar populations for studies of the kinematics, as the young stars generally are brighter than the old stars.

We have also analyzed the radial distribution of the different stellar populations; the positive age gradient of spheroidal galaxies suggests an “outside-in” growth of the spheroids, while for disk galaxies we detect a negative age gradient, which indicates an “inside-out” growth.

We then further subdivided the ETGs according to their kinematical properties, i.e. into non-rotators, regular rotators, distinct core galaxies and prolate rotators; the class of galaxies with distinct cores have on average more young and middle-aged stars than the other classes of ETGs. In addition, the population of distinct core galaxies splits in a similar way compared to the disk galaxies, when dividing them into populations with many and few old stars. On the other hand, kinematically they behave like the spheroidal galaxies. This favors a formation history involving gas rich mergers with retrograde orbital configurations. We confirm results from previous studies that different formation paths can lead to an ETG at present time.

We also tested whether the low DM fractions are connected to declining rotation curves at $z = 2$. Almost 50% of our poster child disk galaxies exhibit declining rotation curves. In addition, they also have radial velocity dispersion that are higher than those of galaxies at $z = 0$. This is expected for galaxies at that redshift, as they are in the process of forming. We conclude that the rotation curves decline due to a relatively thick and turbulent disk. The disk galaxies have similarly low DM fractions as in observations. Since the concentration of their DM halo is as expected, we can exclude that the dark matter fractions of the galaxies are due to the underlying halo. At present day our disks from $z = 2$ span a wide range of morphological types, from which we can rule out that a galaxy with low dark matter fractions at high redshift automatically ends up as an ETG.

Another important aspect is that we find spheroidal galaxies at high redshift that have a massive disk of cold gas, which is indistinguishable from disk galaxies in our mock *HST* images. This emphasizes the need for the consideration of the old stellar component, even

at high redshift.

In summary, we have demonstrated that the galaxy's morphology is tightly connected to its evolutionary history, particularly the distribution of the angular momentum. In addition, we have shown that the environment of a galaxy influences its angular momentum and its morphology. From this we can conclude that the interplay between spin and mass is an important tracer for the morphology.

In general, larger samples are needed in order to study properties of poster child galaxies, and in particular disk galaxies, in a statistically relevant manner. Therefore, boxes with a larger volume and possibly even higher resolution are needed. This would help to study the assembly history in more detail and, in particular, to gain even better insights into the complex interplay between gas, stars, dark matter and the environment and how they shape the morphology of a galaxy.

Bibliography

- M. G. Abadi, B. Moore, and R. G. Bower. Ram pressure stripping of spiral galaxies in clusters. *MNRAS*, 308:947–954, October 1999. doi: 10.1046/j.1365-8711.1999.02715.x.
- M. G. Abadi, J. F. Navarro, M. Steinmetz, and V. R. Eke. Simulations of Galaxy Formation in a Λ Cold Dark Matter Universe. II. The Fine Structure of Simulated Galactic Disks. *ApJ*, 597:21–34, November 2003. doi: 10.1086/378316.
- G. O. Abell. The Distribution of Rich Clusters of Galaxies. *ApJS*, 3:211, May 1958. doi: 10.1086/190036.
- G. O. Abell. Evidence regarding second-order clustering of galaxies and interactions between clusters of galaxies. *Astronomical Journal*, 66:607, December 1961. doi: 10.1086/108472.
- R. G. Abraham, S. van den Bergh, K. Glazebrook, R. S. Ellis, B. X. Santiago, P. Surma, and R. E. Griffiths. The Morphologies of Distant Galaxies. II. Classifications from the Hubble Space Telescope Medium Deep Survey. *ApJS*, 107:1, November 1996. doi: 10.1086/192352.
- A. Abramson, J. D. P. Kenney, H. H. Crowl, A. Chung, J. H. van Gorkom, B. Vollmer, and D. Schiminovich. Caught in the Act: Strong, Active Ram Pressure Stripping in Virgo Cluster Spiral NGC 4330. *Astronomical Journal*, 141:164, May 2011. doi: 10.1088/0004-6256/141/5/164.
- A. Arth, K. Dolag, A. M. Beck, M. Petkova, and H. Lesch. Anisotropic thermal conduction in galaxy clusters with MHD in Gadget. *ArXiv e-prints (arXiv:1412.6533)*, December 2014.
- D. Aubert, C. Pichon, and S. Colombi. The origin and implications of dark matter anisotropic cosmic infall on $\sim L_*$ haloes. *MNRAS*, 352:376–398, August 2004. doi: 10.1111/j.1365-2966.2004.07883.x.
- R. Bacon, Y. Copin, G. Monnet, B. W. Miller, J. R. Allington-Smith, M. Bureau, C. M. Carollo, R. L. Davies, E. Emsellem, H. Kuntschner, R. F. Peletier, E. K. Verolme, and P. T. de Zeeuw. The SAURON project - I. The panoramic integral-field spectrograph. *MNRAS*, 326:23–35, September 2001. doi: 10.1046/j.1365-8711.2001.04612.x.
- J. Bailin and M. Steinmetz. Internal and External Alignment of the Shapes and Angular Momenta of Λ CDM Halos. *ApJ*, 627:647–665, July 2005. doi: 10.1086/430397.
- I. K. Baldry, K. Glazebrook, J. Brinkmann, Ž. Ivezić, R. H. Lupton, R. C. Nichol, and A. S. Szalay. Quantifying the Bimodal Color-Magnitude Distribution of Galaxies. *ApJ*, 600:681–694, January 2004. doi: 10.1086/380092.
- M. L. Balogh, J. F. Navarro, and S. L. Morris. The Origin of Star Formation Gradients in Rich Galaxy Clusters. *ApJ*, 540:113–121, September 2000. doi: 10.1086/309323.

- M. Barnabè, A. A. Dutton, P. J. Marshall, M. W. Auger, B. J. Brewer, T. Treu, A. S. Bolton, D. C. Koo, and L. V. E. Koopmans. The SWELLS survey - IV. Precision measurements of the stellar and dark matter distributions in a spiral lens galaxy. *MNRAS*, 423:1073–1088, June 2012. doi: 10.1111/j.1365-2966.2012.20934.x.
- J. Barnes and G. Efstathiou. Angular momentum from tidal torques. *ApJ*, 319:575–600, August 1987. doi: 10.1086/165480.
- J. E. Barnes and L. Hernquist. Transformations of Galaxies. II. Gasdynamics in Merging Disk Galaxies. *ApJ*, 471:115, November 1996. doi: 10.1086/177957.
- A. M. Beck, G. Murante, A. Arth, R.-S. Remus, A. F. Teklu, J. M. F. Donnert, S. Planelles, M. C. Beck, P. Förster, M. Imgrund, K. Dolag, and S. Borgani. An improved SPH scheme for cosmological simulations. *MNRAS*, 455:2110–2130, January 2016. doi: 10.1093/mnras/stv2443.
- A. G. Bedregal, N. Cardiel, A. Aragón-Salamanca, and M. R. Merrifield. Stellar population gradients in Fornax cluster S0 galaxies: connecting bulge and disc evolution. *MNRAS*, 415:2063–2080, August 2011. doi: 10.1111/j.1365-2966.2011.18752.x.
- P. S. Behroozi, C. Conroy, and R. H. Wechsler. A Comprehensive Analysis of Uncertainties Affecting the Stellar Mass-Halo Mass Relation for $0 < z < 4$. *ApJ*, 717:379–403, July 2010. doi: 10.1088/0004-637X/717/1/379.
- P. S. Behroozi, R. H. Wechsler, and C. Conroy. The Average Star Formation Histories of Galaxies in Dark Matter Halos from $z = 0-8$. *ApJ*, 770:57, June 2013. doi: 10.1088/0004-637X/770/1/57.
- Z. K. Berta, R. Jimenez, A. F. Heavens, and B. Panter. The role of spin in the formation and evolution of galaxies. *MNRAS*, 391:197–204, November 2008. doi: 10.1111/j.1365-2966.2008.13742.x.
- P. Bett, V. Eke, C. S. Frenk, A. Jenkins, and T. Okamoto. The angular momentum of cold dark matter haloes with and without baryons. *MNRAS*, 404:1137–1156, May 2010. doi: 10.1111/j.1365-2966.2010.16368.x.
- V. Biffi and U. Maio. Statistical properties of mass, star formation, chemical content and rotational patterns in early $z \gtrsim 9$ structures. *MNRAS*, 436:1621–1638, December 2013. doi: 10.1093/mnras/stt1678.
- James Binney and Scott Tremaine. *Galactic Dynamics*. Princeton University Press, second edition, 2008.
- J. C. Bird, S. Kazantzidis, D. H. Weinberg, J. Guedes, S. Callegari, L. Mayer, and P. Madau. Inside out and Upside down: Tracing the Assembly of a Simulated Disk Galaxy Using Mono-age Stellar Populations. *ApJ*, 773:43, August 2013. doi: 10.1088/0004-637X/773/1/43.

- J. Bland-Hawthorn and O. Gerhard. The Galaxy in Context: Structural, Kinematic, and Integrated Properties. *Annual review of astronomy and astrophysics*, 54:529–596, September 2016. doi: 10.1146/annurev-astro-081915-023441.
- N. F. Boardman, A.-M. Weijmans, R. van den Bosch, H. Kuntschner, E. Emsellem, M. Cappellari, T. de Zeeuw, J. Falcón-Barroso, D. Krajnović, R. McDermid, T. Naab, G. van de Ven, and A. Yildirim. Integral-field kinematics and stellar populations of early-type galaxies out to three half-light radii. *MNRAS*, 471:4005–4026, November 2017. doi: 10.1093/mnras/stx1835.
- S. Boissier, A. Boselli, P.-A. Duc, L. Cortese, W. van Driel, S. Heinis, E. Voyer, O. Cucciati, L. Ferrarese, P. Côté, J.-C. Cuillandre, S. D. J. Gwyn, and S. Mei. The GALEX Ultraviolet Virgo Cluster Survey (GUViCS). II. Constraints on star formation in ram-pressure stripped gas. *Astronomy and Astrophysics*, 545:A142, September 2012. doi: 10.1051/0004-6361/201219957.
- H. Bondi. On spherically symmetrical accretion. *MNRAS*, 112:195–+, 1952.
- H. Bondi and F. Hoyle. On the mechanism of accretion by stars. *MNRAS*, 104:273, 1944.
- A. Boselli, S. Boissier, L. Cortese, and G. Gavazzi. The Origin of Dwarf Ellipticals in the Virgo Cluster. *ApJ*, 674:742–767, February 2008. doi: 10.1086/525513.
- F. Bournaud, C. J. Jog, and F. Combes. Multiple minor mergers: formation of elliptical galaxies and constraints for the growth of spiral disks. *Astronomy and Astrophysics*, 476:1179–1190, December 2007. doi: 10.1051/0004-6361:20078010.
- C. B. Brook, D. Kawata, B. K. Gibson, and C. Flynn. Stellar halo constraints on simulated late-type galaxies. *MNRAS*, 349:52–56, March 2004. doi: 10.1111/j.1365-2966.2004.07464.x.
- C. B. Brook, A. Di Cintio, A. Knebe, S. Gottlöber, Y. Hoffman, G. Yepes, and S. Garrison-Kimmel. The Stellar-to-halo Mass Relation for Local Group Galaxies. *The Astrophysical Journal, Letters*, 784:L14, March 2014. doi: 10.1088/2041-8205/784/1/L14.
- M. M. Brouwer, M. Cacciato, A. Dvornik, L. Eardley, C. Heymans, H. Hoekstra, K. Kuijken, T. McNaught-Roberts, C. Sifón, M. Viola, M. Alpaslan, M. Bilicki, J. Bland-Hawthorn, S. Brough, A. Choi, S. P. Driver, T. Erben, A. Grado, H. Hildebrandt, B. W. Holwerda, A. M. Hopkins, J. T. A. de Jong, J. Liske, J. McFarland, R. Nakajima, N. R. Napolitano, P. Norberg, J. A. Peacock, M. Radovich, A. S. G. Robotham, P. Schneider, G. Sikkema, E. van Uitert, G. Verdoes Kleijn, and E. A. Valentijn. Dependence of GAMA galaxy halo masses on the cosmic web environment from 100 deg² of KiDS weak lensing data. *MNRAS*, 462:4451–4463, November 2016. doi: 10.1093/mnras/stw1602.
- S. E. Bryan, S. T. Kay, A. R. Duffy, J. Schaye, C. Dalla Vecchia, and C. M. Booth. The impact of baryons on the spins and shapes of dark matter haloes. *MNRAS*, 429:3316–3329, March 2013. doi: 10.1093/mnras/sts587.

- J. J. Bryant, M. S. Owers, A. S. G. Robotham, S. M. Croom, S. P. Driver, M. J. Drinkwater, N. P. F. Lorente, L. Cortese, N. Scott, M. Colless, A. Schaefer, E. N. Taylor, I. S. Konstantopoulos, J. T. Allen, I. Baldry, L. Barnes, A. E. Bauer, J. Bland-Hawthorn, J. V. Bloom, A. M. Brooks, S. Brough, G. Cecil, W. Couch, D. Croton, R. Davies, S. Ellis, L. M. R. Fogarty, C. Foster, K. Glazebrook, M. Goodwin, A. Green, M. L. Gunawardhana, E. Hampton, I.-T. Ho, A. M. Hopkins, L. Kewley, J. S. Lawrence, S. G. Leon-Saval, S. Leslie, R. McElroy, G. Lewis, J. Liske, Á. R. López-Sánchez, S. Mahajan, A. M. Medling, N. Metcalfe, M. Meyer, J. Mould, D. Obreschkow, S. O’Toole, M. Pracy, S. N. Richards, T. Shanks, R. Sharp, S. M. Sweet, A. D. Thomas, C. Tonini, and C. J. Walcher. The SAMI Galaxy Survey: instrument specification and target selection. *MNRAS*, 447:2857–2879, March 2015. doi: 10.1093/mnras/stu2635.
- J. S. Bullock, A. Dekel, T. S. Kolatt, A. V. Kravtsov, A. A. Klypin, C. Porciani, and J. R. Primack. A Universal Angular Momentum Profile for Galactic Halos. *ApJ*, 555:240–257, July 2001. doi: 10.1086/321477.
- K. Bundy, M. Fukugita, R. S. Ellis, T. A. Targett, S. Belli, and T. Kodama. The Greater Impact of Mergers on the Growth of Massive Galaxies: Implications for Mass Assembly and Evolution since $z \sim 1$. *ApJ*, 697:1369–1383, June 2009. doi: 10.1088/0004-637X/697/2/1369.
- K. Bundy, M. A. Bershady, D. R. Law, R. Yan, N. Drory, N. MacDonald, D. A. Wake, B. Cherinka, J. R. Sánchez-Gallego, A.-M. Weijmans, D. Thomas, C. Tremonti, K. Masters, L. Coccato, A. M. Diamond-Stanic, A. Aragón-Salamanca, V. Avila-Reese, C. Badenes, J. Falcón-Barroso, F. Belfiore, D. Bizyaev, G. A. Blanc, J. Bland-Hawthorn, M. R. Blanton, J. R. Brownstein, N. Byler, M. Cappellari, C. Conroy, A. A. Dutton, E. Emsellem, J. Etherington, P. M. Frinchaboy, H. Fu, J. E. Gunn, P. Harding, E. J. Johnston, G. Kauffmann, K. Kinemuchi, M. A. Klaene, J. H. Knapen, A. Leauthaud, C. Li, L. Lin, R. Maiolino, V. Malanushenko, E. Malanushenko, S. Mao, C. Maraston, R. M. McDermid, M. R. Merrifield, R. C. Nichol, D. Oravetz, K. Pan, J. K. Parejko, S. F. Sanchez, D. Schlegel, A. Simmons, O. Steele, M. Steinmetz, K. Thanjavur, B. A. Thompson, J. L. Tinker, R. C. E. van den Bosch, K. B. Westfall, D. Wilkinson, S. Wright, T. Xiao, and K. Zhang. Overview of the SDSS-IV MaNGA Survey: Mapping nearby Galaxies at Apache Point Observatory. *ApJ*, 798:7, January 2015. doi: 10.1088/0004-637X/798/1/7.
- A. Burkert, R. Genzel, N. Bouché, G. Cresci, S. Khochfar, J. Sommer-Larsen, A. Sternberg, T. Naab, N. Förster Schreiber, L. Tacconi, K. Shapiro, E. Hicks, D. Lutz, R. Davies, P. Buschkamp, and S. Genel. High-redshift Star-forming Galaxies: Angular Momentum and Baryon Fraction, Turbulent Pressure Effects, and the Origin of Turbulence. *ApJ*, 725:2324–2332, December 2010. doi: 10.1088/0004-637X/725/2/2324.
- M. Cappellari. Structure and Kinematics of Early-Type Galaxies from Integral Field Spectroscopy. *Annual review of astronomy and astrophysics*, 54:597–665, September 2016. doi: 10.1146/annurev-astro-082214-122432.

- M. Cappellari, E. Emsellem, R. Bacon, M. Bureau, R. L. Davies, P. T. de Zeeuw, J. Falcón-Barroso, D. Krajnović, H. Kuntschner, R. M. McDermid, R. F. Peletier, M. Sarzi, R. C. E. van den Bosch, and G. van de Ven. The SAURON project - X. The orbital anisotropy of elliptical and lenticular galaxies: revisiting the $(V/\sigma, \epsilon)$ diagram with integral-field stellar kinematics. *MNRAS*, 379:418–444, August 2007. doi: 10.1111/j.1365-2966.2007.11963.x.
- M. Cappellari, E. Emsellem, D. Krajnović, R. M. McDermid, N. Scott, G. A. Verdoes Kleijn, L. M. Young, K. Alatalo, R. Bacon, L. Blitz, M. Bois, F. Bournaud, M. Bureau, R. L. Davies, T. A. Davis, P. T. de Zeeuw, P.-A. Duc, S. Khochfar, H. Kuntschner, P.-Y. Lablanche, R. Morganti, T. Naab, T. Oosterloo, M. Sarzi, P. Serra, and A.-M. Weijmans. The ATLAS^{3D} project - I. A volume-limited sample of 260 nearby early-type galaxies: science goals and selection criteria. *MNRAS*, 413:813–836, May 2011a. doi: 10.1111/j.1365-2966.2010.18174.x.
- M. Cappellari, E. Emsellem, D. Krajnović, R. M. McDermid, P. Serra, K. Alatalo, L. Blitz, M. Bois, F. Bournaud, M. Bureau, R. L. Davies, T. A. Davis, P. T. de Zeeuw, S. Khochfar, H. Kuntschner, P.-Y. Lablanche, R. Morganti, T. Naab, T. Oosterloo, M. Sarzi, N. Scott, A.-M. Weijmans, and L. M. Young. The ATLAS^{3D} project - VII. A new look at the morphology of nearby galaxies: the kinematic morphology-density relation. *MNRAS*, 416:1680–1696, September 2011b. doi: 10.1111/j.1365-2966.2011.18600.x.
- G. Chabrier. Galactic Stellar and Substellar Initial Mass Function. *Publications of the ASP*, 115:763–795, July 2003. doi: 10.1086/376392.
- D. N. Chen, Y. P. Jing, and K. Yoshikaw. Angular Momentum Distribution of Hot Gas and Implications for Disk Galaxy Formation. *ApJ*, 597:35–47, November 2003. doi: 10.1086/378379.
- I. V. Chilingarian. Evolution of dwarf early-type galaxies - I. Spatially resolved stellar populations and internal kinematics of Virgo cluster dE/dS0 galaxies. *MNRAS*, 394: 1229–1248, April 2009. doi: 10.1111/j.1365-2966.2009.14450.x.
- E. Churchwell, B. L. Babler, M. R. Meade, B. A. Whitney, R. Benjamin, R. Indebetouw, C. Cyganowski, T. P. Robitaille, M. Povich, C. Watson, and S. Bracker. The Spitzer/GLIMPSE Surveys: A New View of the Milky Way. *Publications of the ASP*, 121:213, March 2009. doi: 10.1086/597811.
- S. Codis, R. Gavazzi, Y. Dubois, C. Pichon, K. Benabed, V. Desjacques, D. Pogosyan, J. Devriendt, and A. Slyz. Intrinsic alignment of simulated galaxies in the cosmic web: implications for weak lensing surveys. *MNRAS*, 448:3391–3404, April 2015. doi: 10.1093/mnras/stv231.
- C. Conroy, F. Prada, J. A. Newman, D. Croton, A. L. Coil, C. J. Conselice, M. C. Cooper, M. Davis, S. M. Faber, B. F. Gerke, P. Guhathakurta, A. Klypin, D. C. Koo, and R. Yan. Evolution in the Halo Masses of Isolated Galaxies between $z \sim 1$ and $z \sim 0$: From DEEP2 to SDSS. *ApJ*, 654:153–171, January 2007. doi: 10.1086/509632.

- M. C. Cooper, J. A. Newman, A. L. Coil, D. J. Croton, B. F. Gerke, R. Yan, M. Davis, S. M. Faber, P. Guhathakurta, D. C. Koo, B. J. Weiner, and C. N. A. Willmer. The DEEP2 galaxy redshift survey: evolution of the colour-density relation at $0.4 < z < 1.35$. *MNRAS*, 376:1445–1459, April 2007. doi: 10.1111/j.1365-2966.2007.11534.x.
- S. Courteau and A. A. Dutton. On the Global Mass Distribution in Disk Galaxies. *The Astrophysical Journal, Letters*, 801:L20, March 2015. doi: 10.1088/2041-8205/801/2/L20.
- L. L. Cowie, A. Songaila, E. M. Hu, and J. G. Cohen. New Insight on Galaxy Formation and Evolution From Keck Spectroscopy of the Hawaii Deep Fields. *Astronomical Journal*, 112:839, September 1996. doi: 10.1086/118058.
- T. J. Cox, S. N. Dutta, T. Di Matteo, L. Hernquist, P. F. Hopkins, B. Robertson, and V. Springel. The Kinematic Structure of Merger Remnants. *ApJ*, 650:791–811, October 2006. doi: 10.1086/507474.
- R. A. C. Croft, T. Di Matteo, V. Springel, and L. Hernquist. Galaxy morphology, kinematics and clustering in a hydrodynamic simulation of a Λ cold dark matter universe. *MNRAS*, 400:43–67, November 2009. doi: 10.1111/j.1365-2966.2009.15446.x.
- S. M. Croom, J. S. Lawrence, J. Bland-Hawthorn, J. J. Bryant, L. Fogarty, S. Richards, M. Goodwin, T. Farrell, S. Miziarski, R. Heald, D. H. Jones, S. Lee, M. Colless, S. Brough, A. M. Hopkins, A. E. Bauer, M. N. Birchall, S. Ellis, A. Horton, S. Leon-Saval, G. Lewis, Á. R. López-Sánchez, S.-S. Min, C. Trinh, and H. Trowland. The Sydney-AAO Multi-object Integral field spectrograph. *MNRAS*, 421:872–893, March 2012. doi: 10.1111/j.1365-2966.2011.20365.x.
- M. Danovich, A. Dekel, O. Hahn, D. Ceverino, and J. Primack. Four phases of angular-momentum buildup in high- z galaxies: from cosmic-web streams through an extended ring to disc and bulge. *MNRAS*, 449:2087–2111, May 2015. doi: 10.1093/mnras/stv270.
- B. Darvish, B. Mobasher, D. Sobral, A. Rettura, N. Scoville, A. Faisst, and P. Capak. The Effects of the Local Environment and Stellar Mass on Galaxy Quenching to $z \sim 3$. *ApJ*, 825:113, July 2016. doi: 10.3847/0004-637X/825/2/113.
- M. Davis, G. Efstathiou, C. S. Frenk, and S. D. M. White. The evolution of large-scale structure in a universe dominated by cold dark matter. *ApJ*, 292:371–394, May 1985. doi: 10.1086/163168.
- T. A. Davis, K. Alatalo, M. Sarzi, M. Bureau, L. M. Young, L. Blitz, P. Serra, A. F. Crocker, D. Krajnović, R. M. McDermid, M. Bois, F. Bournaud, M. Cappellari, R. L. Davies, P.-A. Duc, P. T. de Zeeuw, E. Emsellem, S. Khochfar, H. Kuntschner, P.-Y. Lablanche, R. Morganti, T. Naab, T. Oosterloo, N. Scott, and A.-M. Weijmans. The ATLAS^{3D} project - X. On the origin of the molecular and ionized gas in early-type galaxies. *MNRAS*, 417:882–899, October 2011. doi: 10.1111/j.1365-2966.2011.19355.x.

- G. de Vaucouleurs. Recherches sur les Nebuleuses Extragalactiques. *Annales d'Astrophysique*, 11:247, January 1948.
- G. de Vaucouleurs. Classification and Morphology of External Galaxies. *Handbuch der Physik*, 53:275, 1959.
- P. T. de Zeeuw, M. Bureau, E. Emsellem, R. Bacon, C. M. Carollo, Y. Copin, R. L. Davies, H. Kuntschner, B. W. Miller, G. Monnet, R. F. Peletier, and E. K. Verolme. The SAURON project - II. Sample and early results. *MNRAS*, 329:513–530, January 2002. doi: 10.1046/j.1365-8711.2002.05059.x.
- A. J. Deason, I. G. McCarthy, A. S. Font, N. W. Evans, C. S. Frenk, V. Belokurov, N. I. Libeskind, R. A. Crain, and T. Theuns. Mismatch and misalignment: dark haloes and satellites of disc galaxies. *MNRAS*, 415:2607–2625, August 2011. doi: 10.1111/j.1365-2966.2011.18884.x.
- A. Dekel, Y. Birnboim, G. Engel, J. Freundlich, T. Goerdt, M. Mumcuoglu, E. Neistein, C. Pichon, R. Teyssier, and E. Zinger. Cold streams in early massive hot haloes as the main mode of galaxy formation. *Nat*, 457:451–454, January 2009. doi: 10.1038/nature07648.
- T. Di Matteo, V. Springel, and L. Hernquist. Energy input from quasars regulates the growth and activity of black holes and their host galaxies. *Nat*, 433:604–607, February 2005. doi: 10.1038/nature03335.
- K. Dolag, M. Jubelgas, V. Springel, S. Borgani, and E. Rasia. Thermal Conduction in Simulated Galaxy Clusters. *The Astrophysical Journal, Letters*, 606:L97–L100, May 2004. doi: 10.1086/420966.
- K. Dolag, F. Vazza, G. Brunetti, and G. Tormen. Turbulent gas motions in galaxy cluster simulations: the role of smoothed particle hydrodynamics viscosity. *MNRAS*, 364:753–772, December 2005. doi: 10.1111/j.1365-2966.2005.09630.x.
- K. Dolag, S. Borgani, G. Murante, and V. Springel. Substructures in hydrodynamical cluster simulations. *MNRAS*, 399:497–514, October 2009. doi: 10.1111/j.1365-2966.2009.15034.x.
- K. Dolag, E. Komatsu, and R. Sunyaev. SZ effects in the Magneticum Pathfinder simulation: comparison with the Planck, SPT, and ACT results. *MNRAS*, 463:1797–1811, December 2016. doi: 10.1093/mnras/stw2035.
- K. Dolag, E. Mevius, and R.-S. Remus. Distribution and Evolution of Metals in the Magneticum Simulations. *Galaxies*, 5:35, August 2017. doi: 10.3390/galaxies5030035.
- R. Domínguez-Tenreiro, A. Obreja, G. L. Granato, A. Schurer, P. Alpresa, L. Silva, C. B. Brook, and A. Serna. GRASIL-3D: an implementation of dust effects in the SEDs of simulated galaxies. *MNRAS*, 439:3868–3889, April 2014. doi: 10.1093/mnras/stu240.

- E. D’Onghia, J. Sommer-Larsen, A. D. Romeo, A. Burkert, K. Pedersen, L. Portinari, and J. Rasmussen. The Formation of Fossil Galaxy Groups in the Hierarchical Universe. *The Astrophysical Journal, Letters*, 630:L109–L112, September 2005. doi: 10.1086/491651.
- J. Donnert, K. Dolag, G. Brunetti, and R. Cassano. Rise and fall of radio haloes in simulated merging galaxy clusters. *MNRAS*, 429:3564–3569, March 2013. doi: 10.1093/mnras/sts628.
- A. G. Doroshkevich. The space structure of perturbations and the origin of rotation of galaxies in the theory of fluctuation. *Astrofizika*, 6:581–600, 1970.
- A. Dressler. Galaxy morphology in rich clusters - Implications for the formation and evolution of galaxies. *ApJ*, 236:351–365, March 1980. doi: 10.1086/157753.
- S. P. Driver, P. D. Allen, A. W. Graham, E. Cameron, J. Liske, S. C. Ellis, N. J. G. Cross, R. De Propris, S. Phillipps, and W. J. Couch. The Millennium Galaxy Catalogue: morphological classification and bimodality in the colour-concentration plane. *MNRAS*, 368:414–434, May 2006. doi: 10.1111/j.1365-2966.2006.10126.x.
- Y. Dubois, C. Pichon, C. Welker, D. Le Borgne, J. Devriendt, C. Laigle, S. Codis, D. Pogosyan, S. Arnouts, K. Benabed, E. Bertin, J. Blaizot, F. Bouchet, J.-F. Cardoso, S. Colombi, V. de Lapparent, V. Desjacques, R. Gavazzi, S. Kassin, T. Kimm, H. McCracken, B. Milliard, S. Peirani, S. Prunet, S. Rouberol, J. Silk, A. Slyz, T. Sousbie, R. Teyssier, L. Tresse, M. Treyer, D. Vibert, and M. Volonteri. Dancing in the dark: galactic properties trace spin swings along the cosmic web. *MNRAS*, 444:1453–1468, October 2014. doi: 10.1093/mnras/stu1227.
- A. A. Dutton, C. Conroy, F. C. van den Bosch, F. Prada, and S. More. The kinematic connection between galaxies and dark matter haloes. *MNRAS*, 407:2–16, September 2010. doi: 10.1111/j.1365-2966.2010.16911.x.
- A. A. Dutton, T. Treu, B. J. Brewer, P. J. Marshall, M. W. Auger, M. Barnabè, D. C. Koo, A. S. Bolton, and L. V. E. Koopmans. The SWELLS survey - V. A Salpeter stellar initial mass function in the bulges of massive spiral galaxies. *MNRAS*, 428:3183–3195, February 2013. doi: 10.1093/mnras/sts262.
- V. R. Eke, S. Cole, and C. S. Frenk. Cluster evolution as a diagnostic for Omega. *MNRAS*, 282:263–280, September 1996.
- D. M. Elmegreen, B. G. Elmegreen, T. Ferguson, and B. Mullan. Smooth and Starburst Tidal Tails in the GEMS and GOODS Fields. *ApJ*, 663:734–751, July 2007. doi: 10.1086/518715.
- E. Emsellem, M. Cappellari, D. Krajnović, G. van de Ven, R. Bacon, M. Bureau, R. L. Davies, P. T. de Zeeuw, J. Falcón-Barroso, H. Kuntschner, R. McDermid, R. F. Peletier, and M. Sarzi. The SAURON project - IX. A kinematic classification for early-type galaxies. *MNRAS*, 379:401–417, August 2007. doi: 10.1111/j.1365-2966.2007.11752.x.

- E. Emsellem, M. Cappellari, D. Krajnović, K. Alatalo, L. Blitz, M. Bois, F. Bournaud, M. Bureau, R. L. Davies, T. A. Davis, P. T. de Zeeuw, S. Khochfar, H. Kuntschner, P.-Y. Lablanche, R. M. McDermid, R. Morganti, T. Naab, T. Oosterloo, M. Sarzi, N. Scott, P. Serra, G. van de Ven, A.-M. Weijmans, and L. M. Young. The ATLAS^{3D} project - III. A census of the stellar angular momentum within the effective radius of early-type galaxies: unveiling the distribution of fast and slow rotators. *MNRAS*, 414:888–912, June 2011. doi: 10.1111/j.1365-2966.2011.18496.x.
- G. Erfanianfar, P. Popesso, A. Finoguenov, D. Wilman, S. Wuyts, A. Biviano, M. Salvato, M. Mirkazemi, L. Morselli, F. Ziparo, K. Nandra, D. Lutz, D. Elbaz, M. Dickinson, M. Tanaka, M. B. Altieri, H. Aussel, F. Bauer, S. Berta, R. M. Bielby, N. Brandt, N. Cappelluti, A. Cimatti, M. C. Cooper, D. Fadda, O. Ilbert, E. Le Floch, B. Magnelli, J. S. Mulchaey, R. Nordon, J. A. Newman, A. Poglitsch, and F. Pozzi. Non-linearity and environmental dependence of the star-forming galaxies main sequence. *MNRAS*, 455:2839–2851, January 2016. doi: 10.1093/mnras/stv2485.
- D. Fabjan, S. Borgani, L. Tornatore, A. Saro, G. Murante, and K. Dolag. Simulating the effect of active galactic nuclei feedback on the metal enrichment of galaxy clusters. *MNRAS*, 401:1670–1690, January 2010. doi: 10.1111/j.1365-2966.2009.15794.x.
- S. M. Fall. Galaxy formation - Some comparisons between theory and observation. In E. Athanassoula, editor, *Internal Kinematics and Dynamics of Galaxies*, volume 100 of *IAU Symposium*, pages 391–398, 1983.
- S. M. Fall and G. Efsthathiou. Formation and rotation of disc galaxies with haloes. *MNRAS*, 193:189–206, October 1980.
- S. M. Fall and A. J. Romanowsky. Angular Momentum and Galaxy Formation Revisited: Effects of Variable Mass-to-light Ratios. *The Astrophysical Journal, Letters*, 769:L26, June 2013. doi: 10.1088/2041-8205/769/2/L26.
- R. Feldmann, P. F. Hopkins, E. Quataert, C.-A. Faucher-Giguère, and D. Kereš. The formation of massive, quiescent galaxies at cosmic noon. *MNRAS*, 458:L14–L18, May 2016. doi: 10.1093/mnrasl/slw014.
- G. J. Ferland, K. T. Korista, D. A. Verner, J. W. Ferguson, J. B. Kingdon, and E. M. Verner. CLOUDY 90: Numerical Simulation of Plasmas and Their Spectra. *Publications of the ASP*, 110:761–778, July 1998. doi: 10.1086/316190.
- J. Forbes, M. Krumholz, and A. Burkert. Evolving Gravitationally Unstable Disks over Cosmic Time: Implications for Thick Disk Formation. *ApJ*, 754:48, July 2012. doi: 10.1088/0004-637X/754/1/48.
- N. M. Förster Schreiber, A. E. Shapley, D. K. Erb, R. Genzel, C. C. Steidel, N. Bouché, G. Cresci, and R. Davies. Constraints on the Assembly and Dynamics of Galaxies. I. Detailed Rest-frame Optical Morphologies on Kiloparsec Scale of $z \sim 2$ Star-forming Galaxies. *ApJ*, 731:65, April 2011. doi: 10.1088/0004-637X/731/1/65.

- M. Franx, P. G. van Dokkum, N. M. Förster Schreiber, S. Wuyts, I. Labbé, and S. Toft. Structure and Star Formation in Galaxies out to $z = 3$: Evidence for Surface Density Dependent Evolution and Upsizing. *ApJ*, 688:770-788, December 2008. doi: 10.1086/592431.
- A. Friedmann. Über die Krümmung des Raumes. *Zeitschrift für Physik*, 10:377–386, 1922. doi: 10.1007/BF01332580.
- A. Gallazzi, S. Charlot, J. Brinchmann, S. D. M. White, and C. A. Tremonti. The ages and metallicities of galaxies in the local universe. *MNRAS*, 362:41–58, September 2005. doi: 10.1111/j.1365-2966.2005.09321.x.
- S. Genel, S. M. Fall, L. Hernquist, M. Vogelsberger, G. F. Snyder, V. Rodriguez-Gomez, D. Sijacki, and V. Springel. Galactic Angular Momentum in the Illustris Simulation: Feedback and the Hubble Sequence. *The Astrophysical Journal, Letters*, 804:L40, May 2015. doi: 10.1088/2041-8205/804/2/L40.
- R. Genzel, N. M. F. Schreiber, H. Übler, P. Lang, T. Naab, R. Bender, L. J. Tacconi, E. Wisnioski, S. Wuyts, T. Alexander, A. Beifiori, S. Belli, G. Brammer, A. Burkert, C. M. Carollo, J. Chan, R. Davies, M. Fossati, A. Galametz, S. Genel, O. Gerhard, D. Lutz, J. T. Mendel, I. Momcheva, E. J. Nelson, A. Renzini, R. Saglia, A. Sternberg, S. Tacchella, K. Tadaki, and D. Wilman. Strongly baryon-dominated disk galaxies at the peak of galaxy formation ten billion years ago. *Nat*, 543:397–401, March 2017. doi: 10.1038/nature21685.
- O. Gerhard. Mass distribution in our Galaxy. *Space Science Reviews*, 100:129–138, January 2002.
- D. Goddard, D. Thomas, C. Maraston, K. Westfall, J. Etherington, R. Riffel, N. D. Mallmann, Z. Zheng, M. Argudo-Fernández, J. Lian, M. Bershady, K. Bundy, N. Drory, D. Law, R. Yan, D. Wake, A. Weijmans, D. Bizyaev, J. Brownstein, R. R. Lane, R. Maiolino, K. Masters, M. Merrifield, C. Nitschelm, K. Pan, A. Roman-Lopes, T. Storchi-Bergmann, and D. P. Schneider. SDSS-IV MaNGA: Spatially resolved star formation histories in galaxies as a function of galaxy mass and type. *MNRAS*, 466:4731–4758, April 2017. doi: 10.1093/mnras/stw3371.
- A. H. Gonzalez, S. Sivanandam, A. I. Zabludoff, and D. Zaritsky. Galaxy Cluster Baryon Fractions Revisited. *ApJ*, 778:14, November 2013. doi: 10.1088/0004-637X/778/1/14.
- R. M. González Delgado, R. García-Benito, E. Pérez, R. Cid Fernandes, A. L. de Amorim, C. Cortijo-Ferrero, E. A. D. Lacerda, R. López Fernández, N. Vale-Asari, S. F. Sánchez, M. Mollá, T. Ruiz-Lara, P. Sánchez-Blázquez, C. J. Walcher, J. Alves, J. A. L. Aguerri, S. Bekeraité, J. Bland-Hawthorn, L. Galbany, A. Gallazzi, B. Husemann, J. Iglesias-Páramo, V. Kalinova, A. R. López-Sánchez, R. A. Marino, I. Márquez, J. Masegosa, D. Mast, J. Méndez-Abreu, A. Mendoza, A. del Olmo, I. Pérez, A. Quirrenbach, and S. Zibetti. The CALIFA survey across the Hubble sequence. Spatially resolved stellar

- population properties in galaxies. *Astronomy and Astrophysics*, 581:A103, September 2015. doi: 10.1051/0004-6361/201525938.
- A. C. González-García, J. Oñorbe, R. Domínguez-Tenreiro, and M. Á. Gómez-Flechoso. Shape and kinematics of elliptical galaxies: evolution due to merging at $z < 1.5$. *Astronomy and Astrophysics*, 497:35–40, April 2009. doi: 10.1051/0004-6361/200811452.
- T. Goto, C. Yamauchi, Y. Fujita, S. Okamura, M. Sekiguchi, I. Smail, M. Bernardi, and P. L. Gomez. The morphology-density relation in the Sloan Digital Sky Survey. *MNRAS*, 346:601–614, December 2003. doi: 10.1046/j.1365-2966.2003.07114.x.
- F. Governato, B. Willman, L. Mayer, A. Brooks, G. Stinson, O. Valenzuela, J. Wadsley, and T. Quinn. Forming disc galaxies in Λ CDM simulations. *MNRAS*, 374:1479–1494, February 2007. doi: 10.1111/j.1365-2966.2006.11266.x.
- A. Guérou, E. Emsellem, R. M. McDermid, P. Côté, L. Ferrarese, J. P. Blakeslee, P. R. Durrell, L. A. MacArthur, E. W. Peng, J.-C. Cuillandre, and S. Gwyn. The Next Generation Virgo Cluster Survey. XII. Stellar Populations and Kinematics of Compact, Low-mass Early-type Galaxies from Gemini GMOS-IFU Spectroscopy. *ApJ*, 804:70, May 2015. doi: 10.1088/0004-637X/804/1/70.
- A. Guérou, E. Emsellem, D. Krajnović, R. M. McDermid, T. Contini, and P. M. Weilbacher. Exploring the mass assembly of the early-type disc galaxy NGC 3115 with MUSE. *Astronomy and Astrophysics*, 591:A143, July 2016. doi: 10.1051/0004-6361/201628743.
- J. E. Gunn and J. R. Gott, III. On the Infall of Matter Into Clusters of Galaxies and Some Effects on Their Evolution. *ApJ*, 176:1, August 1972. doi: 10.1086/151605.
- Q. Guo, S. Cole, V. Eke, C. Frenk, and J. Helly. Spatial and luminosity distributions of galactic satellites. *MNRAS*, 434:1838–1848, September 2013. doi: 10.1093/mnras/stt903.
- Q. Guo, E. Tempel, and N. I. Libeskind. Galaxies in Filaments have More Satellites: The Influence of the Cosmic Web on the Satellite Luminosity Function in the SDSS. *ApJ*, 800:112, February 2015. doi: 10.1088/0004-637X/800/2/112.
- N. Gupta, A. Saro, J. J. Mohr, K. Dolag, and J. Liu. SZE observables, pressure profiles and centre offsets in Magneticum simulation galaxy clusters. *MNRAS*, 469:3069–3087, August 2017. doi: 10.1093/mnras/stx715.
- F. Haardt and P. Madau. Modelling the UV/X-ray cosmic background with CUBA. In D. M. Neumann and J. T. V. Tran, editors, *Clusters of Galaxies and the High Redshift Universe Observed in X-rays*, 2001.
- I. Hafez. *Abd al-Rahman al-Sufi and his book of the fixed stars: a journey of re-discovery*. PhD thesis, James Cook University, 2010.
- O. Hahn, R. Teyssier, and C. M. Carollo. The large-scale orientations of disc galaxies. *MNRAS*, 405:274–290, June 2010. doi: 10.1111/j.1365-2966.2010.16494.x.

- X. Hernandez and B. Cervantes-Sodi. A dimensional study of disc galaxies. *MNRAS*, 368: 351–360, May 2006. doi: 10.1111/j.1365-2966.2006.10115.x.
- X. Hernandez, C. Park, B. Cervantes-Sodi, and Y.-Y. Choi. Empirical distributions of galactic λ spin parameters from the Sloan Digital Sky Survey. *MNRAS*, 375:163–170, February 2007. doi: 10.1111/j.1365-2966.2006.11274.x.
- L. Hernquist. Tidal triggering of starbursts and nuclear activity in galaxies. *Nat*, 340: 687–691, August 1989. doi: 10.1038/340687a0.
- P. Hickson. Compact Groups of Galaxies. *Annual review of astronomy and astrophysics*, 35:357–388, 1997. doi: 10.1146/annurev.astro.35.1.357.
- M. Hirschmann, K. Dolag, A. Saro, L. Bachmann, S. Borgani, and A. Burkert. Cosmological simulations of black hole growth: AGN luminosities and downsizing. *MNRAS*, 442: 2304–2324, August 2014. doi: 10.1093/mnras/stu1023.
- M. Hirschmann, G. De Lucia, and F. Fontanot. Galaxy assembly, stellar feedback and metal enrichment: the view from the GAEA model. *MNRAS*, June 2016. doi: 10.1093/mnras/stw1318.
- L. Hoffman, T. J. Cox, S. Dutta, and L. Hernquist. Orbital Structure of Merger Remnants. I. Effect of Gas Fraction in Pure Disk Mergers. *ApJ*, 723:818–844, November 2010. doi: 10.1088/0004-637X/723/1/818.
- F. Hoyle and R. A. Lyttleton. The effect of interstellar matter on climatic variation. *Proceedings of the Cambridge Philosophical Society*, 35:405, 1939. doi: 10.1017/S0305004100021150.
- E. P. Hubble. NGC 6822, a remote stellar system. *ApJ*, 62, December 1925. doi: 10.1086/142943.
- E. P. Hubble. A spiral nebula as a stellar system: Messier 33. *ApJ*, 63, May 1926a. doi: 10.1086/142976.
- E. P. Hubble. Extragalactic nebulae. *ApJ*, 64, December 1926b. doi: 10.1086/143018.
- E. P. Hubble. *Realm of the Nebulae*. 1936.
- M. J. Hudson, B. R. Gillis, J. Coupon, H. Hildebrandt, T. Erben, C. Heymans, H. Hoekstra, T. D. Kitching, Y. Mellier, L. Miller, L. Van Waerbeke, C. Bonnett, L. Fu, K. Kuijken, B. Rowe, T. Schrabback, E. Semboloni, E. van Uitert, and M. Velander. CFHTLenS: co-evolution of galaxies and their dark matter haloes. *MNRAS*, 447:298–314, February 2015. doi: 10.1093/mnras/stu2367.
- M. Huertas-Company, M. Bernardi, P. G. Pérez-González, M. L. N. Ashby, G. Barro, C. Conselice, E. Daddi, A. Dekel, P. Dimauro, S. M. Faber, N. A. Grogin, J. S. Kartaltepe, D. D. Kocevski, A. M. Koekemoer, D. C. Koo, S. Mei, and F. Shankar. Mass

- assembly and morphological transformations since $z \sim 3$ from CANDELS. *MNRAS*, 462: 4495–4516, November 2016. doi: 10.1093/mnras/stw1866.
- Y. L. Jaffé, R. Smith, G. N. Candlish, B. M. Poggianti, Y.-K. Sheen, and M. A. W. Verheijen. BUDHIES II: a phase-space view of H I gas stripping and star formation quenching in cluster galaxies. *MNRAS*, 448:1715–1728, April 2015. doi: 10.1093/mnras/stv100.
- P. H. Johansson, T. Naab, and J. P. Ostriker. Forming Early-type Galaxies in Λ CDM Simulations. I. Assembly Histories. *ApJ*, 754:115, August 2012. doi: 10.1088/0004-637X/754/2/115.
- L. R. Jones, T. J. Ponman, and D. A. Forbes. Multiwavelength observations of an evolved galaxy group: an end-point of galaxy merging? *MNRAS*, 312:139–150, February 2000. doi: 10.1046/j.1365-8711.2000.03118.x.
- S. J. Kannappan, J. M. Guie, and A. J. Baker. E/S0 Galaxies on the Blue Color-Stellar Mass Sequence at $z = 0$: Fading Mergers or Future Spirals? *Astronomical Journal*, 138: 579–597, August 2009. doi: 10.1088/0004-6256/138/2/579.
- Immanuel Kant. *Allgemeine Naturgeschichte und Theorie des Himmels*. J. F. Petersen, Königsberg and Leipzig, 1755.
- S. Kaviraj, K. Schawinski, J. E. G. Devriendt, I. Ferreras, S. Khochfar, S.-J. Yoon, S. K. Yi, J.-M. Deharveng, A. Boselli, T. Barlow, T. Conrow, K. Forster, P. G. Friedman, D. C. Martin, P. Morrissey, S. Neff, D. Schiminovich, M. Seibert, T. Small, T. Wyder, L. Bianchi, J. Donas, T. Heckman, Y.-W. Lee, B. Madore, B. Milliard, R. M. Rich, and A. Szalay. UV-Optical Colors As Probes of Early-Type Galaxy Evolution. *ApJS*, 173: 619–642, December 2007. doi: 10.1086/516633.
- T. Kimm, J. Devriendt, A. Slyz, C. Pichon, S. A. Kassin, and Y. Dubois. The angular momentum of baryons and dark matter halos revisited. *ArXiv e-prints (arXiv:1106.0538)*, June 2011.
- E. Komatsu, K. M. Smith, J. Dunkley, C. L. Bennett, B. Gold, G. Hinshaw, N. Jarosik, D. Larson, M. R. Nolta, L. Page, D. N. Spergel, M. Halpern, R. S. Hill, A. Kogut, M. Limon, S. S. Meyer, N. Odegard, G. S. Tucker, J. L. Weiland, E. Wollack, and E. L. Wright. Seven-year Wilkinson Microwave Anisotropy Probe (WMAP) Observations: Cosmological Interpretation. *ApJS*, 192:18, February 2011. doi: 10.1088/0067-0049/192/2/18.
- J. Kormendy and R. Bender. A Proposed Revision of the Hubble Sequence for Elliptical Galaxies. *The Astrophysical Journal, Letters*, 464:L119, June 1996. doi: 10.1086/310095.
- J. Kormendy and R. C. Kennicutt, Jr. Secular Evolution and the Formation of Pseudobulges in Disk Galaxies. *Annual review of astronomy and astrophysics*, 42:603–683, September 2004. doi: 10.1146/annurev.astro.42.053102.134024.

- D. Krajnović, E. Emsellem, M. Cappellari, K. Alatalo, L. Blitz, M. Bois, F. Bournaud, M. Bureau, R. L. Davies, T. A. Davis, P. T. de Zeeuw, S. Khochfar, H. Kuntschner, P.-Y. Lablanche, R. M. McDermid, R. Morganti, T. Naab, T. Oosterloo, M. Sarzi, N. Scott, P. Serra, A.-M. Weijmans, and L. M. Young. The ATLAS^{3D} project - II. Morphologies, kinematic features and alignment between photometric and kinematic axes of early-type galaxies. *MNRAS*, 414:2923–2949, July 2011. doi: 10.1111/j.1365-2966.2011.18560.x.
- A. V. Kravtsov, A. A. Vikhlinin, and A. V. Meshcheryakov. Stellar Mass—Halo Mass Relation and Star Formation Efficiency in High-Mass Halos. *Astronomy Letters*, 44: 8–34, January 2018. doi: 10.1134/S1063773717120015.
- C. d. P. Lagos, T. Theuns, A. R. H. Stevens, L. Cortese, N. D. Padilla, T. A. Davis, S. Contreras, and D. Croton. Angular momentum evolution of galaxies in EAGLE. *MNRAS*, 464:3850–3870, February 2017. doi: 10.1093/mnras/stw2610.
- C. d. P. Lagos, A. R. H. Stevens, R. G. Bower, T. A. Davis, S. Contreras, N. D. Padilla, D. Obreschkow, D. Croton, J. W. Trayford, C. Welker, and T. Theuns. Quantifying the impact of mergers on the angular momentum of simulated galaxies. *MNRAS*, 473: 4956–4974, February 2018. doi: 10.1093/mnras/stx2667.
- P. Lang, N. M. Förster Schreiber, R. Genzel, S. Wuyts, E. Wisnioski, A. Beifiori, S. Belli, R. Bender, G. Brammer, A. Burkert, J. Chan, R. Davies, M. Fossati, A. Galametz, S. K. Kulkarni, D. Lutz, J. T. Mendel, I. G. Momcheva, T. Naab, E. J. Nelson, R. P. Saglia, S. Seitz, S. Tacchella, L. J. Tacconi, K.-i. Tadaki, H. Übler, P. G. van Dokkum, and D. J. Wilman. Falling Outer Rotation Curves of Star-forming Galaxies at $0.6 \lesssim z \lesssim 2.6$ Probed with KMOS^{3D} and SINS/zC-SINF. *ApJ*, 840:92, May 2017. doi: 10.3847/1538-4357/aa6d82.
- R. B. Larson, B. M. Tinsley, and C. N. Caldwell. The evolution of disk galaxies and the origin of S0 galaxies. *ApJ*, 237:692–707, May 1980. doi: 10.1086/157917.
- A. Leauthaud, J. Tinker, K. Bundy, P. S. Behroozi, R. Massey, J. Rhodes, M. R. George, J.-P. Kneib, A. Benson, R. H. Wechsler, M. T. Busha, P. Capak, M. Cortés, O. Ilbert, A. M. Koekemoer, O. Le Fèvre, S. Lilly, H. J. McCracken, M. Salvato, T. Schrabback, N. Scoville, T. Smith, and J. E. Taylor. New Constraints on the Evolution of the Stellar-to-dark Matter Connection: A Combined Analysis of Galaxy-Galaxy Lensing, Clustering, and Stellar Mass Functions from $z = 0.2$ to $z = 1$. *ApJ*, 744:159, January 2012. doi: 10.1088/0004-637X/744/2/159.
- S.-K. Lee, M. Im, J.-W. Kim, J. Lotz, C. McPartland, M. Peth, and A. Koekemoer. Evolution of Star-formation Properties of High-redshift Cluster Galaxies since $z = 2$. *ApJ*, 810:90, September 2015. doi: 10.1088/0004-637X/810/2/90.
- J. F. Lees, G. R. Knapp, M. P. Rupen, and T. G. Phillips. Molecular gas in elliptical galaxies. *ApJ*, 379:177–215, September 1991. doi: 10.1086/170494.
- A. K. Leroy, F. Walter, E. Brinks, F. Bigiel, W. J. G. de Blok, B. Madore, and M. D.

- Thornley. The Star Formation Efficiency in Nearby Galaxies: Measuring Where Gas Forms Stars Effectively. *Astronomical Journal*, 136:2782–2845, December 2008. doi: 10.1088/0004-6256/136/6/2782.
- S. Lilly, D. Schade, R. Ellis, O. Le Fèvre, J. Brinchmann, L. Tresse, R. Abraham, F. Hammer, D. Crampton, M. Colless, K. Glazebrook, G. Mallen-Ornelas, and T. Broadhurst. Hubble Space Telescope Imaging of the CFRS and LDSS Redshift Surveys. II. Structural Parameters and the Evolution of disk Galaxies to $z \sim 1^1$. *ApJ*, 500:75–94, June 1998. doi: 10.1086/305713.
- L. Liu, B. F. Gerke, R. H. Wechsler, P. S. Behroozi, and M. T. Busha. How Common are the Magellanic Clouds? *ApJ*, 733:62, May 2011. doi: 10.1088/0004-637X/733/1/62.
- Malcolm S. Longair. *Galaxy Formation*. Springer Berlin Heidelberg, second edition, 2008.
- C. López-Sanjuan, O. Le Fèvre, O. Ilbert, L. A. M. Tasca, C. Bridge, O. Cucciati, P. Kampczyk, L. Pozzetti, C. K. Xu, C. M. Carollo, T. Contini, J.-P. Kneib, S. J. Lilly, V. Mainieri, A. Renzini, D. Sanders, M. Scodreggio, N. Z. Scoville, Y. Taniguchi, G. Zamorani, H. Aussel, S. Bardelli, M. Bolzonella, A. Bongiorno, P. Capak, K. Caputi, S. de la Torre, L. de Ravel, P. Franzetti, B. Garilli, A. Iovino, C. Knobel, K. Kovač, F. Lamareille, J.-F. Le Borgne, V. Le Brun, E. Le Floc’h, C. Maier, H. J. McCracken, M. Mignoli, R. Pelló, Y. Peng, E. Pérez-Montero, V. Presotto, E. Ricciardelli, M. Salvato, J. D. Silverman, M. Tanaka, L. Tresse, D. Vergani, E. Zucca, L. Barnes, R. Bordoloi, A. Cappi, A. Cimatti, G. Coppa, A. Koekemoer, C. T. Liu, M. Moresco, P. Nair, P. Oesch, K. Schawinski, and N. Welikala. The dominant role of mergers in the size evolution of massive early-type galaxies since $z \sim 1$. *Astronomy and Astrophysics*, 548:A7, December 2012. doi: 10.1051/0004-6361/201219085.
- J. M. Lotz, P. Madau, M. Giavalisco, J. Primack, and H. C. Ferguson. The Rest-Frame Far-Ultraviolet Morphologies of Star-forming Galaxies at $z \sim 1.5$ and 4. *ApJ*, 636:592–609, January 2006. doi: 10.1086/497950.
- A. V. Macciò, A. A. Dutton, and F. C. van den Bosch. Concentration, spin and shape of dark matter haloes as a function of the cosmological model: WMAP1, WMAP3 and WMAP5 results. *MNRAS*, 391:1940–1954, December 2008. doi: 10.1111/j.1365-2966.2008.14029.x.
- G. A. Mamon. Are cluster ellipticals the products of mergers? *The Astrophysical Journal, Letters*, 401:L3–L6, December 1992. doi: 10.1086/186656.
- R. Mandelbaum, U. Seljak, G. Kauffmann, C. M. Hirata, and J. Brinkmann. Galaxy halo masses and satellite fractions from galaxy-galaxy lensing in the Sloan Digital Sky Survey: stellar mass, luminosity, morphology and environment dependencies. *MNRAS*, 368:715–731, May 2006. doi: 10.1111/j.1365-2966.2006.10156.x.
- R. Mandelbaum, W. Wang, Y. Zu, S. White, B. Henriques, and S. More. Strong bimodality

- in the host halo mass of central galaxies from galaxy-galaxy lensing. *MNRAS*, 457:3200–3218, April 2016. doi: 10.1093/mnras/stw188.
- E. Mármol-Queraltó, I. Trujillo, P. G. Pérez-González, J. Varela, and G. Barro. Satellites around massive galaxies since $z \sim 2$. *MNRAS*, 422:2187–2194, May 2012. doi: 10.1111/j.1365-2966.2012.20765.x.
- T. P. K. Martinsson, M. A. W. Verheijen, K. B. Westfall, M. A. Bershadsky, D. R. Andersen, and R. A. Swaters. The DiskMass Survey. VII. The distribution of luminous and dark matter in spiral galaxies. *Astronomy and Astrophysics*, 557:A131, September 2013. doi: 10.1051/0004-6361/201321390.
- K. L. Masters, M. Mosleh, A. K. Romer, R. C. Nichol, S. P. Bamford, K. Schawinski, C. J. Lintott, D. Andreescu, H. C. Campbell, B. Crowcroft, I. Doyle, E. M. Edmondson, P. Murray, M. J. Raddick, A. Slosar, A. S. Szalay, and J. Vandenberg. Galaxy Zoo: passive red spirals. *MNRAS*, 405:783–799, June 2010. doi: 10.1111/j.1365-2966.2010.16503.x.
- R. M. McDermid, R. Bacon, H. Kuntschner, E. Emsellem, K. L. Shapiro, M. Bureau, M. Cappellari, R. L. Davies, J. Falcón-Barroso, D. Krajnović, R. F. Peletier, M. Sarzi, and T. de Zeeuw. Stellar kinematics and populations of early-type galaxies with the SAURON and OASIS integral-field spectrographs. *New Astronomy Review*, 49:521–535, January 2006. doi: 10.1016/j.newar.2005.10.025.
- R. M. McDermid, K. Alatalo, L. Blitz, F. Bournaud, M. Bureau, M. Cappellari, A. F. Crocker, R. L. Davies, T. A. Davis, P. T. de Zeeuw, P.-A. Duc, E. Emsellem, S. Khochfar, D. Krajnović, H. Kuntschner, R. Morganti, T. Naab, T. Oosterloo, M. Sarzi, N. Scott, P. Serra, A.-M. Weijmans, and L. M. Young. The ATLAS^{3D} Project - XXX. Star formation histories and stellar population scaling relations of early-type galaxies. *MNRAS*, 448:3484–3513, April 2015. doi: 10.1093/mnras/stv105.
- M. McDonald, B. A. Benson, A. Vikhlinin, K. A. Aird, S. W. Allen, M. Bautz, M. Bayliss, L. E. Bleem, and et al. The Redshift Evolution of the Mean Temperature, Pressure, and Entropy Profiles in 80 SPT-Selected Galaxy Clusters. *ApJ*, 794:67, October 2014. doi: 10.1088/0004-637X/794/1/67.
- D. Merritt. Relaxation and tidal stripping in rich clusters of galaxies. II. Evolution of the luminosity distribution. *ApJ*, 276:26–37, January 1984. doi: 10.1086/161590.
- A. Meza, J. F. Navarro, M. Steinmetz, and V. R. Eke. Simulations of Galaxy Formation in a Λ CDM Universe. III. The Dissipative Formation of an Elliptical Galaxy. *ApJ*, 590:619–635, June 2003. doi: 10.1086/375151.
- P. D. Mitchell, C. G. Lacey, C. M. Baugh, and S. Cole. The evolution of the stellar mass versus halo mass relationship. *MNRAS*, 456:1459–1483, February 2016. doi: 10.1093/mnras/stv2741.

- H. J. Mo, S. Mao, and S. D. M. White. The formation of galactic discs. *MNRAS*, 295: 319–336, April 1998. doi: 10.1046/j.1365-8711.1998.01227.x.
- C. E. Moody, A. J. Romanowsky, T. J. Cox, G. S. Novak, and J. R. Primack. Simulating multiple merger pathways to the central kinematics of early-type galaxies. *MNRAS*, 444: 1475–1485, October 2014. doi: 10.1093/mnras/stu1444.
- B. Moore, N. Katz, G. Lake, A. Dressler, and A. Oemler. Galaxy harassment and the evolution of clusters of galaxies. *Nat*, 379:613–616, February 1996. doi: 10.1038/379613a0.
- B. Moore, G. Lake, and N. Katz. Morphological Transformation from Galaxy Harassment. *ApJ*, 495:139–151, March 1998. doi: 10.1086/305264.
- S. More, F. C. van den Bosch, M. Cacciato, R. Skibba, H. J. Mo, and X. Yang. Satellite kinematics - III. Halo masses of central galaxies in SDSS. *MNRAS*, 410:210–226, January 2011. doi: 10.1111/j.1365-2966.2010.17436.x.
- B. P. Moster, R. S. Somerville, C. Maubetsch, F. C. van den Bosch, A. V. Macciò, T. Naab, and L. Oser. Constraints on the Relationship between Stellar Mass and Halo Mass at Low and High Redshift. *ApJ*, 710:903–923, February 2010. doi: 10.1088/0004-637X/710/2/903.
- B. P. Moster, T. Naab, and S. D. M. White. Galactic star formation and accretion histories from matching galaxies to dark matter haloes. *MNRAS*, 428:3121–3138, February 2013. doi: 10.1093/mnras/sts261.
- Viatcheslav Mukhanov. *Physical Foundations of Cosmology*. Cambridge University Press, first edition, 2005.
- F. Munshi, F. Governato, A. M. Brooks, C. Christensen, S. Shen, S. Loebman, B. Moster, T. Quinn, and J. Wadsley. Reproducing the Stellar Mass/Halo Mass Relation in Simulated Λ CDM Galaxies: Theory versus Observational Estimates. *ApJ*, 766:56, March 2013. doi: 10.1088/0004-637X/766/1/56.
- G. Murante, P. Monaco, S. Borgani, L. Tornatore, K. Dolag, and D. Goz. Simulating realistic disc galaxies with a novel sub-resolution ISM model. *MNRAS*, 447:178–201, February 2015. doi: 10.1093/mnras/stu2400.
- T. Naab and J. P. Ostriker. Theoretical Challenges in Galaxy Formation. *Annual review of astronomy and astrophysics*, 55:59–109, August 2017. doi: 10.1146/annurev-astro-081913-040019.
- T. Naab, R. Jesseit, and A. Burkert. The influence of gas on the structure of merger remnants. *MNRAS*, 372:839–852, October 2006. doi: 10.1111/j.1365-2966.2006.10902.x.
- T. Naab, P. H. Johansson, and J. P. Ostriker. Minor Mergers and the Size Evolution of Elliptical Galaxies. *The Astrophysical Journal, Letters*, 699:L178–L182, July 2009. doi: 10.1088/0004-637X/699/2/L178.

- T. Naab, L. Oser, E. Emsellem, M. Cappellari, D. Krajnović, R. M. McDermid, K. Alatalo, E. Bayet, L. Blitz, M. Bois, F. Bournaud, M. Bureau, A. Crocker, R. L. Davies, T. A. Davis, P. T. de Zeeuw, P.-A. Duc, M. Hirschmann, P. H. Johansson, S. Khochfar, H. Kuntschner, R. Morganti, T. Oosterloo, M. Sarzi, N. Scott, P. Serra, G. van de Ven, A. Weijmans, and L. M. Young. The ATLAS^{3D} project - XXV. Two-dimensional kinematic analysis of simulated galaxies and the cosmological origin of fast and slow rotators. *MNRAS*, 444:3357–3387, November 2014. doi: 10.1093/mnras/stt1919.
- J. F. Navarro and W. Benz. Dynamics of cooling gas in galactic dark halos. *ApJ*, 380:320–329, October 1991. doi: 10.1086/170590.
- J. F. Navarro and M. Steinmetz. The Effects of a Photoionizing Ultraviolet Background on the Formation of Disk Galaxies. *ApJ*, 478:13–28, March 1997.
- J. F. Navarro and S. D. M. White. Simulations of dissipative galaxy formation in hierarchically clustering universes-2. Dynamics of the baryonic component in galactic haloes. *MNRAS*, 267:401–412, March 1994.
- A. M. Nierenberg, M. W. Auger, T. Treu, P. J. Marshall, C. D. Fassnacht, and M. T. Busha. Luminous Satellites. II. Spatial Distribution, Luminosity Function, and Cosmic Evolution. *ApJ*, 752:99, June 2012. doi: 10.1088/0004-637X/752/2/99.
- A. M. Nierenberg, T. Treu, N. Menci, Y. Lu, P. Torrey, and M. Vogelsberger. The missing satellite problem in 3D. *MNRAS*, 462:4473–4481, November 2016. doi: 10.1093/mnras/stw1860.
- D. Obreschkow and K. Glazebrook. Fundamental Mass-Spin-Morphology Relation Of Spiral Galaxies. *ApJ*, 784:26, March 2014. doi: 10.1088/0004-637X/784/1/26.
- D. Obreschkow, K. Glazebrook, R. Bassett, D. B. Fisher, R. G. Abraham, E. Wisnioski, A. W. Green, P. J. McGregor, I. Damjanov, A. Popping, and I. Jørgensen. Low Angular Momentum in Clumpy, Turbulent Disk Galaxies. *ApJ*, 815:97, December 2015. doi: 10.1088/0004-637X/815/2/97.
- P. A. Oesch, R. J. Bouwens, C. M. Carollo, G. D. Illingworth, M. Trenti, M. Stiavelli, D. Magee, I. Labbé, and M. Franx. Structure and Morphologies of $z \sim 7-8$ Galaxies from Ultra-deep WFC3/IR Imaging of the Hubble Ultra-deep Field. *The Astrophysical Journal, Letters*, 709:L21–L25, January 2010. doi: 10.1088/2041-8205/709/1/L21.
- T. Okamoto, V. R. Eke, C. S. Frenk, and A. Jenkins. Effects of feedback on the morphology of galaxy discs. *MNRAS*, 363:1299–1314, November 2005. doi: 10.1111/j.1365-2966.2005.09525.x.
- L. Oser, J. P. Ostriker, T. Naab, P. H. Johansson, and A. Burkert. The Two Phases of Galaxy Formation. *ApJ*, 725:2312–2323, December 2010. doi: 10.1088/0004-637X/725/2/2312.

- P. Padovani and F. Matteucci. Stellar Mass Loss in Elliptical Galaxies and the Fueling of Active Galactic Nuclei. *ApJ*, 416:26, October 1993. doi: 10.1086/173212.
- S. Paudel, T. Lisker, and H. Kuntschner. Nuclei of early-type dwarf galaxies: insights from stellar populations. *MNRAS*, 413:1764–1776, May 2011. doi: 10.1111/j.1365-2966.2011.18256.x.
- P. J. E. Peebles. Origin of the Angular Momentum of Galaxies. *ApJ*, 155:393, February 1969. doi: 10.1086/149876.
- P. J. E. Peebles. Rotation of Galaxies and the Gravitational Instability Picture. *Astronomy and Astrophysics*, 11:377, April 1971.
- P. J. E. Peebles. *Principles of Physical Cosmology*. Princeton University Press, first edition, 1993.
- S. Peirani, R. Mohayaee, and J. A. de Freitas Pacheco. The angular momentum of dark haloes: merger and accretion effects. *MNRAS*, 348:921–931, March 2004. doi: 10.1111/j.1365-2966.2004.07412.x.
- Y. Peng, R. Maiolino, and R. Cochrane. Strangulation as the primary mechanism for shutting down star formation in galaxies. *Nat*, 521:192–195, May 2015. doi: 10.1038/nature14439.
- Y.-j. Peng, S. J. Lilly, K. Kovač, M. Bolzonella, L. Pozzetti, A. Renzini, G. Zamorani, O. Ilbert, C. Knobel, A. Iovino, C. Maier, O. Cucciati, L. Tasca, C. M. Carollo, J. Silverman, P. Kampczyk, L. de Ravel, D. Sanders, N. Scoville, T. Contini, V. Mainieri, M. Scodreggio, J.-P. Kneib, O. Le Fèvre, S. Bardelli, A. Bongiorno, K. Caputi, G. Coppa, S. de la Torre, P. Franzetti, B. Garilli, F. Lamareille, J.-F. Le Borgne, V. Le Brun, M. Mignoli, E. Perez Montero, R. Pello, E. Ricciardelli, M. Tanaka, L. Tresse, D. Vergani, N. Welikala, E. Zucca, P. Oesch, U. Abbas, L. Barnes, R. Bordoloi, D. Bottini, A. Cappi, P. Cassata, A. Cimatti, M. Fumana, G. Hasinger, A. Koekemoer, A. Leauthaud, D. Maccagni, C. Marinoni, H. McCracken, P. Memeo, B. Meneux, P. Nair, C. Porciani, V. Presotto, and R. Scaramella. Mass and Environment as Drivers of Galaxy Evolution in SDSS and zCOSMOS and the Origin of the Schechter Function. *ApJ*, 721:193–221, September 2010. doi: 10.1088/0004-637X/721/1/193.
- Donald Perkins. *Particle Astrophysics*. Oxford University Press, first edition, 2003.
- C. Pichon, D. Pogosyan, T. Kimm, A. Slyz, J. Devriendt, and Y. Dubois. Rigging dark haloes: why is hierarchical galaxy formation consistent with the inside-out build-up of thin discs? *MNRAS*, 418:2493–2507, December 2011. doi: 10.1111/j.1365-2966.2011.19640.x.
- Planck Collaboration, P. A. R. Ade, N. Aghanim, M. Arnaud, M. Ashdown, F. Atrio-Barandela, J. Aumont, C. Baccigalupi, A. Balbi, A. J. Banday, and et al. Planck intermediate results. V. Pressure profiles of galaxy clusters from the Sunyaev-Zeldovich

- effect. *Astronomy and Astrophysics*, 550:A131, February 2013. doi: 10.1051/0004-6361/201220040.
- J. R. Primack. Cosmological Structure Formation. *ArXiv e-prints (arXiv:1505.02821)*, May 2015.
- R.-S. Remus and K. Dolag. Connecting Small and Large Scales: The Role of Feedback in Establishing Global Galaxy Properties over Cosmic Times. In *The Interplay between Local and Global Processes in Galaxies*, page 43, June 2016.
- R.-S. Remus, A. Burkert, K. Dolag, P. H. Johansson, T. Naab, L. Oser, and J. Thomas. The Dark Halo—Spheroid Conspiracy and the Origin of Elliptical Galaxies. *ApJ*, 766:71, April 2013. doi: 10.1088/0004-637X/766/2/71.
- R.-S. Remus, K. Dolag, L. K. Bachmann, A. M. Beck, A. Burkert, M. Hirschmann, and A. Teklu. Disk Galaxies in the Magneticum Pathfinder Simulations. In B. L. Ziegler, F. Combes, H. Dannerbauer, and M. Verdugo, editors, *IAU Symposium*, volume 309 of *IAU Symposium*, pages 145–148, February 2015. doi: 10.1017/S1743921314009491.
- R.-S. Remus, K. Dolag, and T. Hoffmann. The Outer Halos of Very Massive Galaxies: BCGs and their DSC in the Magneticum Simulations. *Galaxies*, 5:49, September 2017a. doi: 10.3390/galaxies5030049.
- R.-S. Remus, K. Dolag, T. Naab, A. Burkert, M. Hirschmann, T. L. Hoffmann, and P. H. Johansson. The co-evolution of total density profiles and central dark matter fractions in simulated early-type galaxies. *MNRAS*, 464:3742–3756, January 2017b. doi: 10.1093/mnras/stw2594.
- R. Reyes, R. Mandelbaum, J. E. Gunn, R. Nakajima, U. Seljak, and C. M. Hirata. Optical-to-virial velocity ratios of local disc galaxies from combined kinematics and galaxy-galaxy lensing. *MNRAS*, 425:2610–2640, October 2012. doi: 10.1111/j.1365-2966.2012.21472.x.
- A. Rodríguez-Puebla, V. Avila-Reese, X. Yang, S. Foucaud, N. Drory, and Y. P. Jing. The Stellar-to-Halo Mass Relation of Local Galaxies Segregates by Color. *ApJ*, 799:130, February 2015. doi: 10.1088/0004-637X/799/2/130.
- A. J. Romanowsky and S. M. Fall. Angular Momentum and Galaxy Formation Revisited. *ApJS*, 203:17, December 2012. doi: 10.1088/0067-0049/203/2/17.
- B. Röttgers and A. Arth. SPH to Grid: a new integral conserving method. *ArXiv e-prints (arXiv:1803.03652)*, March 2018.
- Michael Rowan-Robinson. *Cosmology*. Oxford University Press, fourth edition, 2004.
- V. C. Rubin, N. Thonnard, and W. K. Ford, Jr. Extended rotation curves of high-luminosity spiral galaxies. IV - Systematic dynamical properties, SA through SC. *The Astrophysical Journal, Letters*, 225:L107–L111, November 1978. doi: 10.1086/182804.

- P. Ruiz, I. Trujillo, and E. Marmol-Queralt. The abundance of satellites depends strongly on the morphology of the host galaxy. *MNRAS*, 454:1605–1619, December 2015. doi: 10.1093/mnras/stv2030.
- L. V. Sales, J. F. Navarro, T. Theuns, J. Schaye, S. D. M. White, C. S. Frenk, R. A. Crain, and C. Dalla Vecchia. The origin of discs and spheroids in simulated galaxies. *MNRAS*, 423:1544–1555, June 2012. doi: 10.1111/j.1365-2966.2012.20975.x.
- S. Salim and R. M. Rich. Star Formation Signatures in Optically Quiescent Early-type Galaxies. *The Astrophysical Journal, Letters*, 714:L290–L294, May 2010. doi: 10.1088/2041-8205/714/2/L290.
- I. San Roman, A. J. Cenarro, L. A. Daz-Garca, C. Lpez-Sanjuan, J. Varela, R. M. Gonzlez Delgado, P. Snchez-Blzquez, E. J. Alfaro, B. Ascaso, S. Bonoli, A. Borlaff, F. J. Castander, M. Cervio, A. Fernndez-Soto, I. Mrquez, J. Masegosa, D. Muniesa, M. Povi, K. Viironen, J. A. L. Aguerri, N. Bentez, T. Broadhurst, J. Cabrera-Cao, J. Cepa, D. Cristbal-Hornillos, L. Infante, V. J. Martnez, M. Moles, A. del Olmo, J. Perea, F. Prada, and J. M. Quintana. The ALHAMBRA survey: 2D analysis of the stellar populations in massive early-type galaxies at $z < 0.3$. *Astronomy and Astrophysics*, 609:A20, January 2018. doi: 10.1051/0004-6361/201630313.
- S. F. Snchez, R. C. Kennicutt, A. Gil de Paz, G. van de Ven, J. M. Vlchez, L. Wisotzki, C. J. Walcher, D. Mast, J. A. L. Aguerri, S. Albiol-Prez, A. Alonso-Herrero, J. Alves, J. Bakos, T. Bartkov, J. Bland-Hawthorn, A. Boselli, D. J. Bomans, A. Castillo-Morales, C. Cortijo-Ferrero, A. de Lorenzo-Cceres, A. Del Olmo, R.-J. Dettmar, A. Daz, S. Ellis, J. Falcn-Barroso, H. Flores, A. Gallazzi, B. Garca-Lorenzo, R. Gonzlez Delgado, N. Gruel, T. Haines, C. Hao, B. Husemann, J. Iglsias-Pramo, K. Jahnke, B. Johnson, B. Jungwiert, V. Kalinova, C. Kehrig, D. Kupko, . R. Lpez-Snchez, M. Lyubenova, R. A. Marino, E. Mrmol-Queralt, I. Mrquez, J. Masegosa, S. Meidt, J. Mendez-Abreu, A. Monreal-Ibero, C. Montijo, A. M. Mouro, G. Palacios-Navarro, P. Papaderos, A. Pasquali, R. Peletier, E. Prez, I. Prez, A. Quirrenbach, M. Relao, F. F. Rosales-Ortega, M. M. Roth, T. Ruiz-Lara, P. Snchez-Blzquez, C. Sengupta, R. Singh, V. Stanishev, S. C. Trager, A. Vazdekis, K. Viironen, V. Wild, S. Zibetti, and B. Ziegler. CALIFA, the Calar Alto Legacy Integral Field Area survey. I. Survey presentation. *Astronomy and Astrophysics*, 538:A8, February 2012. doi: 10.1051/0004-6361/201117353.
- A. Sandage. *The Hubble Atlas of Galaxies*. 1961.
- C. Scannapieco, P. B. Tissera, S. D. M. White, and V. Springel. Effects of supernova feedback on the formation of galaxy discs. *MNRAS*, 389:1137–1149, September 2008. doi: 10.1111/j.1365-2966.2008.13678.x.
- C. Scannapieco, S. D. M. White, V. Springel, and P. B. Tissera. The formation and survival of discs in a Λ CDM universe. *MNRAS*, 396:696–708, June 2009. doi: 10.1111/j.1365-2966.2009.14764.x.

- C. Scannapieco, M. Wadepuhl, O. H. Parry, J. F. Navarro, A. Jenkins, V. Springel, R. Teyssier, E. Carlson, H. M. P. Couchman, R. A. Crain, C. Dalla Vecchia, C. S. Frenk, C. Kobayashi, P. Monaco, G. Murante, T. Okamoto, T. Quinn, J. Schaye, G. S. Stinson, T. Theuns, J. Wadsley, S. D. M. White, and R. Woods. The Aquila comparison project: the effects of feedback and numerical methods on simulations of galaxy formation. *MNRAS*, 423:1726–1749, June 2012. doi: 10.1111/j.1365-2966.2012.20993.x.
- K. Schawinski, C. Lintott, D. Thomas, M. Sarzi, D. Andreescu, S. P. Bamford, S. Kaviraj, S. Khochfar, K. Land, P. Murray, R. C. Nichol, M. J. Raddick, A. Slosar, A. Szalay, J. VandenBerg, and S. K. Yi. Galaxy Zoo: a sample of blue early-type galaxies at low redshift*. *MNRAS*, 396:818–829, June 2009. doi: 10.1111/j.1365-2966.2009.14793.x.
- J. Schaye, C. Dalla Vecchia, C. M. Booth, R. P. C. Wiersma, T. Theuns, M. R. Haas, S. Bertone, A. R. Duffy, I. G. McCarthy, and F. van de Voort. The physics driving the cosmic star formation history. *MNRAS*, 402:1536–1560, March 2010. doi: 10.1111/j.1365-2966.2009.16029.x.
- Schlachtberger, D.P. The origin of cold gas in the center of massive elliptical galaxies. Master’s thesis, Ludwig-Maximilians-Universität München, 2014.
- Peter Schneider. *Einführung in die Extragalaktische Astronomie und Kosmologie*. Springer Berlin Heidelberg, first edition, 2008.
- F. Schulze, R.-S. Remus, and K. Dolag. On the Kinematics, Stability and Lifetime of Kinematically Distinct Cores: A Case Study. *Galaxies*, 5:41, August 2017. doi: 10.3390/galaxies5030041.
- F. Schulze, R.-S. Remus, K. Dolag, A. Burkert, E. Emsellem, and G. van de Ven. Kinematics of simulated galaxies - I. Connecting dynamical and morphological properties of early-type galaxies at different redshifts. *MNRAS*, 480:4636–4658, November 2018. doi: 10.1093/mnras/sty2090.
- N. Scott, S. Brough, S. M. Croom, R. L. Davies, J. van de Sande, J. T. Allen, J. Bland-Hawthorn, J. J. Bryant, L. Cortese, F. D’Eugenio, C. Federrath, I. Ferreras, M. Goodwin, B. Groves, I. Konstantopoulos, J. S. Lawrence, A. M. Medling, A. J. Moffett, M. S. Owers, S. Richards, A. S. G. Robotham, C. Tonini, and S. K. Yi. The SAMI Galaxy Survey: global stellar populations on the size-mass plane. *MNRAS*, 472:2833–2855, December 2017. doi: 10.1093/mnras/stx2166.
- J. L. Sersic. *Atlas de Galaxias Australes*. 1968.
- N. I. Shakura and R. A. Sunyaev. Black holes in binary systems. Observational appearance. *Astronomy and Astrophysics*, 24:337–355, 1973.
- F. Shankar, H. Guo, V. Bouillot, A. Rettura, A. Meert, S. Buchan, A. Kravtsov, M. Bernardi, R. Sheth, V. Vikram, D. Marchesini, P. Behroozi, Z. Zheng, C. Maraston, B. Ascaso, B. C. Lemaux, D. Capozzi, M. Huertas-Company, R. R. Gal, L. M.

- Lubin, C. J. Conselice, M. Carollo, and A. Cattaneo. On the Intermediate-redshift Central Stellar Mass-Halo Mass Relation, and Implications for the Evolution of the Most Massive Galaxies Since $z \sim 1$. *The Astrophysical Journal, Letters*, 797:L27, December 2014. doi: 10.1088/2041-8205/797/2/L27.
- S. Sharma and M. Steinmetz. The Angular Momentum Distribution of Gas and Dark Matter in Galactic Halos. *ApJ*, 628:21–44, July 2005. doi: 10.1086/430660.
- S. Sharma, M. Steinmetz, and J. Bland-Hawthorn. On the Origin of the Angular Momentum Properties of Gas and Dark Matter in Galactic Halos and Its Implications. *ApJ*, 750:107, May 2012. doi: 10.1088/0004-637X/750/2/107.
- S. Shen, H. J. Mo, S. D. M. White, M. R. Blanton, G. Kauffmann, W. Voges, J. Brinkmann, and I. Csabai. The size distribution of galaxies in the Sloan Digital Sky Survey. *MNRAS*, 343:978–994, August 2003. doi: 10.1046/j.1365-8711.2003.06740.x.
- D. Sijacki, V. Springel, T. Di Matteo, and L. Hernquist. A unified model for AGN feedback in cosmological simulations of structure formation. *MNRAS*, 380:877–900, September 2007. doi: 10.1111/j.1365-2966.2007.12153.x.
- D. Sijacki, M. Vogelsberger, D. Kereš, V. Springel, and L. Hernquist. Moving mesh cosmology: the hydrodynamics of galaxy formation. *MNRAS*, 424:2999–3027, August 2012. doi: 10.1111/j.1365-2966.2012.21466.x.
- R. C. Simons, S. A. Kassin, B. J. Weiner, S. M. Faber, J. R. Trump, T. M. Heckman, D. C. Koo, C. Pacifici, J. R. Primack, G. F. Snyder, and A. de la Vega. $z \sim 2$: An Epoch of Disk Assembly. *ApJ*, 843:46, July 2017. doi: 10.3847/1538-4357/aa740c.
- L. Spitzer. *Physics of Fully Ionized Gases*. 1962.
- V. Springel. Modelling star formation and feedback in simulations of interacting galaxies. *MNRAS*, 312:859–879, March 2000. doi: 10.1046/j.1365-8711.2000.03187.x.
- V. Springel. The cosmological simulation code GADGET-2. *MNRAS*, 364:1105–1134, December 2005. doi: 10.1111/j.1365-2966.2005.09655.x.
- V. Springel and L. Hernquist. Cosmological smoothed particle hydrodynamics simulations: a hybrid multiphase model for star formation. *MNRAS*, 339:289–311, February 2003. doi: 10.1046/j.1365-8711.2003.06206.x.
- V. Springel and L. Hernquist. Formation of a Spiral Galaxy in a Major Merger. *The Astrophysical Journal, Letters*, 622:L9–L12, March 2005. doi: 10.1086/429486.
- V. Springel, S. D. M. White, G. Tormen, and G. Kauffmann. Populating a cluster of galaxies - I. Results at $z=0$. *MNRAS*, 328:726–750, December 2001a. doi: 10.1046/j.1365-8711.2001.04912.x.
- V. Springel, N. Yoshida, and S. D. M. White. GADGET: a code for collisionless and

- gasdynamical cosmological simulations. *Nat*, 6:79–117, April 2001b. doi: 10.1016/S1384-1076(01)00042-2.
- V. Springel, T. Di Matteo, and L. Hernquist. Modelling feedback from stars and black holes in galaxy mergers. *MNRAS*, 361:776–794, August 2005. doi: 10.1111/j.1365-2966.2005.09238.x.
- L. K. Steinborn, K. Dolag, M. Hirschmann, M. A. Prieto, and R.-S. Remus. A refined sub-grid model for black hole accretion and AGN feedback in large cosmological simulations. *MNRAS*, 448:1504–1525, April 2015. doi: 10.1093/mnras/stv072.
- L. K. Steinborn, K. Dolag, J. M. Comerford, M. Hirschmann, R.-S. Remus, and A. F. Teklu. Origin and properties of dual and offset active galactic nuclei in a cosmological simulation at $z=2$. *MNRAS*, 458:1013–1028, May 2016. doi: 10.1093/mnras/stw316.
- K. R. Stewart, T. Kaufmann, J. S. Bullock, E. J. Barton, A. H. Maller, J. Diemand, and J. Wadsley. Orbiting Circumgalactic Gas as a Signature of Cosmological Accretion. *ApJ*, 738:39, September 2011. doi: 10.1088/0004-637X/738/1/39.
- K. R. Stewart, A. M. Brooks, J. S. Bullock, A. H. Maller, J. Diemand, J. Wadsley, and L. A. Moustakas. Angular Momentum Acquisition in Galaxy Halos. *ApJ*, 769:74, May 2013. doi: 10.1088/0004-637X/769/1/74.
- I. Strateva, Ž. Ivezić, G. R. Knapp, V. K. Narayanan, M. A. Strauss, J. E. Gunn, R. H. Lupton, D. Schlegel, N. A. Bahcall, J. Brinkmann, R. J. Brunner, T. Budavári, I. Csabai, F. J. Castander, M. Doi, M. Fukugita, Z. Győry, M. Hamabe, G. Hennessy, T. Ichikawa, P. Z. Kunszt, D. Q. Lamb, T. A. McKay, S. Okamura, J. Racusin, M. Sekiguchi, D. P. Schneider, K. Shimasaku, and D. York. Color Separation of Galaxy Types in the Sloan Digital Sky Survey Imaging Data. *Astronomical Journal*, 122:1861–1874, October 2001. doi: 10.1086/323301.
- B. Swedenborg. *Principia rerum naturalium; sive novarum tentaminum phenomena mundi elementaris philosophia explicandi (English translation: Rendell, J.R. & Tansley, I., 1912, Swedenborg Society, London), Part III, Chap. I-II*. 1734.
- A. F. Teklu, R.-S. Remus, K. Dolag, A. M. Beck, A. Burkert, A. S. Schmidt, F. Schulze, and L. K. Steinborn. Connecting Angular Momentum and Galactic Dynamics: The Complex Interplay between Spin, Mass, and Morphology. *ApJ*, 812:29, October 2015. doi: 10.1088/0004-637X/812/1/29.
- A. F. Teklu, R.-S. Remus, and K. Dolag. Dynamical Properties of Galaxies with Different Morphological Types at $z=0$ and $z=2$. In *The Interplay between Local and Global Processes in Galaxies*, June 2016.
- A. F. Teklu, R.-S. Remus, K. Dolag, and A. Burkert. The morphology-density relation: impact on the satellite fraction. *MNRAS*, 472:4769–4785, December 2017. doi: 10.1093/mnras/stx2303.

- A. F. Teklu, R.-S. Remus, K. Dolag, A. Arth, A. Burkert, A. Obreja, and F. Schulze. Declining Rotation Curves at $z = 2$ in Λ CDM Galaxy Formation Simulations. *The Astrophysical Journal, Letters*, 854:L28, February 2018. doi: 10.3847/2041-8213/aaeb4.
- F.-K. Thielemann, D. Argast, F. Brachwitz, W. R. Hix, P. Höflich, M. Liebendörfer, G. Martinez-Pinedo, A. Mezzacappa, I. Panov, and T. Rauscher. Nuclear cross sections, nuclear structure and stellar nucleosynthesis. *Nuclear Physics A*, 718:139–146, May 2003. doi: 10.1016/S0375-9474(03)00704-8.
- R. Thomas, O. Le Fèvre, M. Scodeggio, P. Cassata, B. Garilli, V. Le Brun, B. C. Lemaux, D. Maccagni, J. Pforr, L. A. M. Tasca, G. Zamorani, S. Bardelli, N. P. Hathi, L. Tresse, E. Zucca, and A. M. Koekemoer. The extended epoch of galaxy formation: Age dating of 3600 galaxies with $2 < z < 6.5$ in the VIMOS Ultra-Deep Survey. *Astronomy and Astrophysics*, 602:A35, June 2017. doi: 10.1051/0004-6361/201628141.
- J. L. Tinker, J. R. Brownstein, H. Guo, A. Leauthaud, C. Maraston, K. Masters, A. D. Montero-Dorta, D. Thomas, R. Tojeiro, B. Weiner, I. Zehavi, and M. D. Olmstead. The Correlation between Halo Mass and Stellar Mass for the Most Massive Galaxies in the Universe. *ApJ*, 839:121, April 2017. doi: 10.3847/1538-4357/aa6845.
- J. L. Tinker, C. Hahn, Y.-Y. Mao, A. R. Wetzel, and C. Conroy. Halo histories versus galaxy properties at $z = 0$ II: large-scale galactic conformity. *MNRAS*, 477:935–945, June 2018. doi: 10.1093/mnras/sty666.
- S. Tonnesen and R. Cen. Do Not Forget the Forest for the Trees: The Stellar-mass Halo-mass Relation in Different Environments. *ApJ*, 812:104, October 2015. doi: 10.1088/0004-637X/812/2/104.
- A. Toomre. Mergers and Some Consequences. In B. M. Tinsley and R. B. G. Larson, D. Campbell, editors, *Evolution of Galaxies and Stellar Populations*, page 401, 1977.
- L. Tornatore, S. Borgani, K. Dolag, and F. Matteucci. Chemical enrichment of galaxy clusters from hydrodynamical simulations. *MNRAS*, 382:1050–1072, December 2007. doi: 10.1111/j.1365-2966.2007.12070.x.
- S. C. Trager, S. M. Faber, G. Worthey, and J. J. González. The Stellar Population Histories of Local Early-Type Galaxies. I. Population Parameters. *Astronomical Journal*, 119:1645–1676, April 2000. doi: 10.1086/301299.
- T. Treu, R. S. Ellis, J.-P. Kneib, A. Dressler, I. Smail, O. Czoske, A. Oemler, and P. Natarajan. A Wide-Field Hubble Space Telescope Study of the Cluster Cl 0024+16 at $z = 0.4$. I. Morphological Distributions to 5 Mpc Radius. *ApJ*, 591:53–78, July 2003. doi: 10.1086/375314.
- H. E. Trowland, G. F. Lewis, and J. Bland-Hawthorn. The Cosmic History of the Spin of Dark Matter Halos within the Large-scale Structure. *ApJ*, 762:72, January 2013. doi: 10.1088/0004-637X/762/2/72.

- I. Trujillo, A. W. Graham, and N. Caon. On the estimation of galaxy structural parameters: the Sérsic model. *MNRAS*, 326:869–876, September 2001. doi: 10.1046/j.1365-8711.2001.04471.x.
- R. B. Tully, J. R. Mould, and M. Aaronson. A color-magnitude relation for spiral galaxies. *ApJ*, 257:527–537, June 1982. doi: 10.1086/160009.
- H. Übler, T. Naab, L. Oser, M. Aumer, L. V. Sales, and S. D. M. White. Why stellar feedback promotes disc formation in simulated galaxies. *MNRAS*, 443:2092–2111, September 2014. doi: 10.1093/mnras/stu1275.
- M. Valentini, G. Murante, S. Borgani, P. Monaco, A. Bressan, and A. M. Beck. On the effect of galactic outflows in cosmological simulations of disc galaxies. *MNRAS*, 470:3167–3193, September 2017. doi: 10.1093/mnras/stx1352.
- J. van de Sande, N. Scott, J. Bland-Hawthorn, S. Brough, J. J. Bryant, M. Colless, L. Cortese, S. M. Croom, F. d’Eugenio, C. Foster, M. Goodwin, I. S. Konstantopoulos, J. S. Lawrence, R. M. McDermid, A. M. Medling, M. S. Owers, S. N. Richards, and R. Sharp. A relation between the characteristic stellar ages of galaxies and their intrinsic shapes. *Nature Astronomy*, 2:483–488, June 2018. doi: 10.1038/s41550-018-0436-x.
- S. van den Bergh, R. G. Abraham, R. S. Ellis, N. R. Tanvir, B. X. Santiago, and K. G. Glazebrook. A Morphological Catalog of Galaxies in the Hubble deep Field. *Astronomical Journal*, 112:359, August 1996. doi: 10.1086/118020.
- S. van den Bergh, J. G. Cohen, D. W. Hogg, and R. Blandford. Caltech Faint Galaxy Redshift Survey. XIV. Galaxy Morphology in the Hubble Deep Field (North) and Its Flanking Fields to $Z=1.2$. *Astronomical Journal*, 120:2190–2205, November 2000. doi: 10.1086/316828.
- F. C. van den Bosch, T. Abel, R. A. C. Croft, L. Hernquist, and S. D. M. White. The Angular Momentum of Gas in Protogalaxies. I. Implications for the Formation of Disk Galaxies. *ApJ*, 576:21–35, September 2002. doi: 10.1086/341619.
- L. B. van den Hoek and M. A. T. Groenewegen. New theoretical yields of intermediate mass stars. *Astronomy and Astrophysics, Supplement*, 123:305–328, June 1997. doi: 10.1051/aas:1997162.
- E. van Uitert, M. Cacciato, H. Hoekstra, M. Brouwer, C. Sifón, M. Viola, I. Baldry, J. Bland-Hawthorn, S. Brough, M. J. I. Brown, A. Choi, S. P. Driver, T. Erben, C. Heymans, H. Hildebrandt, B. Joachimi, K. Kuijken, J. Liske, J. Loveday, J. McFarland, L. Miller, R. Nakajima, J. Peacock, M. Radovich, A. S. G. Robotham, P. Schneider, G. Sikkema, E. N. Taylor, and G. Verdoes Kleijn. The stellar-to-halo mass relation of GAMA galaxies from 100 deg² of KiDS weak lensing data. *MNRAS*, 459:3251–3270, July 2016. doi: 10.1093/mnras/stw747.
- M. Velander, E. van Uitert, H. Hoekstra, J. Coupon, T. Erben, C. Heymans, H. Hildebrandt, T. D. Kitching, Y. Mellier, L. Miller, L. Van Waerbeke, C. Bonnett, L. Fu,

- S. Giodini, M. J. Hudson, K. Kuijken, B. Rowe, T. Schrabback, and E. Semboloni. CFHTLenS: the relation between galaxy dark matter haloes and baryons from weak gravitational lensing. *MNRAS*, 437:2111–2136, January 2014. doi: 10.1093/mnras/stt2013.
- M. Vitvitska, A. A. Klypin, A. V. Kravtsov, R. H. Wechsler, J. R. Primack, and J. S. Bullock. The Origin of Angular Momentum in Dark Matter Halos. *ApJ*, 581:799–809, December 2002. doi: 10.1086/344361.
- B. Vollmer, O. I. Wong, J. Braine, A. Chung, and J. D. P. Kenney. The influence of the cluster environment on the star formation efficiency of 12 Virgo spiral galaxies. *Astronomy and Astrophysics*, 543:A33, July 2012. doi: 10.1051/0004-6361/201118690.
- D. A. Wake, K. E. Whitaker, I. Labbé, P. G. van Dokkum, M. Franx, R. Quadri, G. Brammer, M. Kriek, B. F. Lundgren, D. Marchesini, and A. Muzzin. Galaxy Clustering in the NEWFIRM Medium Band Survey: The Relationship Between Stellar Mass and Dark Matter Halo Mass at $1 < z < 2$. *ApJ*, 728:46, February 2011. doi: 10.1088/0004-637X/728/1/46.
- F. Walter, E. Brinks, W. J. G. de Blok, F. Bigiel, R. C. Kennicutt, Jr., M. D. Thornley, and A. Leroy. THINGS: The H I Nearby Galaxy Survey. *Astronomical Journal*, 136:2563, December 2008. doi: 10.1088/0004-6256/136/6/2563.
- L. Wang, C. Li, and Y. P. Jing. Clustering Properties and Halo Masses for Central Galaxies in the Local Universe. *ApJ*, 819:58, March 2016. doi: 10.3847/0004-637X/819/1/58.
- W. Wang and S. D. M. White. Satellite abundances around bright isolated galaxies. *MNRAS*, 424:2574–2598, August 2012. doi: 10.1111/j.1365-2966.2012.21256.x.
- W. Wang, L. V. Sales, B. M. B. Henriques, and S. D. M. White. Satellite abundances around bright isolated galaxies - II. Radial distribution and environmental effects. *MNRAS*, 442:1363–1378, August 2014. doi: 10.1093/mnras/stu988.
- C. Welker, J. Devriendt, Y. Dubois, C. Pichon, and S. Peirani. Mergers drive spin swings along the cosmic web. *MNRAS*, 445:L46–L50, November 2014. doi: 10.1093/mnrasl/slu106.
- S. D. M. White. Simulations of merging galaxies. *MNRAS*, 184:185–203, July 1978.
- S. D. M. White. Can mergers make slowly rotating elliptical galaxies. *The Astrophysical Journal, Letters*, 229:L9–L13, April 1979. doi: 10.1086/182920.
- S. D. M. White and M. J. Rees. Core condensation in heavy halos - A two-stage theory for galaxy formation and clustering. *MNRAS*, 183:341–358, May 1978.
- R. P. C. Wiersma, J. Schaye, and B. D. Smith. The effect of photoionization on the cooling rates of enriched, astrophysical plasmas. *MNRAS*, 393:99–107, February 2009. doi: 10.1111/j.1365-2966.2008.14191.x.

- C. Wolf, A. Aragón-Salamanca, M. Balogh, M. Barden, E. F. Bell, M. E. Gray, C. Y. Peng, D. Bacon, F. D. Barazza, A. Böhm, J. A. R. Caldwell, A. Gallazzi, B. Häußler, C. Heymans, K. Jahnke, S. Jogee, E. van Kampen, K. Lane, D. H. McIntosh, K. Meisenheimer, C. Papovich, S. F. Sánchez, A. Taylor, L. Wisotzki, and X. Zheng. The STAGES view of red spirals and dusty red galaxies: mass-dependent quenching of star formation in cluster infall. *MNRAS*, 393:1302–1323, March 2009. doi: 10.1111/j.1365-2966.2008.14204.x.
- S. E. Woosley and T. A. Weaver. The Evolution and Explosion of Massive Stars. II. Explosive Hydrodynamics and Nucleosynthesis. *ApJS*, 101:181, November 1995. doi: 10.1086/192237.
- Thomas Wright. *An Original Theory or New Hypothesis of the Universe*. H. Chapelle, London, 1750.
- L. M. Young. Molecular Gas in Elliptical Galaxies: Distribution and Kinematics. *Astronomical Journal*, 124:788–810, August 2002. doi: 10.1086/341648.
- L. M. Young, M. Bureau, T. A. Davis, F. Combes, R. M. McDermid, K. Alatalo, L. Blitz, M. Bois, F. Bournaud, M. Cappellari, R. L. Davies, P. T. de Zeeuw, E. Emsellem, S. Khochfar, D. Krajnović, H. Kuntschner, P.-Y. Lablanche, R. Morganti, T. Naab, T. Oosterloo, M. Sarzi, N. Scott, P. Serra, and A.-M. Weijmans. The ATLAS^{3D} project - IV. The molecular gas content of early-type galaxies. *MNRAS*, 414:940–967, June 2011. doi: 10.1111/j.1365-2966.2011.18561.x.
- L. M. Young, N. Scott, P. Serra, K. Alatalo, E. Bayet, L. Blitz, M. Bois, F. Bournaud, M. Bureau, A. F. Crocker, M. Cappellari, R. L. Davies, T. A. Davis, P. T. de Zeeuw, P.-A. Duc, E. Emsellem, S. Khochfar, D. Krajnović, H. Kuntschner, R. M. McDermid, R. Morganti, T. Naab, T. Oosterloo, M. Sarzi, and A.-M. Weijmans. The ATLAS^{3D} project - XXVII. Cold gas and the colours and ages of early-type galaxies. *MNRAS*, 444:3408–3426, November 2014. doi: 10.1093/mnras/stt2474.
- J. Zavala, T. Okamoto, and C. S. Frenk. Bulges versus discs: the evolution of angular momentum in cosmological simulations of galaxy formation. *MNRAS*, 387:364–370, June 2008. doi: 10.1111/j.1365-2966.2008.13243.x.
- F. Zwicky. Die Rotverschiebung von extragalaktischen Nebeln. *Helvetica Physica Acta*, 6: 110–127, 1933.

List of Figures

1.1.1	Hubble classes at present day, 4 billion and 11 billion years ago	2
1.1.2	Slow and fast rotators	5
1.2.1	Content of the Universe at CMB and today	7
1.2.2	Fluctuations grow	8
1.2.3	SDSS: Cosmic web	9
1.3.1	Overview of <i>Magneticum Pathfinder</i> boxes	13
2.0.1	Merging galaxies	19
2.1.1	$M_* - j_*$ plane	24
2.2.1	Morphology-density relation	25
2.4.1	Observed rotation curves	28
3.1.1	Disk and spheroidal galaxies in <i>Box4</i>	31
3.1.2	λ -distribution for the different components	34
3.1.3	Angle between the total angular momentum vectors of the different components within 10% R_{vir} for different z	36
3.2.1	$M_{\text{star}}-j_{\text{star}}$ -plane, color-coded according to $\varepsilon_{\text{star}}$	37
3.2.2	Averaged ε -distributions of the stars for four redshifts	39
3.2.3	Mean $\varepsilon_{\text{star}}/\varepsilon_{\text{gas}}/\frac{M_{\text{cold}}}{M_{\text{star}}}$ averaged over all halos in the corresponding b -value bin	40
3.2.4	Distribution of the total λ for the halos according to their b -values	41
3.2.5	Angle between the angular momentum vector of the gas and that of the stars within the innermost 10% of R_{vir} according to their b -values	42
3.3.1	Spheroids/disks within the $M_{\text{star}}-j_{\text{star}}$ plane	45
3.3.2	Spheroids/disks within the $M_{\text{star}}-j_{\text{star}}$ plane at $z = 2$	47
3.3.3	$j_{\text{gas}10}$ vs. $j_{\text{star}10}$ for different z	48
3.3.4	$j_{\text{cold}10}$ vs. j_{DM} for different z	50
3.3.5	Angle between gas and stars, both within 10% R_{vir}	51
3.3.6	Angle between total DM and gas within 10% R_{vir} , total DM and all stars, and total DM and stars within 10% R_{vir}	53
3.4.1	Angle between total DM and DM within 10% R_{vir}	55
3.4.2	λ -distribution of the whole halo for different z	57
3.4.3	Cumulative λ -distribution of the whole halo for different z	59

3.4.4	λ -distribution of the DM for different z	60
3.4.5	λ -distribution of the DM in the DM-only run for different z	62
3.5.1	Cumulative fraction of ε -distribution for the determination of spheroids/disks	62
3.5.2	Fraction of cold gas mass and PDF of alignment between galaxies and their DM halo	63
3.5.3	$\lambda_{\text{star}10}$ vs. λ_{DM} and λ -distribution for stars, both at different z	65
3.5.4	λ of the DM in baryon run vs. DM-only run, and radial profiles of average $j_{\text{DM/cold/hot/star}}$ and mass fractions for spheroids/disks	66
3.5.5	Radial profile of the b -value for spheroids/disks	67
4.2.1	M_{200c} vs. $M_{\text{cen}}/M_{200c}/(\Omega_b/\Omega_m)$	73
4.2.2	$\langle M_{200c} \rangle$ as function of M_{cen} at different z	75
4.2.3	M_{star} vs. M_{vir} , color-coded by b -value and SFR	77
4.2.4	Selection of galaxies: in a cylinder and in a sphere	78
4.3.1	$M_{\text{sat}}/M_{\text{gal}}$ vs. $N_{\text{sat}}/N_{\text{gal}}$ and radial profile of $M_{\text{sat}}/M_{\text{gal}}$	79
4.3.2	$M_{\text{sat}}/M_{\text{gal}}$ vs. $N_{\text{sat}}/N_{\text{gal}}$ for cylinder/sphere for different z	81
4.3.3	Radial profile of $N_{\text{sat}}/N_{\text{gal}}$ for different z	82
4.3.4	Scheme: Selection of host galaxies: companions and centrals	83
4.3.5	$M_{\text{sat}}/M_{\text{gal/com/cen}}$ vs. $N_{\text{sat}}/N_{\text{gal/com/cen}}$ for different z	84
4.3.6	Radial distribution of satellites per host galaxy at redshift $z = 0$ for centrals/companions	86
4.3.7	Average number of satellites as function of M_{vir} for different z	87
4.3.8	$M_{\text{sat}}/M_{\text{gal/com/cen}}$ vs. $N_{\text{sat}}/N_{\text{gal/com/cen}}$ for $z = 2$ in <i>Box3</i>	88
4.4.1	Cumulative fraction of centrals as function of SFR in <i>Box3</i> at $z = 2$	89
4.4.2	Cumulative fraction of satellites as function of SFR/formation redshift	91
4.4.3	Formation redshift vs. SFR for $z = 2$ (<i>Box3</i> and <i>Box4</i>) and $z = 0$ (<i>Box4</i>)	92
4.4.4	Fraction of quiescent galaxies around quiescent/star-forming centrals in <i>Box4</i> at different z	94
4.4.5	Fraction of quiescent galaxies around quiescent/star-forming companions in <i>Box4</i> at different z	95
4.5.1	$N_{\text{sat}}/N_{\text{gal/com/cen}}$ at $z = 2$ in physical units	97
4.5.2	Fraction of quiescent galaxies around quiescent/star-forming centrals in <i>Box4</i> at different z	98
5.2.1	Velocity maps for poster child spheroid	104
5.2.2	Velocity maps for poster child disk	105
5.2.3	b -value distribution of young/middle-aged/old stars for poster child spheroids and disks	106
5.2.4	b -value distribution for spheroids/disks	106
5.2.5	Mass fractions of stellar populations for spheroids/disks	108
5.2.6	b -value distributions for young/middle-aged/old stars for spheroids/interm. and disks at different radii	109

5.2.7	b -value distributions for spheroids/intermediates/disks for young/middle-aged/old stars at different radii	110
5.2.8	Mass fractions of spheroids/intermediates/disks at different radii	111
5.2.9	Mass weighted mean stellar age vs. radius	112
5.2.10	Mass/light weighted mean stellar age vs. M_{star}	113
5.3.1	Mass fractions of stellar populations for individual poster child disks and mass fractions of stellar populations vs. b -value of young stars	115
5.4.1	b -value distributions for slow/fast rotators	116
5.4.2	Mass fractions of stellar populations for slow/fast rotators	117
5.4.3	Mass fractions of stellar populations vs. b -value for slow/fast rotators	117
5.4.4	b -value distributions of young/middle-aged/old stars for regular rotators/non-rotators/distinct core/prolate rotators	118
5.4.5	b -value distributions for regular rotators/non-rotators/distinct core/prolate rotators of young/middle-aged/old stars	119
5.4.6	Mass fractions of stellar populations for regular rotators/non-rotators/distinct core/prolate rotators	120
5.4.7	Mass fractions for individual distinct core galaxies	121
5.5.1	b -value distributions of young/middle-aged/old stars for old (>90% old stars) and young (<40% old stars) galaxies	122
5.5.2	Fractions of poster child galaxies split into more than 90% and less than 40% old stars	123
5.5.3	Fractions of spheroids/intermediates/disks split into more than 90% and less than 40% old stars	123
5.5.4	Fractions of slow/fast rotators split into more than 90% and less than 40% old stars	124
5.5.5	Fractions of kinematical groups split into more than 90% and less than 40% old stars	124
6.1.1	Velocity maps/column density maps/simulated HST broadband images of example galaxies	128
6.2.1	Rotation curves for disks/ gas-rich spheroids	130
6.3.1	DM fractions vs. rotational velocities for $z = 2$ and $z = 0$	132
6.4.1	Surface density/rotation curves/radial velocity dispersion of 3 disks and 1 spheroid	134

List of Tables

1.1	Size and resolution of the <i>Magneticum Pathfinder</i> boxes	14
3.1	λ_0 fit value for different components at different z	33
3.2	Number of halos	44
3.3	Misalignment angles between baryons in center	52
3.4	Misalignment angles of DM	54
3.5	Median and fit values of λ -distributions	58
3.6	K-S test for the λ -distributions	58
3.7	K-S test for the λ_{DM} -distributions	61
3.8	Upper/lower limits for the classification criteria	64
3.9	K-S test for the λ_{star} -distributions	65
4.1	Number of host galaxies	72
4.2	Number of centrals/companions	83
4.3	Number of host galaxies in <i>Box3</i>	88
4.4	Number of centrals/companions split into quiescent/star-forming	93

Danksagung

First of all, I want to thank PD Klaus Dolag for giving me the opportunity to write this thesis and always having time for my questions.

Second, I thank Dr. Rhea-Silvia Remus, for always having time to make unclear things clearer. I really enjoyed traveling with you!

I also want to thank Prof. Andi Burkert, for sharing good ideas.

Then I want to thank my room mate Felix Schulze. I really enjoyed our scientific and also non-scientific discussions :-)

Another thanks to Dr. Lisa Steinborn, Dr. Alex Arth, Marcel Lotz, Oliver Friedrich, Stefan Heigl, Dr. David Hubber, and Andi Schmidt for interesting discussions.

A special thanks to Dr. Tadziu Hoffmann for the technical support.

Generally, I felt really comfortable with all the nice people at the USM, thank you!